Karlsruhe Transactions on Biomedical Engineering
Vol. 6

Raz Miri

Computer Assisted Optimization of Cardiac Resynchronization Therapy

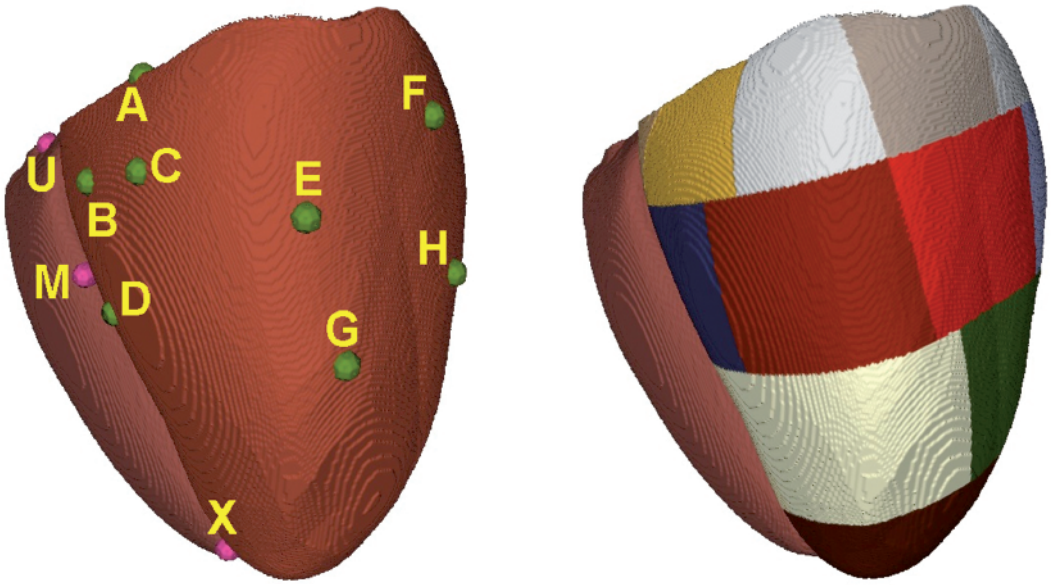

universitätsverlag karlsruhe

Raz Miri

Computer Assisted Optimization of Cardiac Resynchronization Therapy

Vol. 6
Karlsruhe Transactions on Biomedical Engineering

Editor:
Universität Karlsruhe (TH)
Institute of Biomedical Engineering

Computer Assisted Optimization of Cardiac Resynchronization Therapy

by
Raz Miri

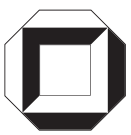

universitätsverlag karlsruhe

Dissertation, Universität Karlsruhe (TH)
Fakultät für Elektrotechnik und Informationstechnik, 2008

Impressum

Universitätsverlag Karlsruhe
c/o Universitätsbibliothek
Straße am Forum 2
D-76131 Karlsruhe
www.uvka.de

Dieses Werk ist unter folgender Creative Commons-Lizenz
lizenziert: http://creativecommons.org/licenses/by-nc-nd/3.0/de/

Universitätsverlag Karlsruhe 2009
Print on Demand

ISSN: 1864-5933
ISBN: 978-3-86644-360-0

Computer Assisted Optimization of Cardiac Resynchronization Therapy

Zur Erlangung des akademischen Grades eines

DOKTOR-INGENIEURS

an der Fakultät für
Elektrotechnik und Informationstechnik
der Universität Fridericiana Karlsruhe
genehmigte

DISSERTATION

von
M. Sc. Raz Miri
geboren in Teheran

Tag der mündlichen Prüfung:	8. Dezember 2008
Hauptreferent:	Prof. Dr. rer. nat. Olaf Dössel
Korreferenten:	Prof. Dr. med. Christian Wolpert
	Prof. i. R. Dr.-Ing. Karsten Meyer-Waarden

Contents

1 Introduction 1
1.1 Motivation 1
1.2 Outline of the Thesis 3

Part I Medical Background and Current State of the Art

2 Medical Foundations 7
2.1 Cardiac Anatomy 7
2.1.1 Cardiac Macroscopic Structure 7
2.1.2 Cardiac Microscopic Structure 13
2.2 Cardiac Cellular Electrophysiology 16
2.2.1 Cell Membrane, Ion Channels and Ion Exchangers 16
2.2.2 Electrophysiological Behavior of Gap Junctions 18
2.2.3 Resting Potential and Action Potential 18
2.2.4 Intracellular Units 20
2.2.5 Cardiac Excitation Conduction System 20
2.2.6 Electrocardiogram (ECG) 21
2.2.7 The Role of Heart Cells in ECG: 21
2.2.8 Depolarization and Repolarization Phases of ECG 24
2.2.9 ECG Leads System 27
2.3 Cardiac Pathology 32
2.3.1 Abnormalities in Rate 32
2.3.2 Abnormalities in Rhythms (Cardiac Arrhythmia) 32
2.3.3 Congestive Heart Failure 35
2.4 Cardiac Function Parameters 37

3 Cardiac Resynchronization Therapy 41
3.1 History of CRT 42
3.2 Etiology of Heart Failure: Indication for CRT 42
3.3 Biventricular Pacing 44

3.3.1 Implantation Techniques . . . 45
3.3.2 Electrode Positions . . . 48
3.3.3 Timing Delays . . . 51
3.4 Optimization Methods Described in Literatures . . . 56
3.4.1 Invasive Measurements . . . 57
3.4.2 Echocardiography . . . 59
3.4.3 Intracardial Electrogram (IEGM) . . . 66
3.4.4 Blood Pressure Measurements . . . 66
3.4.5 Electrocardiography . . . 67
3.5 Conclusion and Unresolved Issues . . . 70

4 Human Heart Modeling . . . 73
4.1 Anatomical Modeling of the Heart . . . 73
4.1.1 Segmentation Algorithms . . . 73
4.1.2 Three Dimensional Model . . . 76
4.1.3 Myocardium Fiber Orientation . . . 77
4.1.4 AHA Classification of Left Ventricle . . . 78
4.2 Modeling the Electrophysiology . . . 79
4.2.1 The Bidomain Model . . . 79
4.2.2 The ten Tusscher Cell Model . . . 81
4.3 Modeling Excitation Propagation . . . 83
4.3.1 Adaptive Cellular Automaton (ACA) . . . 84
4.3.2 Modeling the Excitation Conduction System . . . 85
4.4 Modeling Pathologies . . . 86
4.4.1 Myocardial Infarction: Allocation in AHA Segments . . . 86
4.4.2 Left Bundle Branch Block: Simulation of Blockage in the Excitation Conduction System . . . 87
4.4.3 Reduction of Intra-ventricular Conduction Velocity . . . 87

5 Forward and Inverse Problems of Electrocardiography . . . 89
5.1 Solution of Forward Problem of Electrocardiography . . . 90
5.2 Solution of Inverse Problem of Electrocardiography . . . 93
5.3 Optimization Based Approach . . . 95

Part II Data and Methodology

6 Patient Data . . . 99
6.1 Patients Heart Model . . . 99
6.2 Patients Torso Model . . . 107
6.3 Multichannel ECG Measurements of Patients . . . 109

7 Optimization Algorithms and Methodology 113
7.1 Implementation of BVP into the Models 114
7.2 Optimization of BVP 114
7.2.1 Optimization of Pacing Parameters Based on Isochrones 116
7.2.2 Optimization of Pacing Parameters Based on QRS Duration 116
7.3 Downhill Simplex Algorithm 118
7.4 Statistical Analysis and Student's t Test 119
7.5 Compatibility of the Computer Model with Clinical Data 122
7.5.1 Baseline Wander Correction 123
7.5.2 Denoising 123
7.5.3 QRS Detection 126

Part III Results and Conclusion

8 Results of Simulation 133
8.1 Results for Patient Data Sets 133
8.1.1 Patient-1 133
8.1.2 Patient-2 141
8.1.3 Patient-3 148
8.1.4 Patient-4 155
8.1.5 Patient-5 162
8.1.6 Patient-6 169
8.1.7 Patient-7 176
8.1.8 Patient-8 183
8.1.9 Patient-9 190
8.1.10 Patient-10 197
8.2 Discussion on the Results 204

9 Clinical Verification of the Methods 213
9.1 Verification of the Optimization Method for Patient-11 213
9.1.1 ECG Measurements of Patient-11 213
9.1.2 Parameter Optimization of Patient-11 215
9.1.3 CRT Optimization of Patient-11 219
9.1.4 Forward Calculation of Simulated ECG for Patient-11 after Pacing 220
9.1.5 Discussion on the Results 220
9.2 Verification of the Optimization Method for Patient-12 222
9.2.1 ECG Measurements of Patient-12 223
9.2.2 Parameter Optimization of Patient-12 224
9.2.3 CRT Optimization of Patient-12 228
9.2.4 Forward Calculation of Simulated ECG for Patient-12 after Pacing 229

9.2.5 Discussion on the Results . . . 229
9.3 Verification of the Optimization Method for Patient-13 . . . 232
9.3.1 ECG Measurements of Patient-13 . . . 232
9.3.2 Parameter Optimization of Patient-13 . . . 233
9.3.3 Discussion on the Results . . . 237

10 Discussion . . . 239
10.1 Comparison with Clinical Studies from Literature . . . 239
10.2 Comparison with Clinical Trials in University Hospital Mannheim . . . 240
10.3 Study Limitation . . . 241

11 Conclusions and Future Work . . . 243

A Appendix . . . 245
A.1 Abbreviations . . . 245
A.2 Graphical User Interface for CRT . . . 248
A.3 Graphical User Interface for Clinical Application . . . 250

References . . . 265

Acknowledgments . . . 287

Curriculum Vitae . . . 289

1

Introduction

1.1 Motivation

Cardiovascular diseases are a major cause of mortality in western countries. American Heart Association statistics indicate 5 million individuals in the United States with chronic heart failure [10]. An early diagnosis will reduce the risk factors and enhance the prognosis and life quality of patients.

In patients with heart failure, cardiac resynchronization therapy (CRT) in forms of biventricular pacing (BVP) has emerged as a treatment option for patients with New York Heart Association classification III-IV heart failure. CRT leads to an improvement in hemodynamics and less hospitalization [121, 169]. Nevertheless, about 20 - 30 % of the patients in randomized clinical trials do not respond to biventricular pacing (BVP) therapy. This may be due to a variety of reasons such as patient selection, inappropriate lead positioning or suboptimal pacemaker device programming, especially concerning timing delays [55, 169, 268]. Congestive heart failure leads to a ventricular contraction dyssynchrony which is usually observed in patients with dilated cardiomyopathy and left bundle branch block [10].

The goal of this thesis is to optimize biventricular pacing (BVP) as cardiac resynchronization therapy, using computer based heart models of electrophysiology individualized to the patient in terms of anatomy and pathophysiology. The purpose of BVP optimization is to provide a significant improvement of patient's hemodynamic parameters by increasing cardiac output in patients suffering from left bundle branch block (LBBB) and cardiac contraction dyssynchrony. The three dimensional geometry extracted from the patient imaging data set can be used to create a biophysical detailed computer model of ventricles that incorporates both structural and electrophysiological heterogeneities. Such a model is of great importance because it allows the investigation of underlying electrical excitation conduction in the ventricles at physiological and pathological states.

The present work suggests a pre-operative BVP optimization strategy based on computer simulations, enabling a straightforward parameter optimization for an individual patient. A large amount of work was performed to setup several individual patient models. It can be summarized as follows.

1. Data acquisition: Several MR data sets were acquired from University Hospital Heidelberg and University Hospital Mannheim. The individual models were generated by segmentation of high-resolution imaging techniques (MRI, CT) in order to obtain the patient's anatomy. The model of the left ventricle was subdivided into 17 segments according to the American Heart Association (AHA) suggestion, which simplified the determination of myocardial infarction positions in accordance with the corresponding coronary artery.

2. Heart model creation: A 3D ventricular model was extracted from a series of segmented short axis 2D MR data sets for each patient. The segmentation was done by using interactive deformable contours based on a triangle mesh forming the borders of different parts of the organ. The cardiac conduction system including the bundle of His, left and right bundle branch and Purkinje fibers was implemented into the ventricles. The electrophysiological properties of the heterogeneous ventricle and the pathophysological properties according to the patients symptoms (ischemic cardiomyopathy and left bundle branch block) were implemented into ventricular myocytes.

3. Optimization: Two optimization algorithms were executed for different BVP setups in order to find the optimal electrode positions and timing delays (A-V and V-V delay) for a pathological model, which leads to a depolarization sequence similar to the healthy model. In the first approach, the activation times (isochrones) were optimized while in the second approach, the QRS durations were optimized.

4. Classification: The optimal results achieved by both optimization methods were compared and classified.

5. Torso model creation: A 3D volume conductor model was extracted from a series of segmented frontal axis 2D MR data for each patient.

6. Forward solution: The body surface potential of several patient models based on the optimal BVP setup were simulated. 12 standard ECG channels were extracted in order to estimate the efficacy of the optimization methods for optimal parameters.

7. Clinical measurements: Multichannel ECG measurements were carried out on the patients before and after implantation at University Hospital Mannheim in order to gain the individual patient depolarization sequence by solution of the inverse problem. The

pathophysiological models representing the patient's pathology in addition with the parameters obtained from the inverse problem are implemented into the anatomical models. Hence, accurate simulation of excitation propagation is enabled. Several signal processing algorithms were applied on the ECG signals such as denoising, baseline wander correction, averaging in time, peak and QRS detection.

8. Inverse solution: The epicardial potential of several patient heart models based on the measured pre-implantation body surface potential maps (BSPM) was calculated. This parameter optimization gave a personalized model of the pathology, in which the 64 simulated ECG channels were similar to the measured one.

9. Verification: The simulated ECGs for optimal pacing setup was compared to the measured ECG after implantation. Similarity in QRS duration between measured and simulated channel indicated the success of the method.

The clinical measurements of BSPM will be used to parameterize the computer model of the heart to represent the individual pathology of the patient by solving the inverse problem, which leads to a more realistic and individualized heart model for simulations. The influence of changed pacemaker timings on the BSPM of the patient after implantation is investigated, which will provide valuable information for verification of the BVP optimization method. In addition, given patient specific data by measurements of the body surface potential map and detailed information on contraction delays by Tissue Doppler Imaging (TDI) later can be used to verify the simulation results by forward calculation.

1.2 Outline of the Thesis

Current thesis is divided to three parts. The first five chapters describe the present state of the art, two chapters explain the data acquisition and methodology, two chapters present the results of this work and the last two chapters provide the discussion and conclusion. Chapter 2 provides an overview of the heart's anatomy, electrophysiology and pathology with emphasis on the development of the ECG signal, measuring methods and standard leads system. Current state of the art of therapy is described in chapter 3, which includes recent methods presented in more than one hundred publications. Chapter 4 presents the methods used to create a computer model with respect to anatomy, electrophysiology and pathologies. Then, cellular and excitation propagation models are introduced which are used to precalculate the transmembrane voltage of a myocyte using a number of ionic currents based on a mathematical description. Chapter 5 describes the forward and inverse problem of electrocardiography. Chapter 6 includes the steps of creating the 3 dimensional model of the ventricles for 13 patients data sets. Furthermore, it is explained how the electrophysiology and pathophysiology were modeled in order to investigate the different parameter setups of therapy. Therapy simulation and optimization methods of the cardiac

resynchronization therapy applied in this work are outlined in chapter 7. In addition, a numerical algorithm reducing the time of optimization and several statistical algorithms in order to verify and classify the results are presented. Finally the results of this thesis are presented in chapter 8 and 9 of part III. The discussion and conclusion along with an outlook on future work are explained in chapters 10 and 11, respectively.

Part I

Medical Background and Current State of the Art

2

Medical Foundations

In order to obtain a reliable model of the heart, it is necessary to understand the heart's anatomy and physiology. The anatomy includes the structure of the heart and the cells. The physiology contains the electrophysiological function of the cells and their aggregations. Since the anatomy and physiology are tightly joined together, this chapter considers both anatomy and physiology in the macroscopic and microscopic levels.

2.1 Cardiac Anatomy

The heart, together with the blood vessels compose the cardiovascular system. The main task of the heart is to pump the blood into the vessels in order to supply the body with oxygen and nutrients. This essential task is fulfilled by a periodic contraction and relaxation of the heart. The mechanism of the heart can be investigated through the macroscopic or microscopic point of view in which the anatomy and physiology are correlated.

2.1.1 Cardiac Macroscopic Structure

The heart is a hollow organ with the size of a human fist, which is situated near the center of the chest cavity between the right and left lung. The main axis of the heart is oriented from back-top-right to front-bottom-left with the base at the upper and the apex at the lower end. The heart is supported inside a membranous structure, the pericardial sac. The outer layer of the pericardium surrounds the roots of heart's major blood vessels and is attached by ligaments to the spinal column, diaphragm and other parts of the body. The inner layer of the pericardium is attached to the heart muscle. A coating of fluid separates the two membrane layers, letting the heart move as it beats [14, 23, 108, 241, 266].

There are four major chambers in the heart as well as various accessory tissues (see figure 2.1). The heart is divided into left and right halfes by the septal wall, so there are no internal connections between the opposing chambers through which blood may flow. The larger, lower, thicker walled chambers are the left ventricle and the right ventricle, while the smaller upper chambers are the left atrium and the right atrium. The atria are relatively

thin walled chambers, which collect the blood before feeding it into the ventricles upon contraction.

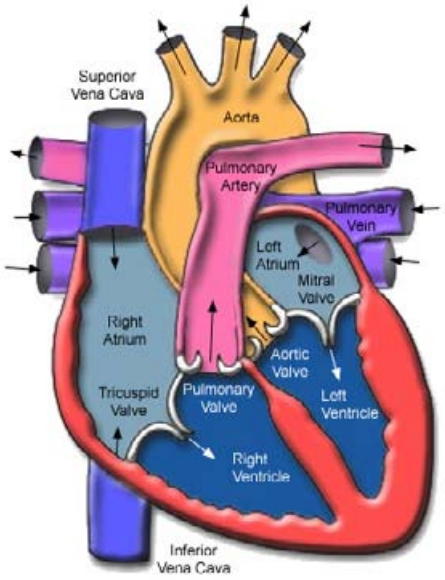

Figure 2.1. The anatomy of the heart and the blood flow. The right and the left atrium are located at the upper half of the heart. The left and the right ventricle are at the lower half of the heart. The venous blood flows through the vena cava superior and vena cava inferior into the right atrium. During the contraction of the atria, the blood is pressed from the atria through the tricuspid and bicuspid valve into the ventricles. During the contraction of the ventricles, the blood from the right ventricle is pumped through the pulmonary circulation into the left atrium; the blood from the left ventricle is ejected into the body circulation through the aorta [115].

In contrast, the ventricles are larger chambers that forcefully contract. Therefore, the heart is separated into two functionally and anatomically similar structures: the right and the left halfes. The right half collects the deoxygenated blood from the body and pumps it to the lungs. The left half receives the oxygenated blood from the lungs to deliver it to the body. Since the circulation path into the body is much longer than the circulation path of the lung, the left half has to generate a higher pressure and is therefore larger [216, 233].

2.1.1.1 Atria and Ventricles

The atria form the upper part of the heart. The right and left atrium are separated by the interatriale septum. Both atria have an appendage, which is capable to store the blood. This leads to a capacity enlargement of the atria. The structure of the atria is developed in a way that the left and right atrium regions get stimulated closely together [222, 241]. The right atrium consists of two parts:

1. A posterior, smooth walled part in which the superior and inferior vena cava enter
2. A very thin walled part, which constitutes the embryonic right atrium

The left atrium consists mainly of a smooth walled sac, the transverse axis of which is somewhat larger than the vertical and sagittal axes. The wall of the left atrium is distinctly

thicker than that of the right atrium. A ridge of muscle called crista terminalis (CT) with a thickness of $5-8\ mm$ is located at the inner side of the right atrium (see figure 2.2). The triangular shaped superior portion of the right atrium called right auricle is filled with pectinate muscles. The left auricle is a continuation of the left upper anterior part of the left atrium with a variable shape. The two ventricles form the lower part of the heart. The right and left ventricles are also separated by a septum. The right ventricular cavity can be divided into a posteroinferior inflow portion including the tricuspid valve and an anterosuperior outflow portion from which the pulmonary trunk originates. A number of papillary muscles attach the tricuspid valve to the right ventricular wall. The pulmonary trunk arises superiorly from the right ventricle and passes backwards and slightly upward [191, 241].

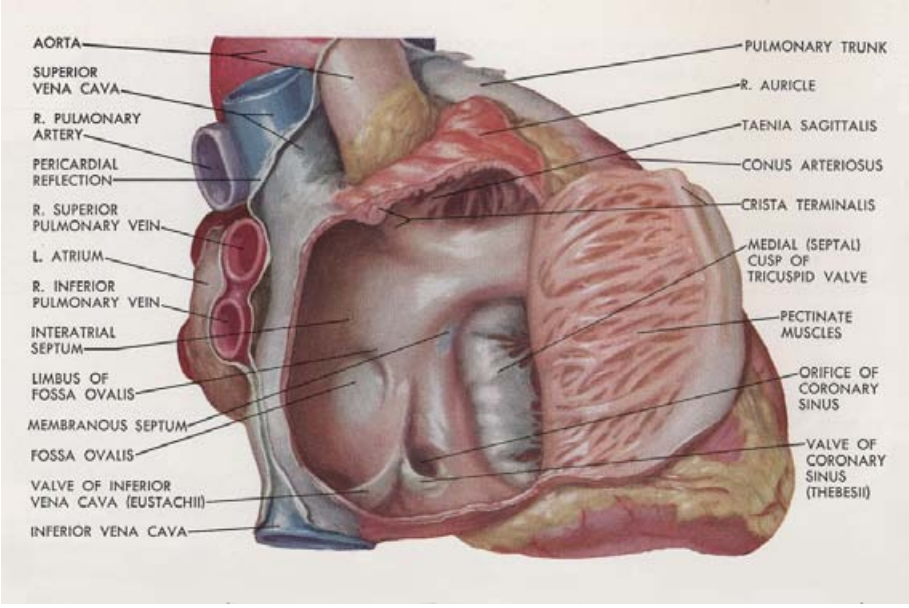

Figure 2.2. View of the right atrium: Interatrial septum, pectinate muscles and tricuspid valve are demonstrated [191].

The left ventricle, which is egg shaped has a thicker wall compared to the right ventricular wall. The mitral and aortic valves are close to each other (see figure 2.3). Papillary muscles are connected on one side to the subendocardial myocardium and on the other side to the mitral valve [171, 191, 241].

The atrio-ventricular valves are composed of similar components: leaflets (3 leaflets for tricuspid valve, 2 leaflets for the bicuspid valve), a fibrous ring that encircles the valve called annulus and fibrous ligaments (chordae tendineae) which connect the leaflets to the papillary muscles which in turn flex during the contraction of the ventricles to stabilize the atrio-ventricular valves. The semilunar valves have simpler structures than the atrio-

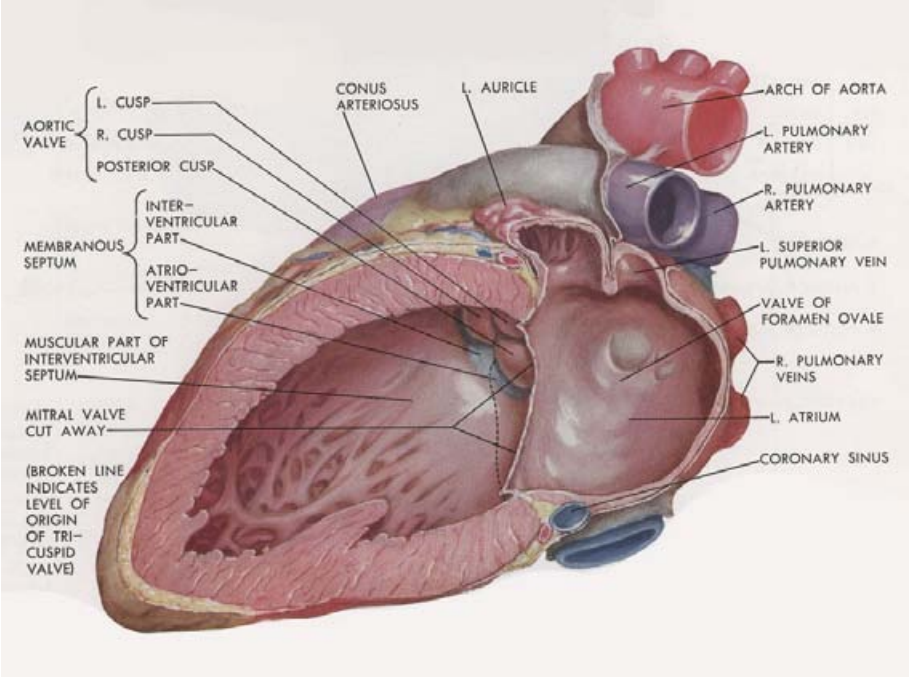

Figure 2.3. View of the left ventricle. Papillary muscles and mitral valve are demonstrated [191].

ventricular valves. The pulmonic and aortic valves are identical although the aortic valve consists of a thicker fibrous structure than the pulmonic valve [191].

The valves are responsible for ensuring the unidirectional blood flow and prevent the back flow of blood. The atrio-ventricular valves are closed during the ventricular systole while the semilunar valves are open to ensure the blood flow in the arteries (see figure 2.4).

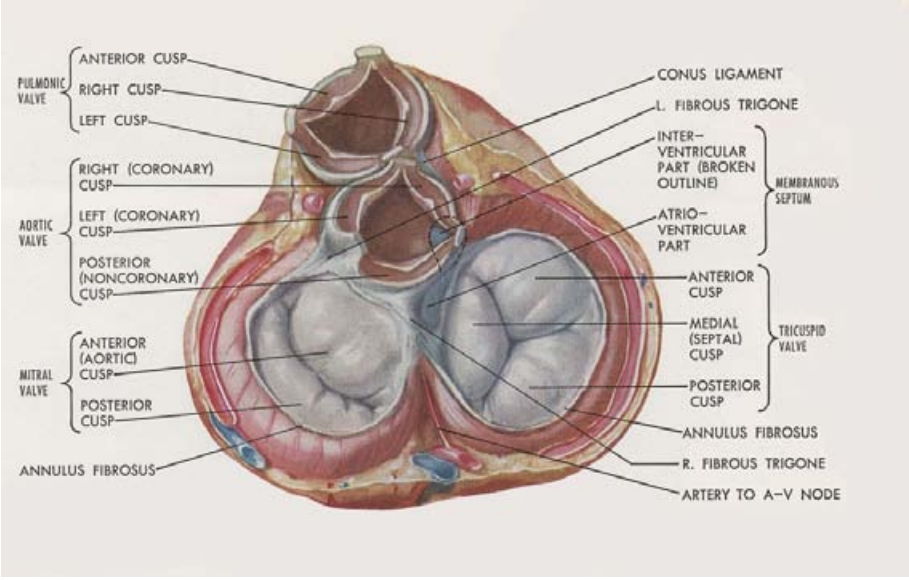

Figure 2.4. Heart in systole. The atrio-ventricular valves are closed [191].

In the ventricular diastole phase, the atrio-ventricular valves are open to ensure the blood flows from atria to ventricles (see figure 2.5).

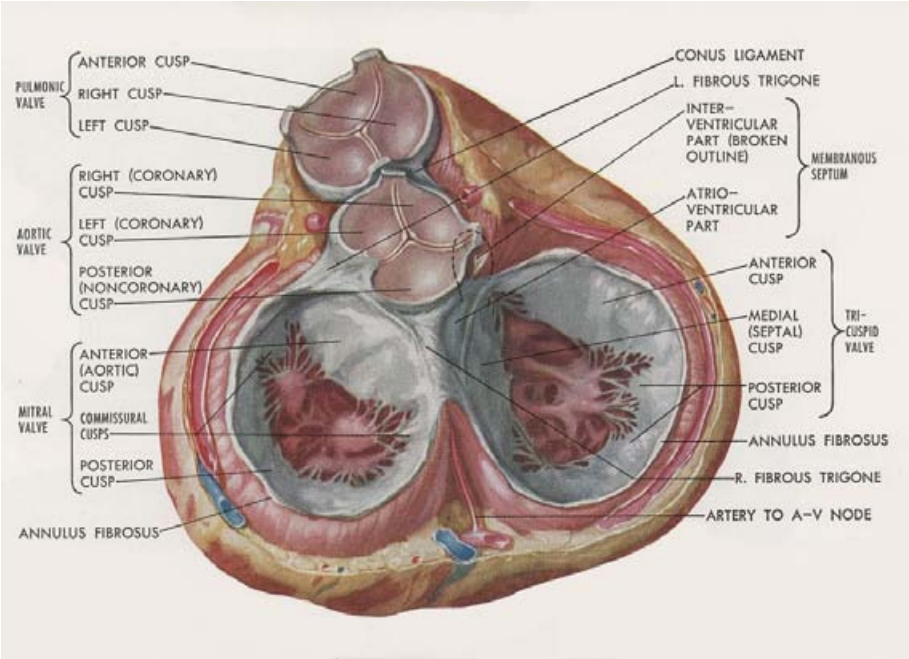

Figure 2.5. Heart in diastole. The semilunar valves are closed [191].

2.1.1.2 Blood Vessels

The blood circulates through the arteries in order to provide oxygen and nutrients to the body. After passing through the body, the blood loaded with carbon dioxide and waste substances flows through the vena cava superior and vena cava inferior to the right atrium. When the ventricles relax, blood from the right atrium passes through the tricuspid valve into the right ventricle. When the ventricles contract, blood from the right ventricle is pumped through the pulmonic valve into the lungs in order to reload with oxygen and remove carbon dioxide. The oxygenated blood then returns to the left atrium and passes through the mitral valve into the left ventricle. Blood is pumped by the left ventricle across the aortic valve into the aorta and the arteries of the body. In general, arteries are blood vessels that carry blood away from the heart. For instance, the pulmonary arteries carry blood from the heart to the lungs. In the circulatory system, a vein is a blood vessel that carries blood towards the heart. All veins except the pulmonary veins transport deoxygenated blood (see figure 2.6).

The heart's oxygen supply is provided by the coronary vessels, especially by two coronary arteries: the left coronary artery and the right coronary artery (see figure 2.7). The left coronary artery, which supplies blood to the left ventricle and left atrium, originates from the aorta above the left cusp of the aortic valve. The left coronary artery (LCA) then

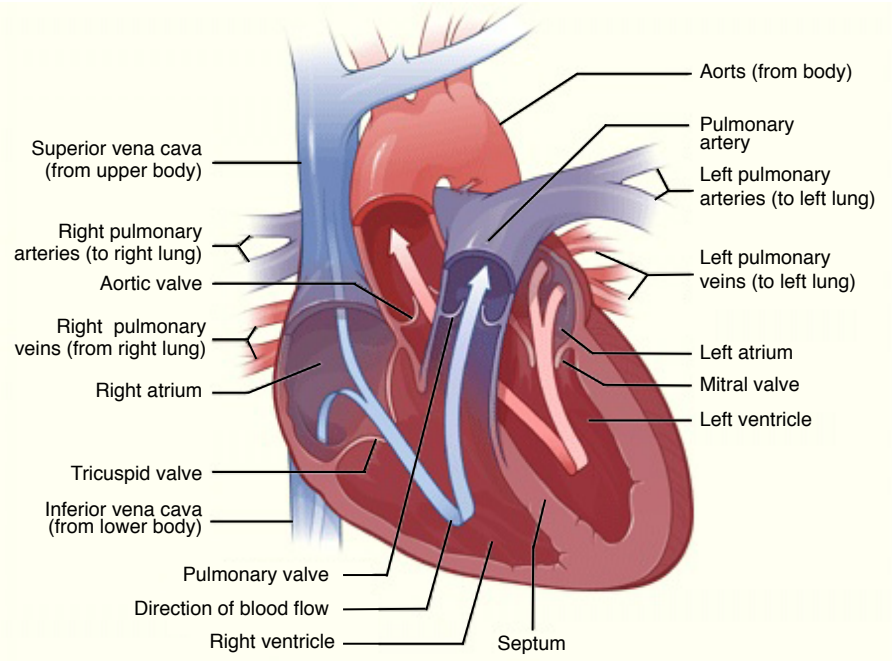

Figure 2.6. Schematic drawing of the connection of the heart's major vessels. On the left side, the vena cava superior and the vena cava inferior are connected to the right atrium. From the right ventricle, the pulmonary artery leads to the pulmonary circulation. On the right side of the schematic, the pulmonary vein returns from the lungs. The aorta carries the blood from the left ventricle into the body circulation [116].

bifurcates into the left anterior descending artery (LAD) and the left circumflex artery (LCX). The LAD branches off the left coronary artery and supplies blood to the front of the left side of the heart.

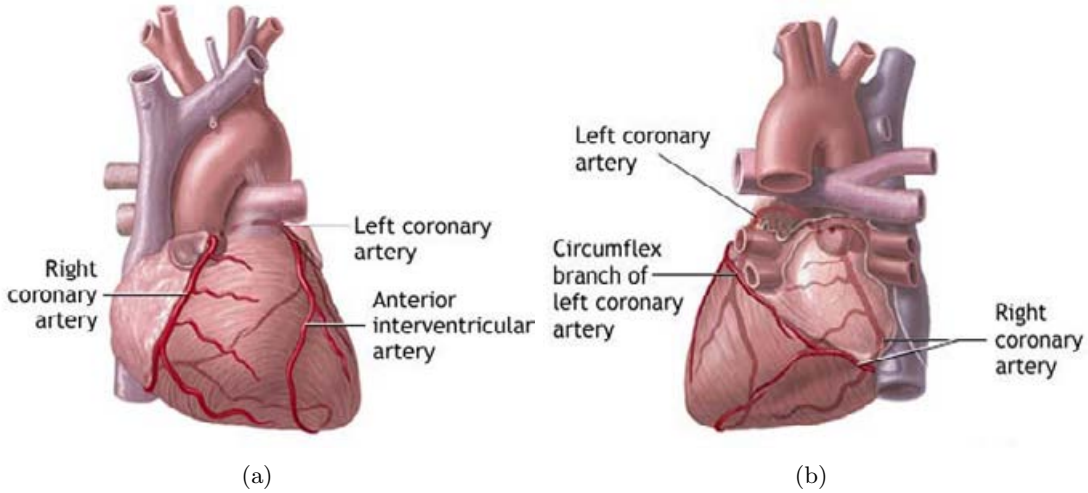

Figure 2.7. Heart and coronary arteries [172]: (a) Anterior view. (b) Posterior view.

The LCX, which branches off the left coronary artery and encircles the heart muscle supplies blood to the lateral side and back of the heart. The right coronary artery (RCA)

which divides into the right posterior descending and acute marginal arteries, supplies blood to the right ventricle, right atrium, and sinoatrial node (cluster of cells in the right atrial wall that regulate the heart's rhythmic rate).

2.1.2 Cardiac Microscopic Structure

The heart consists of millions of cells called myocardial cells. The structure of the myocardial cells is dependent on the electrophysiological function of the specific cell. The vast majority of these cells belong to the working myocardium, which contracts upon excitation. In the working myocardium, the excitation is passed from cell to cell through direct intercellular connections, called gap junctions. A part of the myocardial cells is specialized in electrical excitation initiation and conduction. These cells form the excitation conduction system, which consists of the sinus node, the atrio-ventricular node, the Purkinje fibers and the His bundles. The excitation conduction system is described in section 2.2.5.

2.1.2.1 Myocytes

A myocyte is a cell of the myocardium and hence the basic unit of the heart's muscle. A single working myocyte is approximately $50 - 120\ \mu m$ long and has a diameter of $5 - 25\ \mu m$ [23].

The myocytes are joined together into long fibers by the intercalated discs. The myocytes belonging to the working myocardium are roughly cylindrical shaped cells, which provide the myocardial contraction by generating mechanical tension. The tension is generated by intracellular contractile structures, which produce the necessary force by using adenosine triphosphat (ATP) and calcium ions [192].

The contractile structures of a myocyte consist of longitudinal arranged formations, called myofibrilles. The myofibrilles take up the whole length of a myocyte and are divided into sarcomeres by so-called Z-discs (see figure 2.8). The sarcomeres are the fundamental structural and functional elements of the myofibrilles [192].

The sarcomeres contain filament-shaped structures called the myofilaments. There are two types of myofilaments: thick and thin myofilaments. Within a sarcomere, thick and thin myofilaments overlap, depending on the current state of contraction (see figure 2.9).

The thin myofilamants are formed by actin, while the thick myofilaments consist of myosin. Inside the overlapping zone, the mechanical force is produced using ATP and calcium ions [192]. In order to ensure the supply of the myocytes with oxygen and nutrients, every myocyte is connected to one or more capillary vessels (see figure 2.10).

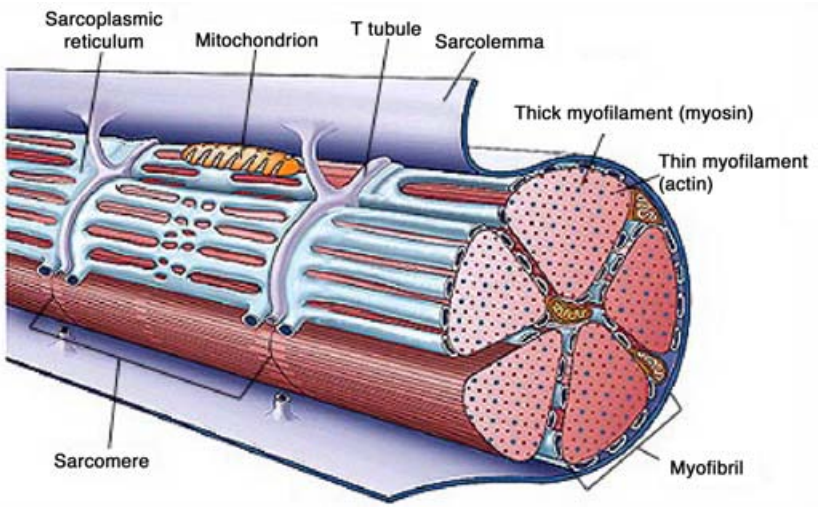

Figure 2.8. A schematic overview of myocardium. The figure shows the myocytes connected into long fibers by the intercalated discs. Every myocyte contains the usual cell organelles like nucleus and mitochondria. The myofibrils are located in the interior of the myocytes. The myofibrils consist of thick and thin myofilaments, which form the contractile structure [188].

The myocyte is sourrounded by a cell membrane in order to separate the interior of the cell (intracellular space) and the surrounding medium (extracellular space). Referring to myocytes, the cell membrane is called sarcolemma and has specific electrophysiological

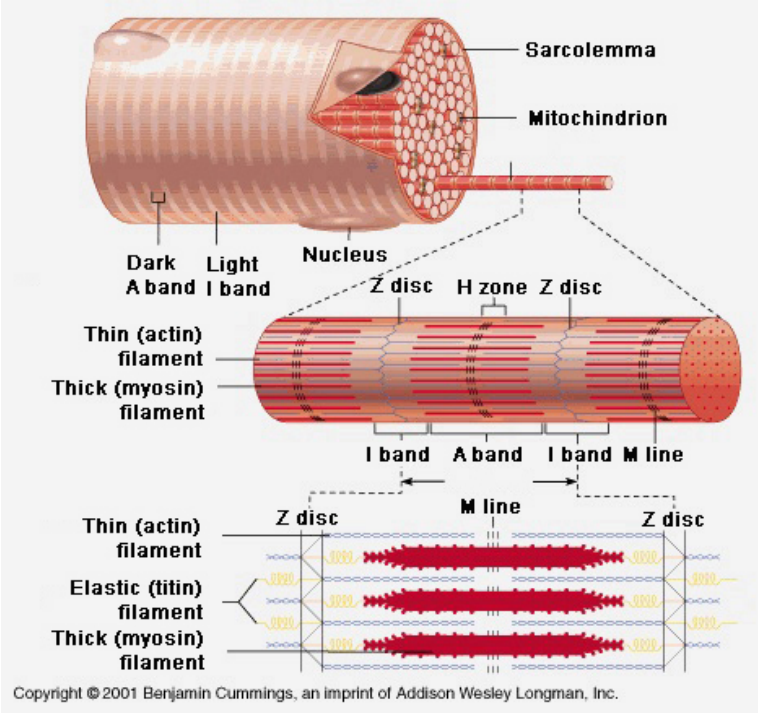

Figure 2.9. A schematic representing the structure of the sarcomeres, myofibrilles and myofilaments. A sarcomere is limited by the Z-discs. Within a sarcomere, there are thin and thick myofilaments, which overlap. The upper figure shows a myofibril in a relaxed state. The overlap of the thin and thick myofilaments is small. The lower figure shows the myofibril in the contracted state. The overlap of the myofilaments results in a contraction of the sarcomere [12].

properties. The sarcolemma is a semi-permeable membrane formed by a pospholipid bilayer of around $3-5\ \mu m$ thickness. The phospholipids molecules have two hydrophobic tails attached to a hydrophilic head. In the phospholipid bilayer membrane, the hydrophobic tails are joined to each other inside the membrane. Hence, the hydrophilic heads of the phospholipid molecules are located on the interior and exterior surface of the membrane [87].

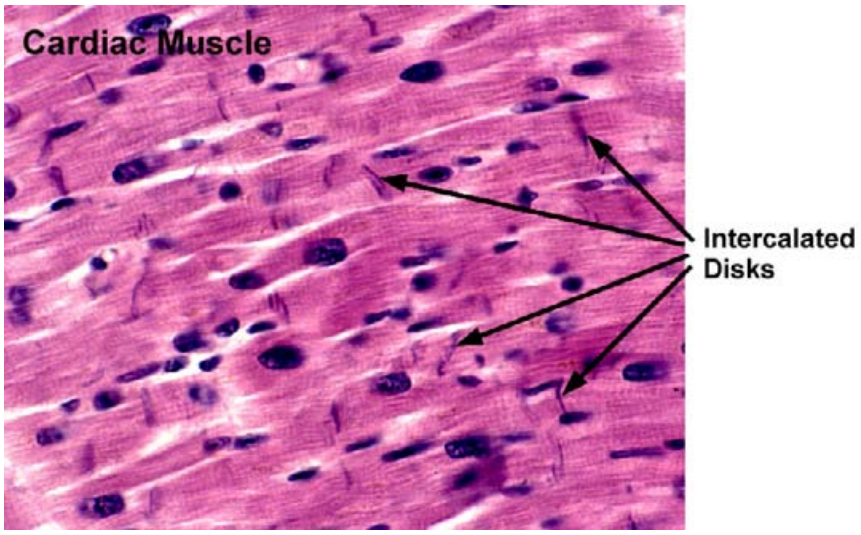

Figure 2.10. A microscopic photography of myocytes surrounded by capillary vessels. Each cell is supplied by capillaries [13].

There are a number of transmembrane proteins essential for the cell's function, such as ionic channels, ionic pump proteins, exchangers and receptors. The ionic channels are usually specific to certain ion types, such as potassium, sodium and calcium.

2.1.2.2 Gap Junctions

Gap junctions are proteins connecting the intracellular spaces of two neighboring myocytes. The gap junctions are usually located at the intercalated discs of the myocytes. They provide a low-ohmic electrical coupling and additionally a mechanical connection between the intracellular spaces of the connected cells. Since the gap junctions have a barrel-shaped structure with a diameter of typically $1.5-2\ nm$, which is much larger than the typical diameter of an ion, free diffusion of ions through the junction is possible without any ion selectivity. In addition, metabolites and cell communication transmitters can be exchanged through the channel [271, 279]. Additionally, the pH value of the extracellular medium affects the gap junction's resistivity [197]. Gap junctions consist of two so-called connexons, each provided by one cell. In myocardium, a gap junction typically has a length of $2-12\ nm$ and bridges a gap of $2-3\ nm$ (see figure 2.11) [74, 75, 137, 185, 241, 290].

Additionally, longitudinal and transversal gap junctions can be differed. A longitudinal gap junction is orientated in parallel with the myocyte, while a transversal gap junction is orientated perpendicular to the myocyte.

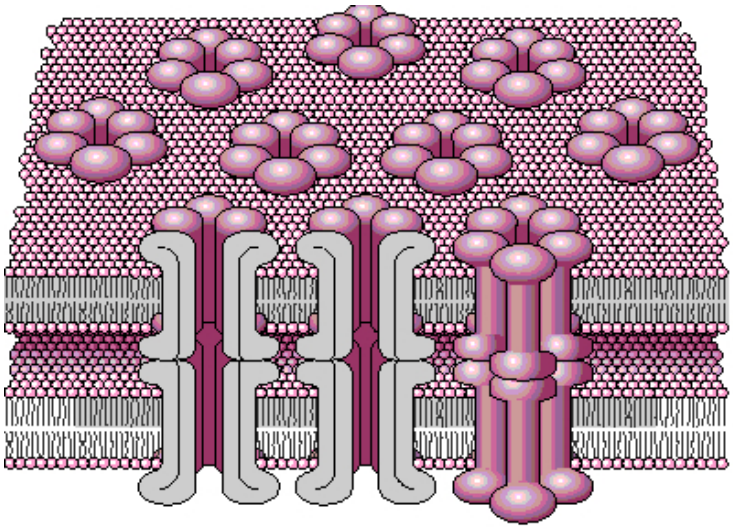

Figure 2.11. Schematic drawing of gap junctions providing electrical and mechanical coupling between the intercellular spaces of cardiac cells. The gap junctions consist of two connexons, each originating from one cell [138].

2.2 Cardiac Cellular Electrophysiology

The periodic mechanical contraction of the heart is the result of a complex interaction of several different types of cardiomyocytes. The electrophysiological properties of specialized myocytes initiate the electrical excitation, conduct the excitation along certain paths in the heart and produce mechanical tension via the electro-mechanical coupling in the myocytes of the working myocardium.

In the following sections, the first description refers to the cell membrane with its embedded ion pores. Then, the electrophysiological behavior of the gap junctions is discussed. Afterwards, the generation of transmembrane voltages and action potentials is explained. An overview over the excitation conduction system and the ECG can be found at section 2.2.6.

2.2.1 Cell Membrane, Ion Channels and Ion Exchangers

As discussed in section 2.1.2.1, the sarcolemma of the cardiac myocytes contains ion channels, ion pumps and exchangers, enabling an exchange of ions between the extracellular space and the myocyte's intracellular space. The ions most relevant in cardiac electrophysiological transport phenomenon are Na^+, K^+ and Ca^{2+} [216]. Ion channels provide

a passive gate through the sarcolemma for ions. The driving forces for ion channels are chemical concentration gradients and electrical gradients across the cell membrane. The concentration gradient and the electrical gradient sum up to the electrochemical gradient.

Ion channels are selective for a distinct type of ion. Ion selectivity of the channels is achieved by chemical reactions. In aqueous solutions, ions are surrounded by water dipoles electrostatically attached to the ion. In order to enable passage of the ion through the channel, the ion must be dehydrated by the binding energy between the channel and the ion. The different hydration energies of different ions in cooperation with the fixed binding energy of the channel enable ion selectivity in such a way that only the ion matching to the channel is dehydrated and passes through the channel. Important ion channels are the Na^+, the K^+ and the Ca^{2+} channels. A schematic of an ion channel can be found in figure 2.12 [241]. Ion channels can be gated, which means they can be activated and deactivated. Transmembrane voltage and several (neuro-)transmitter receptors are possible means for providing the gating trigger of the channels [32, 236, 246, 276].

Ionic pumps transport ions against the electrochemical gradient by using energy in terms of ATP. Ionic pumps produce an electrochemical gradient of specific ions, which is used as the driving force for passive ion channels. Important ion pumps are the (Na-K) pump and the Ca^{2+} pump, both located in the sarcolemma [241]. Ionic exchangers are capable of exchanging ions in an aqueous solution by using either chemical or electrical gradients. Ion exchangers are considered as a means of "secondary active" transport since they transport an ion actively and simultaneously transport an ion passively. An important example is the (Na/Ca) exchanger located in the sarcolemma [241].

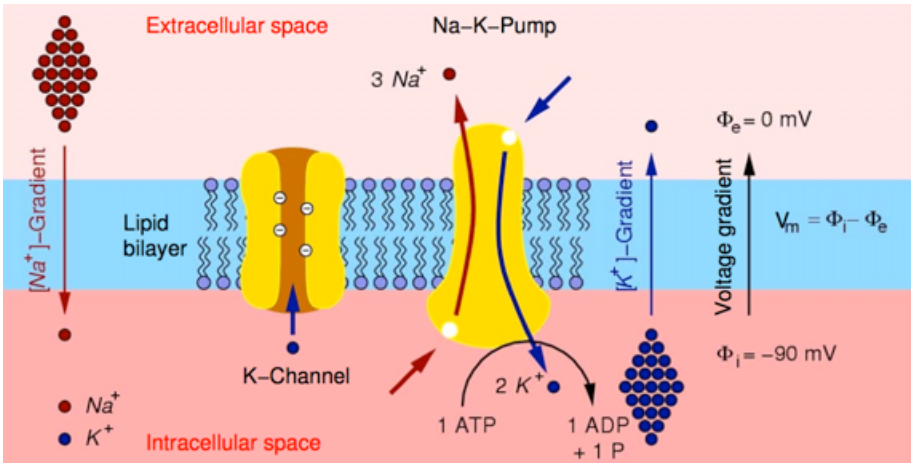

Figure 2.12. A schematic showing the components of a cell membrane. The cell membrane consists of the phospholipide bilayer, in which ion channels and ion pumps are embedded. Red and blue circles characterize Na^+ and K^+ ions, respectively. The Na-K pump and the one exemplary K^+ channel as transmembrane proteins are marked in yellow. The binding sites of the K^+ channel are displayed with a minus sign. The thin arrows across the membrane depict the direction of concentration and voltage gradients. The thick arrow shows the direction of the ion flow through the membrane proteins [87, 241].

2.2.2 Electrophysiological Behavior of Gap Junctions

As discussed in section 2.1.2.2, the myocytes of the working myocardium are connected by gap junctions. The gap junctions conduct the excitation from one cell to another. The resistivity of the gap junctions is dependent on the concentration of several ions, like the $H^+, Ca^{2+}, Na^+, Mg^{2+}$.

Since the pH value of the extracellular medium affects the gap junction's resistivity [197], the resistivity of gap junctions can be altered by drugs affecting the ion concentrations, or by ischemia, which changes the pH value of the extracellular medium.

2.2.3 Resting Potential and Action Potential

Due to the activity of ion pumps and selective ion channels, the concentrations of ions differ between the extracellular and intracellular space (see table 2.1). This electrochemical gradient of ions causes a potential difference across the cell membrane called the transmembrane voltage. The transmembrane voltage is defined as:

$$V_m = \phi_i - \phi_e \tag{2.1}$$

where ϕ_i is the intracellular potential and ϕ_e the extracellular potential.

Ion	Concentration *(mM)*
$[Na^+]_i$	10
$[Na^+]_e$	140
$[K^+]_i$	145
$[K^+]_e$	5.4
$[Ca^{2+}]_i$	0.00012
$[Ca^{2+}]_e$	1.8

Table 2.1. Intracellular and extracellular concentrations of several ions [216].

As discussed in section 2.2.1, driving forces for an ion exchange can be the chemical gradient or the electrical gradient. Since ions have a charge (valence z), every variation in the chemical gradient leads to a change of the electrical gradient in a way, that it opposes the chemical gradient.

For every specific type of ion, there exists an equilibrium voltage, where the chemical and electrical forces are in equilibrium. The equilibrium voltage for a specific ion of a resting cell can be described by the Nernst equation. The Nernst potential E_x for an ion x calculates as:

$$E_x = \frac{RT}{z_x F}\, ln\, \frac{[x]_e}{[x]_i} \tag{2.2}$$

In this equation, R is the universal gas constant, T the absolute temperature, z_x the valance of the ion x, F the Faraday's constant, $[x]_e$ and $[x]_i$ are the extracellular and intracellular concentration of the ion x, respectively [216]. The equation 2.2 is valid if only one ion can pass the membrane. The Nernst equation can be expanded to many types of ions, called the Goldman-Hodgkin-Katz equation. In this equation, each ion concentration $[x]$ is associated with the corresponding permeability of the membrane P_x. The transmembrane potential can be calculated as [103, 125]:

$$E = \frac{RT}{F}\, ln\, \frac{P_{K^+}[K^+]_e + P_{Na^+}[Na^+]_e + P_{Cl^-}[Cl^-]_i}{P_{K^+}[K^+]_i + P_{Na^+}[Na^+]_i + P_{Cl^-}[Cl^-]_e} \tag{2.3}$$

The permeability P_K, P_{Na} and P_{Cl} of K^+, Na^+ and Cl^- ions, respectively, is given by:

$$P_x = \frac{D_x\, \beta_x}{\Delta x} \tag{2.4}$$

with the diffusion coefficent D_x of the ion x, the water-membrane partition coefficient β_x and the thickness Δx of the membrane. The equation 2.3 is valid if multiple ions can pass the membrane.

The resting voltage for cardiac myocytes ranges between $-30\ mV$ and $-100\ mV$, depending on the cell type [88].

Excitable cells, such as nervous cells and cardiac tissue cells, can be depolarized by an external stimulus. The cell reacts with a so-called action potential, which is caused by a sequence of ion fluxes through the cell membrane. During the action potential, the transmembrane voltage rises quickly up to a positive voltage followed by a slow recovery of the equilibrium state. A typical action potential for a working myocardium myocyte is shown in figure 2.13.

The action potential can be divided into 5 typical phases. Phase 0 is the rapid depolarization of the cell. It is caused by a rapid influx of Na^+ ions into the cell. In phase 1, the cell performs a rapid partial repolarization. The Na^+ channels are closed and a slow outflow of K^+ ions causes the repolarization. The flat plateau of the action potential at phase 2 is caused by an inflow of Ca^{2+} ions. The K^+ outflow continues and when the Ca^{2+} inflow stops in phase 3, the cell is repolarized to its resting transmembrane potential (phase 4) [216].

In order to trigger an action potential, the stimulus must be lager than a certain level, which is called the threshold potential. For sub-threshold stimuli only a passive response

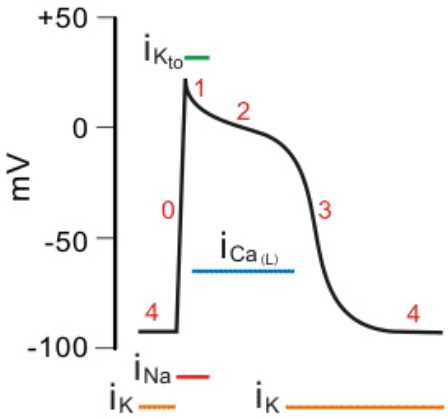

Figure 2.13. Typical action potential of a myocyte with the 5 typical phases. Phase 4 is the resting potential in the beginning and in the end. Phase 0 is the rapid upstroke caused by an Na^+ influx. The fast repolarization in phase 1 is caused by a K^+ outflux. The plateau of phase 2 is caused by a Ca^{2+} influx. The repolarization to equilibrium voltage in phase 3 is caused by a K^+ outflux [7].

occurs to reestablish the equilibrium voltage. For a stimulus larger than the threshold potential, an active response is generated and an action potential will occur [216].

2.2.4 Intracellular Units

In myocytes, the sarcoplasmatic recticulum (SR) plays an important role in intracellular regulation of the calcium ions concentration. During contraction, the sarcoplasmatic recticulum releases Ca^{2+} ions in order to enable coupling between actin and myosin. In relaxation phase, the SR collects the Ca^{2+} ion in order to decrease the intracellular Ca^{2+} concentration and enable relaxation.

2.2.5 Cardiac Excitation Conduction System

The cardiac excitation conduction system consists of pacemakers and conducting tissues. Pacemaker cells are capable of periodical spontaneous depolarization. The main pacemaker of the heart is the sinus-atrial (SA) node located in the right atrium. The rate of pacemaking can be controlled by nervous signals. After depolarization of the pacemaker cells in the sinus-atrial node, the excitation propagates through both atria until it reaches the antrio-ventricular node (AV node). In a healthy heart, the AV node is the only conducting connection between the atria and the ventricles.

The AV node delays the propagation of the excitation from the atria to the ventricles and acts as a frequency limiter. If the rate of pacemaking of the sinus-atrial node gets too high (approx. 180 bpm), the AV node limits the excitation frequency of the ventricles in order to ensure the pumping function of the heart. After passing the AV node, the excitation is propagated by the ventricular conduction system, consisting of the bundle of His and the Purkinje fibers. The excitation is conducted down the septum and from there it is

branched to the left and right ventricle. The conduction system consists of specialized cells ensuring rapid conduction [216]. The sequence of conduction is listed in table 2.2 and visualized in figure 2.14.

Normal sequence of excitation	Conduction velocity ($m\,s^{-1}$)	Time for impulse to traverse structure (s)
SA node	< 0.01	⊤
↓		0.03
Atrial myocardium	1.0-1.2	⊥
↓		
AV node	0.02-0.05	0.09
↓		
Bundle of His	1.2-2.0	⊤
↓		0.04
Bundle branches	⊤	⊥
↓	1.5-4.0	
Purkinje network	⊥	0.03
↓		
Ventricular myocardium	0.3-0.5	0.3

Table 2.2. Sequence of cardiac excitation with corresponding conduction velocities and intrinsic pacemaking frequencies [216].

2.2.6 Electrocardiogram (ECG)

The electrical activity generated in the heart can be recorded on the body surface providing a non-invasive measurement of cardiac electrical function [147]. The ECG signal commonly shows which part of the heart is currently depolarizing and repolarizing. Thus, the ECG signal reflects the combined effect of depolarization and repolarization for all the individual cells in the heart. A typical ECG tracing of a normal heart beat consists of a P wave, a QRS complex and a T wave. The P wave represents the depolarization of the atria from the sinus-atrial node to the AV node, which is a signature of the current atrial contraction. The QRS complex represents the depolarization of the ventricles, which corresponds to the current ventricular contraction. Ventricular depolarization typically occurs rapidly with duration of 0.06 to 0.1 s. The repolarization of the ventricles generates the T wave in the ECG [111]. A typical ECG, as it would be recorded by a modern ECG recording system, is shown in figure 2.14. More detailed information about ECG and standard lead system will be described as follows.

2.2.7 The Role of Heart Cells in ECG:

The heart consists of three types of cells [267]:

Pacemaker cells, which are small cells approximately 5 to 10 μm size as the cells that normally initiate depolarization of the heart. These cells are frequently able to depolarize

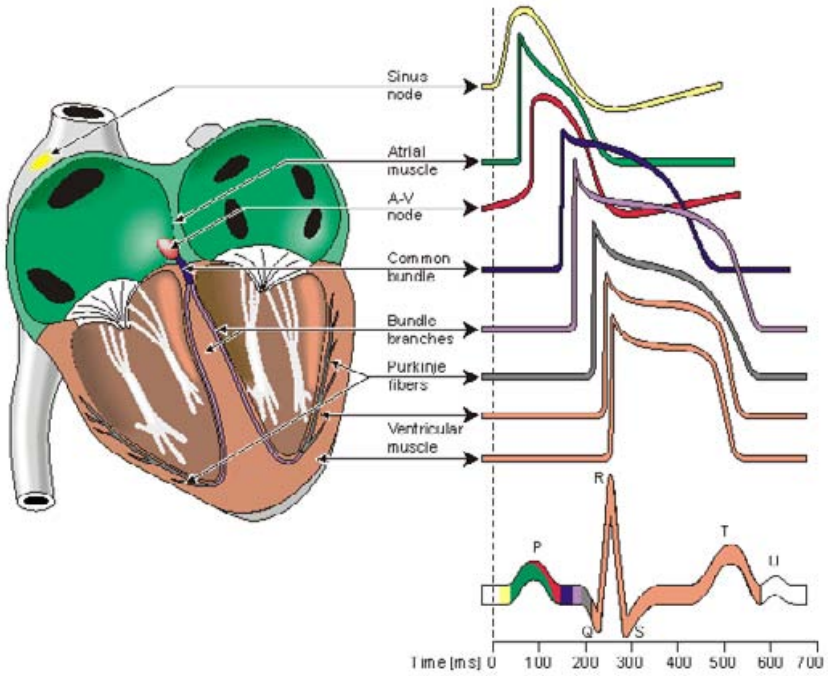

Figure 2.14. Schematic of the cardiac excitation as it propagates from the SA-node through the atria to the AV-node and from there down the septum into the ventricles [67]. Schematic of ECG. The P wave is caused by the depolarization of the atria. Repolarization of the atria and depolarization of the ventricles generates the QRS complex. The repolarization of the ventricles is represented by the T wave [91].

spontaneously at a particular rate. The rate of depolarization is determined by the intrinsic electrical characteristics of the cell and modified by an external neurohormonal input. Each spontaneous depolarization works as the source of the depolarization wave, which initiates one complete cycle of cardiac contraction and relaxation.

An action potential (AP) could be registered by recording one electrical cycle of depolarization and repolarization from a single cell. With each spontaneous depolarization a new AP is generated which in turn stimulates neighboring cells to depolarize and generate their own AP. The AP of a cardiac pacemaker cell differs from the generic AP, since it does not have a true resting potential. Its electrical charge drops to a minimal negative potential, which maintains only for a short time. Afterward it rises gradually until it reaches the threshold for the sudden depolarization that is an action potential. These events are illustrated in figure 2.15.

The SA node is triggered at a rate of 60 to 100 times per minute. The rate can vary depending on to the activity of the autonomic nervous system (see figure 2.16.a).

Every cell in the heart has the ability to behave like a pacemaker cell. The autonomous ability is normally suppressed except once the dominant cells of the sinus node fail or an

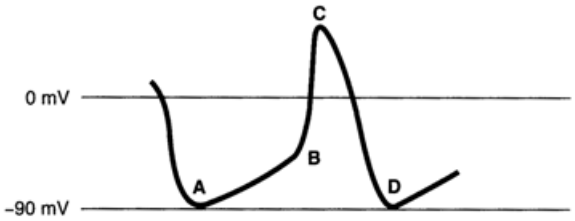

Figure 2.15. The electrical depolarization-repolarization cycle of a cardiac pacemaker cell. Point A is the minimal negative potential. The gentle rising slope between points A and B represents a slow, gradual depolarization. At point B, the threshold is crossed and the cell dramatically depolarizes which means an AP is produced. The downslope between point C and D represents repolarization [267].

external stimulation takes place.

Electrical conduction cells, which are long, thin cells, carry the current rapidly to the distant regions of the heart. The electrical conducting cells of the ventricles join to form distinct electrical pathways (see figure 2.16.b). The conducting pathways in the atria have more anatomic variability, prominent among these are fibers at the top of intra atrial septum in region called Bachman bundle which allow the rapid activation of the left atrium from the right atrium.

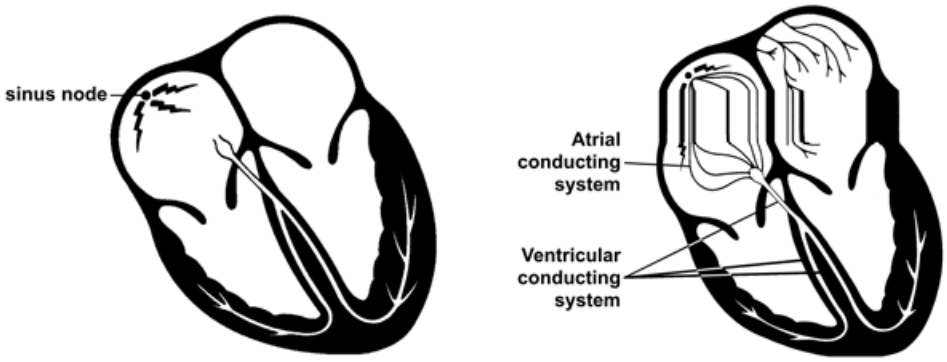

(a) (b)

Figure 2.16. Pacemaker and conduction system [267]: (a) The SA node triggers 60 to 100 times per minute producing a regular series of AP, which initiates a depolarization wave to spread through the heart. (b) Conducting system of the atria and ventricles.

Myocardial cells, which are about 50 to 100 μm size and form the major part of heart tissue. They are responsible for contracting and relaxing, since these cells contain contractile proteins (actin and myosin). Once a depolarization wave reaches a myocyte, calcium is released within the cell causing it to contract (excitation contraction coupling). Myocardial cells can transmit an electrical current similar to electrical conducting cells but they do it less efficiently. Thus, a wave of depolarization upon reaching the myocardial cells will spread slowly across the entire myocardium (see figure 2.17).

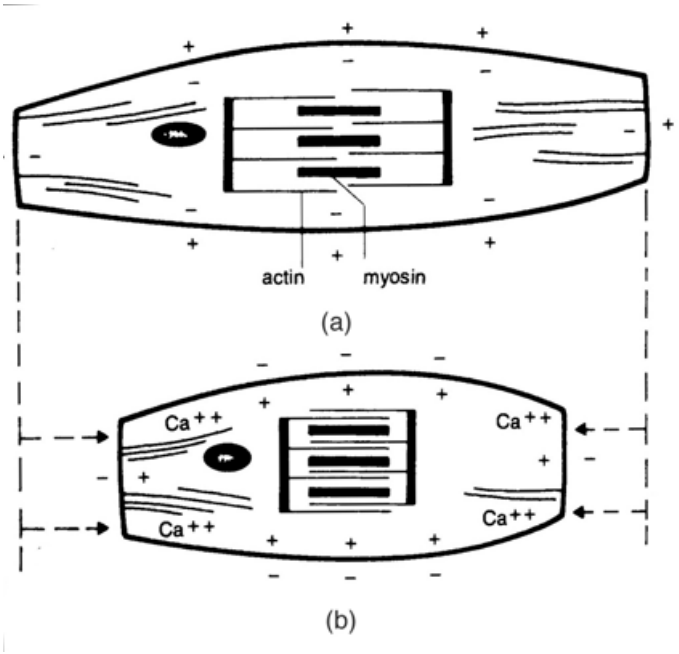

Figure 2.17. Depolarization causes calcium to be released within a myocyte. This influx of calcium allows actin and myosin to interact [267]: (a) A resting myocardial cell. (b) A depolarized, contracted myocardial cell.

2.2.8 Depolarization and Repolarization Phases of ECG

The electrical activity of the heart can be recorded on the body surface providing non-invasive measurements of the cardiac electrical function. The perturbations in normal electrical patterns are useful to diagnose many different cardiac disorders.

Atrial depolarization: The sinus node triggers spontaneously, producing a depolarization wave spreading outwards into the atrial myocardium. The depolarization results in atrial contraction. During atrial depolarization and contraction, electrodes placed on the surface of the body record a small burst of electrical activity lasting a fraction of a second. This is the P wave, which is a recording of the spread of depolarization through the atrial myocardium from beginning to end.

Since the SA is located in the right atrium, the right atrium begins to depolarize before the left atrium and stops earlier as well. Therefore, the first part of the P wave predominantly represents right atrial depolarization and the second part left atrial depolarization (see figure 2.18).

In healthy hearts, there is an electrical gate at the junction of the atria and the ventricles. The wave of depolarization spreads into the atria. Then electrical conduction must be directed along inter-ventricular septum through atrio-ventricular node (AV), which slows down the conduction. This physiological delay in conduction is essential to allow the atria

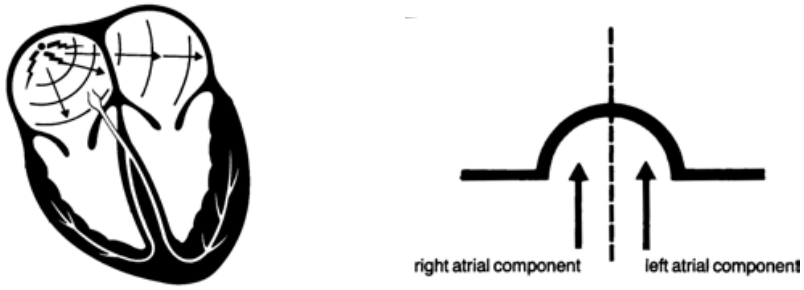

(a) (b)

Figure 2.18. Deploarization of atria [267]: (a) After triggering SA node, the wave of depolarization propagates through both atria, causing them to contract. (b) P wave.

to finish contracting before the ventricles begin to contract.

Ventricular depolarization: The ventricular conducting system consists of bundle of His, bundle branches and Purkinje fibers.

The bundle of His emerges from the AV node and immediately divides into the right and left bundle branches. The right bundle branch carries the current down the right side of the inter-ventricular septum all the way to the apex of the right ventricle. The left bundle branch divides into three major fascicles:

1. Septal fascicle, which depolarizes the inter-ventricular septum in a left to right direction.
2. Anterior fascicle, which runs along the anterior surface of the left ventricle.
3. Posterior fascicle, which sweeps over the posterior surface of the left ventricle.

The right bundle branch and the fascicles terminate in countless tiny Purkinje fibers. These fibers deliver the electrical current into the ventricular myocardium (see figure 2.19).

The ventricular contraction is evident as a QRS complex on the ECG, due to ventricular depolarization. The amplitude of the QRS complex is much bigger than P wave since ventricles contain more muscle mass than atria. The QRS complex is complicated and variable in shape reflecting the greater complexity of the ventricular depolarization pathway. The earliest part of the QRS complex represents the septal depolarization. Although the right and left ventricles depolarize approximately simultaneously, the signal visible on the ECG is caused by the left ventricular activation since the left ventricle has three times more muscle mass than the right ventricle. There is an atrial repolarization wave as well, but it is hidden by the prominent QRS complex.

The QRS complex consists of several distinct waves, which can be identified as follows [267]:

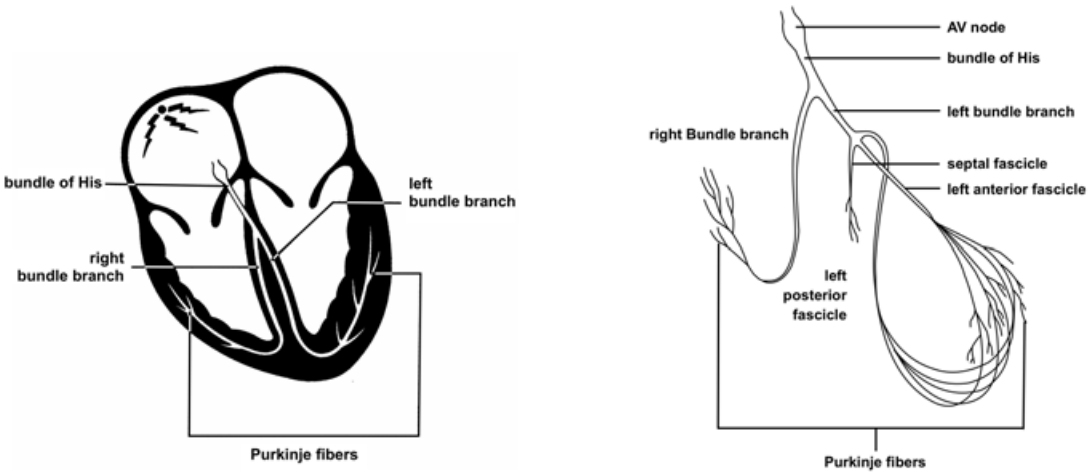

(a) (b)

Figure 2.19. Excitation conduction system [267]: (a) Ventricular conduction system. (b) Ventricular pacemaker and bundles.

1. Q wave as the first downward deflection
2. R wave as the first upward deflection
3. R′ wave as second upward deflection
4. S wave as a downward deflection followed by an upward deflection. Therefore if the first wave of the complex is R wave, the ensuring downward deflection is S wave otherwise Q wave while there is only one downward deflection in the whole complex.
5. QS wave if there is only one downward deflection in the whole complex without any upward deflection.

The above QRS configurations are demonstrated in figure 2.20.

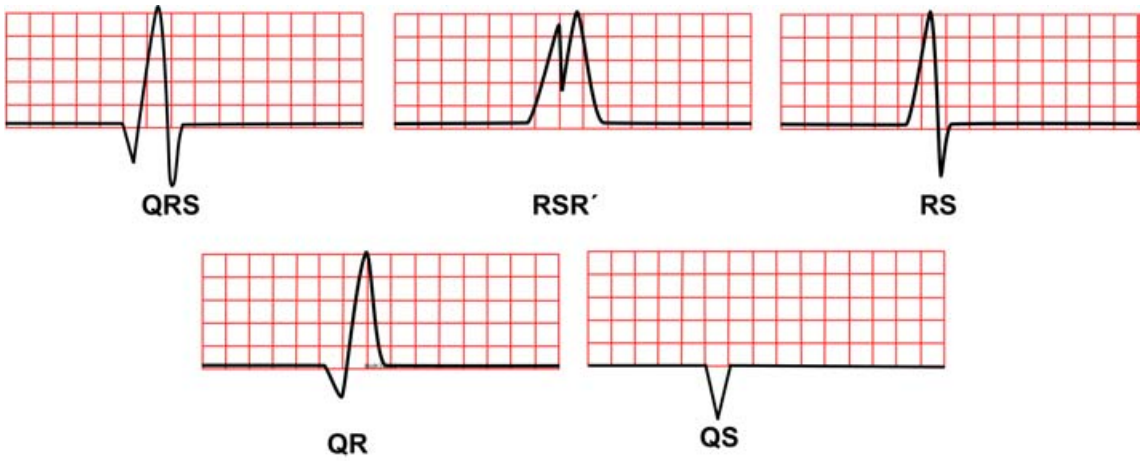

Figure 2.20. Different configurations of the QRS complex [267].

The interval starting at the beginning of atrial depolarization and ending at the beginning of ventricular depolarization is called PQ interval with a duration of 120 to 200 *ms*.

Ventricular repolarization: The third wave on ECG, named repolarization T wave, belongs to the refractory period of ventricular myocardium. Normally, the sign of the T peak amplitude is equal to R peak. The complete ventricular activity is represented by the time interval starting at the Q peak to the end of the T wave (QT interval). QT interval duration depends on the heart rate. Therefore it is useful to correct the QT interval frequency e.g. by the Bazett equation [27, 105]:

$$QT_c = \frac{QT}{\sqrt{RR}} \tag{2.5}$$

where QT is the interval measured in *ms* and RR is the interval from R peak from one cycle to the R Peak of the next cycle. Ventricular repolarization and T wave are demonstrated in figure 2.21.

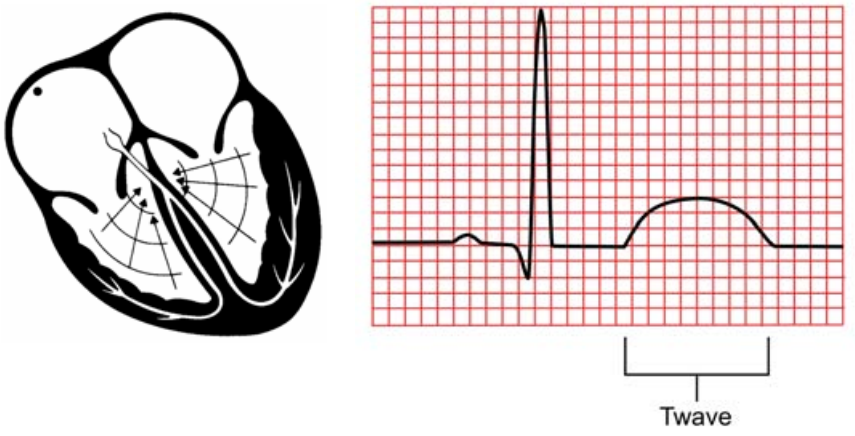

(a) (b)

Figure 2.21. Repolarization of ventricles [267]: (a) Ventricular repolarization. (b) T wave.

The ST segment records the time from the end of ventricular depolarization to the start of ventricular repolarization.

2.2.9 ECG Leads System

The conventional electric connections used for recording the electrocardiogram are the limb leads, augmented limb leads and precordial leads. This 12 leads ECG system has the widest clinical application [193]. Each lead is determined by the placement and orientation of various electrodes on the body. Each lead observes the heart at a unique angle, enhancing its sensitivity to a particular region of the heart at the expense of the others.

The more views, the more information provided [267].

To prepare the setup for the 12 lead ECG, two electrodes are placed on the arms and two on the legs. These provide the six limb leads, which include the three standard leads and three augmented leads. The rest six electrodes are placed across the chest forming the six precordial leads. The 12-lead standard ECG comprises 3 bipolar Einthoven I, II, III, 3 uniploar (Goldberger aVL, aVR, aVF) and 6 chest (Wilson V1 - V6) leads.

The six limb leads: The limb leads view the heart in a vertical plane (frontal plane). To produce the six leads of the frontal plane, each of the electrodes is designated as positive or negative automatically by the internal circuit of ECG device. Each lead has its own specific view of the heart's angle of orientation. The angle of each lead can be determined by drawing a line from the negative to the positive electrode. The resulted angle is then expressed in degrees by superimposing it on 360° circle of the frontal plane [267].

The three standard bipolar limb leads are defined as follows:

1. A positive signal in lead I is created by making the left arm positive and the right arm negative. The orientation angle is 0°.
2. A positive signal in lead II is created by making the legs positive and the right arm negative. The orientation angle is 60°.
3. A positive signal in lead III is created by making the legs positive and the left arm negative. The orientation angle is 120°.

These three standard bipolar limb leads are developed by Einthoven et al. [167] and measured as follows:

$$I = \phi_{LA} - \phi_{RA}, \tag{2.6}$$

$$II = \phi_{LL} - \phi_{RA}, \tag{2.7}$$

$$III = \phi_{LL} - \phi_{LA}, \tag{2.8}$$

$$II = I + III, \tag{2.9}$$

where ϕ_{LA}, ϕ_{RA} and ϕ_{LL} denote the electrical potential recorded on the left arm (LA), right arm (RA) and left leg (LL).

The three augmented limb leads are created differently. A single lead is chosen to be positive and all the others are made negative. The three augmented leads are defined as follows:

1. A positive signal in lead aVL is created by making the left arm positive and the other limbs negative. The orientation angle is $-30°$.

2. A positive signal in lead aVR is created by making the right arm positive and the other limbs negative. The orientation angle is $-150°$.
3. A positive signal in lead aVF is created by making the legs positive and the other limbs negative. The orientation angle is $90°$.

These three augmented limb leads are developed by Goldberger et al. [167] and measured as follows:

$$aVR = \phi_{RA} - \frac{\phi_{LA} + \phi_{LL}}{2}, \tag{2.10}$$

$$aVL = \phi_{LA} - \frac{\phi_{RA} + \phi_{LL}}{2}, \tag{2.11}$$

$$aVF = \phi_{LL} - \frac{\phi_{RA} + \phi_{LA}}{2}, \tag{2.12}$$

where ϕ_{LA}, ϕ_{RA} and ϕ_{LL} denote the electrical potential recorded on the left arm (LA), right arm (RA) and left leg (LL).

All six leads orientation angles are demonstrated in figure 2.22. Leads II, III and aVF are referred to inferior leads on the other hand leads I and aVL are referred to the left lateral leads.

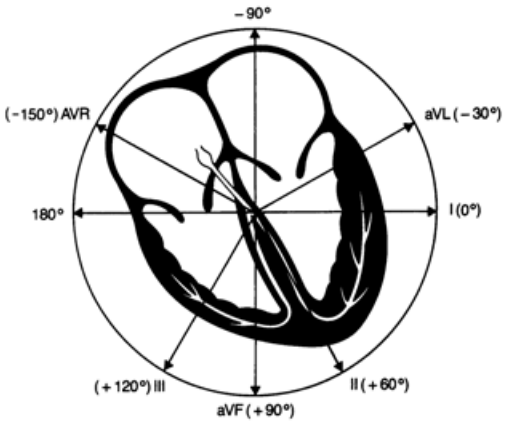

Figure 2.22. Orientation angles of limb leads [267].

The six precordial leads: The six precordial leads are arranged across the chest in a horizontal plane as illustrated in figure 2.23. To create the six precordial leads, each chest electrode is made positive in turn and the whole body is considered as common ground. The six positive electrodes are positioned as follows:

1. Lead V1 is placed in the fourth intercostal space to the right of the sternum.
2. Lead V2 is placed in the fourth intercostal space to the left of the sternum.
3. Lead V3 is placed between V2 and V4.
4. Lead V4 is placed in the fifth intercostal space in the midclavicular line.

5. Lead V5 is placed between V4 and V6.
6. Lead V6 is placed in the fifth intercostal space in the midclavicular line.

All six lead orientation angles are demonstrated in figure 2.23. Leads V1 to V4 are referred to anterior leads on the other hand leads V5 and V6 are referred to left lateral leads.

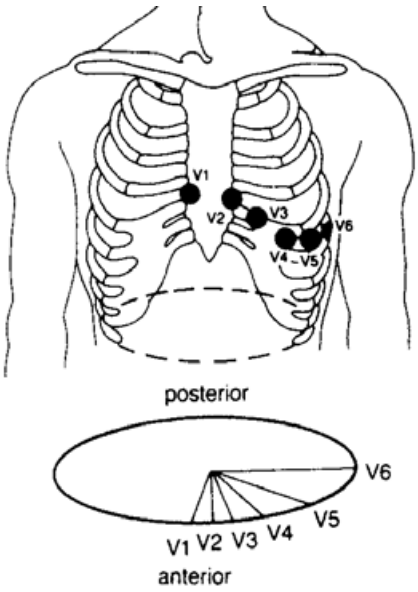

Figure 2.23. Orientation angles of precordial leads [267].

Wilson [267] introduced a common point where the limb leads are connected together through resistors each with 5 $k\Omega$. The potential of this point known as Wilson Central Terminal (WCT) is almost constant over time with respect to the zero potential as infinity. ϕ_{WCT} is calculated as:

$$\phi_{WCT} = \frac{\phi_{RA} + \phi_{LA} + \phi_{LL}}{3} \tag{2.13}$$

Multichannel ECG lead system: In order to measure a body surface potential map (BSPM), a multichannel ECG with more than 12 leads is necessary. Using more leads results in higher spatial resolution, which provides a widespread three dimensional view of cardiac electrical activity. This can be useful in order to solve the inverse problem for setting the patient heart model parameters in which a high correlation between measured and simulated BSPM could be achieved.

A multichannel recording system for biopotential measurements as EEG signals and furthermore ECG signals could be applied to measure the BSPM. The multichannel ECG

recording system used in this work was the ActiveTwo system of Biosemi [34] with 64 electrodes (see figure 2.24) [164, 165].

1. Six limb leads: three bipolar limb leads of Einthoven and the three augmented unipolar leads of Goldberger could be determined through electrodes A13, C13, C24 and equation 2.6 to 2.9.
2. Six precordial leads: six unipolar precordial leads of Wilson could be determined through electrodes A7, B5, B18, C6, C18 and A2.

As shown in figure 2.24, the extracting 12 standard ECG system is possible as follows:

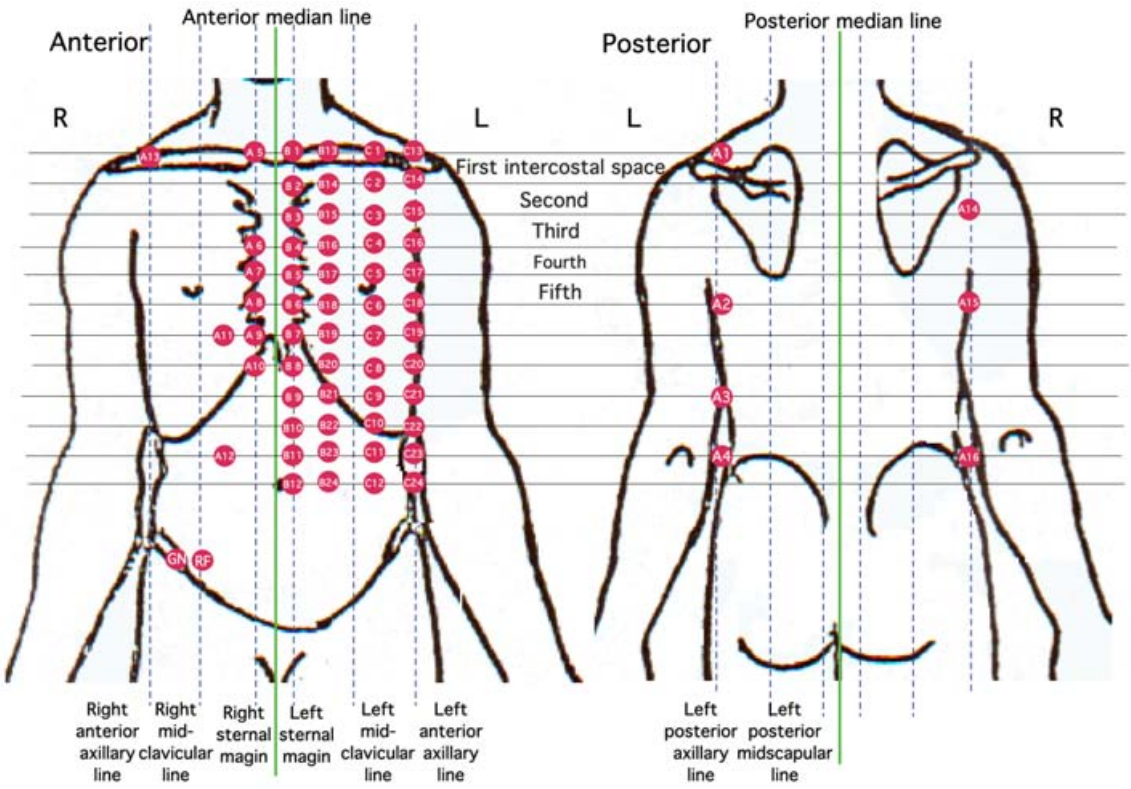

Figure 2.24. The IBT 64-channel ECG lead positions on the human torso with the corresponding electrode labels.

A BSPM can be measured to assess the electrical information of the heart such as infraction location and excitation propagation velocity in the conduction system through the mathematical computations by solving the inverse problem. In addition, BSPM can be helpful to investigate the excitation spread over the thorax related to the forward problem.

2.3 Cardiac Pathology

Since electrical activity triggers mechanical activity, abnormal electrical patterns normally lead to an abnormal contractile activity of the heart. The main differences from physiology are classified as follows [245]:

1. Abnormalities in rate
2. Abnormalities in rhythm
3. Congestive heart failure

However, there is no absolute distinction between above classes while some pathologies belong to more than one groups.

2.3.1 Abnormalities in Rate

A rapid heart rate of more than 100 beats per minute in rest is called tachycardia whereas slow heart rate of fewer than 60 beats per minute is called bradycardia. Different types of tachycardia are as follows [11]:

1. **Supraventricular tachycardia (SVT):** A fast heart rate often over 150 beats minute, which starts in the heart's atria or in the upper part of the electrical conduction system. Symptoms include palpitations, chest pains, upset stomach, decreased appetite, lightheadedness or weakness. Patients often need to have a radiofrequency ablation to cure the problem.

2. **Atrial tachycardia:** A fast heart rate which starts in the heart's atria and is conducted to the ventricles. Atrial tachycardia, sometimes called atrial flutter is a particular type of SVT observed in young adults, which can be classified as rhythm abnormalities too. Besides a fast heart rate, other symptoms are fatigue, dizziness, lightheadedness and fainting. It usually requires treatment with medications, radiofrequency ablation or surgery.

3. **Ventricular tachycardia:** A fast heart rate which starts in the heart's ventricles. It usually results from serious heart disease and often requires prompt or emergency treatment. Symptoms can be mild but are generally severe. They include dizziness, lightheadedness and fainting. Treatment options include medication, radiofrequency ablation, implanting a device that shocks the heart into a normal rhythm or surgery.

2.3.2 Abnormalities in Rhythms (Cardiac Arrhythmia)

Any deviation from the normal rhythm and sequence of excitation of the heart is an arrhythmia. It may result from SA node activity alternation or intervention with conduction. Instances of abnormal rhythm are heart block, atrial flutter, atrial fibrillation, ventricular

fibrillation, extrasystoles or premature ventricular contractions originating from an ectopic focus, which can be detected with ECG. Atrial flutter and atrial fibrillation have a close clinical interrelationship [281]. The most common abnormalities are as follows [245].

1. **Atrial flutter:** A rapid but regular sequence of atrial depolarization at rates between 200 and 380 beats per minute, which is usually associated with a fast heart rate or tachycardia and belongs to the category of supra-ventricular tachycardia. Since the refractory period of conducting tissues is longer than atrial muscle, the AV node is unable to respond to every impulse that converges on it from the atria. Possibly one from every two or three atrial impulses successfully passes through the AV node to the ventricles (2:1 or 3:1 rhythm). Atrial flutter occurs when electrical impulses take an abnormal path through the atria, typically circulating around the tricuspid valve in the right atrium. Atrial flutter is arising from a macro reentrant circuit in the right atrium or around scar tissue [222, 238]. It often occurs in individuals with cardiovascular disease (eg: hypertension, coronary artery disease, and cardiomyopathy).

2. **Atrial fibrillation (AF):** A rapid, irregular, uncoordinated depolarization of atria. Accordingly, the normal electrical impulses generated by the SA node are plagued by disorganized electrical impulses originating in the atria and pulmonary veins. This phenomenon leads to an irregular impulse conduction to the ventricles, which results in an irregular heartbeat. Atrial fibrillation may be continuous (persistent or permanent AF) or alternating between periods of a normal heart rhythm (paroxysmal AF). The natural tendency of AF is to become a chronic condition. Chronic AF leads to a small increase in the risk of death [31, 70, 190, 245, 280]. Atrial fibrillation may be treated with medications, which either slow the heart rate or revert the heart rhythm back to normal. Synchronized electrical cardioversion may also be used to convert AF to a normal heart rhythm. Surgical and catheter-based therapies may also be used to prevent recurrence of AF in certain individuals. In general, atrial flutter should be treated the same as atrial fibrillation. Atrial flutter is considerably more sensitive to electrical cardioversion than atrial fibrillation, and usually requires a lower energy shock. Because of the reentrant nature of atrial flutter, it is often possible to ablate the circuit that causes atrial flutter.

3. **Ventricular fibrillation (VF):** Very serious rhythmic abnormality in ventricular myocardium reveals uncoordinated, chaotic contractions. Multiple impulses travel erratically in all directions within the ventricles. It generally occurs within diseased hearts. In most cases, VF is a manifestation of underlying ischemic heart disease. Ventricular fibrillation is also observed in those patients with cardiomyopathy, myocarditis, and other heart pathologies. If circulation is not restored in less than a few minutes through external cardiac compression or electrical defibrillation, irretrievable brain damage occurs and death is expected [245]. In patients at high risk of ventricular fibrillation,

the use of an implantable cardioverter defibrillator has been shown to be beneficial. A premature contraction of the heart independent of the normal heart rhythm may cause an extrasystole.

4. **Heart block:** A type of arrhythmia appears from the defection in the cardiac conducting system. The atria still beat regularly but the ventricles occasionally fail to be stimulated. Therefore, the ventricles do not contract following atrial contraction. Impulses between atria and ventricles can be blocked to varying degrees [245]. In heart block, the atrial rate is normal but the ventricular rate is less than normal. Complete heart block is characterized by complete distinction between atrial and ventricular activation whereas the impulses from atria could not be conducted to the ventricles. When a bundle branch or fascicle becomes injured, it may affect the conduction of electrical impulses. This results in altered pathways for ventricular depolarization. Since the electrical impulses can no longer use the preferred pathway across the bundle branch, it may move instead through muscle fibers in a way that both slows the electrical movement and changes the direction of the impulses. As a result, there is a loss of ventricular synchrony, ventricular depolarization is prolonged and there may be a corresponding drop in cardiac output. When heart failure is present, a pacemaker may be used to resynchronize the ventricles. The blockage can occur in any stage of conduction system:

   - Atrio-ventricular block (AVB), is a type of heart block involving the disconnection between the atrial and ventricluar conduction of the heart. If the conduction system is blocked after the atrio-ventricular node, the excitation can not propagate to the bundle of His, the AVB is resulted which leads to hardly any excitation of the ventricles [222].

   - Left bundle branch block (LBBB), is a type of heart block involving the disconnection between the bundle of His and left bundle branch. If the conduction system is blocked after bundle of His in which, the excitation can not propagate to the left ventricle, the LBBB is resulted. LBBB leads to a delayed excitation of the left ventricle not via the physiological conduction [222].

   - Right bundle branch block (RBBB), is a type of heart block involving the disconnection between the bundle of His and right bundle branch. If the conduction system is blocked after bundle of His where, the excitation can not propagate to the right ventricle, the RBBB is resulted. RBBB leads to a delayed excitation of the right ventricle not through the physiological conduction system [222]. Both LBBB and RBBB lead to asynchronous ventricular contraction.

2.3.3 Congestive Heart Failure

The traditional view that heart failure is a constellation of signs and symptoms caused by inadequate performance of the heart focuses on only one aspect of the pathophysiology involved in the syndrome [133].

1. **Cardiac myopathy:** is a deterioration of the function of the myocardium. It is the damage of the heart muscle by ischemia, as a most common cause. Ischemic cardiomyopathy is a weakness in the muscle of the heart due to inadequate oxygen delivery to the myocardium with coronary artery blockage as a common cause. This condition is acute myocardial infarction commonly called heart attack. The area of the heart affected by a myocardial infarction will initially become necrotic, and then will be replaced by scar tissue (fibrosis). This tissue is no longer muscle and can not contribute to the heart's function as a pump [68]. Not only working myocardium suffers from ischemic cardiomyopathy but also the conduction pathways can be disturbed, since the conduction system remains at decreased oxygen supply [222]. Figure 2.25 demonstrates the different infarction positions caused by different blocked locations of coronary artery.

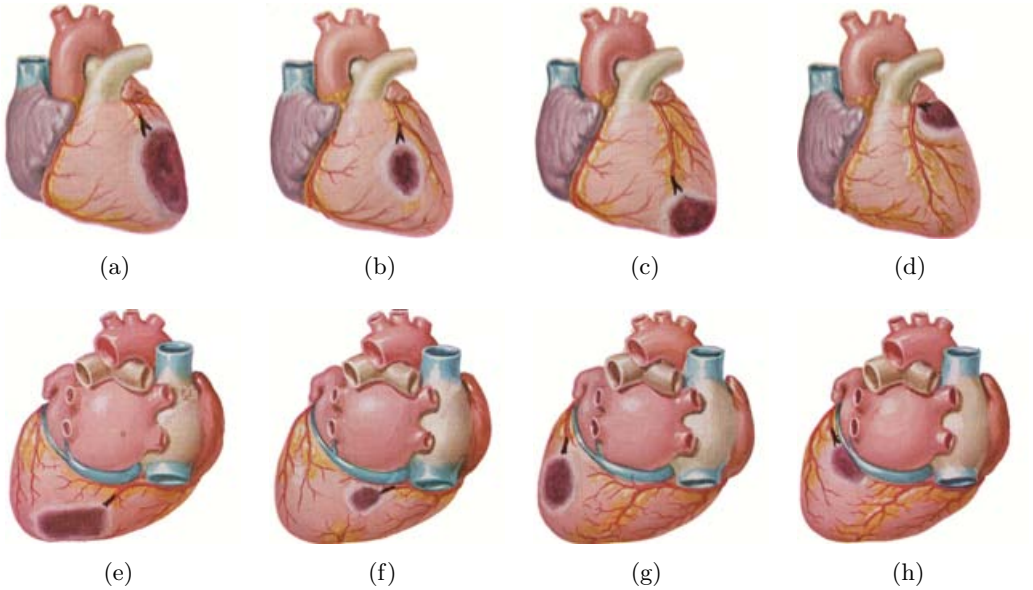

Figure 2.25. Several infarction positions [191]. (a) Anterolateral. (b) Anteroseptal. (c) Apical. (d) Anterobasal. (e) Posteroinferior. (f) Posteroseptal. (g) Posterolateral. (h) Posterobasal.

2. **Left ventricular remodeling:** is the process by which mechanical, neurohormonal and genetic factors alter ventricular size, shape, and function. Remodeling occurs in several clinical conditions, including myocardial infarction, cardiomyopathy, hypertension, and valvular heart disease [92, 133, 259]. For example, after a myocardial infarction, the acute loss of myocardial cells results in abnormal loading conditions that

involve not only the central and border zone of the infarction, but also remote myocardium. These abnormal loading conditions induce dilatation and change the shape of the ventricle, rendering it more spherical, as well as causing hypertrophy. Remodeling continues for months after the initial insult, and the eventual change in the shape of the ventricle becomes deleterious to the overall function of the heart as a pump (see figure 2.26) [133, 205]. In cardiomyopathy, the process of progressive ventricular dilatation or hypertrophy occurs without the initial apparent myocardial injury observed after myocardial infarction (see figure 2.27) [133]. Several trials involving patients who were studied after a myocardial infarction or who had dilated cardiomyopathy found a benefit from ACE (Angiotensin Converting Enzyme) inhibitors, beta-adrenergic antagonists or cardiac resynchronization [49, 109, 112, 133, 237]. Such beneficial effects were associated with so-called reverse remodeling, in which the therapy promoted a return to a more normal ventricular size and shape [49, 109, 112, 133, 237]. The reverse-remodeling process is a mechanism through which a variety of treatments palliate the heart failure syndrome.

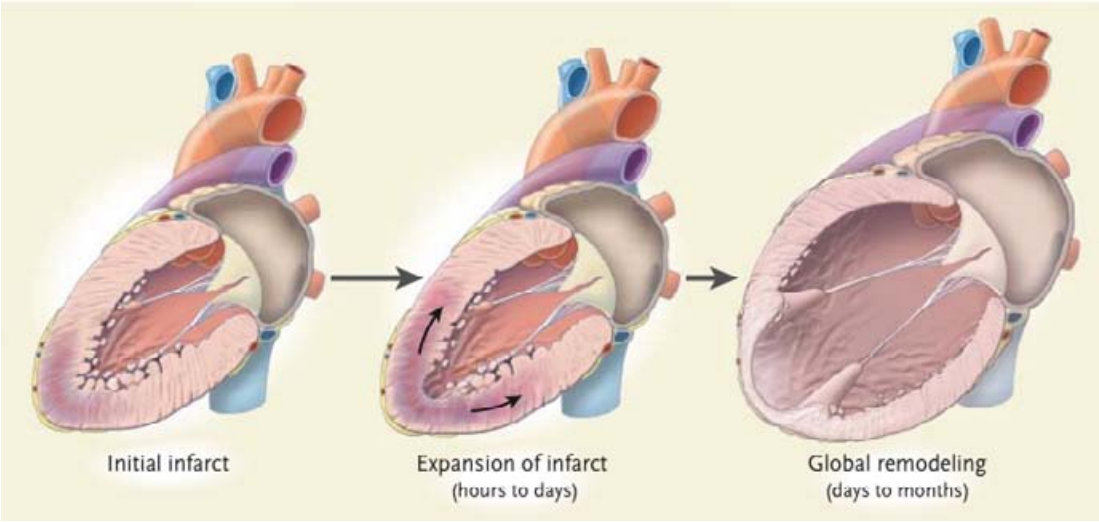

Figure 2.26. Ventricular remodeling after acute infarction [133].

3. **Mitral regurgitation:** An outcome of remodeling is the development of mitral regurgitation. As the left ventricle dilates and the heart assumes a more globular shape, the geometric relation between the papillary muscles and the mitral leaflets changes, causing restricted opening of the leaflets and distortion of the mitral apparatus. Dilatation of the annulus occurs as a result of increasing left ventricular or atrial size or as a result of regional abnormalities caused by myocardial infarction [71, 114, 133, 199]. The presence of mitral regurgitation results in an increasing volume overload on the overburdened left ventricle that further contributes to remodeling, the progression of disease, and to symptoms. Correction of mitral regurgitation has been an appropriate

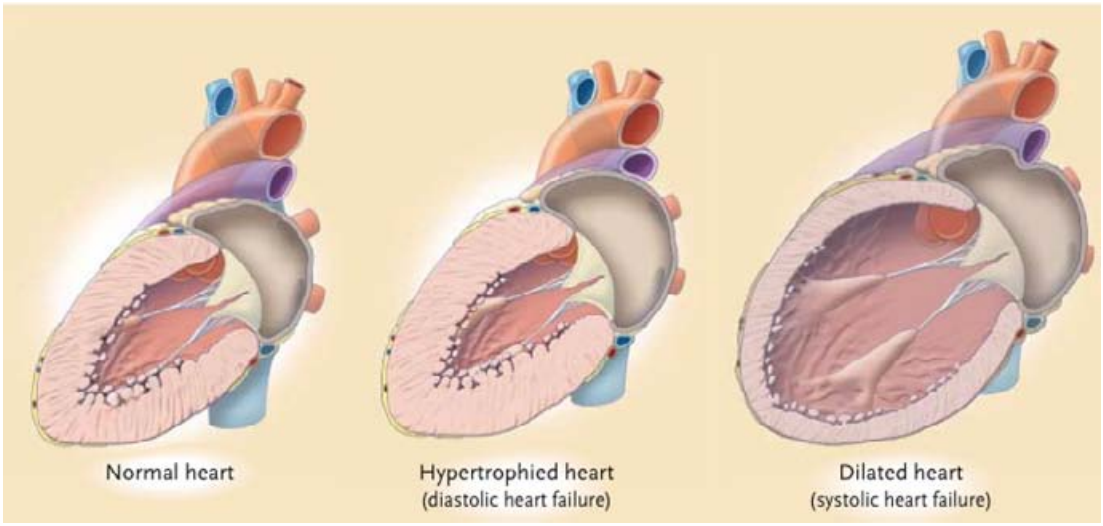

Figure 2.27. Ventricular remodeling in diastolic and systolic heart failure [133].

focus of therapy.

4. **Hypertensive heart disease:** caused by high blood pressure. Hypertensive heart disease is a late complication of hypertension (high blood pressure) in which the heart is affected. High blood pressure increases the heart's workload and over time, this can cause the heart muscle to thicken. As the heart pumps against elevated pressure in the blood vessels, the left ventricle becomes enlarged (hypertrophy) and the amount of blood pumped by the heart each minute (cardiac output) decreases. Without treatment, symptoms of congestive heart may develop [127].

5. **Diastolic heart failure:** Some patients with heart failure have preserved systolic function or a normal left ventricular ejection fraction. Although such hearts contract normally, relaxation (diastole) is abnormal. Cardiac output, especially during exercise, is limited by the abnormal filling characteristics of the ventricles. For a given ventricular volume, ventricular pressures are elevated, leading to pulmonary congestion, dyspnea and edema identical to those seen in patients with a dilated, poorly contracting heart [21, 52, 133, 275, 302]. The diagnosis of diastolic heart failure is usually made by a clinician who recognizes the typical signs and symptoms of heart failure systolic function (i.e., a normal ejection fraction) on echocardiography. Echocardiography may be useful in the detection of diastolic filling abnormalities.

2.4 Cardiac Function Parameters

Abnormal ECG waves are important in recognizing and assessing cardiac myopathies, left bundle branch block, right bundle branch block, extrasystole and some other abnormalities. In order to investigate the function of the heart to determine whether there is

an abnormality or not, following parameters could be measured in clinical studies [60, 245]:

End diastolic volume (EDV): The volume of the blood in the ventricle at the end of diastole, which averages about 135 *ml*.

End systolic volume (ESV): The amount of blood left in the ventricle at the end of systole when ejection is complete. It averages about 65 *ml*.

Stroke volume (SV): The difference between the blood volume in the ventricle before contraction and the volume after contraction.

$$SV = EDV - ESV \tag{2.14}$$

Ejection fraction (EF): The percentage fraction of blood ejected by the ventricle (often left ventricle) during the contraction phase of the cardiac cycle.

$$EF = \frac{SV}{EDV} \times 100\% \tag{2.15}$$

Cardiac output (CO): The volume of blood pumped by each ventricle per minute. This is achieved by multiplication of stroke volume and heart rate (HR). Since the average resting heart rate is 70 beats per minute and the average resting stroke volume is 70 *ml* per beat, an average cardiac output of 4900 *ml/min* is expected for a normal heart.

$$CO = SV \times HR \tag{2.16}$$

Cardiac index (CI): A cardiodynamic measure based on the cardiac output, which is the amount of blood the left ventricle ejects into the systemic circulation in one minute, measured in liters per minute (*l/min*). Cardiac output can be indexed to a patient's body size by dividing by the body surface area (called the BSA) to yield the cardiac index. The normal range of cardiac index is $2.6 - 4.2$ *l/min* per square meter.

$$CI = SV \times \frac{HR}{BSA} \tag{2.17}$$

Maximal oxygen consumption (V_{O2max}): V_{O2max} is reached when oxygen consumption remains at a steady state despite an increase in workload during clinical exercices. V_{O2max} is properly defined by the Fick Equation:

$$V_{O2max} = CO \times (Ca_{O2} - Cv_{O2}) \tag{2.18}$$

where CO is the cardiac output of the heart, Ca_{O2} is the arterial oxygen content, and Cv_{O2} is the venous oxygen content.

Ratio of early to late ventricular filling (E/A): Echocardiographic phases of ventricular filling are defined as early E-wave and atrial A-wave. The area under the E-wave reflects the rapid filling phase in LV diastolic filling. The area under A-wave reflects the contribution of atrial contraction to LV diastolic filling. The E/A ratio is reduced in diastolic dysfunction. Figure 2.28 demonstrates the ECG and transmitral flow velocity curve.

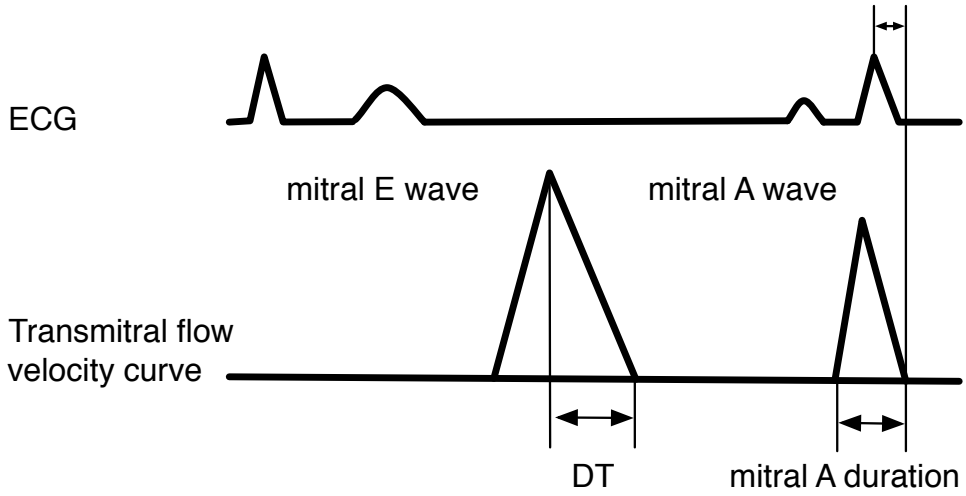

Figure 2.28. ECG and transmitral flow velocity curve. DT ist the deceleration time which is a measure of how rapidly early diastolic filling stops [89].

3

Cardiac Resynchronization Therapy

In patients with heart failure, the first choice of therapy is medication. Nevertheless, resistance to drugs mainly over a long time requires other treatment options. Cardiac resynchronization therapy (CRT) in forms of biventricular pacing (BVP) has emerged as an alternative treatment for patients classified by the New York Heart Association (NYHA) classification as type III-IV heart failure, which is the result of normal ventricular function loss. CRT leads to an improvement in hemodynamics by coordinating the ventricular contraction and results in less hospitalization [2, 50, 64, 66, 121, 169, 230, 292].

Dyssynchronous left ventricular contraction reduces myocardial efficiency, which leads to abnormal diastolic interactions between the ventricles, increasing the mitral regurgitation and the risk of sudden cardiac death. Therefore, the patients with congestive heart failure, who have sufficiently low left ventricular ejection fraction (LVEF) and usually prolonged QRS duration in ECG, are candidates for CRT [143].

It is important to identify the exact patients who may respond to the therapy in order to optimize the lead positioning and device programming to maximize the benefit of CRT. The diagnosis of heart failure patients can be confirmed by a number of tests including electrocardiogram (ECG), echocardiography, magnetic resonance imaging, radionuclide ventriculography, angiography as well as blood tests [95, 189].

At present, the best established evidence of heart failure is the presence of the echocardiographic left ventricular dyssynchrony [25, 53, 203]. However, several different methods have been proposed for assessment and interpretation of dyssynchrony. Further, these parameters can be technically difficult to assess in some patients.

Moreover, studies have demonstrated that dyssynchrony can be determined via longitudinal delay of tissue Doppler imaging [25, 251], color coded dyssynchrony imaging [297] and myocardial speckle tracking [258].

3.1 History of CRT

Cardiac resynchronization therapy was introduced in the early 1990s and developed significantly over time [3]. At the beginning of the 90s, Hochleitner et al. [123] proposed for the first time artificial cardiac pacing (dual chamber pacemaker with a short atrio-ventricular interval) as a treatment for refractory heart failure. Early clinical trials of the CRT were carried out in the USA and Europe from 1995 to 1998 using a thoracoscopic procedure for lead positioning on the lateral wall of the left ventricle [17, 62]. In 1998 Daubert et al. [72] reported a technique of transvenous implantation by passing a lead through a cardiac vein via the coronary sinus to enable left ventricular pacing on the epicardial surface. However, despite further developments, this implantation technique remains challenging and time consuming [97].

Nevertheless, about 20 - 30 % of patients in randomized clinical trials do not respond to CRT [154]. This may be due to a variety of reasons, such as improper patient selection, inappropriate lead positioning or suboptimal pacemaker device programming concerning the timing delays [121, 169, 268].

According to the reasons above, it is important to identify accurately those patients who may respond to the therapy in order to further optimize lead pacing and device programming to maximize the benefit of CRT.

3.2 Etiology of Heart Failure: Indication for CRT

Heart function can be investigated either hemodynamically by left ventricular ejection fraction (LVEF) or electrically by analyzing the shape and duration of QRS complex of an ECG waveform, or mechanically by measuring the contraction delay in Doppler echography.

Patients with an extensive QRS complex frequently have dyssynchronous ventricular contraction while the broad QRS indicates the sequence of electrical activation of the ventricles as well as the time taken for depolarization [189].

Most patients who receive CRT will have an improvement in their symptomatic status. Trials have demonstrated an overall mean increase in maximal oxygen consumption ($V_{O_{2max}}$) during the exercises of patients who are on CRT. In addition, echocardiographic data demonstrate a reduction in left ventricular dimensions and severity of mitral regurgitation [97, 295].

Nevertheless, dramatic treatment results were observed in patients who have no objective clinical benefit after implantation of CRT [1, 223]. For instance Buch et al. [53] hypothesized that in the presence of apical left ventricular (LV) dysfunction, BVP might be less effective.

Moreover Bleeker et al. [37] recently showed that even in the presence of dyssynchrony, patients with posterolateral scar (see figure 2.25) were unlikely to respond to CRT, probably because of ineffective LV pacing. Therefore in the stage of CRT assessment for an individual patient, it is important to identify the exact responders and non-responders.

Analysis of the ventricular activation by vectorcardiography, signal averaged ECG or non-contact endocardial mapping might play a role in patient selection [152]. The accepted patient selection criteria of CRT are described as follows [16, 40, 97, 144, 228]:

1. NYHA functional class III - IV
2. Left ventricular ejection fraction < 35 %
3. Left ventricular end diastolic diameter > 55 mm
4. QRS duration > 120 ms [16, 206, 287] or 135 ms [97, 230]
5. QRS duration < 130 ms with LV intra-ventricular dyssynchrony
6. Left or right bundle branch block and other intra-ventricular delays

Left ventricular ejection fraction (LVEF) can be estimated by echocardiography in which the volume of the left ventricle is measured during the cardiac cycle, contrast ventriculography or radionuclide scanning. Intra-ventricular dyssynchrony in criterion 5 is defined as the difference of at least 60 ms between the timing of the peak systolic velocities of the septum versus the lateral wall by tissue Doppler imaging (TDI) [26, 293].

The impact of age and gender on CRT outcome has been investigated by Zardkoohi et al. [299]. There were no significant differences between men and women regarding age except those suffering from ischemic cardiomyopathy. This finding was also supported by study of Bleeker et al. [38].

Buch et al. [53] showed that the presence of preimplantation apical wall motion abnormality in patients with ischemic cardiomyopathy and cardiac dyssynchrony determined by either prolonged QRS duration or echocardiographic dyssynchrony, was associated with a lower rate of CRT response. This may be attributable to increased wall stress due to late activated myocardial segments but the underlying mechanisms require further investigation. Outcomes in major randomized CRT trials including MIRACLE, MIRACLE-ICD, COMPANION, CARE-HF show an improvement in NYHA functional class, ejection fraction and quality of life [150].

In most studies, echocardiographic parameters including LVEF, left ventricular end diastolic diameter (LVEDd) and regional wall motion were recorded before CRT implantation (baseline) and after implantation weeks or months later (follow up).

Table 3.1 demonstrates several studies in which the parameters determining the responders or non-responders to CRT are investigated.

Study	Criteria	Responders		Non-responders	
		Baseline	Follow up	Baseline	Follow up
Penicka et al. [203]	LVEF (%)	24 ± 5	37 ± 8	27 ± 6	27 ± 8
	LVEDd (mm)	73 ± 7	67 ± 8	73 ± 7	73 ± 7
	LVESd (mm)	61 ± 6	52 ± 7	62 ± 8	60 ± 9
	LVEDV (ml)	289 ± 72	251 ± 79	297 ± 82	298 ± 87
	LVESV (ml)	224 ± 63	159 ± 58	219 ± 75	223 ± 80
	E/A of mitral inflow	1.57 ± 0.97	1.28 ± 0.73	2.16 ± 1.24	1.44 ± 0.74
Buch et al. [53]	LVEF (%)	22.9 ± 6.7	29.8 ± 9.9	23.1 ± 8.3	26 ± 11.1
	LVEDd (mm)	63 ± 9	64 ± 8	63 ± 9	63 ±10
	MR quantification	1.6 ± 0.8	1.1 ± 0.4	1.5 ± 0.7	1.6 ± 0.7
	QRS duration (ms)	159 ± 43	150 ± 18	159 ± 36	167 ± 24
Toggweiler et al. [268]	LVEF (%)	27.5 ± 12.8	29.8 ± 34.5	-	-
	LVEDV (ml)	187 ± 84	183 ± 74	-	-
	LVESV (ml)	144 ± 82	126 ± 65	-	-
	$\text{VTI}_{\text{LVOT}}(cm)$	10.8 ± 3.7	13 ± 4	-	-
Becker et al. [28]	LVEF (%)	31 ± 5	43 ± 7	-	-
	LVEDV (ml)	312 ± 97	289 ± 81	-	-
	LVESV (ml)	214 ± 68	172 ± 60	-	-
	$V_{O_{2max}}(ml/kg/min)$	10.8 ± 3.7	13 ± 4	-	-
Van de Veire et al. [73]	LVEF (%)	23 ± 7	24 ± 8	32 ± 9	25 ± 9
	LVEDV (ml)	266 ± 93	219 ± 74	224 ± 93	215 ± 88
	LVESV (ml)	207 ± 85	170 ± 74	156 ± 77	167 ± 85

LVEF: left ventricular ejection fraction, LVEDd: left ventricular end diastolic diameter, LVESd: left ventricular end systolic diameter, LVEDV: left ventricular end diastolic volume, LVESV: left ventricular end systolic volume, MR: mitral regurgitation, VTI_{LVOT}: velocity time integral in left ventricular outflow tract, $V_{O_{2max}}$: peak oxygen consumption

Table 3.1. Some studies determining the CRT responders and non-responders due to the parameters change representing the efficacy.

3.3 Biventricular Pacing

The pacemaker is an electronic, battery-powered device that is surgically implanted subcutaneously. The purpose of a biventricular pacemaker is to improve the ventricular synchronization and cardiac output. The BVP device comprises 3 electrode leads, which are positioned in the heart to help the ventricles contraction in a more balanced way. The leads are implanted through a vein in the right atrium and right ventricle as well as the coronary sinus vein to pace the left ventricle. Modern pacemakers are externally programmable in which the cardiologist might be able to select the finest pacing mode. Patients with a risk

of cardiac arrest due to ventricular tachycardia or ventricular fibrillation may receive an implantable cardioverter defibrillator (ICD) device to detect and rip such arrhythmia. CRT device can be performed with or without ICD. Two main types of CRT devices available in Europe are CRT-P (without ICD, low energy) and CRT-D (with ICD, high energy)[61].

The CRT devices are available from a variety of companies, for example St. Jude Medical, Medtronic ELA Medical, Biotronik, Sorin and Guidant. Modern pacemakers have multiple functions. The InSync® cardiac resynchonization system (Medtronic) has globally been available since 2001 while the Guidant cardiac resynchronization therapy defibrillator system was approved by the US Food and Drug Administration (FDA) in 2002 (see figure 3.1) [173, 272].

Biventricular pacing either simultaneously or sequentially improves the left ventricular systolic performance and reduces the ventricular dyssynchrony in patients with heart failure and bundle branch block.

(a) (b)

Figure 3.1. BVP devices from Medtronic [128].

3.3.1 Implantation Techniques

The BVP device can be implanted using endocardial or epicardial approach with the aid of a fluoroscopy machine to perform correct electrode conduction. A small incision after a local anesthetic or general anesthesia is made on the chest where the leads and device are inserted. The leads are guided transvenously through a vein into the heart. The leads are directed to the right atrium, right ventricle and left ventricle (see figure 3.2). Therefore,

implantation of the lead, which previously required thoracotomy, has been very simplified with the adoption of the endocavitary access, being performed with local anesthesia. The lead tips are attached to the heart muscle, while the other ends of the leads are attached to the pulse generator, which is placed under the chest skin. Since the left ventricle belongs to the cardiovascular high-pressure system, the left ventricular (LV) implantation is more difficult. The LV lead is usually positioned at the lateral, anterolateral or posterolateral wall of left ventricle and this is performed transvenously using a coronary sinus branch. Implantation of an epicardial pacemaker lead in the left ventricle which previously required thoracotomy has been simplified with the adoption of the endocavity access [98]. There are several studies, which investigate the influence of various pacing sites on the LV in cardiac output [100, 228, 273, 274].

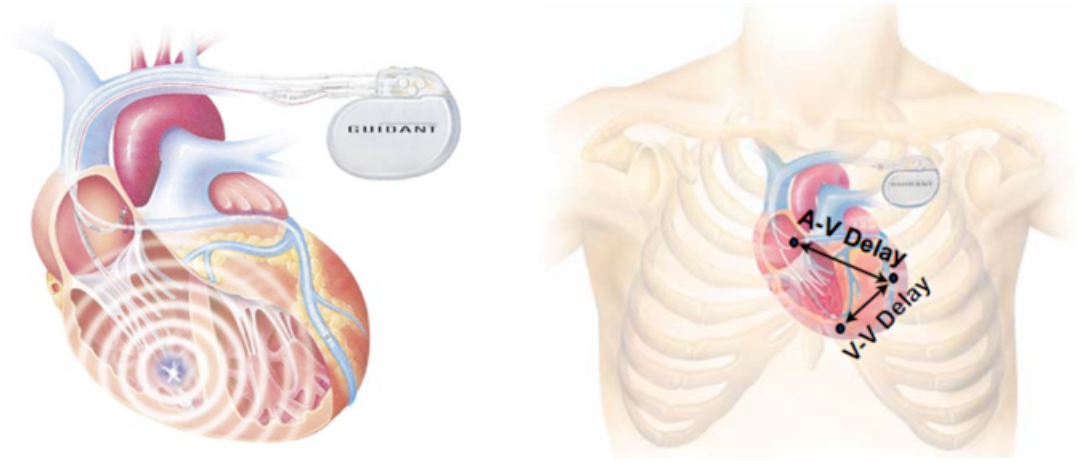

(a) (b)

Figure 3.2. Biventricular pacing device: (a) Passing the electrodes through the venous system [210]. (b) Location of the device under the chest skin [120].

Several studies illustrated techniques for BVP implantation in clinical trials and the effects of BVP on the patient heart [150, 264]. The techniques involve obtaining of venous access using either the cephalic vein cut-down or subclavian puncture. The coronary sinus is then cannulated using an electrophysiological catheter and a long guiding sheath. Once the coronary sinus is cannulated, the sheath is advanced into the coronary sinus. After removing the electrophysiological catheter, a balloon tipped catheter is inserted via the sheath into the coronary sinus. The balloon is inflated temporarily to occlude flow in the coronary sinus. Then an amount of non-ionized contrast medium is injected to visualize the venous system and the branches of the coronary sinus (see figure 3.3). Images are captured generally at 30 degrees right anterior oblique, 60 degrees left anterior oblique and anteroposterior. The catheter is then removed and the left ventricular lead advanced into the coronary sinus. Soft tines at the tip of the lead enable successful passive fixation

in the coronary sinus [264]. The optimal site for left ventricular pacing is in the lateral or posterolateral cardiac vein, while pacing from the mid lateral wall or posterior wall results in a raise in pulse pressure and left ventricular dP/dt [295].

However, if there is not enough time to carry out the pacing procedure, a stable position is not achievable. Therefore in these cases, the lead is positioned in the anterior great cardiac vein. Once the left ventricular lead is secured, the right ventricular apex lead and right atrial lead are then implanted in the usual manner for a dual chamber pacemaker. Where possible, the RV and LV lead should however be anatomically as far apart as possible (see figure 3.4). The three leads are then connected to the pulse generator device and the whole system placed in the subcutaneous pocket just above the pectoralis major muscle on the chest (Guidant or the Medtronic Insync CRT devices are used commonly).

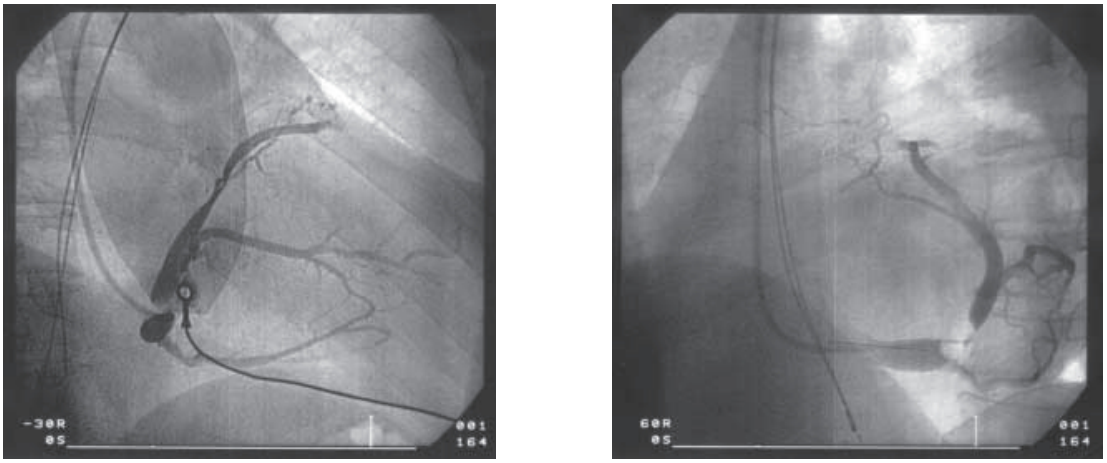

(a) (b)

Figure 3.3. Illustration of coronary sinus branches using angiography [264]: (a) Right anterior oblique 30 degree view. (b) Left anterior oblique 60 degree view.

Buch et al. [53] utilized a similar implantation approach. The LV lead implantation was performed via coronary sinus in order to achieve permanent epicardial stimulation from a lateral or posterolateral vein. If these veins were not accessible, the LV lead was implanted in a diagonal vein near the lateral LV wall. The RV lead was placed in the RV apex. The lead position was determined during implantation by fluoroscopy in the left anterior oblique and right anterior oblique projections. Final lead position was assessed by postoperative chest radiograph in the anteroposterior and lateral views.

Implantation of a BVP device is expensive, time consuming and involves risks, so it is important to accurately identify patients who are responders and to optimize lead positioning and device programming in order to maximize the patient's benefit.

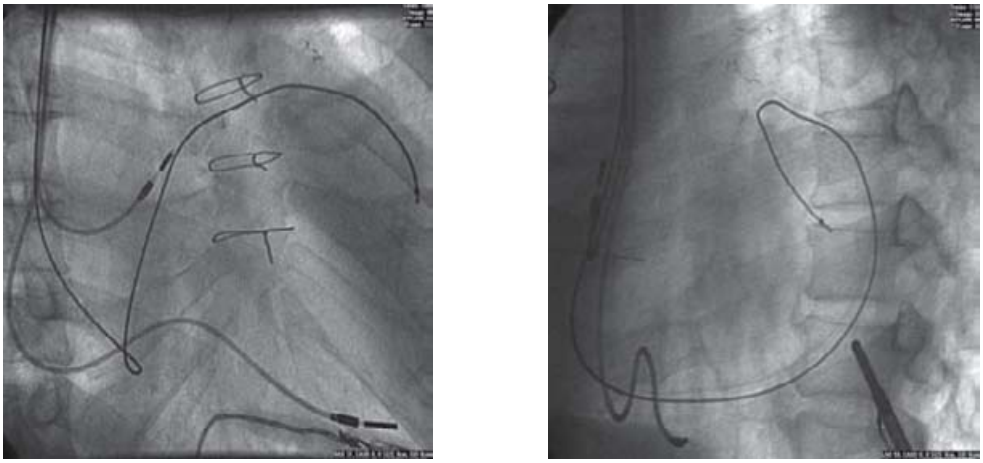

(a) (b)

Figure 3.4. Illustration of leads position using radiographs [264]: (a) Right anterior oblique 30-degree view. (b) Left anterior oblique 60-degree view.

3.3.2 Electrode Positions

Butter et al. [57] showed that the LV pacing site was a crucial factor in determining the effects of CRT, with lateral sites constantly producing better hemodynamic response than anterior sites. Most studies suggest a posterolateral position for the LV lead. This can be explained by the fact that these sites are consistently the latest to be activated during contraction. Contrarily, anterior wall sites are usually activated earlier [6, 19].

Pacing on the free wall includes the implantation of the lead in lateral, anterolateral and posterolateral veins. It is difficult to deliver a lead to the most suitable site of the ventricle and this may be one reason for the proportion of the non-responders. In these cases the surgical epicardial lead implantation should be applied instead of transvenous pacing.

Several studies investigated the influence of the various electrode positions on the cardiac output improvement. For instance, Sogaard et al. [252] examined the high inter-ventricular septum or the right ventricular outflow tract (RVOT) for pacing the RV electrode and the LV free wall for the LV pacing. Liberman et al. [157] has also suggested the RVOT as a more physiological site for cardiac pacing. Once the boundaries of the RVOT have been defined, it is necessary to define the actual pacing positions within this area. For simplicity, the RVOT was divided into four quadrants. The RVOT is divided horizontally by a line midway between the pulmonary valve and the lower border, forming an upper and lower half. These two halves can be divided vertically by a line that connects the pulmonary valve to the RVOT lower border and in this way dividing the RVOT into the right ventricular septal and free wall. The created quadrants define high and low septal RVOT and high and low free-wall RVOT positions. The ECG confirmation of pacing in the right ventricular septum is manifested by a negative QRS morphology in lead I, whereas

pacing in the right ventricular free wall manifests as a positive QRS morphology in lead I. Furthermore, ventricular pacing in a high position will result in an upright QRS in aVF, whereas with a lower position it will have a less positive QRS deflection in aVF.

A study of Analson et al. [15] showed that the probability of the latest mechanical activation in the lateral wall is 35 %. This existence probability decreases in anterior and posterior regions to 26 % and 23 % respectively, whereas the inferior wall (septum) infrequently shows the latest mechanical activity (16 %). The study has demonstrated that optimal resynchronization could be obtained when the region with the latest activity determined by echocardiography is paced. From this perspective, 3D echocardiography may potentially identify the latest activated region for electrode pacing [24].

A recent study of Becker et al. [28] has investigated the efficacy of the CRT according to a proper selection of the LV lead. This study sought: firstly to identify the LV segment with latest mechanical contraction based on the myocardial deformation imaging method using tracking procedure of acoustic markers in 2D echocardiographic images [80, 106]. Secondly to determine the CRT efficacy for the LV lead position in the segment selected according to its greatest mechanical delay. The study demonstrates a relative simple approach to determine the LV position based on a detailed analysis of the myocardial contraction sequence before and on CRT. The LV lead position determined by circumferential strain analysis was found to be in high agreement with the anatomical LV lead position defined by fluoroscopy. A great reduction of QRS duration has been demonstrated to be an electrical marker of optimal CRT pacing [155]. This study evaluated concordance of the segment with earliest peak strain after CRT and the segment having the latest peak strain before CRT as a mechanical marker for optimal CRT. There was a significant relationship between the distance of the assumed LV lead position defined by a detailed myocardial deformation imaging analysis to the segment with greatest need for pacing and the improvement of LV function. Agreement of the assumed LV position and segment with latest contraction prior to CRT resulted in greatest functional response.

A study of Helm et al. [118] has searched an optimal LV pacing site for hearts with delayed lateral contraction due to LBBB. The study was conducted in 10 canine hearts. Hemodynamic pressure volume data were recorded and results for each pacing site were derived from an average of 10 sequential cycles. These data were used to derive arterial pulse pressure (dP/dt_{max}). Mechanical dyssynchrony was indexed by the circumferential uniformity ratio estimate (CURE) [118, 119, 153]. The optimal pacing sites were at lateral wall based on the maximal dP/dt_{max} response. The optimal pacing region was determined using a cost function defined as the ratio of the mean benefit from pacing within a given region divided by its relative size as a percentage of the LV surface. Very selective regions may have the highest mean CRT response. The regions defining the optimal response more

than 70 %, 80 % and 90 % are demonstrated in figure 3.5.

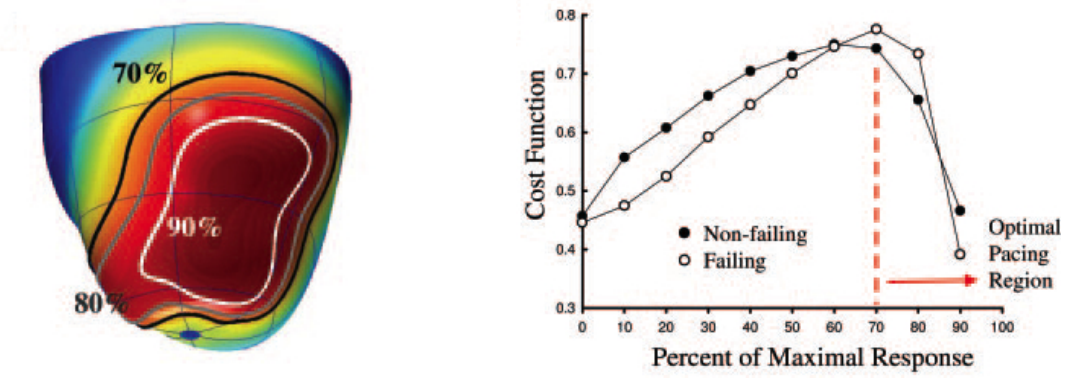

(a) (b)

Figure 3.5. Optimal LV pacing region with cost function: (a) Isoregions of 70 %, 80 % and 90 % corresponding to maximal CRT response for different LV pacing sites. The maximal response is an average from several electrodes yielding peak or nearly peak responses. (b) Cost function is calculated as the ratio of the mean functional response divided by the size of territory (percent of LV free wall). Function is plotted for regions providing varying percent levels of the maximal obtainable CRT benefit. The peak trade off between response and region size was at more than 70 % level and was considered as optimal regions. Optimal pacing region is achieved by minimal cost function and maximal cardiac response [118].

The main achievements in the study of Helm et al. [118] were:

1. The optimal LV pacing region is fairly broad and centered over the mid to apical lateral LV wall
2. Reasonable concordance exists between regions that yield the most mechanical synchrony and those achieved optimal LV systolic and diastolic performance

A summary of the studies in which different lead positions are investigated is demonstrated in table 3.2.

Author	Right electrode position	Left electrode position
Kass et al. 1999 [139]	RVA, midseptal	free wall
Sogaard et al. 2002 [252]	high inter-ventricular septum, RVOT	free wall
Teo et al. 2003 [264]	RVA	lateral, postolateral
*Verbeek et al. 2003 [278]	RVA, RVOT	anterolateral, posterolateral
Van Campen et al. 2006 [273]	RVA, RVOT	anterolateral, posterolateral
Yoshida et al. 2007 [291]	RVA, (RVOT in case of Tri-V)	lateral
Helm et al. 2007 [118]	RVA	entire free wall

RVA: right ventricular apex, LVA: left ventricular apex, RVOT: right ventricular outflow tract, Tri-V: triangle ventricular pacing, * implemented on the dogs heart

Table 3.2. Several studies since 1999 on CRT in which various positions of the electrodes have been investigated.

3.3.3 Timing Delays

As discussed, a BVP device constitutes 3 electrodes: one sensing electrode in the right atrium and two pacing electrodes in the left and right ventricle. When the sensing electrode measures an excitation, either the left or the right electrode stimulates the ventricle after a programmed delay (A-V delay). However the A-V delay varies according to each patient, the relative timing of inter-ventricular delay (V-V delay) might result in a better parameter setup for the BVP device (see right panel of figure 3.2). Compared to the conventional simultaneous pacing, sequential pacing using V-V delay yields incremental benefit from 25 % to 35 % in terms of contractility [160, 204, 274]. Several studies suggested that cardiac function might be improved by proper time programming of the BVP device [17, 42, 139, 186, 203, 207, 225, 250, 251, 270, 273, 277, 287].

Sogaard et.al [252] used tissue tracking and 3D echocardiography to evaluate the impact of sequential CRT with individualized timing delay programming. Tissue tracking and 3D echocardiography were carried out before and on the day after pacemaker implantation for twenty consecutive patients with severe heart failure and LBBB. The adjustment of A-V delay was performed during the simultaneous pacing according to the Ritter method [226], which means choosing the longest A-V delay without truncation of the A-wave (see section 2.4) by means of pulsed Doppler analysis of the transmitral flow. A similar study proposed that the optimal A-V delay should provide the longest LV filling time without early truncation of the A-wave by mitral valve closure [146]. The study has established that the refinement of ventricular offset (V-V delay) achieved even more benefits in systolic and diastolic function measured by TDI.

A recent study by Becker et al. [28] sought an optimal A-V delay using Doppler echocardiography. At first a long A-V delay was considered and this time was shortened step by step until a maximal mitral inflow profile (maximal time velocity integral) was achieved without reducing the A-wave duration. The study supposed a simultaneous pacing.

In a study of Boriani [43] a similar method is used to determine the appropriate A-V delay by echcardiographic evaluation of the transmitral filling pattern. The goal was to obtain the widest separation between E- and A-wave, preventing an early closure of the mitral valve. In order to optimize the V-V delay, Doppler echocardiography was used to obtain LV forward flow information or stroke volume. The stroke volume was derived from measurements of the left ventricular outflow tract (LVOT) diameter and the velocity time integral (VTI) of aortic flow. Stroke volume was calculated as:

$$Stroke\,volume = \frac{\pi}{4} \times LVOT \times VTI \tag{3.1}$$

The results were similar to the study of Becker et al. [28] since the optimized value of V-V delay in most patients was zero.

A summary of the studies in which different timing delays are investigated, is demonstrated in table 3.3.

A recent study by Whinnett et al. [287] proved the importance of an optimal choosing of timing delays (A-V, V-V delay) in CRT response by measuring the systolic blood pressure using a finometer. The study optimized A-V intervals using a finometer for measuring beat-to-beat changes in blood pressure. The technique was highly reproducible and indicated that changes in A-V intervals had a more pronounced effect on systolic blood pressure at higher paced atrial rates than at resting heart rates, with a parabolic relationship between A-V intervals and systolic blood pressure.

Another method for determining timing delays has been recently proposed by Lunati et al. [160] based on the observation that sequential ventricular pacing with an appropriate V-V delay can further increase the mechanical efficacy of the heart. This method is based on intracardial electrograms (IEGM) and estimates the V-V delay. The system measures the conduction delays between all following IEGMs:

1. Sensed IEGM from atrium to the LV lead
2. Sensed IEGM from atrium to the RV lead
3. Sensed IEGM from RV pacing to the LV
4. Sensed IEGM from LV pacing to the RV

Author	**A-V delay (*ms*)**	**V-V delay (*ms*)**
Ritter et al. 1999 [226]	60, 120, 180, 240, 300	-
Sogaard et al. 2002 [252]	avgd: 106.5 ± 26.6	L-R: **12, 20**, 40, 60, 80 R-L: 12, 20, 40, 60, 80
Perego et al. 2003 [204]	**80 - 160**	L-R: **20, 40, 60** R-L: 20, 40, **0**
Turner et al. 2004 [270]	**90 - 110**	-
Bruns et al. 2005 [51]	110 - 130	-
Whinnett et al. 2006 [287]	40, 60, 80, 120, **140, 160, 200**	L-R:**20**, 40, 60 R-L: 20, 40
Boriani et al. 2006 [43]	-	L-R: 20, 40, 80 R-L: 20, 40, 80, **0**
Becker et al. 2007 [28]	100 - 150	0

L-R: left before right, R-L: right before left, avgd: average delay

Table 3.3. Several studies since 1999 on CRT in which different timing delays have been investigated. Bold values state the optimal values chosen by the authors. In some studies, no optimal values were achieved.

The optimal V-V delay is defined by adding the correction factor to the difference between the atria and RV IEGM, with final multiplication by 0.5 (see equations 3.5 and 3.6 in section 3.4.3). The correction factor is assigned to the inter-ventricular conduction delay between pacing in one ventricle to sensing from the other ventricle.

Figure 3.6, illustrates a summary of optimization methods for timing delays. According to figure 3.6, several echocardiographic techniques have been developed in order to optimize the A-V interval. In the Ritter method [225], A-V intervals are programmed to a short and a sufficient long value in a way that the A-wave is not truncated (e.g. 60 ms and 160 ms). Then the delay between QRS onset and the end of the A-wave (QA interval) is measured at both setups. The optimized A-V delay values are gained through the following formulas:

$$AV_{opt} = AV_{short} + [(AV_{long} + QA_{long}) - (AV_{short} + QA_{short})] \tag{3.2}$$

This could be simplified to:

$$AV_{opt} = AV_{long} - (QA_{short} - QA_{long}) \tag{3.3}$$

A simplified method has been described by Meluzin et al. [175], whereby a single Doppler measurement at mitral inflow is required, with substraction of the interval between the end of the A-wave and onset of the systolic component of mitral regurgitation, from the programmed A-V interval with biventricular capture. The technique predicted settings with maximal cardiac output (measured by catheterization). This approach relies on the presence of mitral regurgitation.

On the iterative method a long A-V interval (e.g. 75 % of the intrinsic A-V interval) is programmed and the A-V interval decremented in 20 ms steps, until A-wave truncation is observed. The A-V interval may then be incremented in 10 ms steps to obtain the optimal setting [66].

The aortic Velocity-Time Integral (VTI) Method includes the measurement of aortic VTI, which is a surrogate of stroke volume and could be measured at different programmed A-V delays. Continuous-wave Doppler may provide more stable measurements as compared to pulsed-wave Doppler [132].

Recently, Jansen et al. [132] measured the LV dP/dt_{max} in order to optimize A-V intervals in patients with CRT using the pulsed-wave transmitral VTI (maximal VTI of E- and A-waves), diastolic filling time (maximal EA duration), the aortic VTI and Ritter's formula. Measurement of the maximal VTI of mitral inflow was the most accurate method, yielding identical results to LV dP/dt_{max} in 29 of 30 patients. The diastolic filling time and aortic VTI method performed worse (with concordant results in 20/30 and 13/30 patients

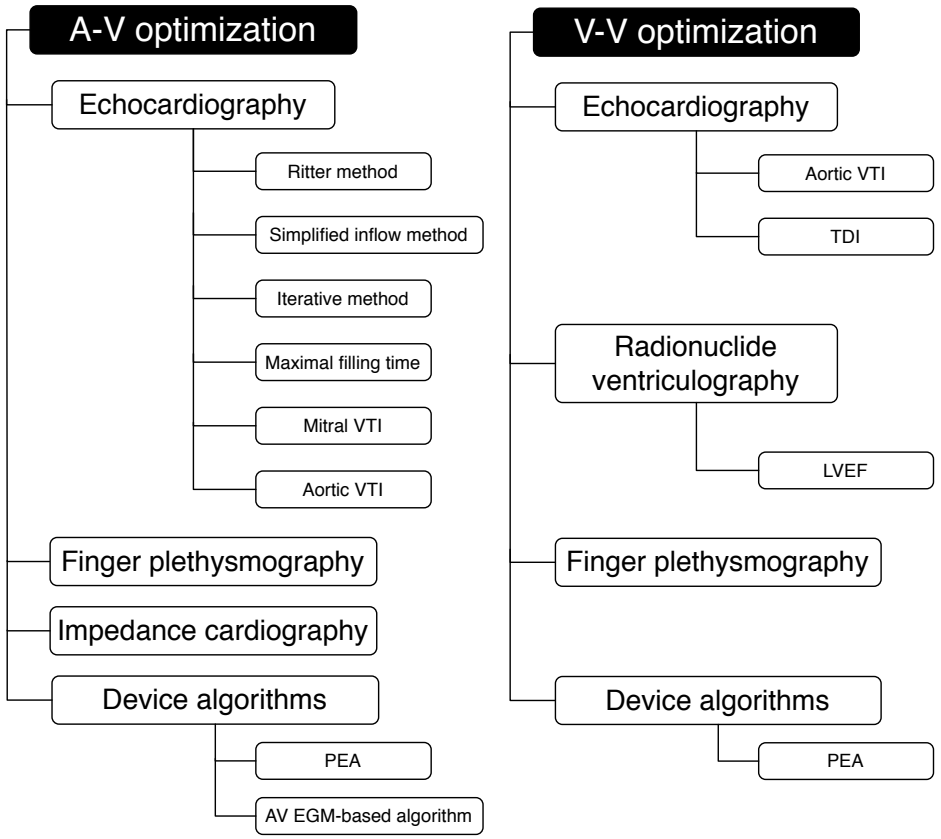

Figure 3.6. Techniques used for optimization of timing delays [55]: (a) A-V delay optimization. (b) V-V delay optimization. PEA: peak endocardial accleration, VTI: velocity time integral, TDI: tissue Doppler imaging.

respectively) and the Ritter method performed worst, with results differing to invasive measurements in all patients. Shortcomings of methods using VTI measurements are that they are relatively time consuming and may have limited reproducibility in the clinical setting.

Optimization of A-V intervals in patients with biventricular pacing by finger plethysmography using a conventional pulse oxymetry probe was reported by Butter et al. [58]. This technique correctly identified the optimal A-V interval that yielded maximum pulse pressure (measured invasively).

Impedance cardiography has been used for optimizing A-V intervals and was found to give similar results as echocardiography [45, 269]. As described by Braun et al. [45, 117], two electrodes were placed at the inferior chest wall and at the neck respectively. Low-amplitude high-frequency current was delivered via these surface electrodes and transthoracic impedance to this current flow was measured. Changes in transthoracic impedance (mainly influenced by changes of systolic aortic blood flow) were measured by means of

four additional surface electrodes: one pair placed bilaterally to the sternum and the second pair bilaterally to the abdomen. Cardiac output was calculated on a beat-to-beat basis from the transthoracic impedance signal (see figure 3.7). A-V interval values relate to the atrio-RV stimulation interval and V-V intervals relate to inter-ventricular interval with negative figures implying LV pre-excitation. Cardiac output is measured by impedance cardiography at different V-V delays and A-V delays until the optimal values according to maximal cardiac output are achieved.

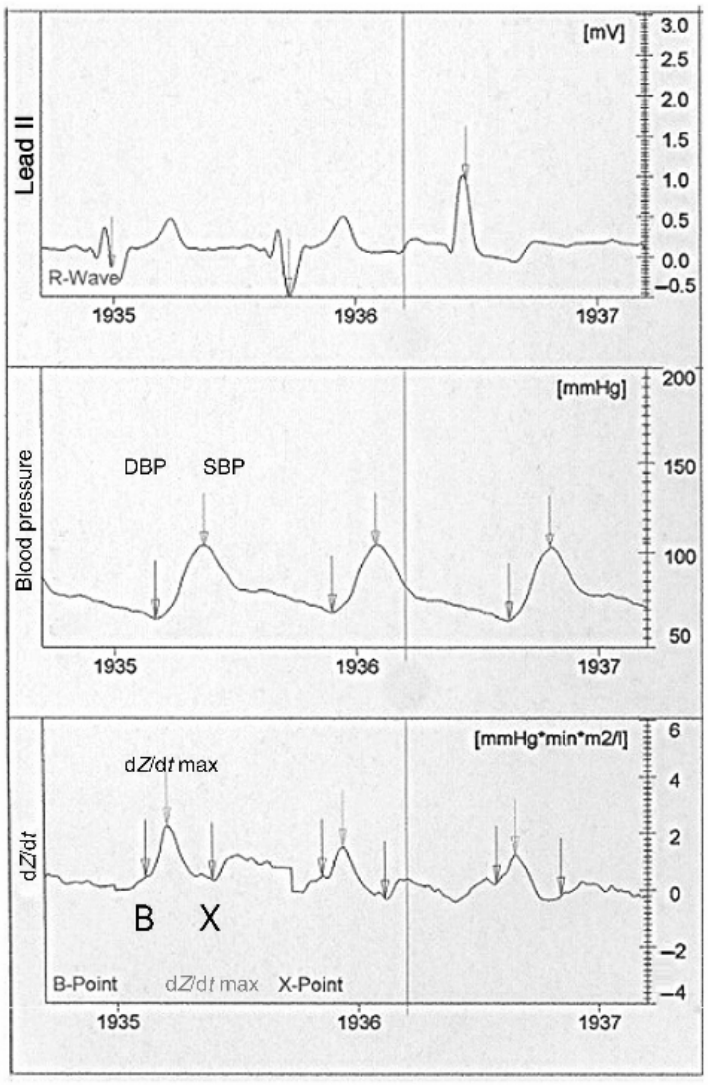

Figure 3.7. Example of the impedance cardiography measurement acquired by the Task Force Monitor System. There are two paced beats and one beat without pacing. From top to bottom: lead II of ECG, blood pressure and the first derivative dZ/dt of the impedance [117]. DBP: diastolic blood pressure, SBP: systolic blood pressure, B: aortic valve opening, dZ/dt_{max}: maximum of the first derivative of the impedance signal, X: aortic valve closure.

A number of treatment modalities still remain unsolved even though CRT suggests a therapy in moderate to severe heart failure patients with prolonged QRS. Investigation of some aspects of treatment modalities offers an improvement in hemodynamics.

Analysis of the BVP parameters in order to find the best locations for the electrode leads in the left and right ventricle in concurrent with optimized timing delays are crucial to reduce the number of non-responders to the therapy.

3.4 Optimization Methods Described in Literatures

In current clinical practice, there are several approaches for optimization of the BVP parameters; some using invasive measurements while others depend on measurements gained non-invasively. Most of the established BVP optimization methods are summarized in a review paper from Burri et al. [55].

The best value for the atrio-ventricular delay (A-V delay) is determined by approaches based on three principles, each evaluating a different hemodynamic parameter: echocardiography, beat-to-beat blood pressure determination and electrical measurements. The first method based on echocardiography is used often in daily clinical practice, either gauging the E- and A-waves of the inflowing blood (Ritter Method [226], Mitral Inflow Method [175]) or measuring the velocity-time-integral (VTI) of the aortic outflow or mitral inflow, respectively.

The second A-V delay optimization approach presented in [55] is the measurement of beat-to-beat changes in blood pressure using appropriate means, for instance finger plethysmography [58]. The third approach for A-V optimization utilizes electrical measurements, including impedance cardiography [269], determination of the QRS width in ECG and acceleration measurements of the ventricular wall using acceleration sensors placed at the tip of a catheter. The latter two methods are provided as built-in algorithms in several pacemaker models [55].

According to Burri et al. [55], the inter-ventricular stimulation delay (V-V delay) is optimized in clinical practice by methods based on four non-invasive measurement principles, while measuring the aortic pressure directly is negligible in clinical practice, since it is invasive and difficult to perform. The non-invasive methods are discussed below.

The echocardiographic methods act as an important approach for V-V delay optimization, including Tissue Doppler Imaging and aortic VTI measurement [224, 252]. The second alternative is the evaluation of the ejection fraction using nuclear angiography [56]. Thirdly, beat-to-beat blood pressure change measurements and finally the determination of ven-

tricular wall acceleration could be used for optimization of V-V delay.

A recent study from Toggweiler et al. [268], investigates the eligibility of acoustic cardiography for A-V and V-V delay optimization. The third and fourth heart sound are detected and evaluated in strength. This data together with an ECG is used to calculate the electromechanical activation time, which is minimized in order to determine the optimal A-V and V-V parameters. Results in study [268] show, that this method is also suitable for clinical optimization.

The above mentioned optimization methods have some advantages and disadvantages. The advantages are the non-invasive approach and the usability in daily clinical routine, especially for the echocardiography-based methods. Amongst others, some of the disadvantages are the lack of temporal resolution of nuclear angiography and delivery of suboptimal results of beat-to-beat blood pressure measurements for V-V optimization. A common disadvantage of all methods presented is that an optimization of the pacing electrode positioning is not performed [55, 268].

Electrode positioning influence on hemodynamic parameters was evaluated by van Campen et al. [273], who tested 9 different pacing sites while keeping the A-V and V-V delay constant. The optimal electrode setup was determined by measurement of cardiac index using Doppler flow imaging during a trial with 48 patients. It was shown that an individual adaptation of electrode positions improves the BVP efficacy [273].

Contrary to the methods described above, the optimization method presented in chapter 7 enables a pre-operative optimization of all three BVP parameters A-V delay, V-V delay and electrode positioning, which are all computed automatically. This may lead to significantly improved therapy success.

3.4.1 Invasive Measurements

Several studies recommend an implantable hemodynamic monitor (IHM) to be a reliable method for continuous measuring and recording of cardiac filling pressures in heart failure (HF) Patients [8, 46, 51, 166, 254]. IHM consists of a pressure lead and a memory device, which continuously records the heart rate, RV systolic/diastolic pressures in order to estimate the pulmonary artery diastolic pressure (ePAD). Furthermore, ePAD denotes the pressure at time of pulmonary valve opening. An external pressure reference is used to correct the barometric alteration of measured pressure. The maximum positive dP/dt of the RV pressure curve stands for ePAD. The pressure lead sensor is usually placed in the right ventricular high septum or right ventricular outflow tract (see figure 3.8).

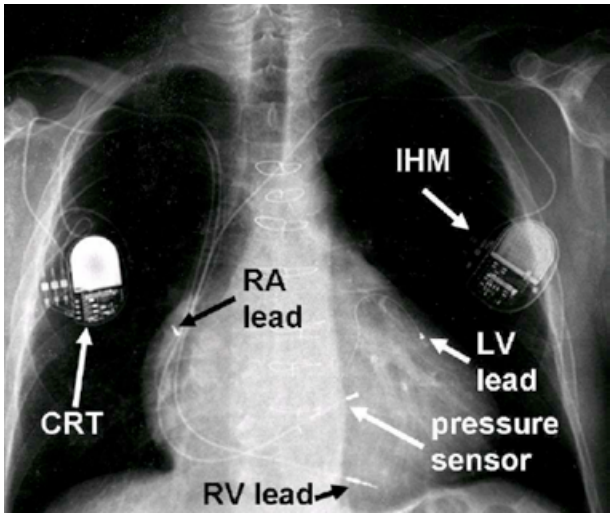

Figure 3.8. Chest X-ray of a patient under CRT with an IHM. CRT device is composed of three leads: RA, RV and LV lead. The pressure sensor lead belongs to the IHM [51].

Hemodynamic sensors, including pressure sensors and chemical sensors (pH, temperature) were tested in pacemakers. Most of them did not overcome the technological challenge needing an implantable sensor overtime. Recently, the available technology in the field of CRT is the peak endocardial acceleration (PEA) sensor [160]. During isovolumetric contraction and relaxation phases, myocardium generates mechanical vibrations which will be transmitted to the PEA sensor located in the cardiac wall. The measured peak to peak amplitude corresponds to the first heart sound, represents mitral valve closure which is correlated with the LV dP/dt_{max} [209]. According to the concept of the first heart sound detection, the PEA sensor is able to optimize the A-V delay [226]. In the CRT device, the optimization procedure is automatically launched every week without an external intervention. PEA can also be used to optimize the V-V delay.

Bruns et al. [51] measured the ePAD value for different A-V delays in order to find the optimal A-V delay. It was considered that the minimal ePAD maximizes the diastolic filling time without truncation of the active left ventricular filling by the left atrium. Accordingly, those A-V delays, which result in minimal ePAD, are the optimal ones.

In a study of Perego et al. [204], pressure signals were analyzed on beat by beat basis in order to obtain maximum systolic rate of change of pressure dP/dt_{max}, the minimum diastolic rate of pressure dP/dt_{min}, the maximum systolic pressure (SP) and end diastolic pressure (EDP). For each protocol step and for each patient, LV dP/dt_{max} values were compared by means of variance analysis, considering each beat as an individual case. In the whole study population, optimized synchronous CRT was associated with a significant increase in the maximal rate of LV pressure (LV dP/dt_{max}). The left ventricular EDP was significantly reduced compared to the baseline. In a minority of patients, RV dP/dt_{max}

changed in the opposite direction to LV dP/dt_{max} when timing delays were modified. Despite these observations, optimization of A-V and V-V delay based on maximal LV dP/dt_{max} was not associated with significant decrease in RV dP/dt_{max}. After pacing setup, a positive correlation between LV dP/dt_{max} and LV dP/dt_{min} was observed (see figure 3.9). In addition, the study underlined that RV dP/dt_{max} was a significantly weaker measure of RV mechanical efficiency than LV dP/dt_{max} for the left ventricle.

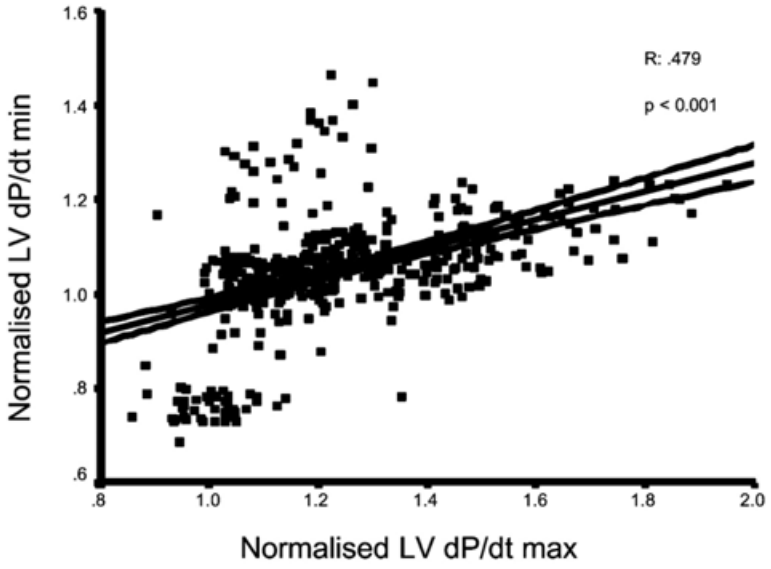

Figure 3.9. Linear correlation between maximal systolic rate of LV pressure change (LV dP/dt_{max}) and minimal diastolic rate of LV pressure change (LV dP/dt_{min}). The data from all the pacing steps of all patients are normalized to baseline [204].

3.4.2 Echocardiography

Multiple echocardiographic modalities including Doppler echocardiography have been applied in almost all studies as a non-invasive clinical tool, to analyze the temporal course of the LV contraction relying on the longitudinal motion [18, 25, 35, 65, 156, 203, 220, 255]. This ultrasound technique aimed to determine the level of dyssynchrony in LV contraction and additionally predicting the effectiveness of CRT on symptoms, functional capacity, mitral regurgitation and left ventricular reverse remodeling in patients [2, 25, 145, 237, 260]. Ahead of investigating the efficacy of the CRT, a baseline echocardiography is usually carried out in order to assess the left ventricular ejection fraction, mitral regurgitation severity and early to late transmitral flow velocity ratio (E/A) [273].

Although Doppler echocardiography is the preferred method for optimization of dual chamber and biventricular pacemaker programming after the implantation, there is a lack of guidelines for programming and the selection of appropriate echocardiographic method.

Optimization by Doppler echocardiography resulted in an improvement in LVEF, aortic velocity time integral (VTI) and maximum pressure increase [175, 268]. Optimization using the aortic VTI leads to better results in comparison with mitral inflow method [142, 175]. Systolic and diastolic parameters can also be obtained through conventional Doppler echocardiography such as diastolic filling time, myocardial cardiace index, E/A ratio, E-deceleration time, isovolumetric relaxation and pulmonary vein flow. Some of these parameters can be measured in order to determine the efficacy of CRT [237, 260].

The time difference between the aortic and the pulmonary pre-ejection period can be estimated by standard pulsed wave Doppler. The larger the difference between the aortic and pulmonary pre-ejection period, the greater the chance of response to CRT independent of QRS duration [97, 208].

Displacement imaging is a new tissue Doppler imaging (TDI) method which is used to transform the Doppler velocity data to a quantitative display of wall displacement toward the probe [235]. It has been demonstrated that left ventricular dyssynchrony can be quantified using displacement imaging by measuring the time difference to peak longitudinal systolic contraction of the septal and lateral mitral annulus [234].

Acoustic cardiography has been developed to measure diastolic heart sounds and systolic time intervals with assistance of ECG. This leads to detection of the third and the fourth heart sounds for measuring the electromechanical activation time (EMAT). EMAT is the time between the onset of the QRS complex and the mitral valve component of the first heart sound. Invasive studies indicate that EMAT and the third heart sound are correlated with LV function [168, 229, 244, 303].

The TDI technique for identification of mechanical dyssynchrony can be elaborated by measuring the time to peak myocardial sustained systolic (Ts) and diastolic velocity in different myocardial segments. Since typical appearance in heart failure patients is evidenced by earliest activation in the basal anterior septum and latest in the basal lateral segments [208], tissue Doppler imaging (TDI) and tissue tracking (TT) could be used to detect the LV systolic performance moreover LV asynchrony (see figure 3.10) [200, 251, 252, 253]. The reduction of myocardium showing the delayed longitudinal contraction (DLC) predicts the improvement in LV systolic performance and reversion of LV remodeling during CRT [251, 252, 253]. The hypothesis behind is that pre-activation of myocardium displaying DLC improves the overall response to CRT (see figure 3.11). Thus, TDI can be used to optimize the lead positioning (see section 3.3.2). As described in section 3.3.3, echocardiography is very often used to determine the optimal A-V delay. It can be also used to demonstrate and to assess the inter-ventricular and intra-ventricular resynchronization. Strain rate analysis was carried out in each segment and motion toward the apex in di-

astole was registered as DLC if negative strain rate analysis documented that the motion reflected true shortening.

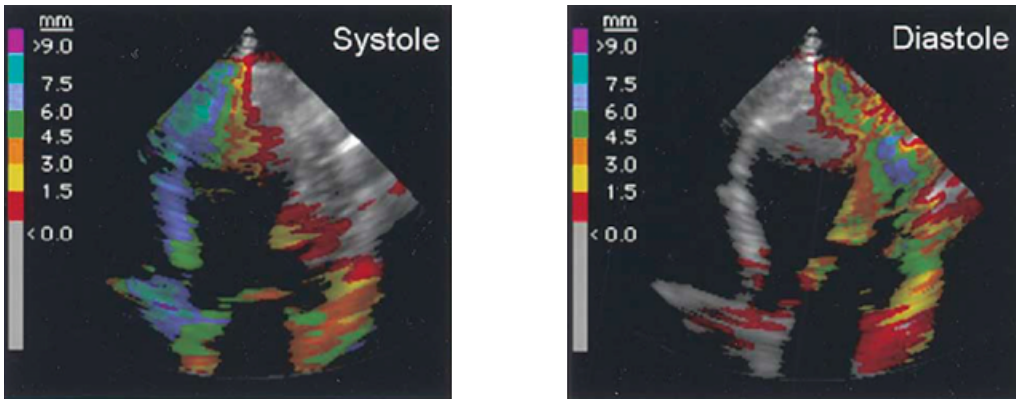

(a) (b)

Figure 3.10. Tissue tracking (TT) in a patient with LBBB. An irregular distribution of color-bands is seen during systole (left panel), indicating poor systolic performance of the lateral wall. Systolic apical displacement occurs only in the basal part of the lateral wall, whereas the remaining parts of the lateral wall show no net apical displacement during systole (gray color). After adjusting the TT time interval to left ventricular diastole (identified by aortic valve closure and mitral valve closure), the delayed longitudinal shortening of the lateral wall can be visualized by the apical displacement during diastole (right panel) [25].

Nowadays, the most commonly used tool for V-V delay optimization is either standard echocardiography or tissue Doppler imaging. Both methods could be used to determine the left ventricular outflow tract velocity-time integral (VTI) for calculation of stroke volume and myocardial performance index (MPI) and to assess dP/dt from the spectrum of mitral regurgitation [42, 252, 274]. Echocardiographic methods, however, have several limitations: they are time consuming, require two persons and are operator-dependent. The optimal V-V delay varies over time and should be re-evaluated during follow-ups [82]. Therefore, in routine CRT pacemaker follow-up, there is a strong need for an easier, faster and more cost-effective method of V-V delay optimization.

In the study of Teo et al. [264], echocardiography was performed pre-implant and post-implant to assess the left ventricular function. Additionally, the optimal AV delay was derived from the Doppler signal of the transmitral flow (Ritter method [226]). Furthermore, based on assessment of the site of latest activation in the LV, echocardiography can guide LV lead positioning and may be used to optimize A-V delay and V-V delay. Finally, echocardiography allows assessment of resynchronization and follow-up after CRT.

Since contraction of the ventricle myocardium is three dimensional, it includes longitudinal, radial and circumferential movement. Most studies investigate the longitudinal movement,

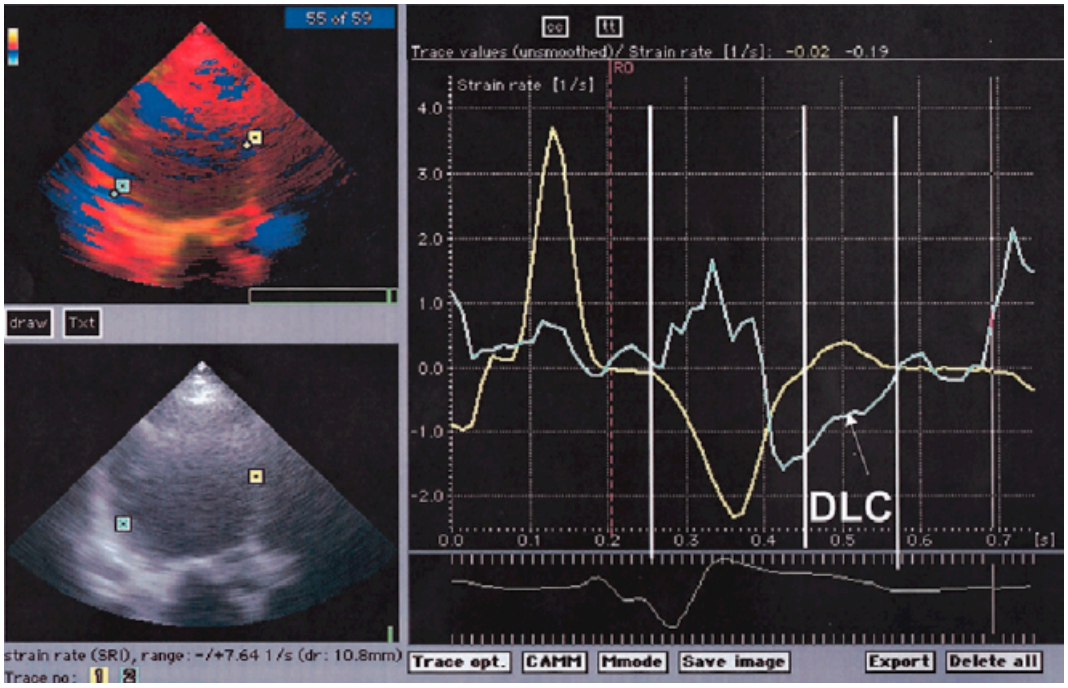

Figure 3.11. Apical long-axis view in patient with dilated cardiomyopathy and LBBB. One Doppler sample (yellow) is positioned at high septal area and another (green) is in posterior wall. In each of the 2 points, strain rate analysis is carried out. First vertical line (right) shows onset of negative strain rate (yellow curve), indicating active contraction in systole. Second vertical line indicates cessation of systole where strain rate (yellow curve) becomes positive. Shortly before second line, negative strain rate is observed in posterior wall (green curve) and this persists between second and third line, indicating active shortening in early diastole, i.e. longitudinal contraction delay (DLC) [251].

which explains the LV movement along the basal apical axis. During systole, the left ventricle condenses along its longitudinal axis, the base of the LV moving towards the apex. This motion is overturned during diastole while the base moves away from the apex.

Helm et al. [119] demonstrated that longitudinal motion analysis might be less sensitive to dyssynchrony since it follows different time courses than circumferential deformation and is not an adequate CRT efficacy significant. Therefore, the technique developed by Becker [28] using 2D echocardiographic analysis allows determination of circumferential deformation parameters, which leads to an optimal analysis of cardiac asynchrony. The distortion or circumferential deformation of the LV is the most complex motion since the LV generates a wringing motion with clockwise rotation at the base and counterclockwise rotation at the apex during systole.

The study of Becker et al. [28] investigated the impact of LV lead position in CRT using circumferential strain analysis, LVEF, LV end-systolic volume and LV end-diastolic volume which were determined by manual tracing of end-systolic and end-diastolic endocardial borders in 2D echo images. End-systole was marked as aortic valve closure in apical long axis views. Four parasternal short axis views (mitral valve level, papillary mus-

cle level, apical level and an additional apical level which allowed just visualization of the LV cavity) were acquired using 2D tissue harmonic imaging. The focus was adjusted to the centre of the LV cavity to optimize myocardial tissue characterization of all segments of the short axis views. The system followed acoustic markers accurately within the myocardium during several consecutive frames [220, 255]. It was assumed that the natural acoustic markers change their position from frame to frame in accordance with the surrounding tissue motion. The system calculated mean strain values for whole predefined LV segments. Regarding the width between endocardial and pericardial trace, a tracking setting was selected which included as much myocardium as possible, but prevented inclusion of tissue outside the myocardium. For analysis of LV myocardial deformation, the AHA 17 segments model was applied on the parasternal short axis views. For the parasternal short axis views on the basal and papillary muscle level six segments were analysed, for the short axis view on the apical level four segments were analysed and for the most apical level only one segment was analysed. For each segment with adequate tracking quality, circumferential strain was calculated as a mean over the whole segment.

Circumferential strain relates to circumferential deformation along the curvature of the left ventricle in the parasternal short axis. The circumferential strain values over time for each segment were given as strain-time curves (see figure 3.12). For each point on these curves, the exact time after the QRS complex and the strain value are displayed on demand. The segment having the latest peak negative circumferential strain before CRT in relation to the QRS complex was determined (see figure 3.12). Strain-time curves before CRT during intrinsic conduction and on active CRT one day after implantation were compared to determine the segment with the maximal temporal difference in peak negative circumferential strain (see figure 3.13). This segment was assumed to be the location of the LV lead. The distance between the assumed LV lead position and the segment with maximal baseline dyssynchrony was counted in number of segments referring to the four apico-basal levels and up to six segments within one circumference. One distance step was related either to the apico-basal level or to the circumferential level. Optimal position of the LV lead was defined as a concurrence of segments or immediate neighboring (one distance step) of the segment with maximal dyssynchrony and the segment with assumed location of the LV lead.

Hence, there are several tasks performed by 2D echocardographic images [28]:

1. Circumferential strain analysis based on tracking of acoustic markers in parasternal 2D echocardiographic images can be used in CRT to describe the temporal course of LV contraction.
2. Myocardial deformation imaging analysis allows an accurate assumption on the LV lead position in CRT based on a detailed analysis of the myocardial contraction sequence.

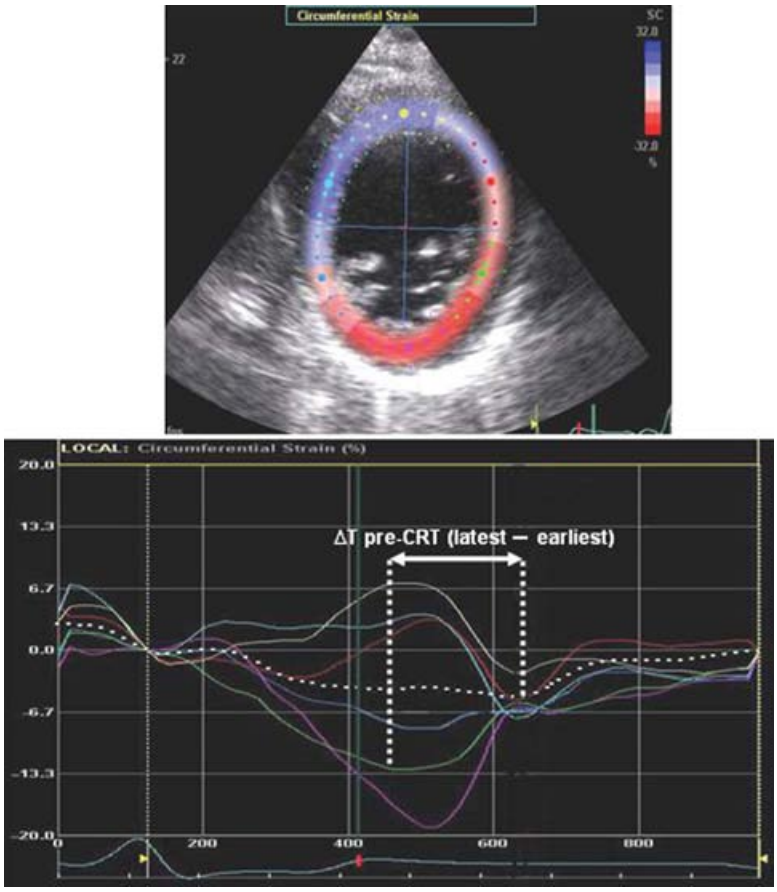

Figure 3.12. Upper panel: short axis view with circumferential strain display prior to cardiac resynchronization therapy at end-systole with inhomogeneous color distribution due to dyssynchronous contraction. Lower panel: there are six circumferential strain tracings for the six evaluated segments within the circumference. The dotted white line indicates the mean circumferential strain of all six segments. The time difference between segment with earliest and latest peak strain is marked [28].

3. Search for concurrence or neighborhood of the segment with assumed LV lead position based on circumferential strain analysis. Since results of pacing the LV segment with latest peak systolic strain show significantly greater improvement in LV function.

Hence, there are several tasks performed by 2D in order to investigate the mechanical displacement [234, 235]:

1. Measurement of myocardial contraction and relaxation velocities based on the phase shift of the ultrasound signal reflected from the contracting myocardium in order to identify the dyssynchrony.
2. Evaluation of septal to lateral wall contraction delay (longitudinal contraction delay) and assessing the distortion (circumferential deformation).
3. Calculation of the time-to-peak tissue displacement by time velocity integral (underlying TDI velocity integration).

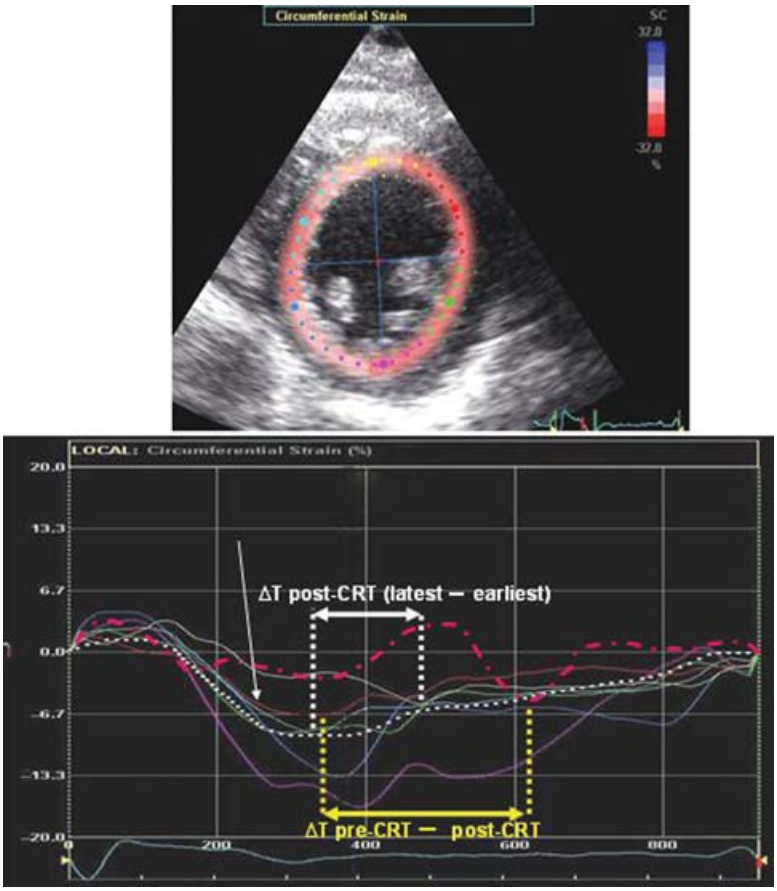

Figure 3.13. Upper panel: short axis view with circumferential strain display during cardiac resynchronization therapy at end-systole with homogenous color distribution due to synchronous contraction. Lower panel: circumferential strain tracings from the six evaluated segments within the circumference. The time difference between segment with earliest and latest peak strain during cardiac resynchronization therapy is given in white. The tracing obtained prior to cardiac resynchronization therapy from the segment with latest peak strain is added as an interrupted purple line. The tracing of the segment during resynchronization therapy is marked with a white arrow. The reduction in contraction delay with cardiac resynchronization therapy compared to prior to therapy for this segment is marked as yellow distance. It was greatest among all 17 left ventricular-segments of this patient indicating the left ventricular lead position [28].

Recently, tissue synchronization imaging (TSI) has been introduced by Van de Veire et al. [73], which is a signal processing algorithm of tissue Doppler data to detect the peak positive velocities for measuring the ventricular asynchrony. The value of TSI can predict the acute response to CRT. TSI automatically calculates the time to peak myocardial sustained systolic velocity (Ts) in every position in the image with reference to the QRS interval. To prevent TSI system of measuring peak systolic velocities outside the ejection phase, the tool is adjusted manually at the beginning and the end time intervals. The beginning and end time are set at aortic valve opening and at aortic valve closure time respectively.

Amongst studies on LV function improvement after CRT, a study of Rajagopalan et al. [218] investigated the RV function following CRT. The study showed the beneficial effects of CRT on RV function in terms of increasing the myocardial velocities at the region of interests (base, mid RV segments) using TDI. The improvement is verified by measuring the increased LVEF.

3.4.3 Intracardial Electrogram (IEGM)

A novel method of determining optimal V-V delay using intracardiac electrogram (IEGM) signals has recently been described [107, 160, 174]. This method assumes that optimal V-V timing occurs when the paced activations RV and LV leads meet in the intra-ventricular septum [149].

In this method, the delay in milliseconds (ms) between RV and LV intrinsic depolarization (Δ) is measured initially on the real-time IEGM from the LV and RV. Afterwards, the different wave front velocities left to right (IVCD: pacing LV, sensing in RV and measuring the distance between the two events in ms on IEGM) and right to left (IVCD: pacing RV, sensing in LV) are measured and then the two values are subtracted one from the other:

$$\epsilon = IVCD_{LR} - IVCD_{RL} \tag{3.4}$$

The optimal V-V timing is calculated:

$$V_{opt} = 0.5 \times (\Delta + \epsilon) \tag{3.5}$$

In most cases, the so-called correction coefficient (ϵ) is equal or close to 0 ms and the formula can be simplified to:

$$V_{opt} = 0.5 \times \Delta \tag{3.6}$$

As described in section 3.3.3, Lunati et al. [160] optimized the V-V delay according to the IEGM method.

3.4.4 Blood Pressure Measurements

Acute changes in blood pressure are potentially a good measure of the effect of changing pacing parameters on cardiac function. Whereas one may be concerned, in principle, that a change in blood pressure would instead be a result of a change in peripheral vascular tone, it is reassuring to remember that the stimulus for such a change in vascular tone must be a change in cardiac performance. Additionally, addressing the early few seconds after a change in pacing configuration allows us to focus on the primary cardiac effects rather than any secondary (vascular) effects. Even if secondary vascular effects do occur, they are likely to attenuate, rather than augment, the changes in blood pressure and so

this approach cannot overestimate the immediate effects on cardiac function [287].

In the study of Whinnett et al. [287] beat-to-beat blood pressure was recorded during adjustment of the A-V and V-V delay of the participants BVP device while paced at a rate of 110 beats/min. Testing was performed at raised heart rates because previous work from this unit has shown that, at higher heart rates, altering A-V delay had a more pronounced effect on blood pressure and that the peak A-V delay became clearer at higher heart rates. The systolic blood pressure was used as the hemodynamic target for optimization because this would have increased two indications if cardiac output rose:

1. The rise in cardiac output would increase the mean arterial pressure
2. The rise in stroke volume would increase the pulsatility of blood pressure.

To minimise the effects of background variation in blood pressure, each tested A-V and V-V delay was compared with an arbitrary fixed reference delay of A-V and V-V delay. The applied algorithm was based on beat-by-beat blood pressure, measured non-invasively with the finometer device, to assess the hemodynamic effect of simultaneously adjusting A-V and V-V delays. The relative change in systolic blood pressure (SBP_{rel}) was calculated by comparing the mean of the 10 beats immediately after a transition with the 10 beats immediately before (see figure 3.14).

Verbeek et al. [278] investigated the pacing results on inter-ventricular and intra-ventricular asynchrony in the left ventricular function with the assist of measured pressures. The aim of the study was to explore the mechanism of hemodynamic improvement during LV based pacing of hearts with LBBB. The pacing was performed in canine hearts. Various sites of LV were performed in different A-V delay in order to measure the maximum rate of increase of LV pressure (dP/dt_{max}) and LV stroke work (SW). Inter-ventricular delay was measured between upslope of LV and RV pressures. Intra-ventricular delay was measured from endocardial electrical activation maps. Typical examples of pressure-volume loops during pacing illustrate that pacing from various sites increased SW at essentially unchanged end diastolic volume (see figure 3.15).

3.4.5 Electrocardiography

Traditionally, the duration of the QRS complex on surface electrocardiograms has been used as a marker of LV dyssynchrony and consequently only patients with a wide QRS complex (more than 120 ms) were included in large trials [257, 260]. However, recent data indicated that the QRS duration does not adequately reflect LV dyssynchrony. The lack of a relation between QRS duration and LV dyssynchrony has been reported not only in patients with wide QRS complex but also in patients with narrow QRS complex. Moreover, various studies demonstrated that severe LV dyssynchrony might be present in 20 % to 50 % of patients with narrow QRS complex [39, 231, 296]. The fact that CRT may also be

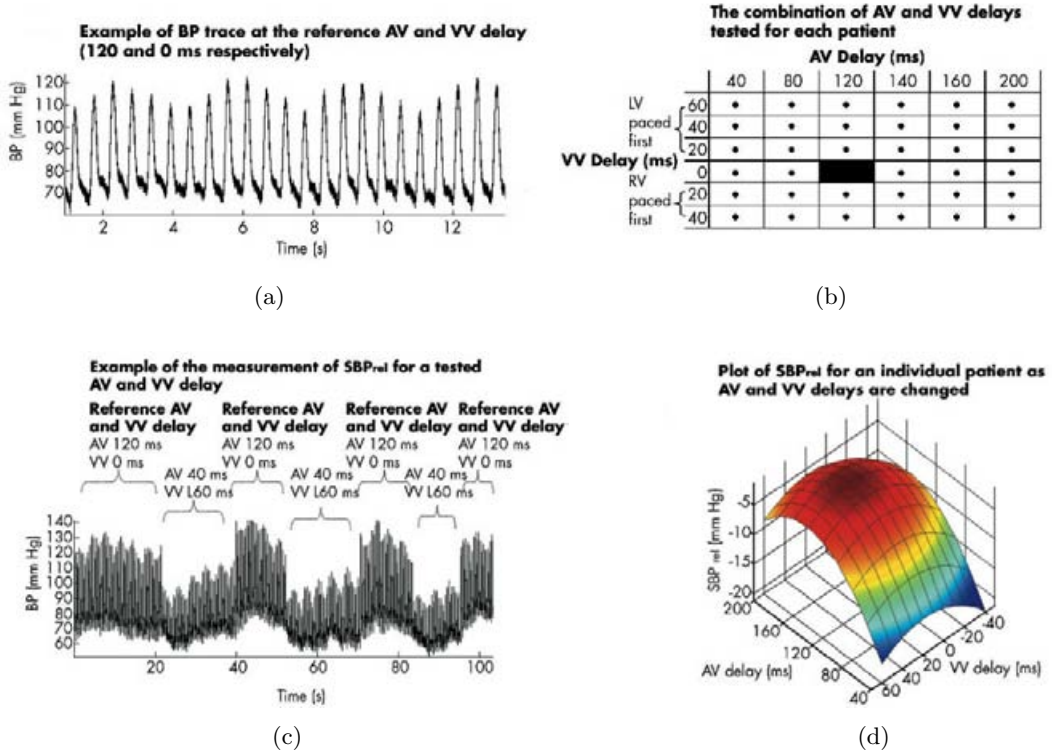

Figure 3.14. Example of the data acquired for measuring relative change in systolic blood pressure (SBP) for the tested atrio-ventricular (A-V) and inter-ventricular (V-V) delays [287]: (a) Each tested A-V and V-V delay was compared with the reference A-V and V-V delays (A-V 120 ms and V-V 0 ms); this reference delay was returned to between each tested delay. (b) Thirty five different combinations of A-V and V-V delay were measured, each time returning to the reference A-V and V-V delay. (c) To reduce the effect of background noise the relative change in systolic blood pressure (SBP_{rel}) (the mean of 10 beats before a change and the 10 beats immediately after a change) was calculated and the mean for at least six replicate transitions was established. (d) Constructing a surface plot of SBP_{rel} for each patient tested was then possible. LV: left ventricle; RV: right ventricle.

beneficial in heart failure patients with narrow QRS complex and severe LV dyssynchrony is an important issue, since the majority of heart failure patients may not show prolongation of the QRS complex and recent observations suggested that QRS widening more than 120 ms may occur in only 30 % of heart failure patients [36]. Therefore, the majority of heart failure patients have a narrow QRS complex and are currently not eligible for CRT. However, preliminary data from studies suggested that heart failure patients with narrow QRS complex may benefit from CRT.

Turner et al. [270] studied only the acute effects of CRT in a group of 20 heart failure patients with a QRS duration of 120 ms. In these patients, CRT resulted in an acute hemodynamic improvement, particularly in patients with a pulmonary capillary wedge pressure more than 15 $mmHg$.

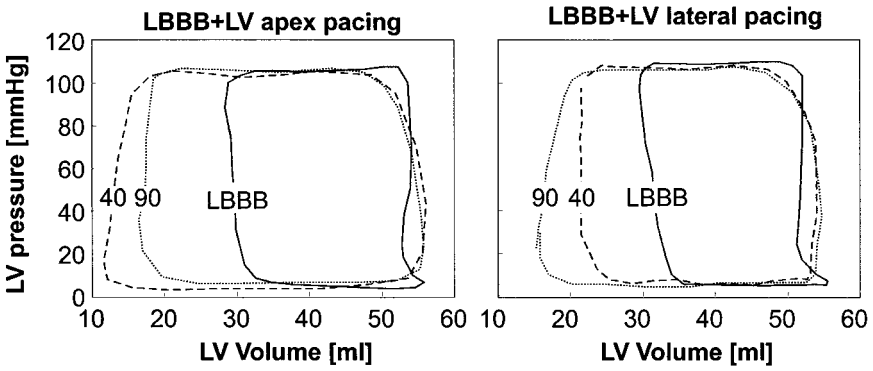

Figure 3.15. Pressure-volume loops measured with the conductance catheter, showing the short-term effect of pacing during left bundle branch block (LBBB) for left ventricular (LV) apex (left panel) and LV lateral pacing (right panel) at paced atrio-ventricular delays of 40 and 90 *ms*. The results for anterior and posterior wall pacing were comparable to those for lateral wall pacing [278].

In addition, Achilli et al. [5] studied the effects of CRT in a group of 14 heart failure patients with a QRS duration of 120 *ms* and compared these effects with a control group of 38 heart failure patients with a QRS duration more than 120 *ms*. All patients had evidence of LV dyssynchrony on M-mode echocardiography in combination with inter-ventricular dyssynchrony. The authors demonstrated that the clinical and functional benefit was similar in heart failure patients with wide and narrow QRS complex.

There are studies suggesting the QRS interval as an unreliable marker of the underlying mechanical dyssynchrony in the heart, since the absence of correlation between LV dP/dt_{max} and QRS duration has practical and theoretical implications. Several studies have provided conflicting results about the role of QRS shortening as a predictor of the hemodynamic results [59, 204, 298]. The results of Perego et al. [204] hypothesized that the minimal QRS length is not necessarily associated with the most efficient mechanical ventricular activation.

Analson et al. [59] explained that the degree of QRS narrowing under biventricular pacing was associated with symptomatic and functional improvement during follow-up in patients with congestive heart failure.

Gianfranchi et al. [102] has investigated the fusion band in ECG in order to optimize the resynchronization. The study delivered an electrocardiographic fusion band by programming the stimulator. The native electrocardiogram was recorded and measured with an intrinsic atrio-ventricular interval. Afterwards, atrio-ventricular interval was progressively shortened by steps of 20 *ms* down to 100 *ms*. Twelve leads electrocardiogram were recorded at each step. The fusion band is the range of A-V intervals at which surface electrocardiogram (mainly in V1 of Wilson lead) presents an intermediate morphology between the native left bundle branch block (upper limit of the band) and the paced right

bundle branch block (lower limit). The patient underwent echocardiographic examination at each atrio-ventricular interval chosen inside the fusion band. The following parameters were evaluated in order to verify the optimal results gained by electrocardiography: ejection fraction, diastolic filling time, E-wave deceleration time, aortic VTI and myocardial performance index (MPI). All the echocardiographic parameters showed an improvement inside the fusion band, with a plateau behaviour (see figure 3.16). As the fusion band in this study was ranged from an atrio-ventricular delay of 200 ms to an atrio-ventricular delay of 120 ms, an intermediate atrio-ventricular delay of 160 ms might guarantee the persistence of fusion even during any possible physiological atrio-ventricular conduction variation.

A recent study by Mohindra et al. [183] investigated the use of body surface potential mapping and computer model simulations to optimize the CRT device. The outcome was the influence of pacing locations on reducing dyssynchrony. Placing the LV pacing tip on the posterobasal section of LV and pacing both leads simultaneously helps to greatly reduce dyssynchrony without the need for optimal programming of the delay. This suggests that in patients with optimal lead placement, programming of the V-V timing may not be necessary [157, 183].

3.5 Conclusion and Unresolved Issues

Clinical trials of CRT have demonstrated considerable improvements in quality of life and exercise capacity, but a significant number of non-responders have decreased the overall benefits. The use of ECG criteria alone might result in selection of some patients who are unlikely to benefit and also exclusion of potential responders. Assessment of the regional left ventricular mechanical activation and viability with the echocardiography should be considered before implantation of the BVP device and further studies are required to refine the selection process. Once a decision has been made to proceed with the CRT then appropriate placement of the leads and optimal programming of the device will maximize the therapeutic effect. Several studies have shown that QRS duration is a relatively poor predictor of the symptomatic response to CRT in an individual patient [207, 223] and there is increasing evidence that the patients with ventricular dysfunction and normal QRS can benefit [20]. Several studies have assessed various invasive and non-invasive methods for optimizing the timing delays including beat-to-beat analysis of cardiac output and hemodynamical techniques. Table 3.4 demonstrates a summary of methods used for CRT optimization.

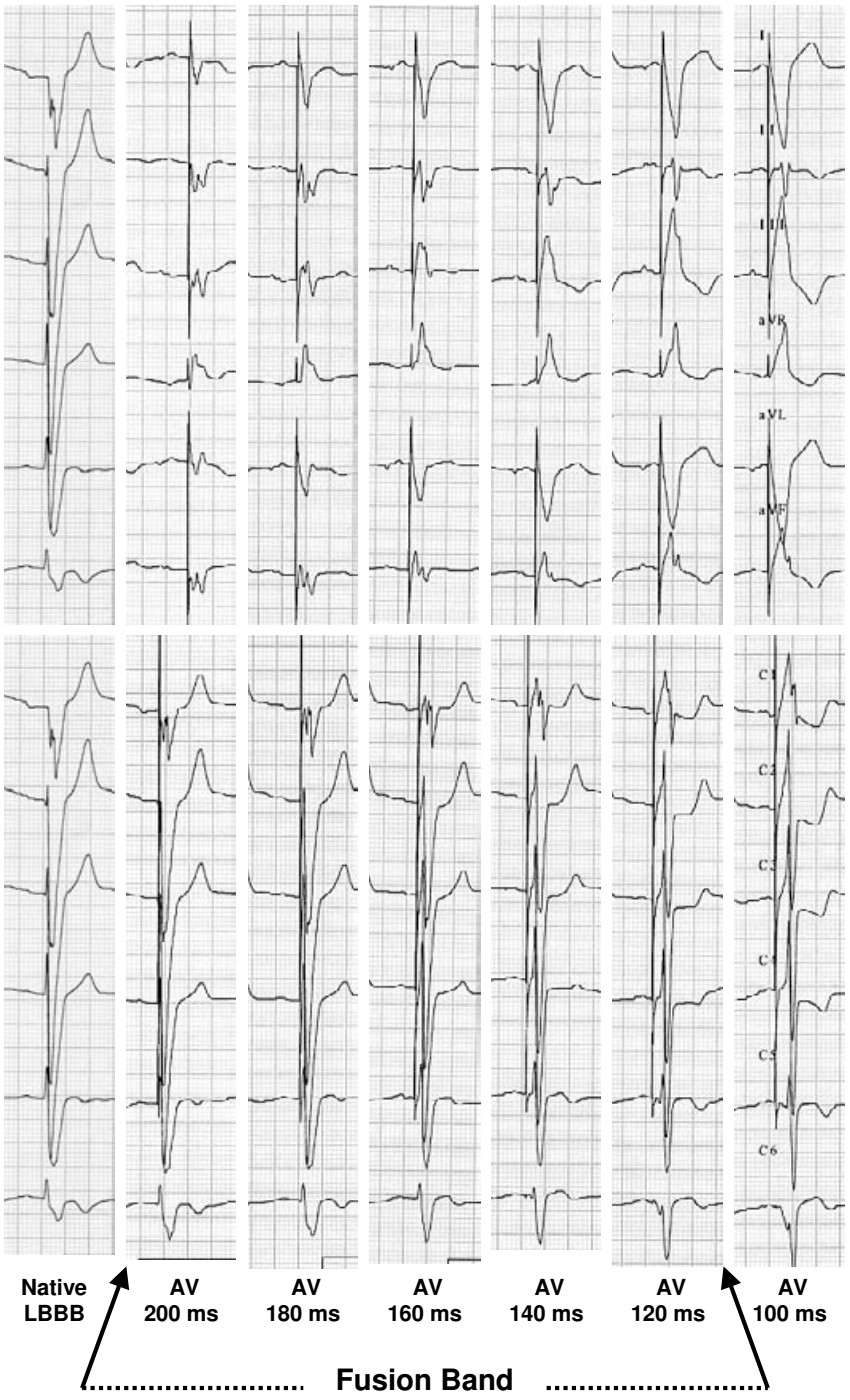

Figure 3.16. ECG morphology at different A-V intervals. Different ECG morphology corresponding to each programmed A-V interval, including the basal ECG of the patient without ventricular pacing. With the progressive shortening of the programmed A-V interval, QRS morphology (mainly in V1 lead) changes from LBBB to a RBBB-like trace at the shortest A-V interval, corresponding to a complete capture of both ventricles by LV pacing. Different degrees of ventricular fusion between RV spontaneous activation and LV pacing can be seen for A-V intervals programmed in the range $200 - 120\ ms$ [102].

Optimized parameters	Techniques	Measuring methods
Timing delays	Echocardiography	Ritter method Transmitral inflow Iterative method Diastolic filling time Mitral VTI Aortic VTI Myocardial performance index E/A ratio
	Intracardial electrogram (IEGM)	IVCD
	Radionuclide ventriculography	LVEF
	Finger plethysmography	Beat to beat blood pressure changes
	Impedance cardiography	dZ/dt
	Electrocardiography	QRS duration analysis
	Invasive with implanted device	PEA ePAD LV dP/dt EDP SP
	Finometer	Blood pressure measurements
Electrode positions	Echocardiography	Circumferential strain analysis DLC analysis
	Electrocardiography	QRS duration analysis
	Invasive with implanted device	Hemodynamic monitor (IHM) Pressure sensor Chemical sensor

Table 3.4. Clinical methods used for optimization of CRT parameters.

The work presented in chapter 7 proposes a non-invasive optimization algorithm to find the best electrode positioning sites and timing delays for BVP in patients with LBBB and MI. This algorithm can be used to plan an optimal therapy for an individual patient. The optimization algorithm is applied once on the activation time and other time on ECG intervals to investigate the BVP parameter optimization. Furthermore, optimization algorithms results are compared in this thesis.

4

Human Heart Modeling

The present chapter describes the methodology for setting up a volumetric 3D heart model from different image modalities. The construction of such a heart model consists of four stages:

1. Anatomical modeling
2. Cellular electrophysiology modeling
3. Excitation propagation modeling
4. Pathological modeling

Since the optimization methods of the research in chapter 7 will be verified in chapter 9, a simulation environment including a volume conductor model is provided. Therefore, an anatomical torso model with conductivity values is used in order to validate the optimized results by generating the corresponding ECG.

4.1 Anatomical Modeling of the Heart

Detailed anatomical models were achieved by segmentation of the MR data sets [84]. Thirteen 3D anatomical data sets were used. Ten of those were the segmented data sets of patients suffering from left bundle branch block (LBBB) and myocardial infarction (MI). The segmentation was done by using interactive deformable contours based on a triangle mesh forming the borders of different parts of the organ. A detailed description of the anatomical models including the geometrical characteristics and the pathological symptoms of the corresponding patients is included in chapter 6.

4.1.1 Segmentation Algorithms

The goal of segmentation is to separate an image into homogeneous regions with respect to one or more characteristics [22]. In medical imaging, segmentation is important for extracting various features and parameters, such as longitudinal contraction delay between two regions of interest in different slices of a 2D frame series. The aim of the study is to classify the MR images to the anatomical regions such as left ventricle, right ventricle

and blood vessels. Nowadays, a wide variety of segmentation techniques are available. However, there is no standard segmentation technique that can provide satisfactory result for all imaging application. Segmentation techniques are classified as follows [22]:

1. Region based techniques, which seek for a region fulfilling homogenous criterion.
2. Edge based techniques that look for edges between regions with different characteristics.

Two and three dimensional deformable models have been used to segment, visualize and quantify a variety of anatomical structures ranging in scale from the macroscopic to the microscopic. These include the brain, heart, arteries, kidney, lungs, stomach, liver and torso. Segmenting manually 3D image volumes slice by slice is a difficult process and requires good technical expertise in detecting the borders between different anatomical regions in MR images, because mostly the MR images are not taken in frontal view with enough slices.

Applying a 2D active contour model to an initial slice and the propagation of the model to neighboring slices can significantly improve the volume segmentation process. However, the use of a true 3D deformable surface model can potentially result in even greater improvements in efficiency. Deformable surface models in 3D were first used in computer vision [265]. Miller et al. [176] built a polygonal approximation to a sphere and deformed the geometry of the balloon model until the surface of the balloon conforms to the object surface of interest. The segmentation process is formulated as the minimization of a cost function where the desired behavior of the balloon model is determined by a local cost function associated with each model vertex. The cost function is a weighted sum of three terms: a deformation potential, which expands the model vertices toward the object border, an image term that identifies features such as edges and opposes the balloon expansion and a term that maintains the topology of the model by constraining each vertex to remain close to the center of its neighbors.

The energy of a contour $v(s)$, which in 2D is a function of $x(s)$ and $y(s)$ is defined as equation 4.1. The energy function is a summation of internal deformation energy and an external potential and should be minimized [22].

$$\mathcal{E}(\nu) = \mathcal{E}_i(\nu) + \mathcal{E}_e(\nu) \tag{4.1}$$

$$\mathcal{E}_i = \int_0^1 w_1(s)\left|\frac{\partial v}{\partial s}\right|^2 + w_2(s)\left|\frac{\partial^2 v}{\partial s^2}\right|^2 ds \tag{4.2}$$

$$\mathcal{E}_e(v) = \int_0^1 P(v(s))ds \tag{4.3}$$

where $w_1(s)$ controls the tension and $w_2(s)$ controls the rigidity. $P(v(s))$ denotes a scalar potential function on the image plane. The contour $v(s)$ that minimizes the energy $\mathcal{E}(\nu)$ must satisfy the Euler Lagrange equation [22]:

$$-\frac{\partial}{\partial s}\left(w_1\frac{\partial v}{\partial s}\right)+\frac{\partial^2}{\partial s^2}\left(w_2\frac{\partial^2 v}{\partial s^2}\right)+\nabla P(v(s,t))=0 \tag{4.4}$$

In the present study, the original mesh in the form of a sphere is created with a center in the middle of the region of interest [232, 300]. The sphere radius has an average value between the longest and shortest distance of the area boundary from the middle point. This sphere itself contains a number of triangular meshes in order to reproduce the border of the organ. This leads to ability of stretching and expanding interactively. The manual segmentation offers the pull and push possibility, allowing the user to decide where the next node of triangular mesh should be located. However, the placement of a new node may change the neighborhood locations (see figure 4.1).

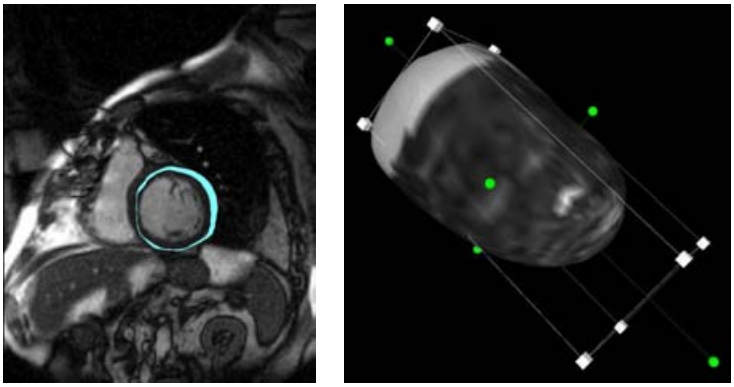

(a) (b)

Figure 4.1. Segmentation of left ventricle in short axis view: (a) Example of tracking the left ventricular epicardium. (b) Three dimensional volume representing the left ventricle based on the selected mesh.

In order to speed up the process of manual segmentation for the ventricles, a semi automatic algorithm is implemented for generating the endocardium from epicardium using the assumption of no difference between their structural shape. After segmenting the epicardium of the ventricle, the 2D slices of ventricle are investigated in the axial plane. The center of gravity (COG) is obtained for each epicardial slice and considered as the reference point in the polar coordinates. Several pairs of points are selected in the epi- and endocardium. Each pair of points and the COG are on a straight line. The reduction in radial direction is computed by averaging the differences of each pairs. The reduction or scaling coefficient is then multiplied by the epicardial points in each slice. This procedure offers a simple way to generate the endocardium. The steps of generating the endocardium is summarized as follows:

- Calculating the COG for each epicardial slice as a reference point

- Selecting at least 3 pairs of points from the epi- and endocardium respectively in one or different slices
- Calculating the average of the difference between epicardial and endocardial radii as a multiplication coefficient
- Multiplying the epicardial points to the scaling coefficient

The cross section of the segmented ventricle is demonstrated in figure 4.2.

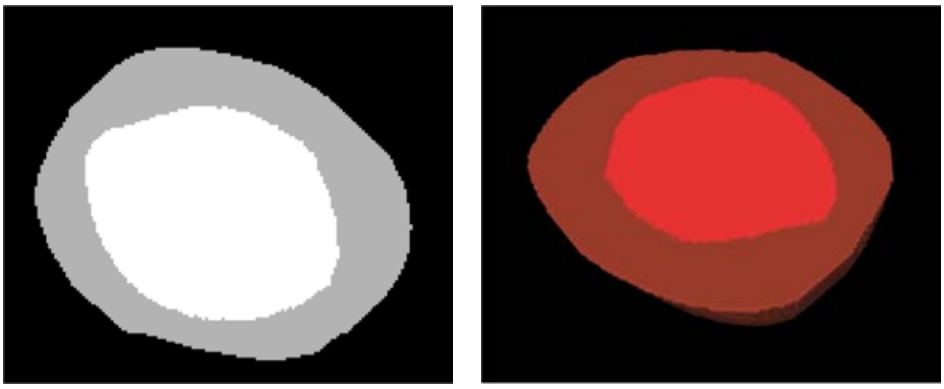

(a) (b)

Figure 4.2. Cross section of segmented left ventricle in axial view: (a) 2D view. (b) 3D view.

4.1.2 Three Dimensional Model

A 3D model is the next step after creating the volumetric mesh of the heart corresponding to left and right ventricle including epicardium and endocardium. Each extracted segment is associated with a certain value selected by the user from a codebook containing all organs with the corresponding values. The assignment of tissue values leads to the identification of each organ using a numerical label as a tissue class that simplifies further modeling steps. The classes' assignment is useful for modeling the conduction system, since the excitation propagation possibility in different tissues should be taken into account in the electrophysiological properties of different tissues. A sample of segmented ventricles with different tissue classes is demonstrated in figure 4.3.a.

The representation of the three dimensional image is based on the segmented volume extracted from series of 2D MR images (figure 4.3.b). The voxel side length can differ, according to the image resolution. Normally, due to the lack of sufficient slices in z axis direction, an interpolation between slices is necessary, resulting in an isotropic cubic voxel data set. This process is implemented prior to the segmentation.

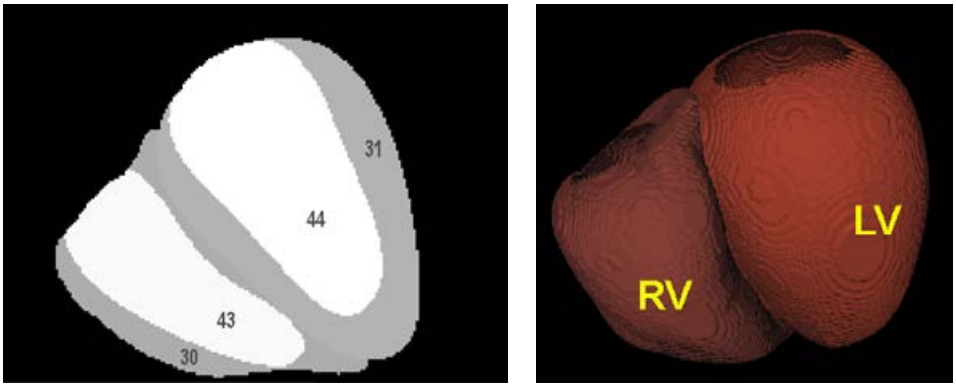

(a) (b)

Figure 4.3. A segmented ventricular model: (a) A slice of a segmented data set including left and right ventricular myocardium with tissue classes 31 and 30 respectively. The tissue classes 44 and 43 are assigned to the blood inside the left and right cavity respectively. (b) Three dimensional representation of the ventricles.

4.1.3 Myocardium Fiber Orientation

Fiber orientation affects the excitation conduction in the heart. The extraction of myocardial fiber orientation in this research is established by the software tool created by Weiss [282] based on Streeter et al. [256]. Streeter proposed two angles for each transmural position within the myocardium in order to define the fiber orientation in Cartesian coordinates (see figure 4.4):

1. Helix angle which depicts the fiber orientation rotation through the ventricular wall.
2. Transverse angle which depicts how the fibers are deflecting from the epicardial angle.

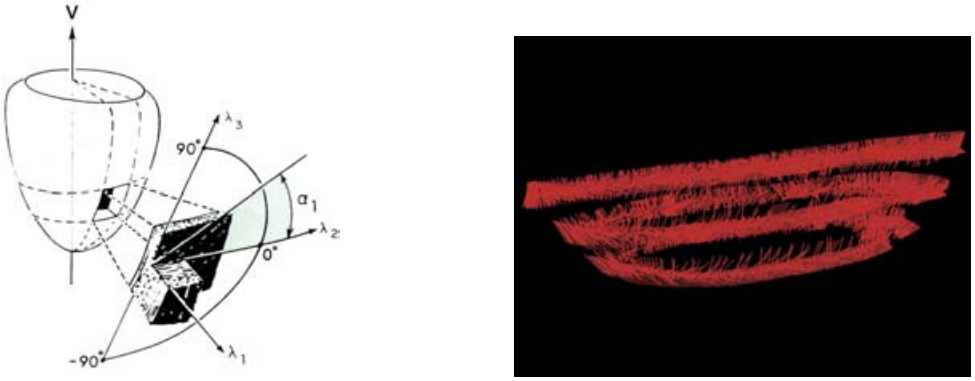

(a) (b)

Figure 4.4. (a) A transmural course of the LV myocardium (α_1 as helix angle and α_3 as transverse angle) [256]. (b) View of three axial slices illustrating the fiber orientation.

No noticeable change in transverse angle was measured, despite a small change of 6° from apex to base. The transverse angle was constantly varying from epicardium (-75.3°) over

0° in midmyocardium to 55.5° in endocardium [240, 256].

A rule-based algorithm, derived from anatomical studies by Streeter [256], was implemented to define the fiber orientation in the ventricular myocardium model. The fiber orientation is integrated to allow the assignment of anisotropic electrical properties to the tissue.

4.1.4 AHA Classification of Left Ventricle

The left ventricular subdivision algorithm was based on a publication of American Heart Association (AHA), proposing standardized myocardial segmentation for tomographic images in order to identify the region of investigation (see figure 4.5) [65]. The left ventricle was subdivided into 17 segments.

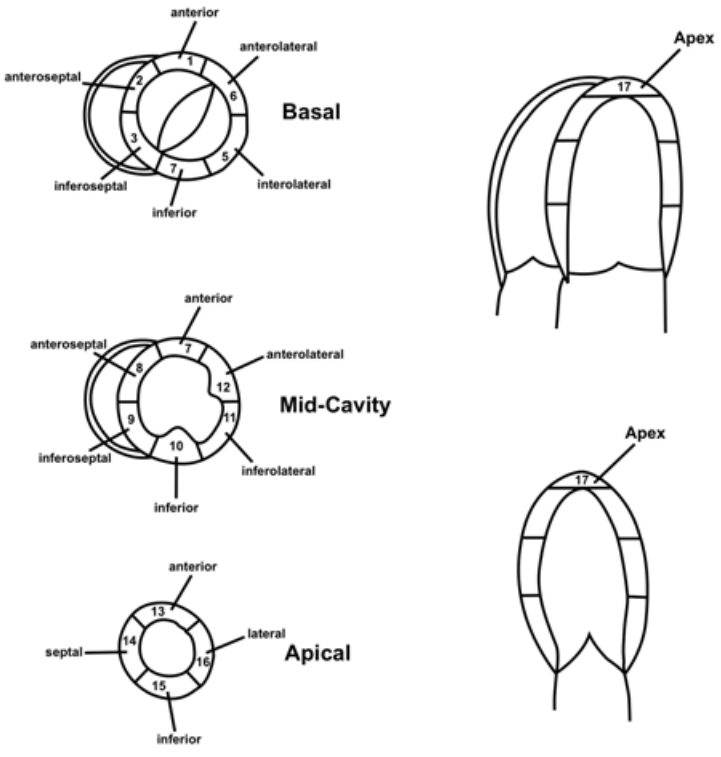

Figure 4.5. Subdivision of the left ventricle according to the AHA [65]: (a) Short axis view. (b) Long axis view.

The subdivision algorithm can also be applied to the right ventricle. The 17 segments can be enhanced to more segments in order to create more detailed standardized structure. The software developed by Keller [140] is applied to the 3D model of the left ventricle in

order to mark different locations specific for myocardial infarction (see figure 4.6).

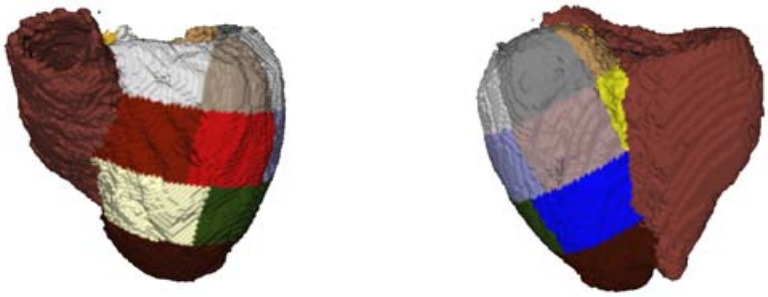

(a) (b)

Figure 4.6. AHA standard subdivision of the patient left ventricle. Different colors are used to indicate different segments. (a) Anterior. (b) Posterior.

Subdivision is done by a fully automatic algorithm. First, the long axis of the left ventricle is determined using principal component analysis. Then, the left ventricle is subdivided into 3 equal slices from basal to apical endocardium perpendicular to the long axis. The apex is defined as the fourth slice. In the last step, these slices are subdivided into the segments with equal angles. The segments are numbered from 1 to 17 according to AHA suggestion shown in figure 4.5.

4.2 Modeling the Electrophysiology

The second step in constructing a cardiac ventricular model is the implementation of electrophysiology. The electrophysiological behavior of myocytes was simulated by the ten Tusscher ionic cell model [261]. The mathematical system derives the transmembrane voltage of a myocyte from a number of ionic currents. With such a model, both the amplitude and the duration of the action potential (AP) can be calculated.

Additionally, a transmural heterogeneity of action potentials was included in the myocardial model. The heterogeneity of AP is achieved by changing the certain electrophysiological parameters, such as the slow delayed rectifier current (I_{ks}) and transient potassium outward current (I_{to}) from epi- to endocardium.

4.2.1 The Bidomain Model

The bidomain model considers two domains, respectively the intra- and extracellular space each with a potential and a conductivity tensor. The Poisson's equation describes the ionic currents and concentration in both intra- and extracellular spaces considering no external stimulus current [216].

$$\nabla \cdot (\sigma_i \nabla \phi_i) = A_m I_m \tag{4.5}$$

$$\nabla \cdot (\sigma_e \nabla \phi_e) = -A_m I_m \tag{4.6}$$

where A_m is defined to be the surface to volume ratio of the cell membrane and I_m is the transmembrane current density per unit area. ϕ_i and ϕ_e are the potential fields of the intra- and extracellular space. The conductivity tensors of these spaces are σ_i and σ_e. This leads to:

$$\nabla \cdot (\sigma_i \nabla \phi_i) = -\nabla \cdot (\sigma_e \nabla \phi_e) \tag{4.7}$$

The transmembrane voltage (V_m) is assumed as a potential difference across the cell membrane.

$$V_m = \phi_i - \phi_e \tag{4.8}$$

The following equation yields with subtracting $\nabla \cdot (\sigma_i \nabla \phi_e)$ from both sides of equation 4.7.

$$\nabla \cdot (\sigma_i \nabla V_m) = -\nabla \cdot ((\sigma_i + \sigma_e) \nabla \phi_e) \tag{4.9}$$

In addition, the transmembrane current (I_m) is expressed according to Hodgkin and Huxley [124] as follows (see figure 4.7):

$$I_m = C_m \frac{\partial V_m}{\partial t} + I_{mem} \tag{4.10}$$

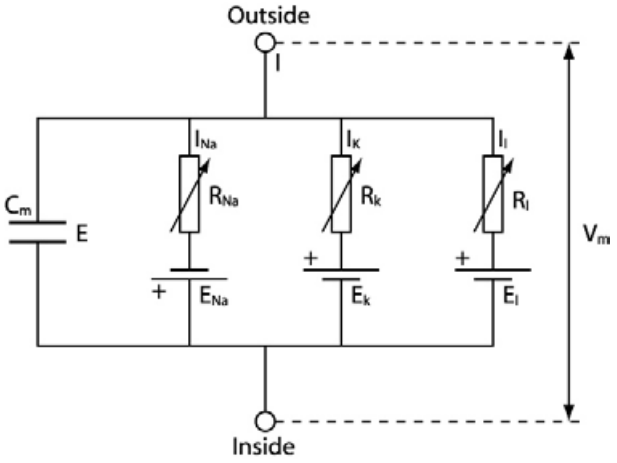

Figure 4.7. The electrical equivalent circuit representing the cell membrane of Hodgkin and Huxley [124]. The conductive components are a function of potential difference across the cell membrane (V_m) and the equilibrium potentials (E) of the ions. I_{Na}, I_K and I_l represent the sodium, potassium and leakage currents, R_{Na}, R_K and R_l are the corresponding resistances and V_{Na}, V_K and V_l are the corresponding Nernst potential [9].

where C_m is the membrane capacitance and I_{mem} is the sum of all ionic currents that are calculated from the cellular models. According to equation 4.6 , the equation 4.9 can be rewritten as follows:

$$\nabla \cdot (\sigma_i \nabla V_m) + \nabla \cdot (\sigma_i \nabla \phi_e) = A_m \cdot (C_m \frac{\partial V_m}{\partial t} + I_{mem}) \tag{4.11}$$

4.2.2 The ten Tusscher Cell Model

Different cell models were developed for describing the atrial or ventricular electrophysiology of a specific mammal, as illustrated in table 4.1.

In the human ventricular model of ten Tusscher, the complete ionic current I_{mem} consists of twelve components [261]:

$$I_{mem} = I_{Na} + I_{K1} + I_{to} + I_{Kr} + I_{Ks} + I_{CaL} + I_{NaCa} + I_{NaK} + I_{pCa} + I_{pK} + I_{bCa} + I_{bNa} \tag{4.12}$$

The description of the ionic currents components is in table 4.2.

Furthermore, a schematic of the ten Tusscher model is illustrated in figure 4.8. The intracellular compartments and the ionic currents taken into account are displayed. Additionally, a transmural heterogeneity of action potentials was considered.

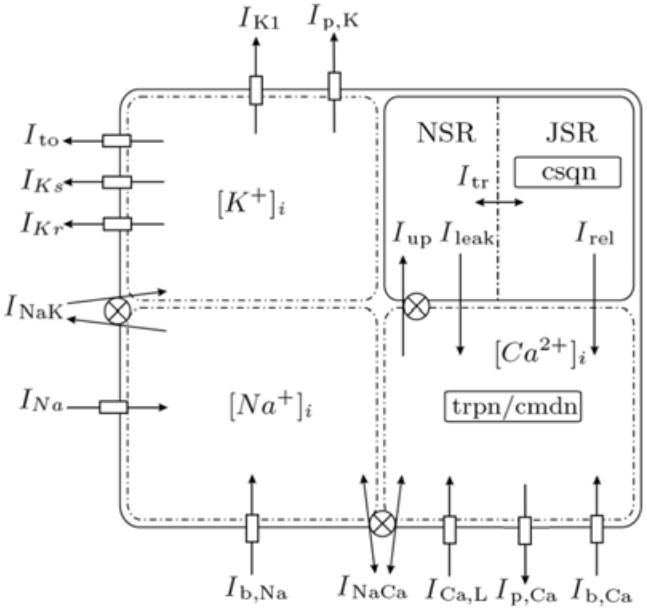

Figure 4.8. Schematic description of the ventricular cell model based on ten Tusscher. It contains detailed description of ion currents, pumps and exchangers in three cell compartments: myoplasm, sarcoplamatic reticulum (SR) and junctional sarcoplasmic reticulum (JSR) [261].

Year	Author	Specimen	Species
1975	McAllister, Noble, Tsien [170]	Purkinje fiber	-
1977	Beeler, Reuter [30]	Ventricular myocardium	Mammalian
1980	Yanagihara, Noma, Irisawa [289]	Sinoatrial node	Rabbit
1982	Bristow, Clark [47]	Sinoatrial node	Rabbit
1983	Bristow, Clark [48]	Sinoatrial node	Rabbit
1984	Noble, Noble [195]	Sinoatrial node	Rabbit
1985	DiFrancesco, Noble [79]	Purkinje fiber	Mammalian
1987	Hilgemann, Noble [122]	Atrial working myocardium	Rabbit
1990	Earm, Noble [90]	Atrial working myocardium	Rabbit
1991	Luo, Rudy [161]	Ventricular myocardium	Mammalian
1994	Luo, Rudy [162, 163]	Ventricular myocardium	Guinea-pig
1994	Demir, Clark, Murphey, Giles [77]	Sinoatrial node	Rabbit
1996	Dokos, Celler, Lovell [81]	Sinoatrial node	Mammalian
1996	Lindblad, Murphey, Clark, Giles [158]	Atrial working myocardium	Rabbit
1996	Demir, O'Rourke, Tomaselli, Marban, Winslow [78]	Ventricular myocardium	Rabbit
1998	Courtemanche, Ramirez, Nattel [69]	Atrial working myocardium	Human
1998	Nygren, Fiset, Firek, Clark, Lindblad, Clark, Giles [198]	Atrial working myocardium	Human
1998	Jafri, Rice, Winslow [130]	Ventricular myocardium	Guinea-pig
1998	Noble, Varghese, Kohl, Noble [196]	Ventricular myocardium	Guinea-pig
1998	Priebe, Beuckelmann [214]	Ventricular myocardium	Human
1999	Demir, Clark, Giles [76]	Sinoatrial node	Rabbit
1999	Winslow, Rice, Jafri, Marbán, O'Rourke [288]	Ventricular myocardium	Canine
2000	Ramirez, Nattel, Courtemanche [219]	Atrial working myocardium	Canine
2000	Zhang, Holden, Kodoma, Honjo, Lei, Varghese, Boyett [301]	Sinoatrial node	Rabbit
2001	Boyett, Zhang, Garny, Holden [44]	Sinoatrial node	Rabbit
2001	Pandit, Clark, Giles, Demir [201]	Ventricular myocardium	Rat
2001	Puglisi, Bers [215]	Ventricular myocardium	Rabbit
2002	Kneller, Ramirez, Chartier, Courtemanche, Nattel [148]	Atrial working myocardium	Canine
2002	Kurata, Hisatome, Imanishi, Shibamoto [151]	Sinoatrial node	Rabbit
2002	Bernus, Wilders, Zemlin, Verschelde, Panfilov [33]	Ventricular myocardium	Human
2004	Lovell, Cloherty, Celler, Dokos [159]	Sinoatrial node	Rabbit
2004	ten Tusscher, Noble, Noble, Panfilov [261]	Ventricular myocardium	Human
2004	Iyer, Mazhari, Winslow [129]	Ventricular myocardium	Human
2006	ten Tusscher II, Panfilov [262]	Ventricular myocardium	Human

Table 4.1. Ionic models of cardiac cells [241]

	Current	Definition
Sodium currents	I_{Na}	fast sodium influx
	I_{bNa}	background sodium current
Potassium currents	I_{K1}	inward rectifier current
	I_{Kr}	rapid delayed rectifier current
	I_{Ks}	slow delayed rectifier current
	I_{to}	transient potassium outward current
	I_{pK}	plateau potassium current
Calcium currents	I_{CaL}	L-type calcium current
	I_{bCa}	background calcium current
	I_{pCa}	plateau calcium current
Mixed currents	I_{NaK}	sodium/potassium pump current
	I_{NaCa}	sodium/calcium exchanger current

Table 4.2. I_{mem} components according to the ten Tusscher cell model [261].

Figure 4.9 shows how the AP of myocytes changes from endo- to epicardium. The heterogeneity of AP is achieved by changing the model parameters of slow delayed rectifier current (I_{ks}) and transient potassium outward current (I_{to}) from epi- to endocardium. The electrophysiological model of this work is based on the model of a human ventricular myocyte provided by ten Tusscher et al. [261]. The model is adjusted for epicardial, endocardial and midmyocardial cells to allow for the transmural heterogeneity of the human ventricular myocardium [93]. The midmyocardial cells have the longest AP duration. Action potential curves have been calculated for cells embedded into myocardial tissue using the bidomain model [211, 283].

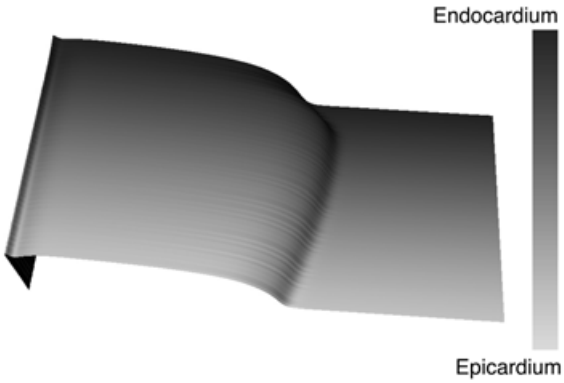

Figure 4.9. The simulated AP curves changing from endocardium to epicardium [94].

4.3 Modeling Excitation Propagation

The excitation conduction between two adjacent cells can be determined by either solving the Poisson's equation in bidomain model or by using simplified models, for generating the excitation propagations according to a set of rules. An adaptive cellular automaton (ACA), belonging to the rule-based heart models, was used in the present work.

4.3.1 Adaptive Cellular Automaton (ACA)

The ACA model does not consider explicitly the ionic flow interaction between the intra- and extracellular spaces in order to simulate the excitation propagation. Instead, the pre-calculated APs derived from the ionic current equations based on the ten Tusscher model are applied as a set of rules stored in a predefined library for the fast computation of ventricular excitation. The calculation partition results in a greatly reduced computation time in comparison to the bidomain model. The calculation time of the ACA used is approximately 4 minutes for the simulation of one heart beat on a PowerPC 2GHz. The ACA computes the three dimensional excitation propagation according to the fiber orientation, location of the cell and its recent course of transmembrane voltage. The ACA is composed of a finite number of nodes. Each node corresponds to a set of heart myocytes possessing the same properties in a small region of the heart. By a given time instant, the state of each node in the cellular automaton changes depending on the states of a finite number of neighboring nodes and the node's own state in the previous time steps. Different nodes may obey different criteria for state transition. The state of each node is interpreted as transmembrane voltage at a given time instant. The criteria describing the transition include the electrophysiological parameters, type of cardiac tissue, time course of the transmembrane voltage during current and previous excitation, conduction velocity and fiber orientation in myocardium.

The ACA developed by Werner, Sachse and Dössel [285, 286] was applied in this work for the heart model representing isotropic cubic voxels. The excitation is conducted between the voxels (nodes) of the heart model if the following rules are satisfied (see figure 4.10):

1. Both nodes are excitable.
2. The excitation propagation between both nodes is permitted.
3. The node going to be excited, is not already excited and is in absolute refractory phase.
4. If the node is already in relative refractory phase, the produced action potential has a smaller amplitude and duration compared to a not excited node.

The ACA uses precalculated action potential courses, which were calculated by cardiac cell models. For each (node) tissue type, there are several action potential course possibilities, depending on the various stimulus rates and different cardiac cell time states. If the cell is stimulated during refractory period, there is no AP generated. If the stimulus occurs during relative refractory period, the resulting AP has smaller amplitude and shorter duration. With all these rules, the ACA selects the proper AP course for each node from the precalculated AP courses. Also, the ACA excites the neighboring cells according to the rule set.

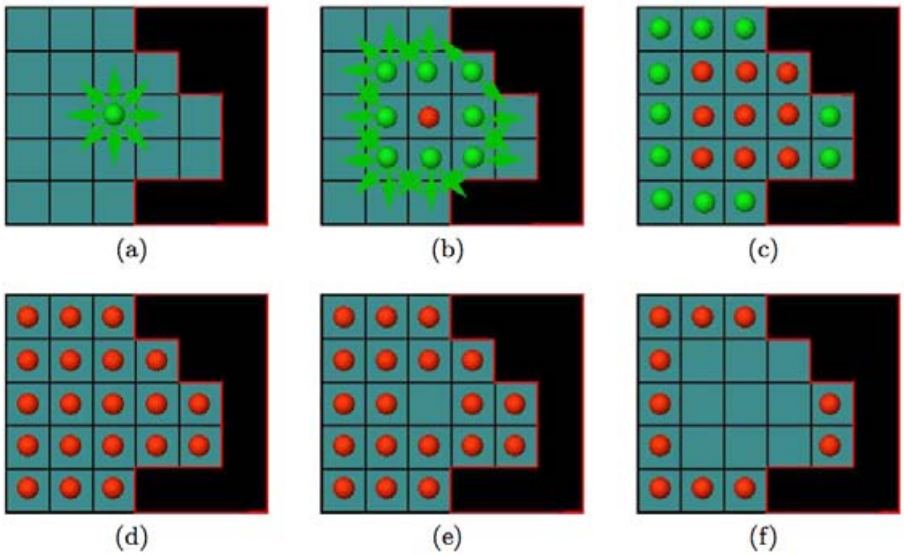

Figure 4.10. Cellular automaton function [239]: (a) Excitation initiation in one cell. (b) Propagation into the neighboring cells and refractory phase of initial excited cell. (c) Refractory phase of the last neighboring cells and the further conduction of excitation to the adjacent cells. (d) All the cells in refractory phase. (e) Repolarization of the initial cell. (f) Repolarization of the neighboring cells which returns them to the excitable cells.

4.3.2 Modeling the Excitation Conduction System

In order to simulate electrical excitation initiation and propagation, a pacemaker model and an excitation conduction system are implemented into the cardiac model. The excitation conduction system up to the left and right bundle is generated manually according to an anatomical atlas. The right bundle branch usually originates from the most distal part of the His bundle as a single slender bundle and crosses through the muscular inter-ventricular septum to the right ventricular endocardial septal wall [131]. The bundle emerges at the right septal surface and continues to the moderator band, where it branches into two different parts, one carrying excitation to the anterior papillary muscle, and the other to the RV free wall. The left bundle branch (LBB) has a highly variable anatomy in different individuals. The LBB consists of three main branches with multiple interconnections, which ramify over the left ventricular septal wall and extend to the bases of the anterior and posterior papillary muscles, carrying excitation to the septum and the inferior and superior free wall [263].

In this research, the end points of Purkinje fibers are generated on the endocardium based on a density given by the user. The program then automatically connects the end points of the Purkinje fibers with the Tawara bundles using an optimal tree. The algorithm is based on Graph theory with minimization of the cost function [284]. Figure 4.11 shows a generated conduction system for a patient data set.

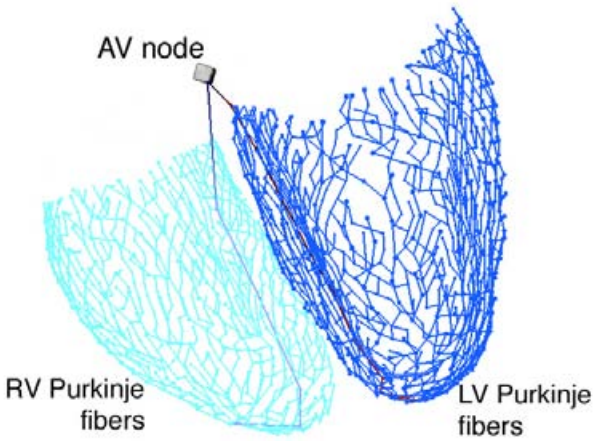

Figure 4.11. Simulated excitation conduction system of the ventricles starting from AV node to Purkinje fibers.

4.4 Modeling Pathologies

The pathologies simulated in this study were a total left bundle branch block (LBBB) in conjunction with reduced intra-ventricular conduction velocities and myocardial infarction (MI).

4.4.1 Myocardial Infarction: Allocation in AHA Segments

Myocardial infarction consists of necrotic tissue in the center and a surrounding transition zone of ischemic tissues with gradually changing properties. This results in a change of excitation propagation ability for cardiac cells. In the study, the myocardial infarction is modeled by a spherical area of about $30 - 50$ voxel volume including the necrotic tissues with excitation propagation velocity of zero in the center and a surrounding ischemic area with slower conduction velocity [134]. Since, the center of the infarction consists of dead necrotic tissue showing no electrical activity. The necrotic center is surrounded by an ischemic area, with gradually increasing electrical activity (see figure 4.12.a).

According to figure 4.12.a, the diagram shows the dependency of excitation propagation velocity and excitation amplitude dependent on the normalized distance from infarction center. In the center, propagation velocity and excitation amplitude are 0. Starting from distance factor 0.5, propagation velocity and excitation amplitude increase up to the normal value. Figure 4.12.b illustrates a cross section of the ventricles with simulated infarction, which shows activation of the myocardium. The area of infarction is clearly visible with no activation.

In order to simulate several infarction locations, the AHA recommendation for ventricular classification was implemented. This standard ventricular classification enables an abstract

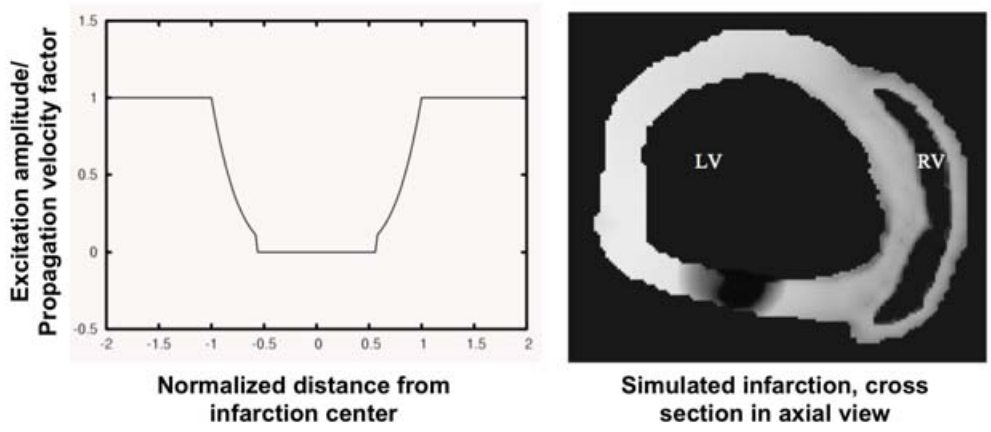

(a) (b)

Figure 4.12. Myocardium infarction: (a) Modeling a myocardial infarction by adapting the excitation amplitude factor and the propagation velocity factor to the normalized distance from infarction center [134] . In the center of the infarction there is a necrotic area showing no electrical activity (factor 0). The necrotic area is surrounded by an ischemic area with gradually increasing activity (factor increasing up to 1). (b) An axial cross section of the ventricles with the myocardial infarction through a delayed activation (gray spot) and no activation (black spot).

description of infarction location and later allocation of corresponding optimal electrode positions. An excitation propagation velocity of zero and a slower conduction velocity were assigned to the necrotic and ischemic area at the corresponding AHA segment, respectively. Therefore, AHA segments enable a standard description of nomenclature, allocation of MI and additionally the corresponding optimal lead positioning [177]. The 17 AHA segments are assigned to the territories of the coronary arteries, according to AHA proposal. This is considered to make sense, due to the coronary arteries' vital role in oxygen supply.

4.4.2 Left Bundle Branch Block: Simulation of Blockage in the Excitation Conduction System

The LBBB pathology was modeled by setting a disconnection in the excitation conduction system after the bundle of His. Moreover the LBBB was modeled by adjusting the cellular automaton parameters in a way that the electrical excitation transmission failed along the left bundle branch. The LBBB could also be modeled by setting the excitation conduction velocity to zero along the left bundle.

4.4.3 Reduction of Intra-ventricular Conduction Velocity

In patients with Congestive Heart Failure (CHF), heart tissue shows a larger amount of fibrotic tissue. In order to model this, the ventricular excitation conduction velocity was simulated with 100 %, 80 % and 60 % of the physiological case.

Inter-ventricular delay can be modeled by reducing the electrical conduction velocity in both ventricles. In LBBB patients, in addition the excitation of left ventricle is delayed. Hence, in order to simulate the total inter-ventricular delay, a disconnection of excitation conduction and a reduction of conduction velocity in the left ventricle were performed. In this work, namely the intra-ventricular conduction velocity was set to 100 %, 80 % and 60 % of physiological value.

5

Forward and Inverse Problems of Electrocardiography

The most important aim in electrocardiography is to increase the information about cardiac electrical activity, which is extracted by non-invasive measurements on the body surface. The general objective of the forward and inverse problems of electrocardiography is a better qualitative and quantitative understanding of the heart's electrical activity. To this end, an equivalent source model, in conjunction with a specified volume conductor is usually taken into account as the subject's torso.

The forward problem of electrocardiography refers to the computation of the body surface potentials starting from either equivalent current dipoles representing the electrical activity of the heart or from known potentials on the epicardium. In general, two approaches are used in order to solve the forward problem [110]: surface methods and volume methods

In surface based methods, an isotropic conductivity is considered into different regions of the torso hence only the boundaries between different regions are isolated and characterized in the numerical torso. If an anisotropic region such as skeletal muscle should be included into the torso model, the first step is converting it to an approximately isotropic region before forward calculation. These computations involve the solution of integral equations for the potentials of the discrete surfaces of the torso model (Boundary Element Method).

In volume based methods, the entire three dimensional torso model is represented numerically by a combination of tetrahedral or hexahedral elements. Volume based methods may be subdivided into finite differences, finite element and finite volume methods.

In comparison to others, surface methods utilize simpler torso models with fewer elements. However the matrix characterizing the set of equations to be solved is fully populated, since the principal integral equations couple the potential of each element to the potential of other elements [110]. Nevertheless, in volume methods the potential at each point is expressed only in terms of potentials at its nearest neighbors.

In contrast to the forward problem, which can be solved uniquely to a constant potential, the inverse problem does not possess a mathematically unique solution and considers the reconstruction of cause by its effects. The cardiac sources should be computed from the measured BSPM on the body surface. The primary cardiac sources cannot be uniquely determined as long as the active cardiac region containing these sources is inaccessible for potential measurements. This is because the electric field that these sources generate outside any closed surface completely enclosing them, may be duplicated by equivalent single-layer (monopole) or double-layer (dipole) current sources on the closed surface itself. Many equivalent sources, and hence inverse solutions, are thus possible. However, once an equivalent source is selected, its parameters can usually be determined uniquely from the body-surface potentials [202].

Since one of the major applications of the forward problem is simulating the cardiac pathologies with computer heart models, this chapter describes the forward problem of electrocardiography. Modeling of the generated bioelectric fields from cardiac sources in the tissues and surface of the human body is incorporated with ECG and the standard leads (see chapter 2). The simulation of electrocardiograms, which were used in this work under idealized conditions, will be described later. In addition, the solutions of forward and inverse problem will be declared.

5.1 Solution of Forward Problem of Electrocardiography

The construction of geometry models of the heart and torso is essential to solve the forward and inverse problem of electrocardiography. Once the geometry models containing torso, lungs, heart, stomach, liver etc. are available, a numerical approach is required to solve the field problem. As discussed at the beginning of this chapter, the numerical methods are classified to [85, 242, 247]:

1. Surface approach, which is based on integral function technique. The typical algorithm is the boundary element method (BEM) [4, 96, 101, 136].
2. Volume approach, which is based on differential equations techniques. The typical algorithms include finite element method (FEM) [135, 136], finite difference method (FDM) [194] and finite volume method (FVM) [113].

In the surface approach, the interfaces of different conductivity regions are detected for modeling. Therefore, this approach can considerably reduce the number of unknown variables. However, it is very difficult to handle anisotropic regions, while the volume approach is very suitable to model the inhomogeneous areas. These two approaches have their own advantages and can be applied to different problems. In the BEM, the BE mesh is critical and directly influences the solution accuracy [54, 96, 101, 242].

Since the computation of BSPM and ECG in this research is performed via finite element based human body model, this section provides a brief description on volume approach method.

As discussed in section 4.2.1, the bidomain model is a macroscopic way to consider the cellular electrophysiology of the myocyte with dividing the region in two subspaces (intra and extracellular) while considering potential and conductivity for each subspace [94].

The conductivity tensor σ which contains the conductivity of myocyte tissue is defined as follows:

$$\sigma_S = \begin{pmatrix} \sigma_{Sl} & 0 & 0 \\ 0 & \sigma_{St} & 0 \\ 0 & 0 & \sigma_{St} \end{pmatrix} \tag{5.1}$$

for S = i, is referred to the intracellular domain
for S = e, is referred to the extracellular domain

where σ_{Sl} and σ_{St} are respectively the longitudinal and transversal scalar conductivities according to the fiber direction of the myocardiun tissues. This is due to the anisotropic characteristic of the excitation propagation along the fibers. The anisotropy ratio R is defined as a ratio between the longitudinal and transversal conductivity [233]:

$$R = \frac{\sigma_{Sl}}{\sigma_{St}} \tag{5.2}$$

The bidomain equations for extra and intracellular spaces are defined as follows [94, 233]:

$$\nabla.(\sigma_i \nabla \varphi_i) = f \tag{5.3}$$

$$\nabla.(\sigma_e \nabla \varphi_e) = -f \tag{5.4}$$

where σ_i and σ_e are conductivity tensors of intra and extracellular space. φ_i and φ_e are respectively intra and extracellular potential. The current source density f is related to the divergence of the impressed current density J_s as follows:

$$f = \nabla \cdot J_s \tag{5.5}$$

Adding equation 5.3 and 5.4 together with considering the transmembrane voltage as $V_m = \varphi_i - \varphi_e$, the following equation is obtained:

$$\nabla.((\sigma_i + \sigma_e)\nabla \varphi_e) = -\nabla.(\sigma_i \nabla V_m) \tag{5.6}$$

substitution of following parameters as

$$\sigma_i + \sigma_e = \sigma \tag{5.7}$$

$$\nabla.(\sigma_i \nabla V_m) = f \tag{5.8}$$

leads to the Poisson equation of:

$$\nabla.(\sigma \nabla \varphi) = -f \qquad in\ \Gamma \tag{5.9}$$

where Γ is a finite domain of volume conductor. The boundaries are taken as the zero reference potential and the area between body surface and air to satisfy the Dirichlet and Neumann boundary conditions respectively [94]. The equation 5.9 can be discretized by finite element method with tetrahedral unstructured grids and an adaptive mesh refinement. The linear system equations achieved by finite element approximation can be solved by numerical solution algorithms iteratively. In the current work using the forward solver software of IBT, Cholesky decomposition and conjugate gradient method are used in order to solve the forward problem [94, 104, 249]. The finite element model leads to size reduction of the problem. Since the computation of the body surface is resulted from heart sources, a high resolution geometry should be considered in the heart region. Therefore, more nodes and vertices are assigned to the heart geometry whereas less nodes are considered for homogeneous regions. The current source density is computed by interpolation of the transmembrane voltages to the finite element grid [94]. An example of finite element model is demonstrated in figure 5.1.

(a) (b)

Figure 5.1. The Meet Man finite element model: (a) torso. (b) heart.

5.2 Solution of Inverse Problem of Electrocardiography

As already mentioned, the inverse problem does not possess a unique solution. This difficulty is solved by using simplified models for the cardiac current sources and regularization techniques. These models introduce implicit constraints, enabling model parameters to be uniquely computed from the surface potentials. Therefore, the solution of the inverse problem will lead to recover an approximation of the electrical activity of the equivalent source based on the measured potentials on the torso surface. The different solutions to the inverse problem may be presented according to the type of the heart model whose parameters are being sought.

To stabilize inverse solutions against sensitivity to small perturbations in the input, additional constraints based on supplementary *a priori* information, must be imposed on the solution. Straightforward least-squares solutions will not give reliable results due to the presence of the common small singular value decomposition (SVD). Even truncated SVD solutions are not very effective because of the lack of a clear distinction between significant and insignificant singular values [86, 94, 202].

The most common approach to this problem is a technique known as Tikhonov regularization: the least-squares residual error cost function is supplemented by a second term that penalizes for large values of a chosen property of the solution. Thus, a tradeoff is constructed between fidelity to the data (small residual error) and fidelity to the constraint represented by the second term (small regularization error). This tradeoff is controlled by a multiplicative weight known as the regularization parameter. Among areas of recent development have been the incorporation of more constraints, and especially, temporal and spatial ones. Inverse solutions in general clinical application will need to incorporate such sophisticated techniques to impose physiologically realistic constraints as precisely as possible. Such solutions hold the promise of greatly improved characterizations, quantification, and localization of cardiac abnormalities from non-invasive body surface measurements [202].

As discussed in section 4.2.1, the bidomain model gives a linear relationship between the distributions of TMV within the myocardium and the BSPM. To solve the inverse problem, a simplified finite element model is constructed. Different conductivities for various geometry elements are considered. The transfer matrix in the following equation is computed by a series of forward computations [94],

$$A.\overrightarrow{x} = \overrightarrow{y} \tag{5.10}$$

where $A \in \mathbb{R}^{m \times n}$ is the transfer matrix describing the relationship between cardiac sources and BSPM. $\overrightarrow{x} \in \mathbb{R}^n$ is the vector of cardiac sources and $\overrightarrow{y} \in \mathbb{R}^m$ is the vector of measured

BSPM [94, 249]. A random column vector $\overrightarrow{N}$ can be added to the left part of equation 5.10 where each component corresponds to a Gaussian random variable that models the additive zero mean Gaussian noise added to the measure. In general, at least one solution exists because the number of recorded samples on the body surface is larger than the quantity of epicardial potential nodes. The opposite situation will lead directly to an extremely undeterminated system of equations, providing a non-unique solution.

Hence, from an algebraic point of view, at least m uncorrelated samples leading to m linear independent equations will be enough to solve the problem. However, the proximity between them and the fact that they are recording a common electrical source cause an important correlation and similarity between observed signals in the electrodes. But despite this dependence, they stay linearly independent, with infinite precision, even with no noise, due to the Gauss' Law. More observed data is expected to add some new information into the problem. Nevertheless, as the body surface is finite, the more samples, the more correlation between them. So the quantity of information incorporated by each new sample decreases as a function of the total of observed points [202].

The relation between epicardial and ECG potentials is concentrated in the forward matrix. When a matrix suffers from all the former problems, it is called an ill-conditioned matrix. The degree of ill-conditioning can be numerically determined as the proportion of the largest and smallest singular value of the SVD decomposition of the forward matrix. This classification can also be interpreted from SVD point of view, through the degree of ill-conditioning. There are two important classes of problems to consider, and many practical problems belong to one of these two classes.

1. Rank-deficient problems which are characterized by the matrix A having a cluster of small singular values, and there is a well-determined gap between large and small singular values.
2. Ill-posed problems, where all the singular values of A, as well as the SVD components of the solution, on average, decay gradually to zero.

For discrete ill-posed problems, the goal is to find a balance between the residual norm and the size of the solution that matches the errors in the data as well as one's expectations to the computed solution.

Further examples of regularization methods are generalized singular value decomposition (GSVD), Tikhonov regularization zero, first and second order. Tikhonov regularization is applied in IBT inverse solver software. The Tikhonov regularization solution is obtained by minimizing the objective function as [94, 216]:

$$\overrightarrow{x}_{\lambda} = \arg\min_{\overrightarrow{x}}(||A\overrightarrow{x} - \overrightarrow{y}||_2^2 + \lambda^2||L\overrightarrow{x}||_2^2). \tag{5.11}$$

The regularization term $L\overrightarrow{x}$ incorporates the *a priori* information about the solution $\overrightarrow{x}$. L is a linear operator. It is assumed that the measurement noise is uncorrelated and has a diagonal covariance matrix.

Summarizing, the degree of ill-posedness in the inverse problem will cause an ill-conditioned inverse problem. Anyway, in both interpretations the consequence is that the system remains ambiguous, so multiple solutions are possible, and small perturbations of the observed data can cause an arbitrary large perturbation of the solution. The mathematical treatment of this kind of systems, like ill-conditioned systems is the challenge of the regularization techniques.

5.3 Optimization Based Approach

An alternative approach for solving the inverse problem of electrocardiography is the optimization based method. The electrophysiological model parameters are varied until the simulated ECG gets similar to the measured ECG. As it will be demonstrated in chapter 9, the parameters of the cellular automaton (CA) such as myocardial excitation conduction velocity and infarction position are iteratively varied until the measured and simulated ECG are as similar as possible. The comparison between the measured and simulated ECG was performed as follows [94]:

1. Both data sets were normalized, so that the difference between the maximal and minimal values is 1.
2. The simulated ECG was interpolated to the sample rate of the measured one.
3. The difference between the measured and simulated signals was calculated in terms of root mean square error (E_{RMS}).
4. The resulting E_{RMS} were averaged using all channels. The averaged E_{RMS} in each ECG channel is used as the criterion of optimization using Powell and downhill simplex methods [212].

Part II

Data and Methodology

6

Patient Data

Several MR data sets were acquired from University Hospital Mannheim and University Hospital Heidelberg. The individual models were generated by segmentation of imaging data (MRI, CT) in order to obtain the patients' anatomy. The model of the left ventricle was subdivided into 17 segments according to the American Heart Association (AHA) suggestion, which simplifies the determination of MI position in accordance with the corresponding coronary artery.

The 3D ventricular model was extracted from a series of segmented short axis 2D MR data sets for each patient. The segmentation was done by using interactive deformable contours based on a triangle mesh forming the borders of different parts of the organ. The cardiac conduction system including the bundle of His, left and right bundle and Purkinje fibers were implemented into the ventricles. The electrophysiological properties of the heterogeneous ventricle and the pathophysiological properties according to the patient symptoms (ischemic cardiomyopathy and left bundle branch block) were implemented into the ventricular model. The 3D volume conductor model of the thorax was extracted from a series of frontal axis 2D MR data sets for each patient. The segmentation was done by using interactive deformable contours based on a triangle mesh forming the borders of different organs. The tetrahedral mesh of the thorax was created including the heart and the other organs.

Multichannel ECG measurements with the Biosemi device of the patients' pre- and post-implantation at University Hospital Mannheim were completed. Figure 6.1 illustrates the steps from data acquisition to heart and torso model creation.

6.1 Patients Heart Model

Nine data sets including ten MR data sets and one CT data set were acquired from patients mostly suffering from LBBB and MI. One data set was acquired from a patient with extrasystole. Two additional data sets from a healthy person and the Visible Man

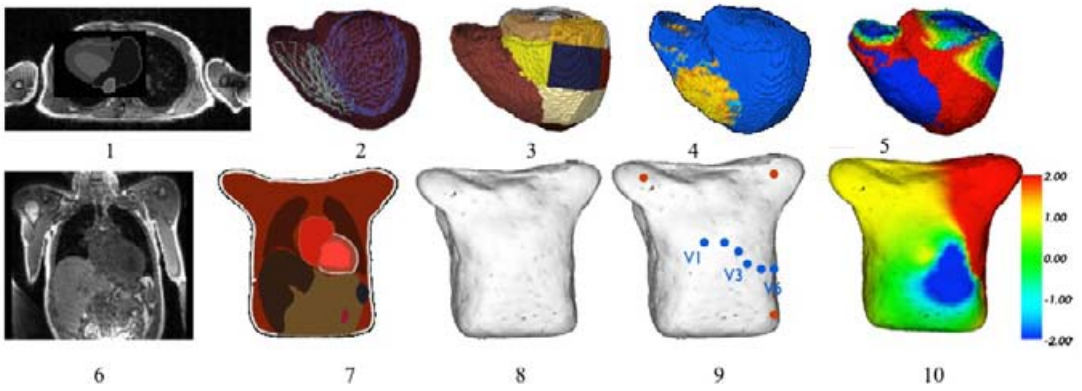

Figure 6.1. The steps of generating the patient model: (1) Segmented ventricles extracted from axial MR data. (2) 3D ventricular model with the conduction system. (3) Subdivided left ventricular model based on AHA standard. (4) Distribution of the simulated transmembrane voltage. (5) Distribution of the simulated epicardial potential. (6) Fontal MR data set. (7) Segmented Torso from MR data set. (8) Volume conductor model. (9) 3D Torso model with standard ECG electrodes. (10) Distribution of the simulated BSPM.

were used in the work. The individual models were generated by segmentation of the 2D data set in diastole and interpolating the slices in case of MR data to increase the z-axis resolution.

The description of the segmented models is demonstrated in table 6.1. The ventricular models and AHA segmented models are demonstrated in figures 6.2 to 6.14.

P-ID	Gender/age	Cardiac pathology	Res. (mm^3)	Dimension	Size
1	male	LBBB, MI (sim. only)	1×1×1	145×126×197	3599446
2	male (62)	LBBB, ischemic	.39×.39×.39	381×361×224	30809440
3	male (65)	LBBB, MI	1×1×1	180×164×137	4044496
4	male (76)	LBBB, DCMP, ischemic	1×1×1	179×163×154	4493514
5	male (80)	LBBB, MI, ischemic	1×1×1	155×157×130	3163806
6	male (25)	LBBB, MI (sim. only)	.5×.5×.5	265×210×230	12799756
7	male (50)	LBBB, MI	1×1×1	218×188×147	6024904
8	female (70)	LBBB, MI	1×1×1	166×138×110	2520136
9	male (54)	LBBB, MI	1×1×1	145×165×150	3589006
10	male (46)	LBBB, MI	1×1×1	192×163×180	5633536
11	male(80+)	LBBB,MI	1×1×1	200×200×200	8000256
12	female (70+)	ventricular asynchrony	1×1×1	200×200×200	8000256
13	female(40+)	extrasystole	1×1×1	160×140×140	3136256

The first and the sixth data sets are referred respectively to the Visible Man and a healthy subject in which the pathologies were simulated. P-ID: patient-ID, Res: resolution, LBBB: left bundle branch block, MI: myocardial infarction, DCMP: dilated cardiomyopathy. For patient 2, the data set was achieved from a high resolution CT in which no interpolation was needed. Ventricular models 9 and 10 are related to the work of Farina [94].

Table 6.1. Overview of the 13 different data sets used in this study.

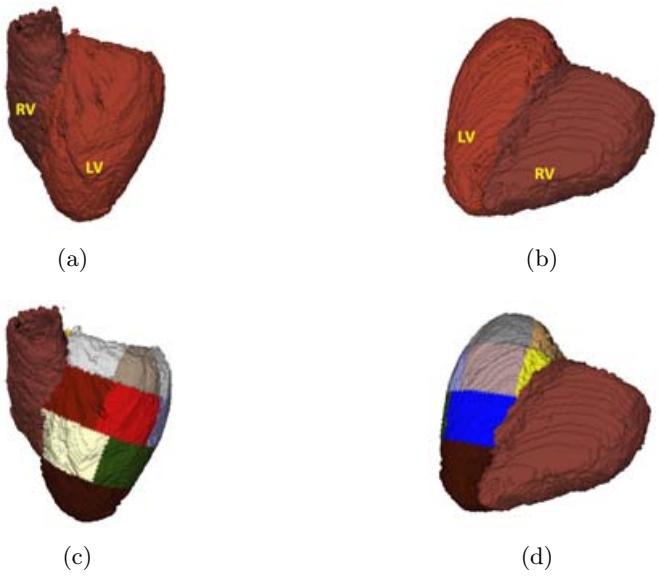

(a) (b)

(c) (d)

Figure 6.2. Patient-1: (a) Ventricular model in anterior view. (b) Ventricular model in posterior view. (c) Subdivided ventricular model based on AHA in anterior view. (d) Subdivided ventricular model based on AHA in posterior view.

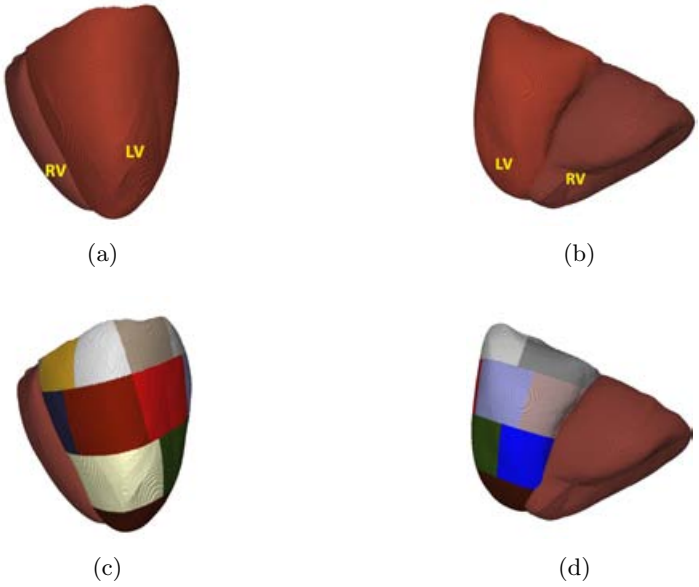

(a) (b)

(c) (d)

Figure 6.3. Patient-2: (a) Ventricular model in anterior view. (b) Ventricular model in posterior view. (c) Subdivided ventricular model based on AHA in anterior view. (d) Subdivided ventricular model based on AHA in posterior view.

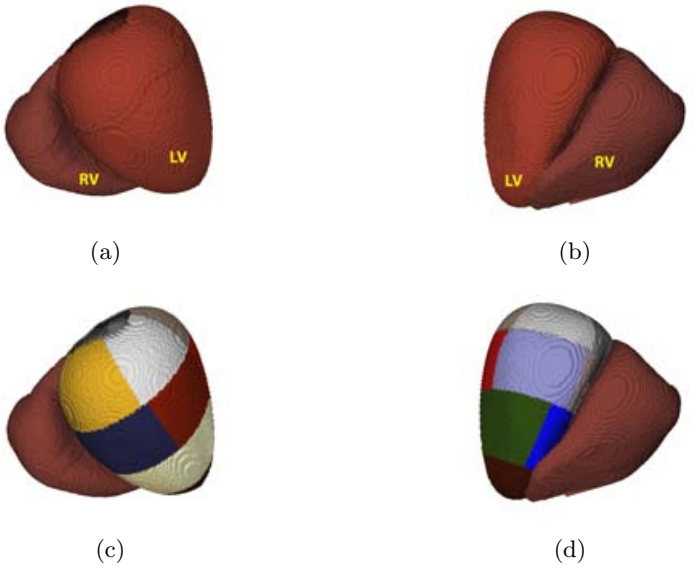

(a) (b)

(c) (d)

Figure 6.4. Patient-3: (a) Ventricular model in anterior view. (b) Ventricular model in posterior view. (c) Subdivided ventricular model based on AHA in anterior view. (d) Subdivided ventricular model based on AHA in posterior view.

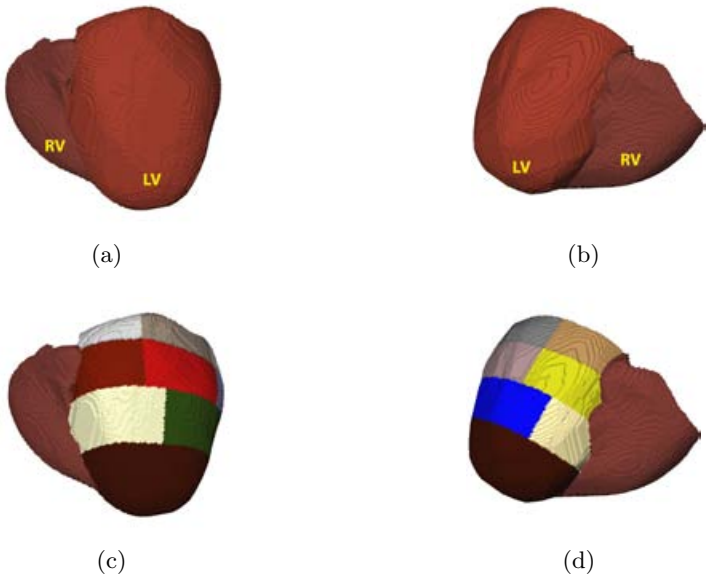

(a) (b)

(c) (d)

Figure 6.5. Patient-4: (a) Ventricular model in anterior view. (b) Ventricular model in posterior view. (c) Subdivided ventricular model based on AHA in anterior view. (d) Subdivided ventricular model based on AHA in posterior view.

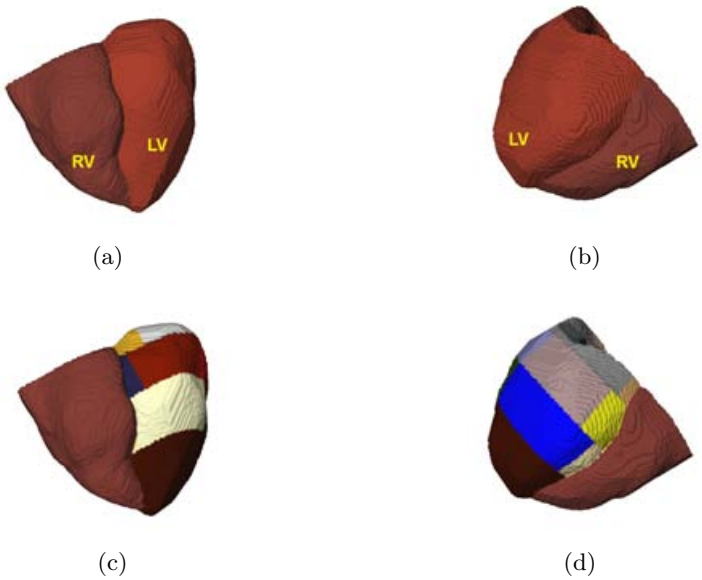

(a) (b)

(c) (d)

Figure 6.6. Patient-5: (a) Ventricular model in anterior view. (b) Ventricular model in posterior view. (c) Subdivided ventricular model based on AHA in anterior view. (d) Subdivided ventricular model based on AHA in posterior view.

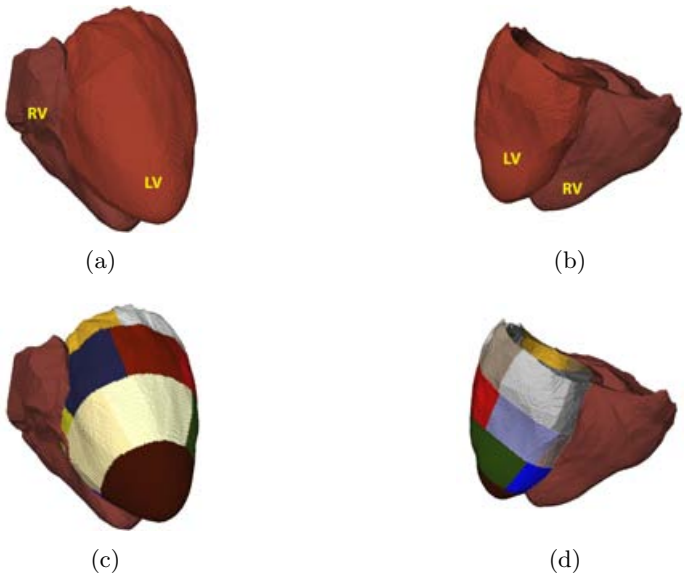

(a) (b)

(c) (d)

Figure 6.7. Patient-6: (a) Ventricular model in anterior view. (b) Ventricular model in posterior view. (c) Subdivided ventricular model based on AHA in anterior view. (d) Subdivided ventricular model based on AHA in posterior view.

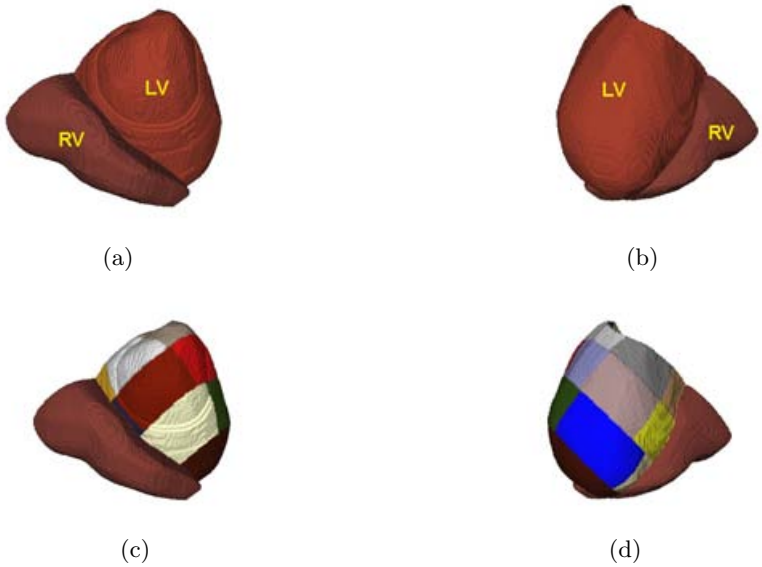

(a) (b)

(c) (d)

Figure 6.8. Patient-7: (a) Ventricular model in anterior view. (b) Ventricular model in posterior view. (c) Subdivided ventricular model based on AHA in anterior view. (d) Subdivided ventricular model based on AHA in posterior view.

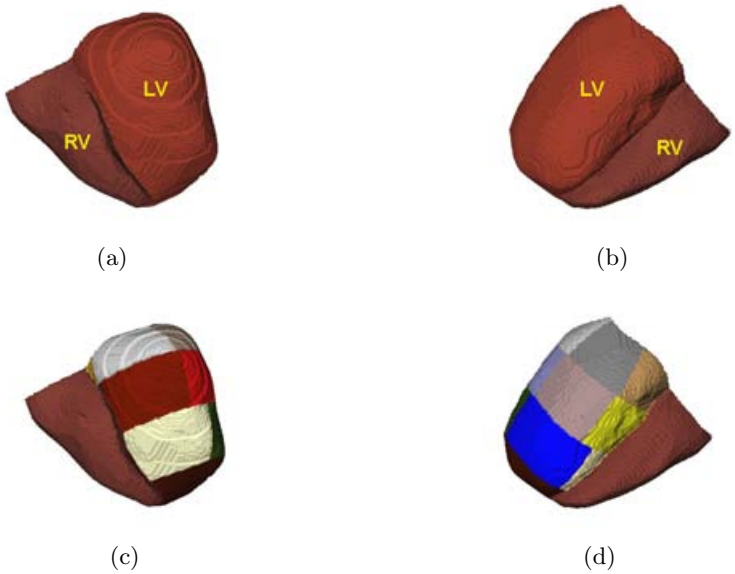

(a) (b)

(c) (d)

Figure 6.9. Patient-8: (a) Ventricular model in anterior view. (b) Ventricular model in posterior view. (c) Subdivided ventricular model based on AHA in anterior view. (d) Subdivided ventricular model based on AHA in posterior view.

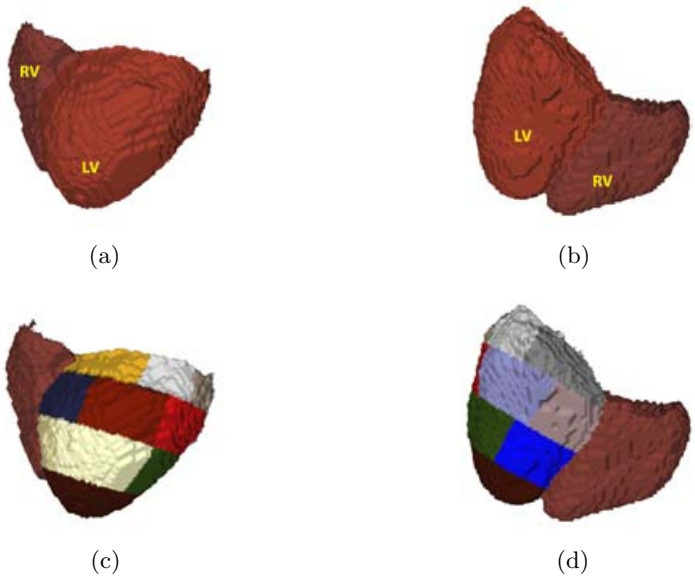

(a) (b)

(c) (d)

Figure 6.10. Patient-9: (a) Ventricular model in anterior view. (b) Ventricular model in posterior view. (c) Subdivided ventricular model based on AHA in anterior view. (d) Subdivided ventricular model based on AHA in posterior view.

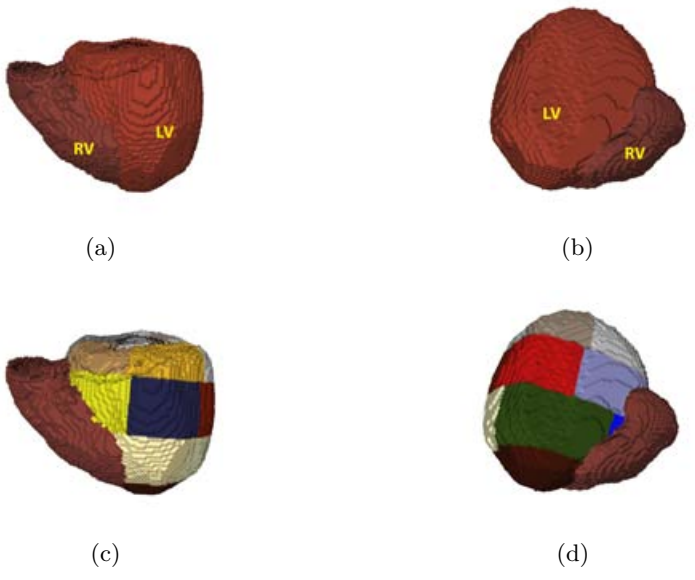

(a) (b)

(c) (d)

Figure 6.11. Patient-10: (a) Ventricular model in anterior view. (b) Ventricular model in posterior view. (c) Subdivided ventricular model based on AHA in anterior view. (d) Subdivided ventricular model based on AHA in posterior view.

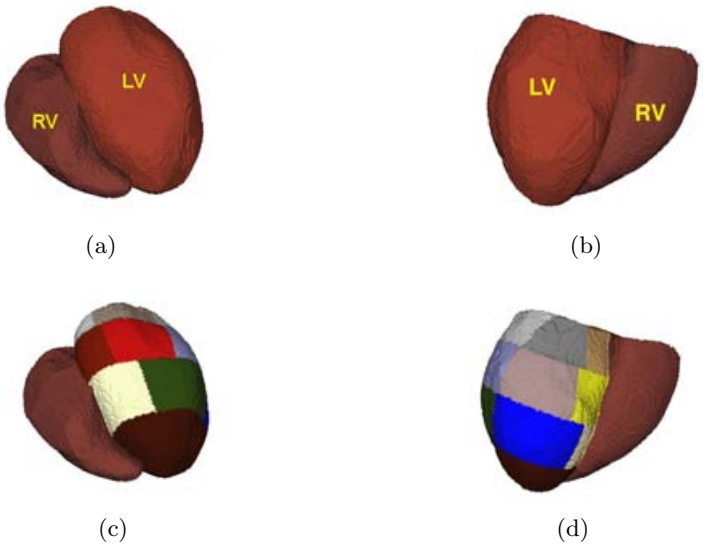

(a) (b)

(c) (d)

Figure 6.12. Patient-11: (a) Ventricular model in anterior view. (b) Ventricular model in posterior view. (c) Subdivided ventricular model based on AHA in anterior view. (d) Subdivided ventricular model based on AHA in posterior view.

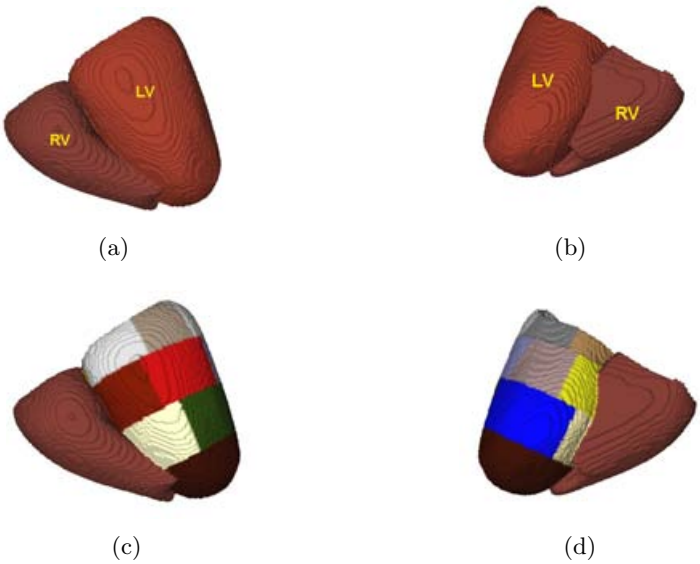

(a) (b)

(c) (d)

Figure 6.13. Patient-12: (a) Ventricular model in anterior view. (b) Ventricular model in posterior view. (c) Subdivided ventricular model based on AHA in anterior view. (d) Subdivided ventricular model based on AHA in posterior view.

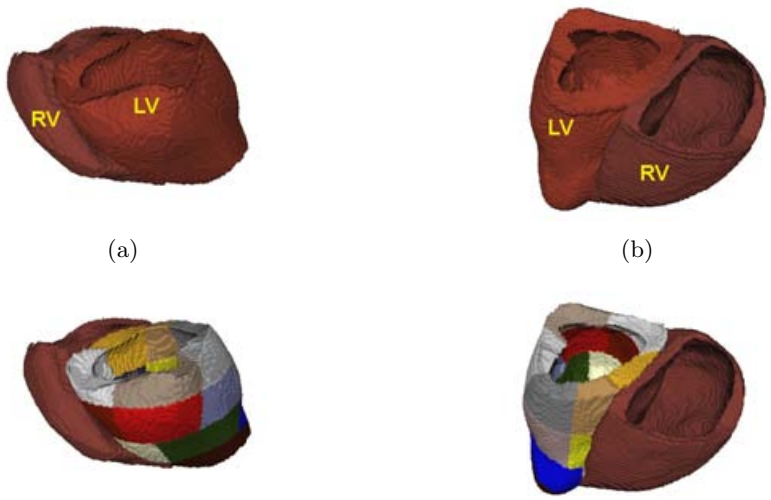

(a) (b)

(c) (d)

Figure 6.14. Patient-13: (a) Ventricular model in anterior view. (b) Ventricular model in posterior view. (c) Subdivided ventricular model based on AHA in anterior view. (d) Subdivided ventricular model based on AHA in posterior view.

6.2 Patients Torso Model

The torso model of the thorax was generated by segmentation of the 2D frontal axis data sets of thorax. Further, the volume conductor was achieved by selecting a proper number of nodes and assigning the related conductivity tensor. The information of the generated volume conductors of four patients are shown in table 6.2. The torso models are demonstrated in figures 6.15 to 6.18.

ID	Number of nodes	Number of tetrahedra	Distance between nodes
Patient-10	162841	991472	2 mm
Patient-11	44678	283641	2 mm
Patient-12	81612	503765	2 mm
Patient-13	93570	583647	2 mm

Torso model 10 is related to the work of Farina [94].

Table 6.2. Overview of the 4 different volume conductor models used in this study.

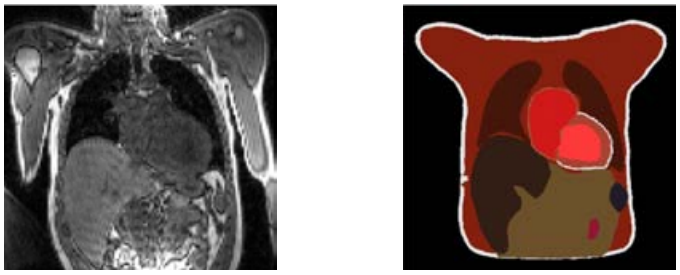

(a) (b)

(c) (d)

Figure 6.15. Patient-10: (a) MR data set in frontal axis. (b) Segmented torso. (c) Volume conductor model. (d) Inner organs model.

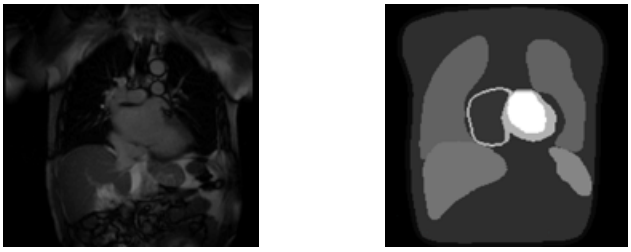

(a) (b)

(c) (d)

Figure 6.16. Patient-11: (a) MR data set in frontal axis. (b) Segmented torso. (c) Volume conductor model. (d) Inner organs model.

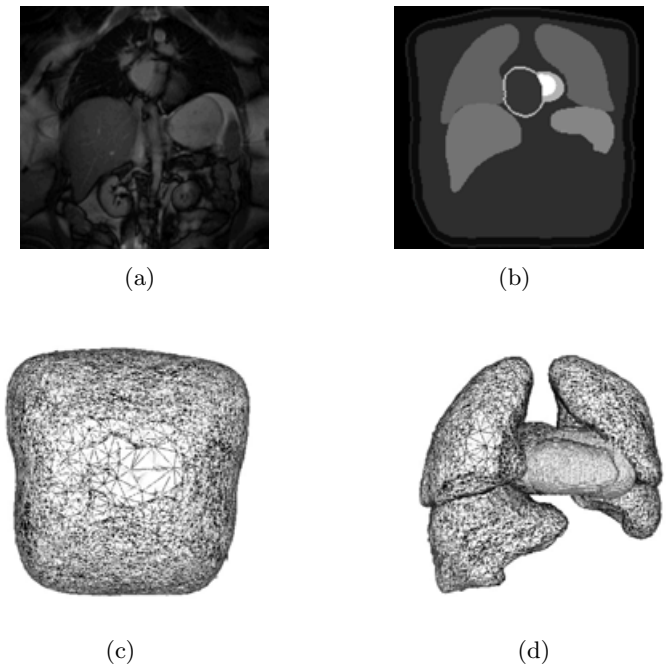

(a) (b)

(c) (d)

Figure 6.17. Patient-12: (a) MR data set in frontal axis. (b) Segmented torso. (c) Volume conductor model. (d) Inner organs model.

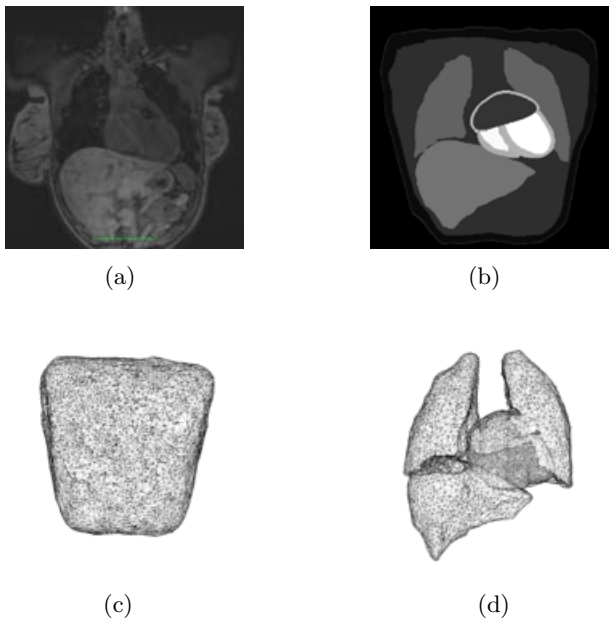

(a) (b)

(c) (d)

Figure 6.18. Patient-13: (a) MR data set in frontal axis. (b) Segmented torso. (c) Volume conductor model. (d) Inner organs model.

6.3 Multichannel ECG Measurements of Patients

Multichannel ECGs were measured on several patients at University Hospital Mannheim before pacemaker implantation. The multichannel ECGs after implantation were mea-

sured on three of those patients who underwent MR tomography. A tracking system (FASTRACK) was used to localize the electrode positions. The post processing of the measured ECGs including denoising, baseline wander cancellation and averaging in time which was performed will be described in chapter 7. A sample of recorded ECG is illustrated in figure 6.19.

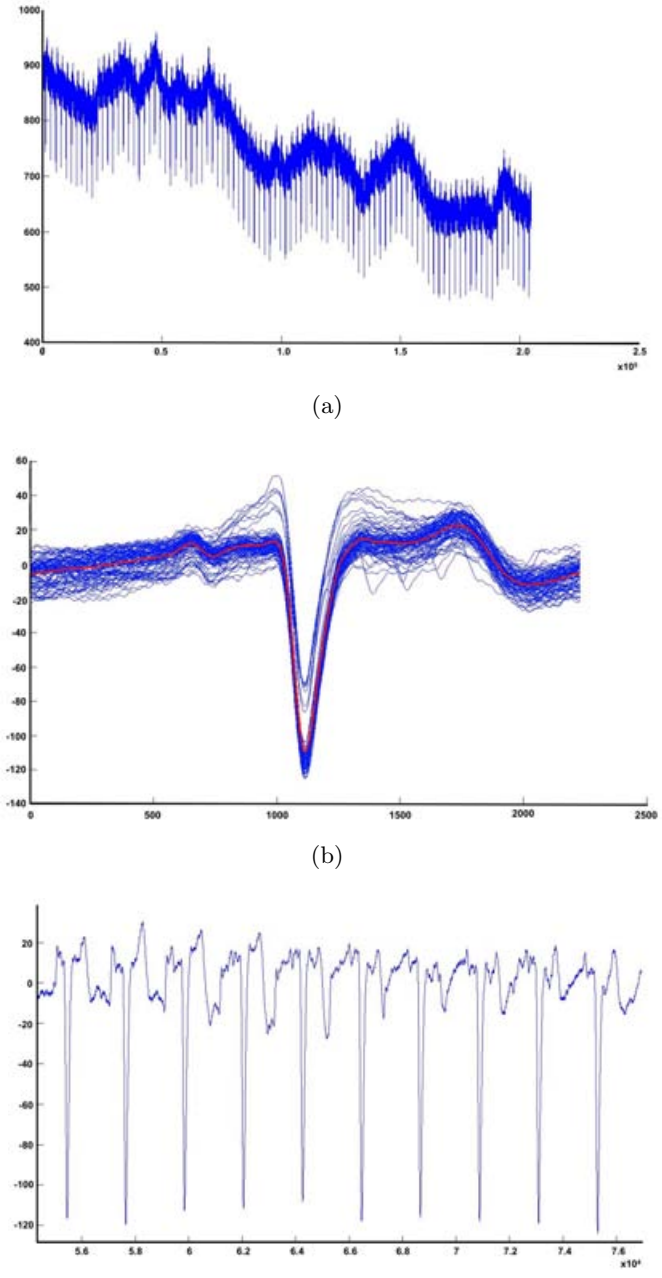

Figure 6.19. Patient-13: (a) One channel of recorded ECG. (b) Averaging over the time of different ECG cycles in one channel after baseline wander cancellation. (c) Denoised and baseline corrected ECG channel.

Measuring 64 channels ECG on the patients before implantation lead to BSPM of 64 positions. The BSPM was interpolated on the surface of the mesh in torso model in order to compute the epicardial potential distribution. The inverse solution results in a better parameter setting of the patient heart model. Comparing 64 measured ECGs with simulated computer ECGs for patients after implantation gave evidence on the applicability of the computer model of heart and thorax.

7

Optimization Algorithms and Methodology

As discussed in chapter 4, an optimization environment including an anatomical model of the heart, cellular electrophysiology, excitation propagation and pathological model was setup in order to find the optimal CRT parameters. A simulation environment including a volume conductor model (anatomical torso model and conductivity values) is used to validate the method results by generating the corresponding ECG.

The aim of BVP is to maximize patient's cardiac output, in order to improve the hemodynamic parameters of the patient as described in chapter 3. Ideally, a computerized optimization of BVP would use a model of the cardiac contraction in order to calculate the cardiac output. Since these models require an extensive calculation time and were not available at the time of this analysis, an alternative approach is used. If the temporal and spatial excitation propagation of the pathological heart with pacing is as close as possible to the physiological excitation propagation, it is assumed that the cardiac output will be optimal. Thus, the activation times for each cardiac cell (isochrones) are computed for physiological, pathological and therapeutic case (pathology with pacing). The optimization strategies based on isochrones are presented in sections 7.2. The purpose of the work is classified in two strategies: the first is outlined in chapter 8 and the second in chapter 9.

The structure of the first strategy is:

1. Construction of an individual patient heart model considering the LBBB and MI extracted from MR data sets according to the description from chapter 4.
2. Assessement of the optimal pacing configurations as well as the best electrode setup and timing delays in the course of two electrophysiologically based optimization algorithms.
3. Comparison of the results obtained from the two optimization methods and reconcilement of the derived results.

The results of the two optimization algorithms may differ. In this case, a trade off between optimal results could be performed, ensuring a proper selection of pacing parameters.

The structure of the second strategy is:

1. Creation of an individual patient torso model considering the inner organs such as heart, lungs, liver.
2. Solution of the inverse problem by setting the patient model parameters to achieve a personalized model of the pathology by measuring the multichannel ECG from a patient before implantation.
3. Calculation of the BSPM for the patient under therapy based on the optimal BVP setup.
4. Extraction of the 12 standard ECG channels.
5. Verification of the optimal pacing results with respect to comparison of measured ECG of the patient after implantation with the simulated ECG for optimal pacing parameters.

7.1 Implementation of BVP into the Models

As discussed in chapter 3, biventricular cardiac pacemakers stimulate the right and left ventricle either simultaneously or sequentially as a means to resynchronize ventricular contraction. Standard atrial and ventricular pacing leads are placed on the right atrium (sensing electrode), right ventricle (right stimulation electrode) and left ventricle (left stimulation electrode), respectively. To accomplish ventricular resynchronization in clinical practice, the left ventricular lead is implanted via the coronary sinus to achieve permanent epicardial stimulation from lateral or posterolateral vein. The right ventricular lead is implanted on the apex of the right ventricle.

In the present research, the lead positions to investigate, were chosen interactively to obtain equally spaced positions covering the whole surface of the left ventricle. Different pathologies according to 17 infarction positions and 3 reduced conduction velocities were simulated. For each pathology, 36 lead positioning setups in parallel with various A-V (60 to 260 ms) and V-V delays (-30 to 70 ms) were investigated [177, 178, 179, 180, 181, 182, 221].

Overall 36 electrode setups were investigated. Eight different electrode positions were chosen in the anterior (A, B, C, D) and posterior (I, J, K, L) branches of coronary sinus. Four positions were chosen in the left ventricular free wall (E, F, G, H) based on several studies [16]. The right ventricular electrodes were placed in the apex (X), upper (U) and middle (M) septal wall (see figure 7.1).

7.2 Optimization of BVP

The optimization strategy used was based on the assumption that the optimal cardiac output was given during sinus rhythm if no pathological changes in the electrophysiology were present. Thus, the aim of the pacing therapy was to achieve a cardiac activation as

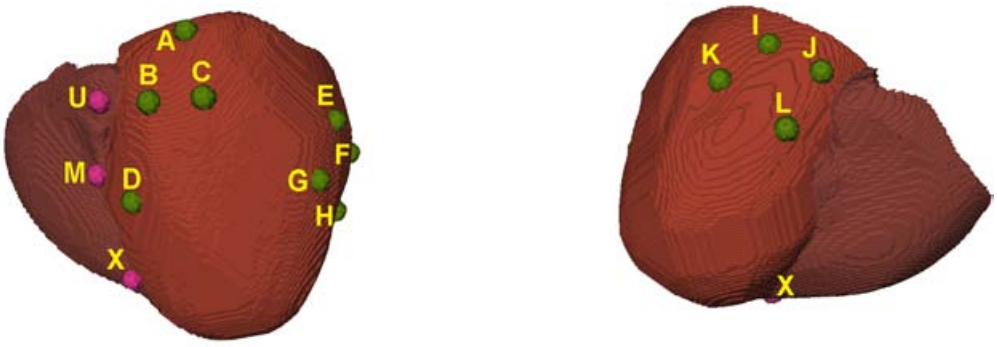

(a) (b)

Figure 7.1. The electrode positions chosen for the patient-4 heart model. The electrodes A, B, C and D are referred to the anterior branches of coronary sinus. The electrodes I, J, K and L are referred to the posterior branches of coronary sinus. The electrodes E, F, G and H are located on the left ventricular free wall. The electrodes U, M and X are located respectively at the right ventricular upper septum, middle septum and apex.

close to the sinus rhythm as possible. For this purpose, the isochrones representing the excitation front, i.e. the time of activation for each cardiac cell, represented by a voxel in the anatomical data set model, were computed for one cardiac cycle. The activation time or isochrone, was defined as the time of action potential initiation. The isochrones as cardiac output for physiology, pathology, pacing and the differences between them are represented in figure 7.2.

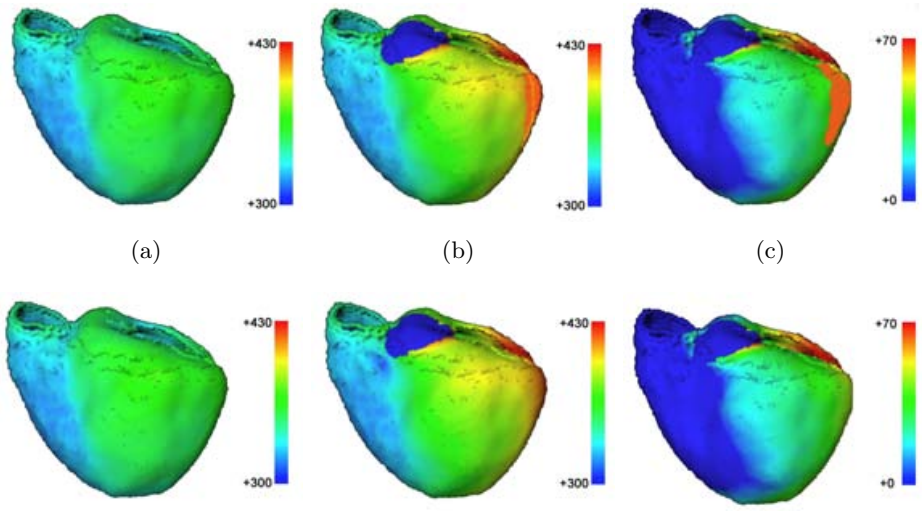

(a) (b) (c)

(d) (e) (f)

Figure 7.2. Isochrones of the excitation for a cardiac model: (a) Physiology. (b) Pathology. (LBBB and MI) (c) Error between physiology and pathology. (d) Physiology. (e) Pathology with therapy (pacing) (f) Error between physiology and pacing.

7.2.1 Optimization of Pacing Parameters Based on Isochrones

The activation times for each cardiac cell (isochrones) were computed for the physiological, pathological and therapeutic case (pathology with pacing). The difference of the isochrones was expressed as a root mean square error (E_{RMS}) [178, 179, 221]. Hence, the E_{RMS} was a measure for the difference between physiological and pathological excitation propagation. In the present research, the E_{RMS} was minimized in order to find a pacing setup delivering temporal and spatial excitation propagation as close as possible to the natural physiological state.

The E_{RMS} was a function of three variables: A-V delay, V-V delay and electrode positioning. The smallest error yields the optimal pacemaker setups with respect to the cardiac activation.

$$E_{RMS} = \sqrt{\frac{1}{N}\sum_{i=1}^{N}(x_i - e_i)^2} \tag{7.1}$$

x_i : the activation time of voxel i in physiological case
e_i : the activation time of voxel i in pathological/pacing case

The method was independent from QRS duration, a measure often used for BVP optimization in clinical practice. The steps of the optimization algorithm can be described as follows:

1. Calculation of the $E_{RMS.path}$ for the isochrones between the physiological and pathological case.
2. Calculation of the $E_{RMS.pace}$ for the isochrones between the physiological and pacing case.
3. Determination of the minimal error with pacing ($E_{RMS.pace}$), expected to be smaller than the error without pacing ($E_{RMS.path}$) for the isochrones.

7.2.2 Optimization of Pacing Parameters Based on QRS Duration

The method based on isochrones optionally provides a measure of QRS duration in parallel with the first optimization algorithm by calculating the QRS duration from the time difference between the last and the first activated cell. Measuring the QRS duration yields an additional confirmation of the algorithm based on isochrones computation. This method mimics the clinical procedure used nowadays to optimize CRT (see section 3.4.5). In the first optimization method, the activation times in each cardiac cell were computed for physiological (case 1), pathological (case 2) and therapeutical state (case 3). Since the ECG of a patient with a LBBB is characterized by a QRS complex with the duration of more than 120 ms, the QRS duration is computed for case 1 to 3. The QRS duration is calculated as the difference of the activation time of the first and last activated cardiac

cell (see figure 7.3). With this second optimization method, the optimal CRT parameters are those leading to minimal QRS duration difference between case 1 and 3.

$$t_{QRS} = t_{act,last} - t_{act,first} \tag{7.2}$$

t_{act} : the activation time of the corresponding voxel
t_{QRS} : the QRS duration time

$$t_{error} = t_{QRS,path(pace)} - t_{QRS,phys} \tag{7.3}$$

t_{error} : the difference time between physiological and pathological/pacing case

The steps of the optimization algorithm are as follows:

1. Calculation of the QRS durations for the physiological and pathological case.
2. Calculation of the QRS duration for pacing case.
3. Finding the minimal difference of QRS duration between physiological and pacing case.

In order to calculate the QRS duration without ECG simulation, the minimal and the maximal value of the isochrones matrix are explored. The QRS duration is established from the difference of the achieved values, corresponding to the activation time of the early activated cardiac cell and the last activated cardiac cell respectively.

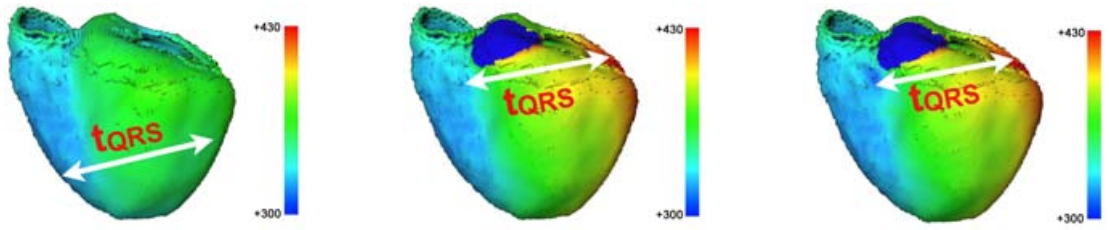

(a) (b) (c)

Figure 7.3. QRS duration in the isochrones of the excitation for a cardiac model: (a) Physiology. (b) Pathology (LBBB and MI). (c) Pacing.

It must be considered, that every evaluation of the E_{RMS} or QRS function requests a simulation with the computer heart model, leading to long computation time. So it is important, that the minimization algorithm needs the smallest possible number of function evaluations. The conventional, gradient-based minimization algorithms need at least 9 function evaluations for one iteration step. Hence, it was decided to use the downhill simplex algorithm (DSA) for optimization in this work [222]. The DSA uses a simplex (in this case a triangle) starting at arbitrary values of E_{RMS}. The simplex moves in the two

dimensional parameter space including A-V and V-V delays for each electrode positioning towards the minimum. A more detailed description of the DSA is included in section 7.3.

7.3 Downhill Simplex Algorithm

The downhill simplex algorithm (DSA) was proposed by Nelder & Mead [213]. Since DSA does not compute derivatives but relies only on function evaluations, it is a promising candidate to speed up the calculation process for timing delay optimization.

The first point must be chosen manually or randomly to start the DSA. The DSA algorithm is supposed to make its own way downhill through the unimaginable complexity of an N-dimensional topography, until it encounters local minimum. The downhill simplex starts with N+1 points, defining an initial simplex. If there is one initial point P_0 then the other N points can be expressed by

$$P_i = P_0 + a_i e_i \tag{7.4}$$

where e_i are N unit vectors, and a_i are constants that characterize the length scale for each vector direction [248].

The DSA implements a series of steps. Most steps include moving the highest point (the point of simplex where the function is largest) through the opposite face of the simplex to a supposed lower point (P_{mirror}). These steps are called reflections, and they are constructed to conserve the volume of the simplex. An example of DSA applying on a 2D function is illustrated in figure 7.4.

In case, the value of the function in point P_{mirror} is between the second highest and lowest value of the vertices of the simplex, then the highest point is changed to P_{mirror} (figure 7.4.b). When the value of function in point P_{mirror} is lower than or equal to in the lowest point of the simplex the value is checked in point $P_{mirror.expand}$ to see if the function drops further in direction of P_{mirror}. The lower of points P_{mirror} and $P_{mirror.expand}$ replaces then the highest point of the simplex. If point P_{mirror} is greater, then the simplex expands in direction to $P_{mirror.expand}$, thus its volume grows (figure 7.4.c). When the value of the function in point P_{mirror} is higher than or equal to the value in the highest point of the simplex, the value is checked in point $P_{contract}$ and the triangle compresses in one dimension along the last expansion direction (figure 7.4.d). While the $P_{contract}$ is still higher than the initial highest value, the contraction would be two dimensionally performed that means the two other nodes are contracted (figure 7.4.e).

The DSA is a numerical method to minimize a multidimensional function without using the gradient of the function. So a minimum can be found with fewer calculations compared

to the conventional methods.

The optimization process is started with 3 arbitrary values for A-V and V-V, since the DSA needs three starting points. The parameter representing the efficacy of BVP either E_{RMS} or QRS difference is calculated for this three start values. The DSA estimates new values for A-V and V-V delay. Then, another parameter representing the efficacy of the optimization method is calculated. This way, the program iterates to an optimal set of parameters. The iteration process is terminated by the user termination criterion, when the optimized values are satisfactory.

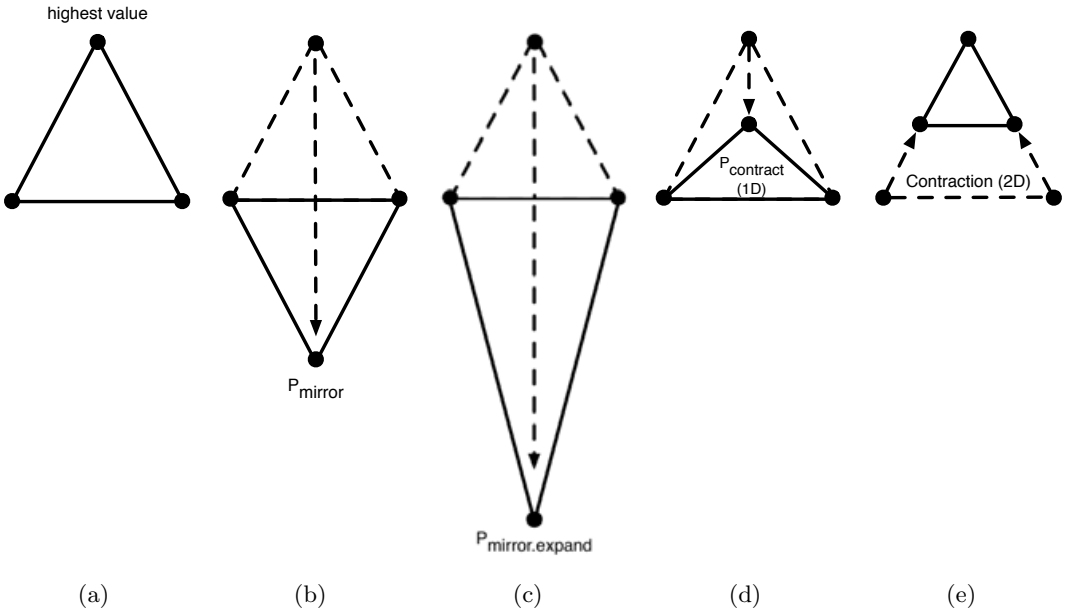

Figure 7.4. Steps of performing DSA [213, 222]. (a) The initial simplex in triangular form. (b) Resulting P_{mirror} from reflection of the highest value. (c) Resulting $P_{mirror.expand}$ from expansion of highest value. (d) Resulting $P_{contract}$ from one dimensional contraction of highest value. (e) Resulting two dimensional contraction of two other values.

7.4 Statistical Analysis and Student's t Test

Many populations encountered in clinical practice are well approximated by the normal distribution, so this assumption will lead to confidence interval procedures of wide applicability.

In most studies discussed in chapter 3, statistical analysis was performed on patients who underwent CRT. Continuous data were expressed as mean ± standard deviation (SD) [17, 28, 63, 139, 203, 207, 252, 264, 273, 287, 294]. Therefore, investigation by variance

analysis or Student's t test was appropriate in clinical studies.

In a study of Becker et al. [29], a comparison of parametric variables before and after CRT in a form of fitted covariance model was implemented. In a study of Cazeau et al. [63], all analysis were based on the intention-to-treat principle. Baseline characteristics were assessed with the use of the chi-square test for dichotomous variables and Student's t test or Wilcoxon's nonparametric test for quantitative or categorical variables.

Pitzalis et al. [207] presented the data as mean values $\pm$ SD. The continuous variables were compared using Student's t test for dependent (intragroup comparisons) and independent (intergroup comparisons) variables, and frequencies by means of the Fisher's exact test. Survival was analyzed using the Cox proportional hazards model, and expressed as hazard ratios (HR) and confidence intervals (CI). In study of van Campen et al. [273], data sets were presented similar to Pitzalis et al. [207] study. Groups were compared using the two-sided t test for unpaired data, and the data of the whole group were compared using the two-sided t test for paired data.

Considering a normal distribution with unknown mean and unknown variance for a population leads to a t distribution with n-1 freedom degrees [184]. The random variable T is calculated as:

$$T = \frac{\overline{X} - \mu}{S/\sqrt{n}} \tag{7.5}$$

where $X_1, X_2, ...X_n$ are random samples from a normal distribution with unknown mean μ and unknown variance σ^2, standard deviation S and the sample size n.

The t probability density function is:

$$f(x) = \frac{\Gamma[(k+1)/2]}{\sqrt{\pi k}\Gamma(k/2)} \cdot \frac{1}{[(x^2/k)+1]^{(k+1)/2}} \quad -\infty < x < \infty \tag{7.6}$$

where k is the number of degrees of freedom. The mean and variance of the t distribution are zero and $k/(k-2)$(for $k > 2$), repectively.

Several t distributions are shown in figure 7.5. The general appearance of the t distribution is similar to the standard normal distribution in that both distributions are symmetric and the maximum ordinate value is reached when the mean is zero. However, the t distribution has heavier tails than the normal, which means more probability in the tails than the normal distribution.

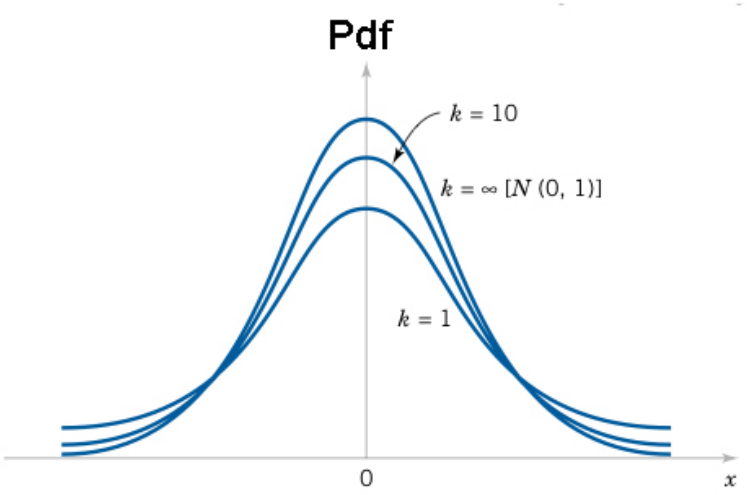

Figure 7.5. Probability density functions of several t distributions [184].

Defining $t_{\alpha,k}$ as value of the random variable T with k degrees of freedom, an area of α as a probability can be detected in figure 7.6.

Knowing the distribution of the test statistic under the null hypothesis allows accurate calculation of probability values (p-values).

A t test is any statistical hypothesis test in which the test statistic has a Student's t-distribution if the null hypothesis is true. It is applied when sample sizes are small. The t tests are divided to dependent and independent type:

1. **Independent** t test consists of two groups with no relationship.
2. **Dependent** t test consists of a matched sample where two groups are matched on a particular variable.

The compared groups may have similar or different sample sizes and variances. For each condition, the random variable T is calculated from a specific equation defined in table 7.1.

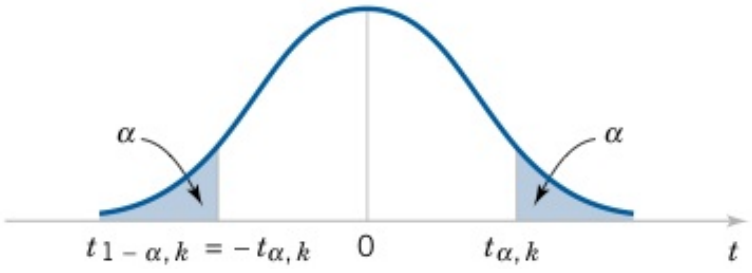

Figure 7.6. Percentage points of the t distribution [184].

Type of t test	Assumption			Random variable T
Independent	1-sample			$\frac{\overline{X}-\mu}{S/\sqrt{n}}$
	2-samples	equal sample sizes		$\frac{\overline{X_1}-\overline{X_2}}{\sqrt{\frac{S_1^2+S_2^2}{n}}}$
		unequal	equal variance	$\frac{\overline{X_1}-\overline{X_2}}{\sqrt{\frac{(n_1-1)s_1^2+(n_2-1)s_2^2}{n_1+n_2-2}(\frac{1}{n_1}+\frac{1}{n_2})}}$
			unequal variance	$\frac{\overline{X_1}-\overline{X_2}}{\sqrt{\frac{S_1^2}{n}+\frac{S_2^2}{n_2}}}$
Dependent	repeated samples			$\frac{\overline{X_D}-\mu}{S_D/\sqrt{N}}$

X_1, X_2: random samples, μ: mean, n: sample size, S: standard deviation, X_D: average of differences between all pairs, S_D: standard devation of differences between all pairs.

Table 7.1. Calculation of random variable T based on t test type.

7.5 Compatibility of the Computer Model with Clinical Data

The computation of BSPM corresponding to a given distribution of transmembrane voltages within the heart was used to verify the results obtained from the optimization algorithms based on electrophysiological heart models. The ECG was calculated for the physiological, pathological and therapeutical cases with optimal pacing suggested by the optimization method for those patient models with available MR data sets of the torso. The QRS duration of each channel was computed and then compared to the corresponding QRS duration of the physiological case in order to determine the efficacy of the optimization method. To measure the QRS duration a wavelet-based segmentation method was applied to the ECG signals in order to detect the R peak and the QRS complex.

In addition, for those patient models with available MR data sets of torso and multichannel ECGs before and after implantation, an optimization strategy was performed. The optimization included setting the cellular automaton parameters, such as changing the conduction velocity in different segments to get a similar simulated ECGs as the measured one. Goal of this parameter optimization is to achieve a personalized model of the pathology, in which the 64 simulated ECG channels will be as similar as possible to the measured one. A high correlation coefficient between measured and simulated channel is a good indicator of the success of the method. Further investigations were performed to measure the influence of the pacemaker timing changes on the BSPM of the patient after the implantation. This provided valuable information to verify our CRT optimization

method. Therefore, preprocessing was performed on the ECGs in order to detect the R peaks and measure the QRS duration as the indicator of pacing efficacy in LBBB patients.

7.5.1 Baseline Wander Correction

Removal of baseline wander is necessary in order to minimize undesired changes in beat morphology. Baseline wander is caused by patient movement, breathing and other undesired artifacts. Linear filtering, polynomial fitting and wavelet transforms are methods used to remove the baseline wander. The wavelet transform is applied to the ECG signals in order to decompose them to the low and high scales coefficients.

Based on the study of Mozaffary et al. [187], the wavelet transform of the ECG signal is computed. In each scale, the wavelet coefficients energy for both coarse and detail levels are calculated. Once comparing the energies of coarse and detailed levels, the branch of the tree with the higher energy is chosen. The higher energy branches will be followed until a point is reached where energy difference exceeds a preset threshold level. In this point, the binary tree is completed and the baseline wander signal is identified. Using the obtained wavelet coefficients, the inverse wavelet transform is calculated after substracting the baseline wander from the wavelet coefficients. Thus, a baseline wander free ECG signal is achieved.

The implemented program at IBT [41] utilizing mother wavelet Daubechies (db11) is applied to the measured ECGs (see figure 7.7). The decomposition level was 10 according to the sample rate of 2048 Hz.

7.5.2 Denoising

The implemented program at IBT is applied on ECG signals, including the following steps [41]:

1. Applying discrete wavelet transform (DWT) with Daubechies mother wavelet (db1) to the signal in order to determine the approximated and detailed coefficients.
2. Selecting a threshold according to Donoho's thresholding method [41, 83].

$$t_r = \sigma\sqrt{2\ log(n)} \tag{7.7}$$

where n is the length of the noise signal and σ is the standard deviation of the noise. Since the σ is often unknown, an estimation of σ would be as follows:

$$\hat{\sigma} = \frac{1}{0.6745}\ MAD \tag{7.8}$$

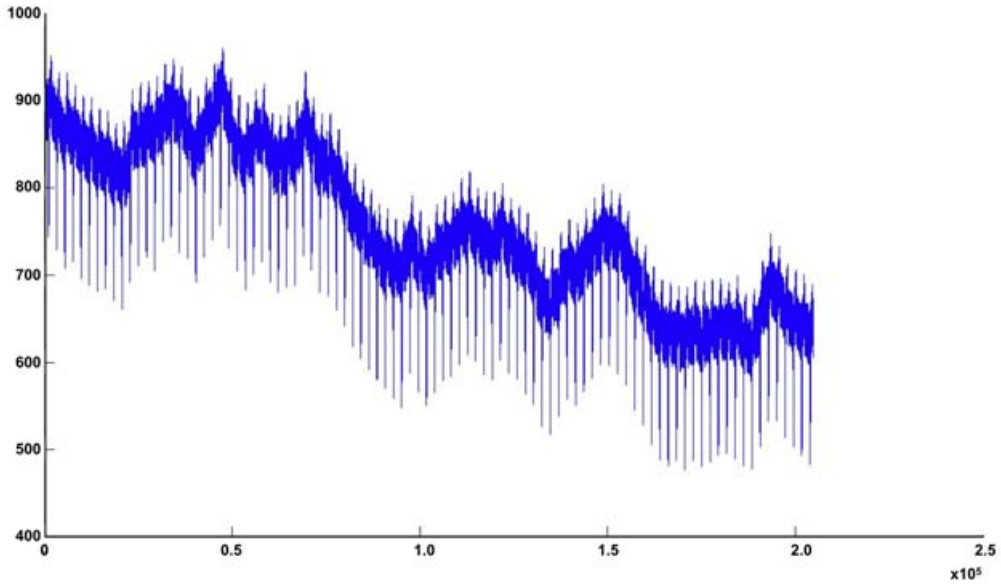

(a)

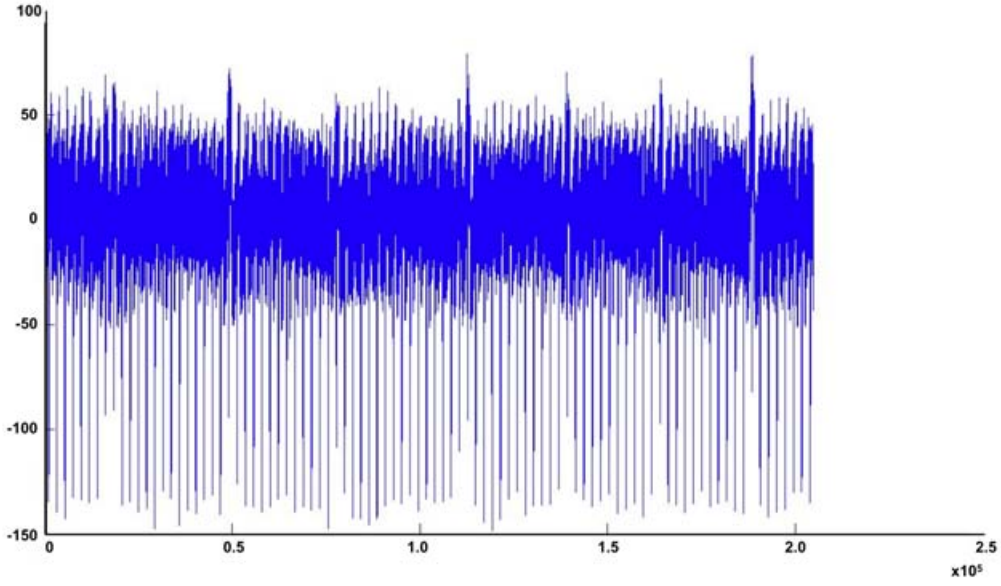

(b)

Figure 7.7. Baseline wander cancellation in measured ECG: (a) Initial ECG signal. (b) Reconstructed ECG signal after baseline wander removal.

where MAD is the median absolute deviation of the appropriately normalized fine scale wavelet coefficients.

3. Applying soft thresholding to the detailed wavelet coefficients.
4. Applying inverse DWT to reconstruct the ECG signal.

A block diagram showing the steps of the denoising system is demonstrated in figure 7.8. A noisy and denoised ECG signal are illustrated in figure 7.9

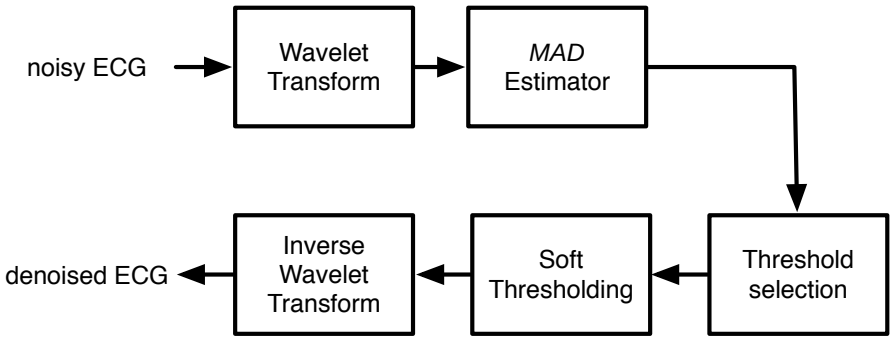

Figure 7.8. Block diagram of a simple wavelet shrinkage denoising system [83].

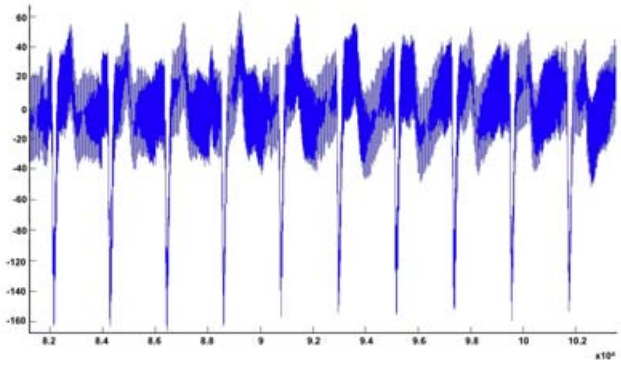

(a)

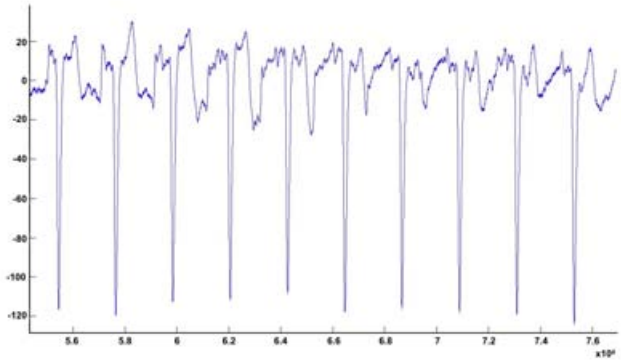

(b)

Figure 7.9. Noise removal in measured ECG signal: (a) Noisy measured ECG signal (b) Denoised ECG signal with mother wavelet db1.

7.5.3 QRS Detection

The ECG signal can be segmented to the P wave, QRS complex and T wave. The aim of the optimization algorithm in the research is to decrease the QRS duration after implantation. Therefore the QRS complex should be detected properly both for pre- and post-implantation data.

The implemented IBT software utilizes the Haar wavelet because of its similar function to the derivative operator. For measured ECGs, the R peaks are detected and translated to overlap each other. Averaging of the ECG cycles over time is performed to obtain an averaged ECG signal (see figure 7.10).

The ECG signal is decomposed using wavelet transform. The number of decomposition levels depends on the region of interest. Since the QRS complex is carried by frequencies between 5-25 Hz, a decomposition level of 6 is chosen although it can be changed due to the sample rate frequency.

Table 7.2 demonstrates the frequency range of different decomposed signal levels. The local maximum and minumum of the proper level is searched with comparing the values to a threshold obtained from energy of wavelet coefficients over a certain time period [41].

sample rate (Hz)	level 1 (Hz)	level 2 (Hz)	level 3 (Hz)	level 4 (Hz)	level 5 (Hz)	level 6 (Hz)
2048	512 - 1024	256 - 512	128 - 256	64 - 128	32 - 64	16 - 32
1024	256 - 512	128 - 256	64 - 128	32 - 64	16 - 32	8 - 16
512	128 - 256	64 - 128	32 -64	16 - 32	8 - 16	4 - 8

Table 7.2. Frequency contents of different levels with respect to the sample rate [41].

The application of the Haar wavelet results in an enhancement of slopes and extremum points. The changes in sign of the ECG signal can be determined by a derivative operator or by zero-crossing in the wavelet coefficients. The closest zero-crossing to the obtained maximum within the region of interest is determined as the location of the R peak. Detection of the Q and S points is similar to the R peak due to the zero crossing in the corresponding level. Finding a minimum followed by a maximum or vice versa depends to the morphology of the measured signal, where the ECG lead was located (see figure 7.11).

For ECGs measured after implantation, a proper thresholding is performed based on wavelet coefficients in order to eliminate the stimulus from ECG signal (see figure 7.12).

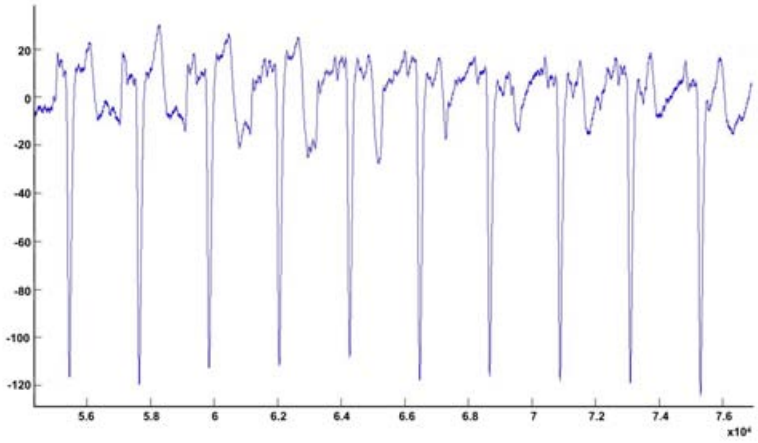

(a)

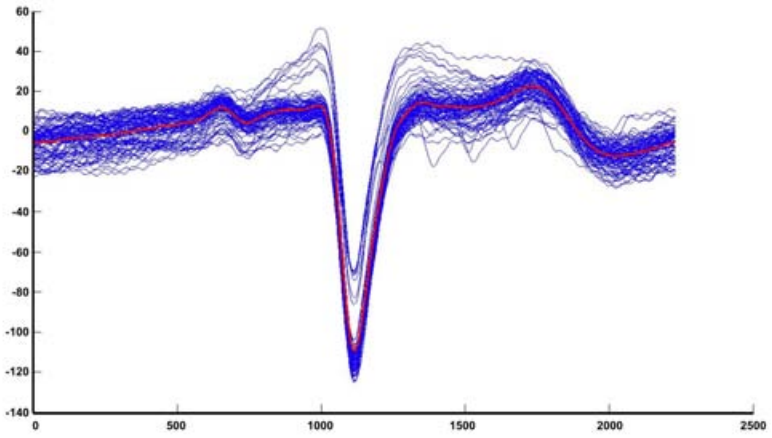

(b)

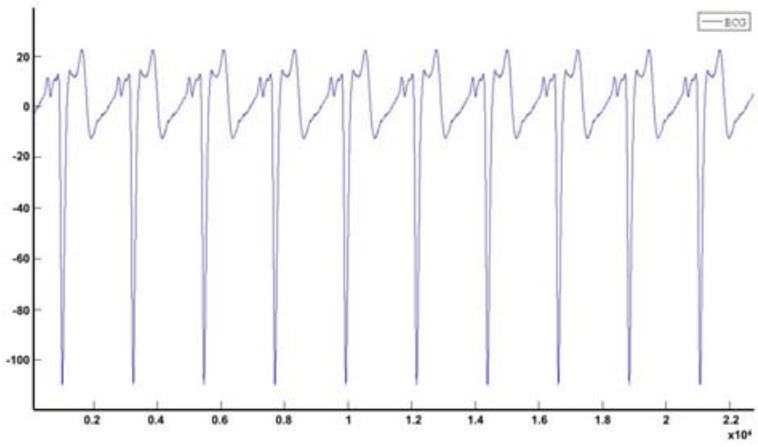

(c)

Figure 7.10. Time averaging in measured ECG signal: (a) Sequence of measured ECG. (b) Time averaging of different ECG cycles (The red ECG signal is the averaged one). (c) A sequence constructed by averaged ECG signal.

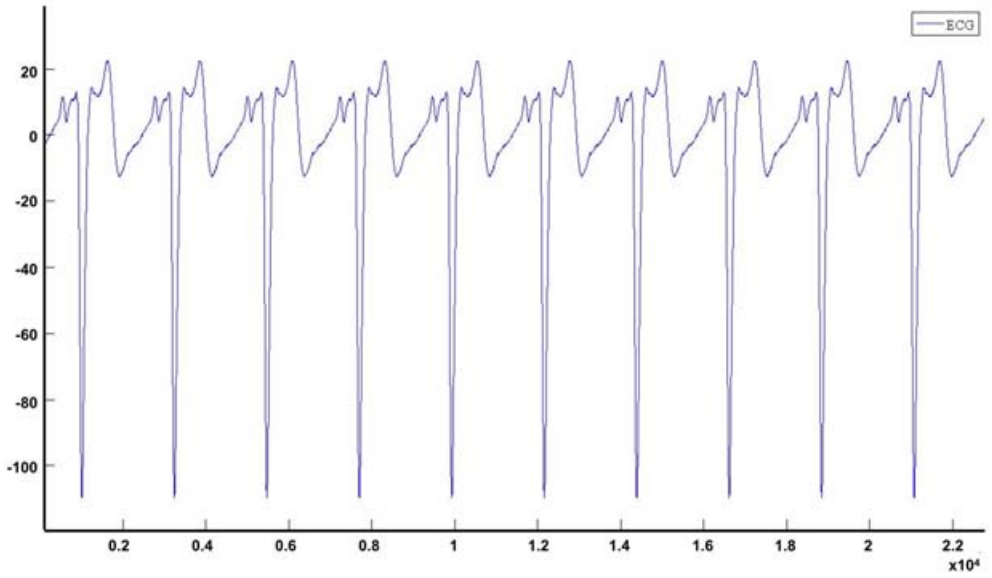

(a)

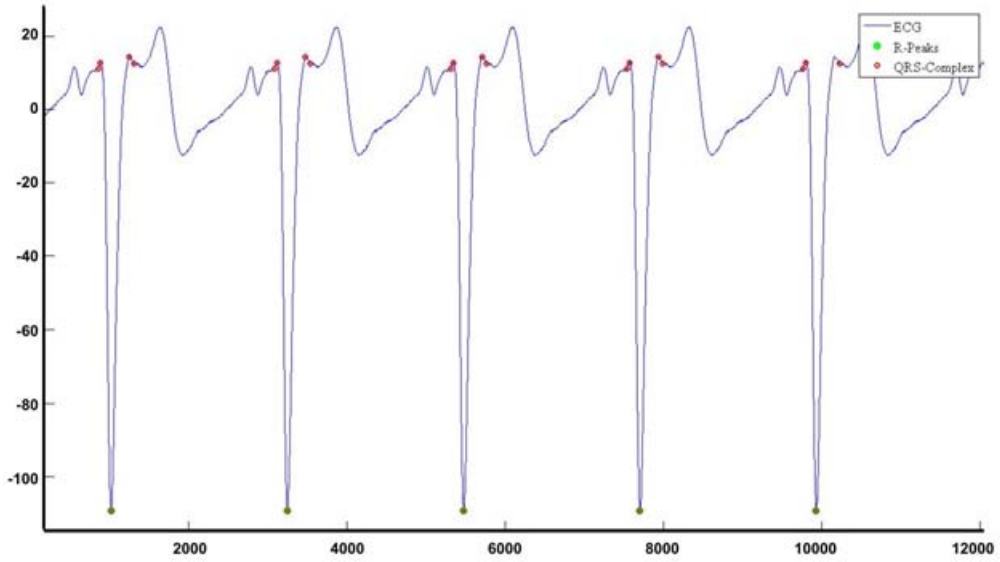

(b)

Figure 7.11. Peak detection in ECG signal before implantation: (a) ECG signal sequence. (b) QRS detection.

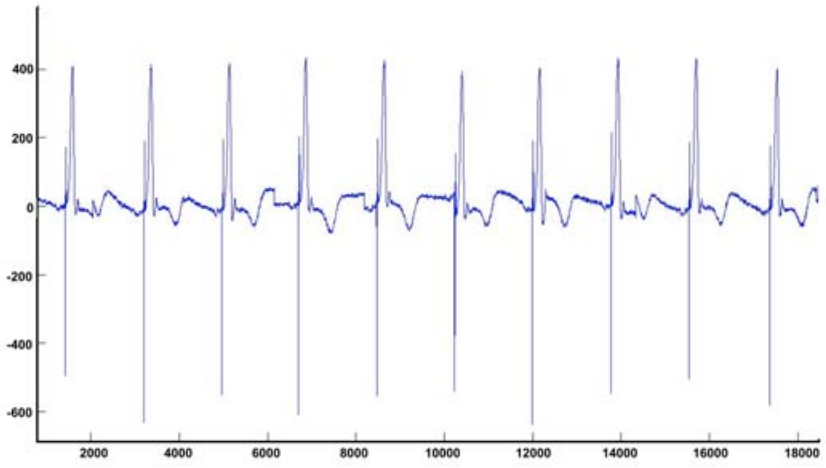

(a)

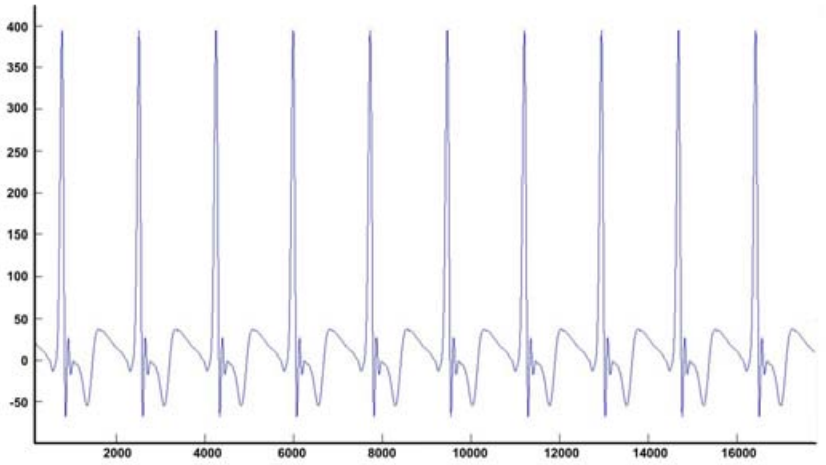

(b)

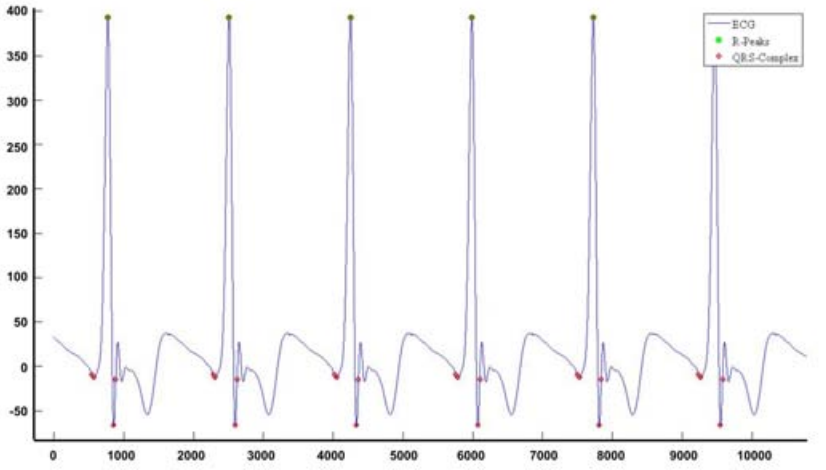

(c)

Figure 7.12. Stimulus artifact removal in ECG signal: (a) ECG signal sequence including the stimulus artifact for a patient after pacemaker implantation. (b) Stimulus artifact removal. (c) QRS detection.

Part III

Results and Conclusion

8

Results of Simulation

Different pathologies according to 17 infarction positions and 3 reduced conduction velocities were simulated. For each pathology, 36 lead positioning setups in parallel with various A-V (60 to 260 ms) and V-V delays (-30 to 70 ms) were investigated as discussed in section 7.1. For each infarction, the optimal electrode setup and optimal timing delays, which lead to minimal E_{RMS}, were identified due to the first optimization method (E_{RMS} based algorithm) described in section 7.2.1. Furthermore, the optimal setup parameters were discovered due to the second optimization method (QRS duration based algorithm) described in section 7.2.2.

8.1 Results for Patient Data Sets

The electrode positioning setup is demonstrated for each patient ventricular model. The results of the optimal pacing parameters for all data sets with respect to the lowest error are included in this section. In addition, an illustration of minimal error assoiciated with 36 electrode setups related to each MI position is presented for each patient data set. All optimal results for V-V delays are positive values which is expected, due to the LBBB. The natural exitation of the left ventricle is delayed in case of LBBB, requiring an earlier stimulation. Positive values show the pre-stimulation of the left ventricle. The physiological excitation conduction velocity is assumed to be 1000 mm/s [285].

8.1.1 Patient-1

The electrode positioning setup is demonstrated in figure 8.1. The results of both optimization methods are summarized in tables 8.1 - 8.6 for the several conduction velocities. The minimal errors associated with each electrode setup for each MI position are illustrated in figures 8.2 - 8.7.

(a) (b)

Figure 8.1. The electrode positions chosen for the Patient-1 heart model. The electrodes A, B, C and D are referred to the anterior branches of coronary sinus. The electrodes I, J, K and L are referred to the posterior branches of coronary sinus. The electrodes E, F, G and H are located on the left ventricular free wall. The electrodes U, M and X are located at the right ventricular upper septum, middle septum and apex respectively.

With both optimization methods the most frequently found optimal electrode positions were in the anterior branches of coronary sinus close to the base and RV upper septal (electrode pairs UA and UB). In case of 80 % of conduction velocity when the infarction is located in AHA7, the best electrode setup indicated by the first optimization method is UD. At the same conduction velocity when the infarction is located in AHA16, the best electrode setup suggested by the second optimization method is UL. Both optimization methods yield similar results for the optimal timing delays as 160 ms for A-V delay and 70 ms for V-V delay.

Although DSA optimization reduces the number of computations, still more than 200 simulations with the first optimization method and more than 500 simulations with the second optimization method must be performed for each pathological case. A maximum improvement of up to 26 %, the reduction percentage of E_{RMS} and an improvement of up to 77 %, the reduction percentage of $Error_{QRS}$, can be reached.

Infarction position	E_{RMS} (phy-path) ms	E_{RMS} (phy-pac) ms	% E_{RMS} reduction	Opt. elec positions	Opt. A-V ms	Opt. V-V ms	Nr. of sim.
AHA1	86.05	69.42	19.32	UA	160.00	70.00	228
AHA2	87.80	72.50	17.42	UB	160.00	70.00	222
AHA3	85.06	70.26	17.39	UA	160.00	70.00	216
AHA4	85.47	72.01	15.74	UA	160.00	70.00	216
AHA5	87.36	70.66	19.11	UA	160.00	70.00	222
AHA6	89.22	71.40	19.97	UA	160.00	70.00	228
AHA7	86.85	72.05	17.03	UA	160.00	70.00	234
AHA8	89.57	75.17	16.07	UA	160.00	70.00	456
AHA9	88.49	71.36	19.35	UA	160.00	70.00	186
AHA10	87.42	70.01	19.91	UA	160.00	70.00	192
AHA11	87.84	70.44	19.80	UA	160.00	70.00	222
AHA12	88.69	72.19	18.60	UA	160.00	70.00	228
AHA13	89.66	70.22	21.68	UA	160.00	70.00	228
AHA14	89.51	70.15	21.62	UA	160.00	70.00	222
AHA15	82.53	69.63	15.63	UA	160.00	70.00	210
AHA16	80.12	70.08	12.53	UA	160.00	70.00	222
AHA17	80.86	70.09	13.31	UA	160.00	70.00	228

phy-path: between physiology and pathology, phy-pac: between physiology and pacing, Opt: optimal, elec: electrodes, Nr. of sim: number of simulations.

Table 8.1. Results of the first optimization method for Patient-1 with 100 % conduction velocity.

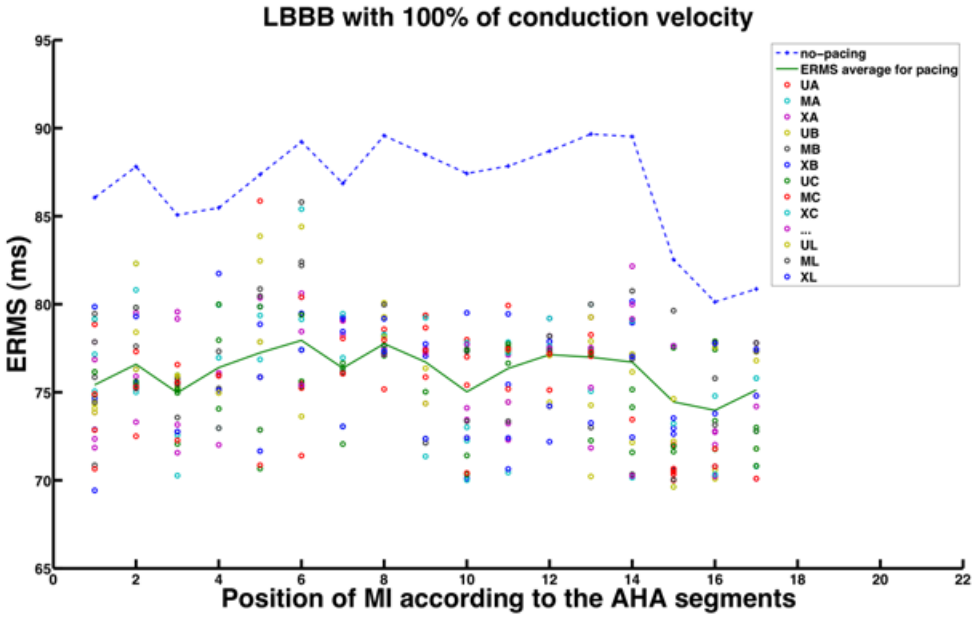

Figure 8.2. The minimal E_{RMS} achieved by the first optimization method versus AHA segments 1 to 17 corresponding to the 17 different infarction positions. (Each circular point is related to one pair of electrodes. The average of optimal electrode setups is demonstrated with a green line while the blue line shows the E_{RMS} pathology without pacing.)

Infarction position	E_{RMS} (phy-path) ms	E_{RMS} (phy-pac) ms	% E_{RMS} reduction	Opt. elec positions	Opt. A-V ms	Opt. V-V ms	Nr. of sim.
AHA1	85.93	70.63	17.80	UB	160.00	70.00	234
AHA2	86.51	73.01	15.60	UB	160.00	70.00	228
AHA3	85.94	70.13	18.39	UB	160.00	70.00	216
AHA4	89.19	74.61	16.34	UA	160.00	70.00	216
AHA5	89.97	70.71	21.40	UA	160.00	70.00	222
AHA6	81.36	70.06	13.88	UA	160.00	70.00	228
AHA7	85.03	70.83	16.69	UD	120.00	49.84	246
AHA8	88.28	70.08	20.61	UB	160.00	70.00	268
AHA9	88.26	70.11	20.56	UA	160.00	70.00	210
AHA10	89.14	72.41	18.76	UA	160.00	70.00	210
AHA11	85.06	70.00	17.70	UA	160.00	70.00	222
AHA12	89.88	72.06	19.82	UA	160.00	70.00	228
AHA13	88.22	70.55	20.02	UA	160.00	70.00	228
AHA14	86.66	70.10	19.10	UA	160.00	70.00	228
AHA15	90.23	75.64	16.16	UA	160.00	70.00	210
AHA16	86.72	70.31	18.92	UA	160.00	70.00	234
AHA17	89.75	72.71	18.98	UA	160.00	70.00	228

phy-path: between physiology and pathology, phy-pac: between physiology and pacing, Opt: optimal, elec: electrodes, Nr. of sim: number of simulations.

Table 8.2. Results of the first optimization method for Patient-1 with 80 % conduction velocity.

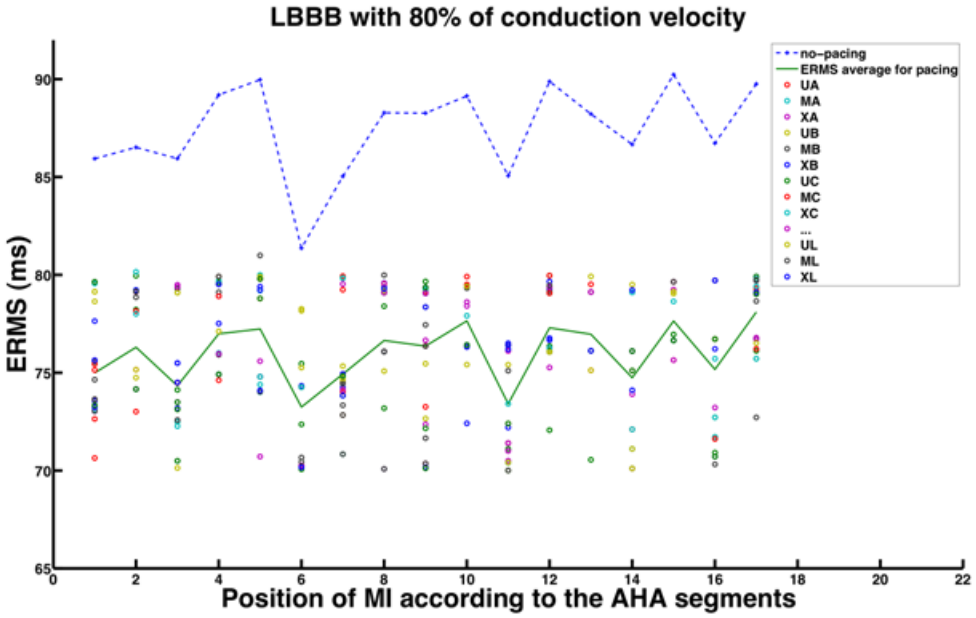

Figure 8.3. The minimal E_{RMS} achieved by the first optimization method versus AHA segments 1 to 17 corresponding to the 17 different infarction positions. (Each circular point is related to one pair of electrodes. The average of optimal electrode setups is demonstrated with a green line while the blue line shows the E_{RMS} pathology without pacing.)

Infarction position	E_{RMS} (phy-path) ms	E_{RMS} (phy-pac) ms	% E_{RMS} reduction	Opt. elec positions	Opt. A-V ms	Opt. V-V ms	Nr. of sim.
AHA1	86.26	71.86	16.69	UB	160.00	70.00	234
AHA2	85.20	72.28	15.16	UB	160.00	70.00	228
AHA3	89.62	72.91	18.64	UB	160.00	70.00	222
AHA4	89.36	73.38	17.88	UB	160.00	70.00	222
AHA5	83.11	70.23	15.49	UB	160.00	70.00	228
AHA6	85.75	72.59	15.34	UB	160.00	70.00	228
AHA7	89.88	73.06	18.71	UB	160.00	70.00	246
AHA8	82.43	74.49	9.63	UB	160.00	70.00	268
AHA9	88.55	72.85	17.72	UB	160.00	70.00	222
AHA10	87.33	72.95	16.47	UB	160.00	70.00	210
AHA11	82.78	70.18	15.22	UB	160.00	70.00	222
AHA12	82.52	69.23	16.10	UB	160.00	70.00	228
AHA13	88.46	65.24	26.24	UB	160.00	70.00	240
AHA14	88.97	70.05	21.26	UB	160.00	70.00	234
AHA15	88.12	70.19	20.34	UB	160.00	70.00	216
AHA16	88.44	70.18	20.64	UB	160.00	70.00	234
AHA17	89.33	75.07	15.96	UB	160.00	70.00	234

phy-path: between physiology and pathology, phy-pac: between physiology and pacing, Opt: optimal, elec: electrodes, Nr. of sim: number of simulations.

Table 8.3. Results of the first optimization method for Patient-1 with 60 % conduction velocity.

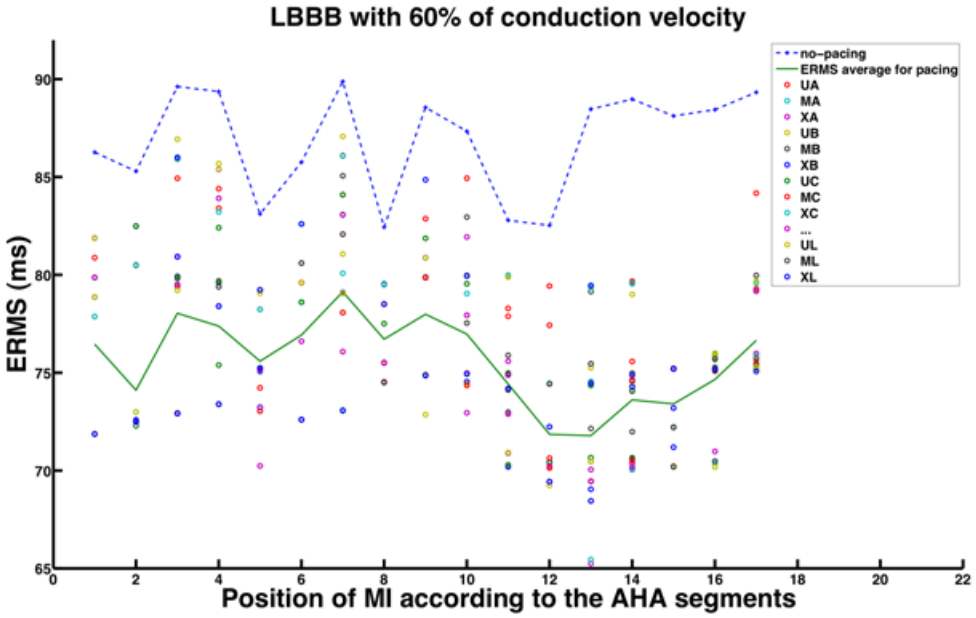

Figure 8.4. The minimal E_{RMS} achieved by the first optimization method versus AHA segments 1 to 17 corresponding to the 17 different infarction positions. (Each circular point is related to one pair of electrodes. The average of optimal electrode setups is demonstrated with a green line while the blue line shows the E_{RMS} pathology without pacing.)

Infarction position	$Error_{QRS}$ (phy-path) ms	$Error_{QRS}$ (phy-pac) ms	% $Error_{QRS}$ reduction	Opt. elec positions	Opt. A-V ms	Opt. V-V ms	Nr. of sim.
AHA1	128	49	61.72	UA	160.00	70.00	529
AHA2	121	43	64.46	UB	160.00	70.00	540
AHA3	123	52	57.72	UA	160.00	70.00	591
AHA4	124	53	57.26	UA	160.00	70.00	582
AHA5	119	48	59.66	UA	160.00	70.00	561
AHA6	105	34	67.62	UA	160.00	70.00	471
AHA7	104	33	68.27	UA	160.00	70.00	550
AHA8	117	46	60.68	UA	160.00	70.00	598
AHA9	123	47	61.79	UA	160.00	70.00	562
AHA10	122	51	58.20	UA	160.00	70.00	569
AHA11	112	41	63.39	UA	160.00	70.00	530
AHA12	103	32	68.93	UA	160.00	70.00	571
AHA13	102	40	60.78	UA	160.00	70.00	517
AHA14	107	36	66.36	UA	160.00	70.00	545
AHA15	114	39	65.79	UA	160.00	70.00	577
AHA16	102	31	69.61	UA	160.00	70.00	563
AHA17	112	40	64.28	UA	160.00	70.00	527

phy-path: between physiology and pathology, phy-pac: between physiology and pacing, Opt: optimal, elec: electrodes, Nr. of sim: number of simulations.

Table 8.4. Results of the second optimization method for Patient-1 with 100 % conduction velocity.

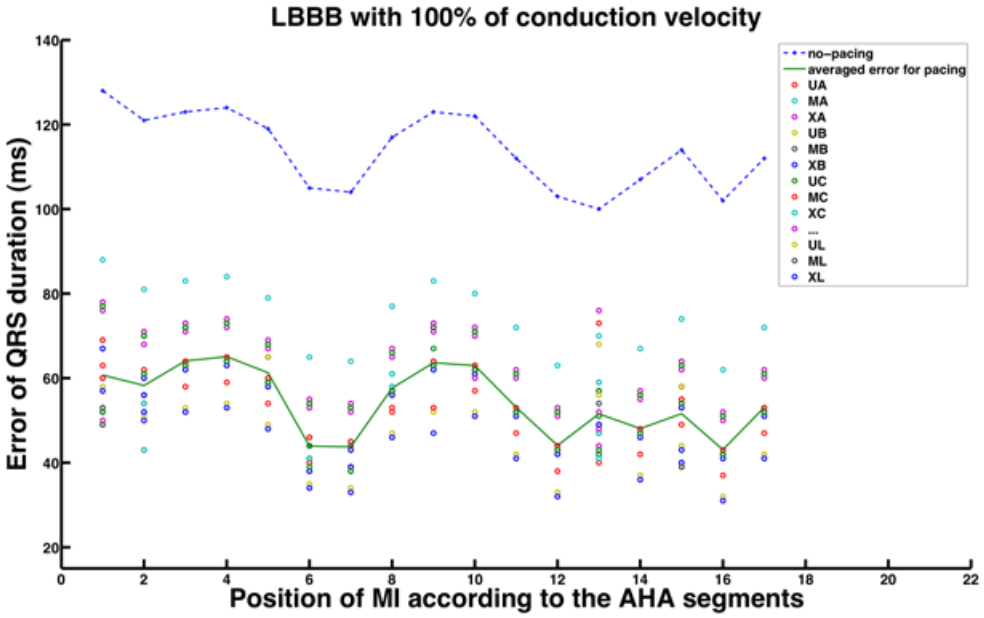

Figure 8.5. The minimal $Error_{QRS}$ achieved by the second optimization method versus AHA segments 1 to 17 corresponding to the 17 different infarction positions. (Each circular point is related to one pair of electrodes. The average of optimal electrode setups is demonstrated with a green line while the blue line shows the $Error_{QRS}$ pathology without pacing.)

Infarction position	$Error_{QRS}$ (phy-path) ms	$Error_{QRS}$ (phy-pac) ms	% $Error_{QRS}$ reduction	Opt. elec positions	Opt. A-V ms	Opt. V-V ms	Nr. of sim.
AHA1	160	34	77.50	UB	160.00	70.00	454
AHA2	150	46	69.33	UB	160.00	70.00	561
AHA3	153	43	71.89	UB	160.00	70.00	589
AHA4	154	42	72.72	UA	160.00	70.00	559
AHA5	149	47	68.45	UA	160.00	70.00	554
AHA6	127	41	67.71	UA	160.00	70.00	468
AHA7	123	37	69.91	UB	160.00	70.00	617
AHA8	146	50	65.75	UB	160.00	70.00	568
AHA9	152	46	69.73	UA	160.00	70.00	595
AHA10	151	52	65.56	UA	160.00	70.00	600
AHA11	139	53	61.87	UA	160.00	70.00	576
AHA12	126	40	68.25	UA	160.00	70.00	590
AHA13	110	30	72.72	UA	160.00	70.00	580
AHA14	134	48	64.17	UA	160.00	70.00	583
AHA15	142	52	63.38	UA	160.00	70.00	576
AHA16	126	39	69.04	UL	160.00	70.00	556
AHA17	139	53	61.87	UA	160.00	70.00	570

phy-path: between physiology and pathology, phy-pac: between physiology and pacing, Opt: optimal, elec: electrodes, Nr. of sim: number of simulations.

Table 8.5. Results of the second optimization method for Patient-1 with 80 % conduction velocity.

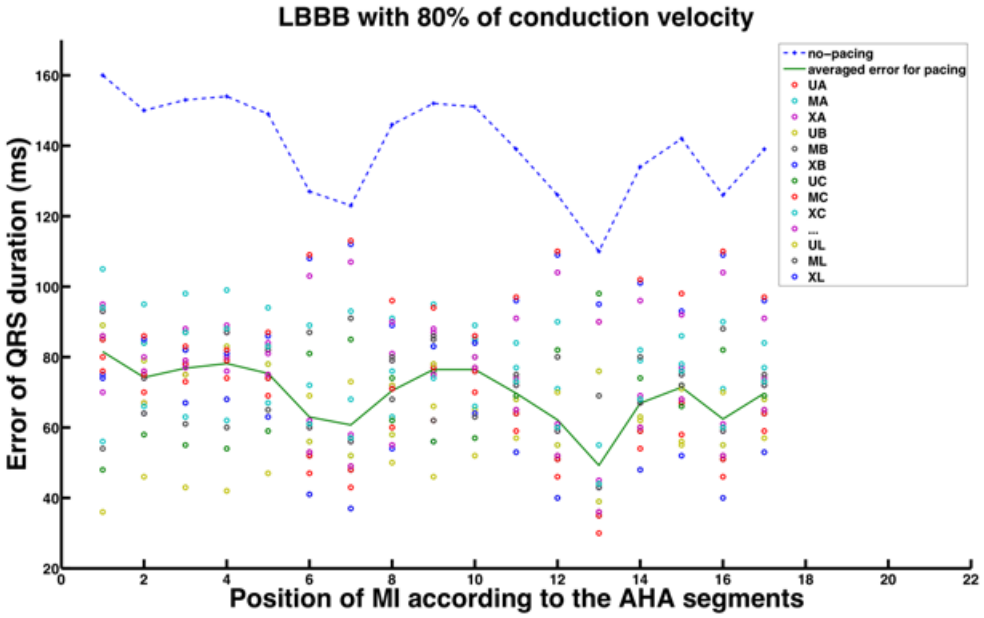

Figure 8.6. The minimal $Error_{QRS}$ achieved by the second optimization method versus AHA segments 1 to 17 corresponding to the 17 different infarction positions. (Each circular point is related to one pair of electrodes. The average of optimal electrode setups is demonstrated with a green line while the blue line shows the $Error_{QRS}$ pathology without pacing.)

Infarction position	$Error_{QRS}$ (phy-path) ms	$Error_{QRS}$ (phy-pac) ms	% $Error_{QRS}$ reduction	Opt. elec positions	Opt. A-V ms	Opt. V-V ms	Nr. of sim.
AHA1	211	96	54.50	UB	160.00	70.00	499
AHA2	196	77	60.71	UB	160.00	70.00	434
AHA3	201	84	58.21	UB	160.00	70.00	455
AHA4	205	98	52.20	UB	160.00	70.00	442
AHA5	197	97	50.76	UB	160.00	70.00	484
AHA6	167	67	59.88	UB	160.00	70.00	414
AHA7	156	47	69.87	UB	160.00	70.00	577
AHA8	185	68	63.24	UB	160.00	70.00	540
AHA9	199	94	52.76	UB	160.00	70.00	496
AHA10	200	100	50.00	UB	160.00	70.00	472
AHA11	185	85	54.05	UB	160.00	70.00	529
AHA12	160	60	62.50	UB	160.00	70.00	522
AHA13	144	44	69.44	UB	160.00	70.00	521
AHA14	176	76	56.82	UB	160.00	70.00	482
AHA15	186	86	53.76	UB	160.00	70.00	549
AHA16	165	65	60.61	UB	160.00	70.00	491
AHA17	182	82	54.95	UB	160.00	70.00	454

phy-path: between physiology and pathology, phy-pac: between physiology and pacing, Opt: optimal, elec: electrodes, Nr. of sim: number of simulations.

Table 8.6. Results of the second optimization method for Patient-1 with 60 % conduction velocity.

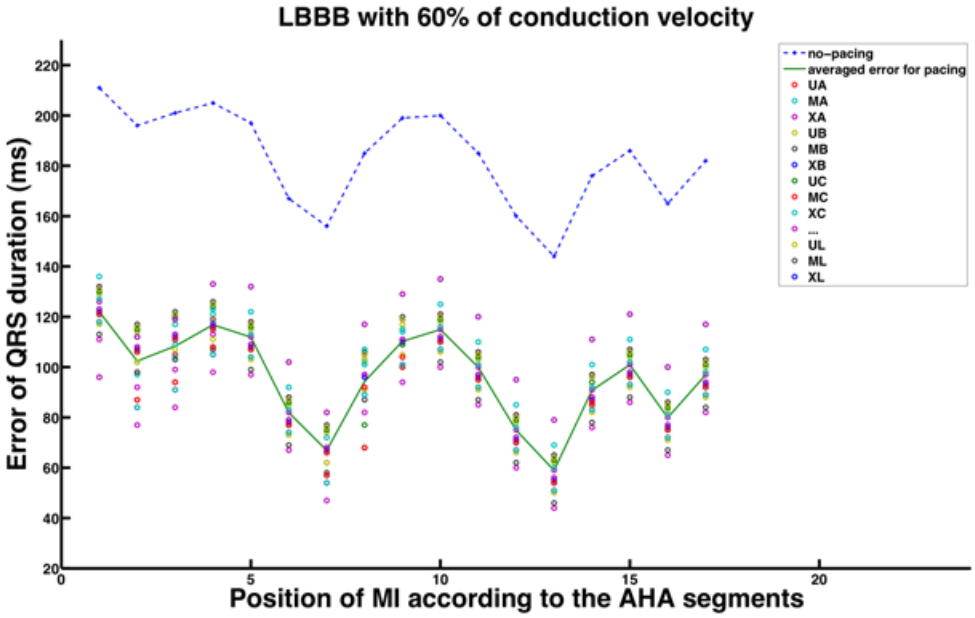

Figure 8.7. The minimal $Error_{QRS}$ achieved by the second optimization method versus AHA segments 1 to 17 corresponding to the 17 different infarction positions. (Each circular point is related to one pair of electrodes. The average of optimal electrode setups is demonstrated with a green line while the blue line shows the $Error_{QRS}$pathology without pacing.)

8.1.2 Patient-2

The electrode positioning setup is demonstrated in figure 8.8. The results of both optimization methods are summarized in tables 8.7 - 8.12 for the several conduction velocities. The minimal errors associated with each electrode setup for each MI position are illustrated in figures 8.9 - 8.14. Both optimization methods mostly found the optimal left electrode

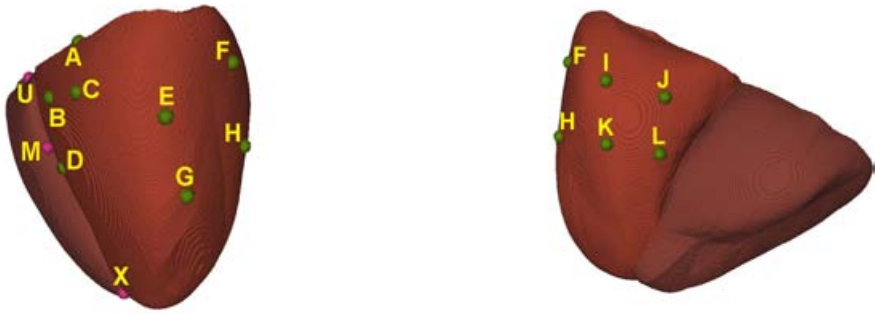

(a) (b)

Figure 8.8. The electrode positions chosen for the Patient-2 heart model. The electrodes A, B, C and D are referred to the anterior branches of coronary sinus. The electrodes I, J, K and L are referred to the posterior branches of coronary sinus. The electrodes E, F, G and H are located on the left ventricular free wall. The electrodes U, M and X are located at the right ventricular upper septum, middle septum and apex respectively.

position in the lateral wall of the left ventricle or anterior branches of coronary sinus close to the base (electrode E, G and C). The optimal RV electrode varied according to the underlying pathology (electrode U, M and X). The best timing delays range assessed by the first optimization method is $120 - 160\ ms$ for the A-V delay and $48 - 70\ ms$ for V-V delay. However the timing delays achieved by the second optimization method is always the same values of 160 ms for A-V delay and 70 ms for V-V delay. The first optimization delivers a number between 317 to 533 simulations for each pathological case. More than 500 simulations with the second optimization method are performed for each pathological case. A maximum improvement of up to 39 %, the reduction percentage of E_{RMS} and an improvement of up to 91 %, the reduction percentage of $Error_{QRS}$, can be achieved.

Infarction position	E_{RMS} (phy-path) ms	E_{RMS} (phy-pac) ms	% E_{RMS} reduction	Opt. elec positions	Opt. A-V ms	Opt. V-V ms	Nr. of sim.
AHA1	18.69	13.92	25.54	UE	160.00	70.00	367
AHA2	19.30	14.94	22.58	XC	140.00	57.58	414
AHA3	19.56	15.57	20.40	MC	140.31	60.23	359
AHA4	20.41	16.53	19.01	UE	160.00	70.00	390
AHA5	21.30	17.27	18.91	ME	160.00	70.00	337
AHA6	19.97	15.33	23.22	UE	160.00	70.00	388
AHA7	19.23	14.72	23.46	UE	160.00	70.00	357
AHA8	20.07	15.87	20.95	UE	160.00	70.00	356
AHA9	19.99	16.13	19.28	XE	130.00	49.81	355
AHA10	20.07	16.04	20.06	UG	140.00	57.58	386
AHA11	21.12	17.09	19.08	UE	160.00	70.00	336
AHA12	22.50	18.38	18.31	ME	160.00	70.00	339
AHA13	19.25	14.65	23.90	UE	160.00	70.00	373
AHA14	19.05	14.27	25.09	ME	160.00	70.00	358
AHA15	20.68	16.66	19.42	UE	160.00	70.00	355
AHA16	21.64	17.73	18.06	UE	160.00	70.00	317
AHA17	19.45	14.85	23.65	ME	160.00	70.00	353

phy-path: between physiology and pathology, phy-pac: between physiology and pacing, Opt: optimal, elec: electrodes, Nr. of sim: number of simulations.

Table 8.7. Results of the first optimization method for Patient-2 with 100 % conduction velocity.

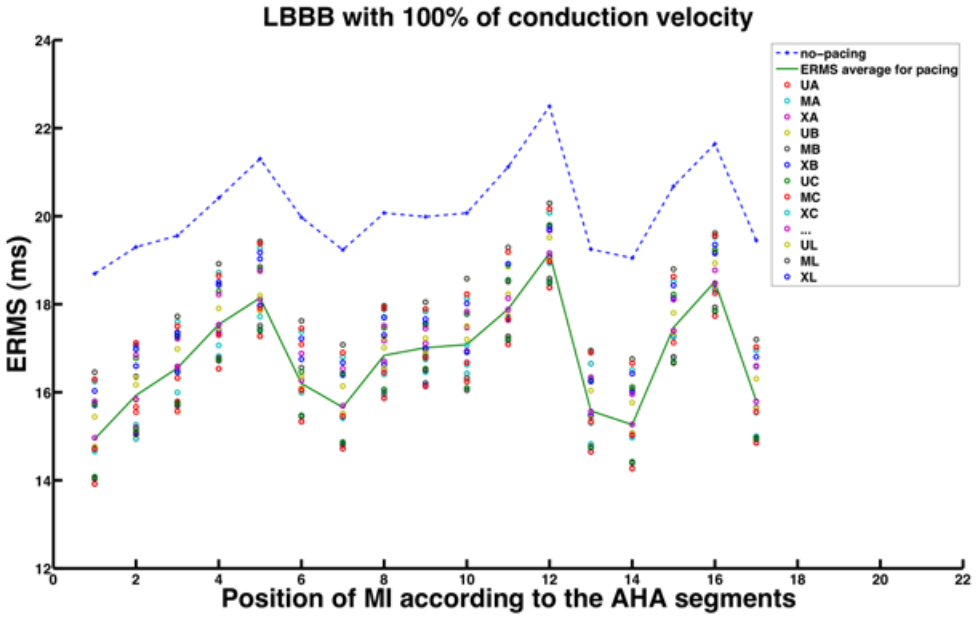

Figure 8.9. The minimal E_{RMS} achieved by the first optimization method versus AHA segments 1 to 17 corresponding to the 17 different infarction positions. (Each circular point is related to one pair of electrodes. The average of optimal electrode setups is demonstrated with a green line while the blue line shows the E_{RMS} pathology without pacing.)

Infarction position	E_{RMS} (phy-path) ms	E_{RMS} (phy-pac) ms	% E_{RMS} reduction	Opt. elec positions	Opt. A-V ms	Opt. V-V ms	Nr. of sim.
AHA1	20.67	14.24	31.13	UG	140.00	57.58	478
AHA2	21.23	15.09	28.93	XC	125.00	52.56	459
AHA3	21.35	15.82	25.87	XC	127.50	54.31	482
AHA4	22.12	16.57	25.09	XE	130.00	52.15	495
AHA5	23.11	17.47	24.43	XE	130.00	49.81	447
AHA6	22.02	15.62	29.06	UG	140.00	57.58	461
AHA7	21.19	15.04	29.05	UG	140.00	57.58	460
AHA8	21.97	16.13	26.58	UG	140.00	57.58	452
AHA9	21.78	16.20	25.59	ME	125.00	51.00	449
AHA10	21.80	16.15	25.92	MG	126.09	50.74	478
AHA11	22.93	17.35	24.36	UG	140.00	57.58	433
AHA12	24.34	18.62	23.48	UG	140.00	57.58	408
AHA13	21.27	14.91	29.87	XE	131.25	48.04	499
AHA14	21.09	14.58	30.86	UG	140.00	57.58	453
AHA15	22.45	16.80	25.16	UG	140.00	57.58	427
AHA16	23.38	17.98	23.11	UG	140.00	57.58	421
AHA17	21.43	15.11	29.48	UG	140.00	57.58	428

phy-path: between physiology and pathology, phy-pac: between physiology and pacing, Opt: optimal, elec: electrodes, Nr. of sim: number of simulations.

Table 8.8. Results of the first optimization method for Patient-2 with 80 % conduction velocity.

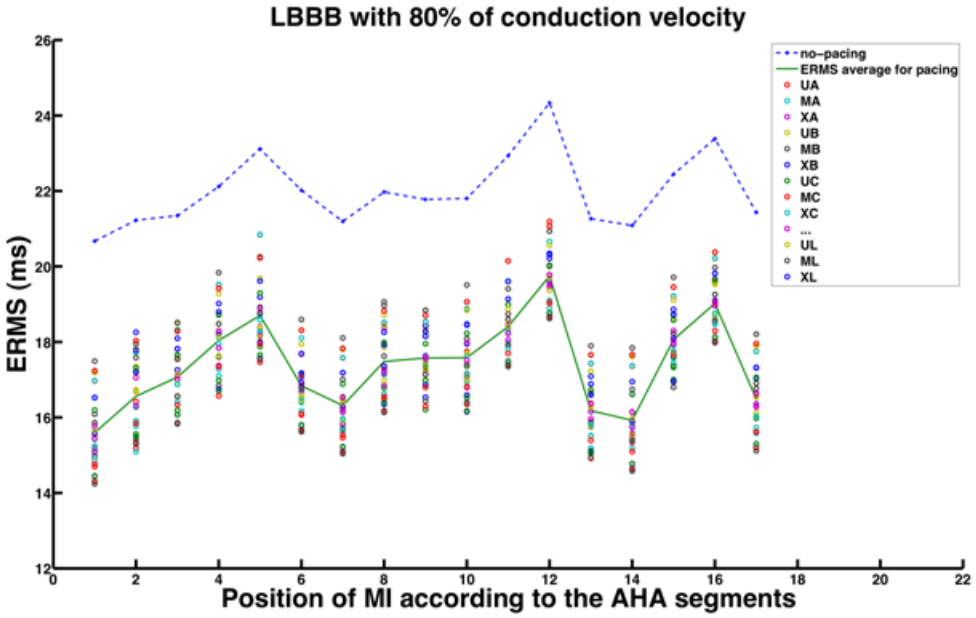

Figure 8.10. The minimal E_{RMS} achieved by the first optimization method versus AHA segments 1 to 17 corresponding to the 17 different infarction positions. (Each circular point is related to one pair of electrodes. The average of optimal electrode setups is demonstrated with a green line while the blue line shows the E_{RMS} pathology without pacing.)

Infarction position	E_{RMS} (phy-path) ms	E_{RMS} (phy-pac) ms	% E_{RMS} reduction	Opt. elec positions	Opt. A-V ms	Opt. V-V ms	Nr. of sim.
AHA1	24.12	14.68	39.15	XE	125.00	51.00	554
AHA2	24.68	15.65	36.57	MG	125.00	51.00	533
AHA3	24.50	16.34	33.30	MG	120.00	49.84	529
AHA4	25.12	17.11	31.89	ME	120.00	49.84	534
AHA5	26.32	17.89	32.03	XE	125.00	51.00	513
AHA6	25.60	16.01	37.47	XE	125.00	51.00	529
AHA7	24.58	15.44	37.21	XE	125.00	51.00	544
AHA8	25.30	16.50	34.76	XE	125.00	51.00	521
AHA9	24.92	16.84	32.43	UG	120.00	49.84	502
AHA10	24.84	17.04	31.40	MG	120.00	49.84	536
AHA11	26.12	17.68	32.31	XE	125.00	51.00	516
AHA12	27.57	19.00	31.09	XE	125.00	51.00	501
AHA13	24.76	15.37	37.93	XE	123.75	52.27	526
AHA14	24.60	14.98	39.11	XE	125.00	51.00	556
AHA15	25.54	17.25	32.48	MG	120.00	49.84	505
AHA16	26.46	18.32	30.76	ME	120.00	49.84	502
AHA17	24.85	15.55	37.43	XE	120.00	49.84	546

phy-path: between physiology and pathology, phy-pac: between physiology and pacing, Opt: optimal, elec: electrodes, Nr. of sim: number of simulations.

Table 8.9. Results of the first optimization method for Patient-2 with 60 % conduction velocity.

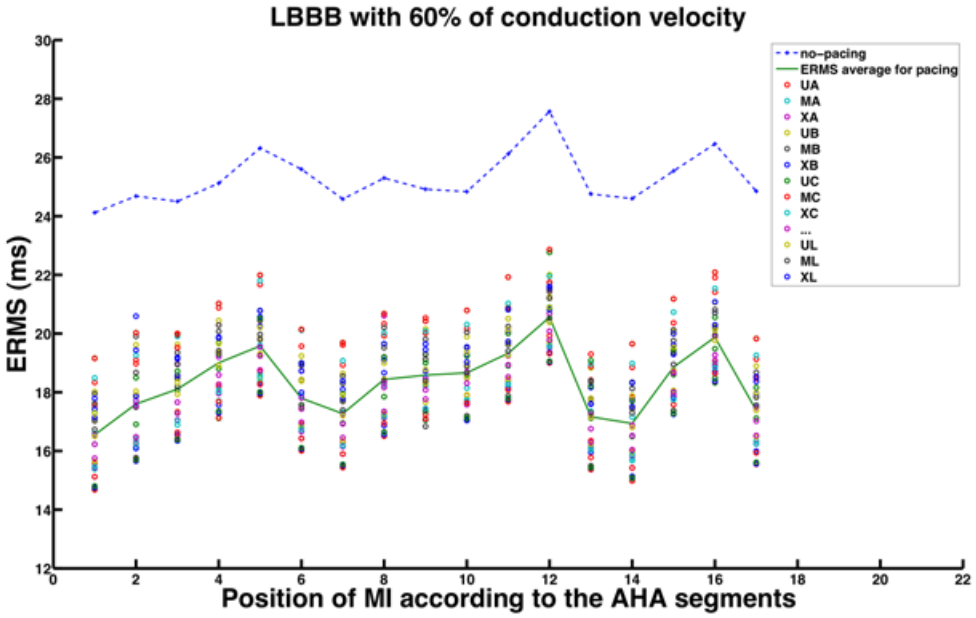

Figure 8.11. The minimal E_{RMS} achieved by the first optimization method versus AHA segments 1 to 17 corresponding to the 17 different infarction positions. (Each circular point is related to one pair of electrodes. The average of optimal electrode setups is demonstrated with a green line while the blue line shows the E_{RMS} pathology without pacing.)

Infarction position	$Error_{QRS}$ (phy-path) ms	$Error_{QRS}$ (phy-pac) ms	% $Error_{QRS}$ reduction	Opt. elec positions	Opt. A-V ms	Opt. V-V ms	Nr. of sim.
AHA1	69	12	82.60	UE	160.00	70.00	547
AHA2	72	10	86.11	UE	160.00	70.00	525
AHA3	101	22	78.21	UG	160.00	70.00	471
AHA4	103	10	90.29	ME	160.00	70.00	501
AHA5	91	8	91.20	ME	160.00	70.00	527
AHA6	75	21	72.00	UE	160.00	70.00	567
AHA7	68	8	88.23	UE	160.00	70.00	567
AHA8	68	10	85.29	UE	160.00	70.00	514
AHA9	120	25	79.16	UE	160.00	70.00	333
AHA10	92	8	91.30	UE	160.00	70.00	478
AHA11	69	12	82.60	ME	160.00	70.00	583
AHA12	74	8	89.18	ME	160.00	70.00	531
AHA13	68	8	88.23	UE	160.00	70.00	529
AHA14	68	8	88.23	ME	160.00	70.00	556
AHA15	81	24	70.37	UE	160.00	70.00	531
AHA16	68	23	66.17	UE	160.00	70.00	493
AHA17	68	15	77.94	ME	160.00	70.00	555

phy-path: between physiology and pathology, phy-pac: between physiology and pacing, Opt: optimal, elec: electrodes, Nr. of sim: number of simulations.

Table 8.10. Results of the second optimization method for Patient-2 with 100 % conduction velocity.

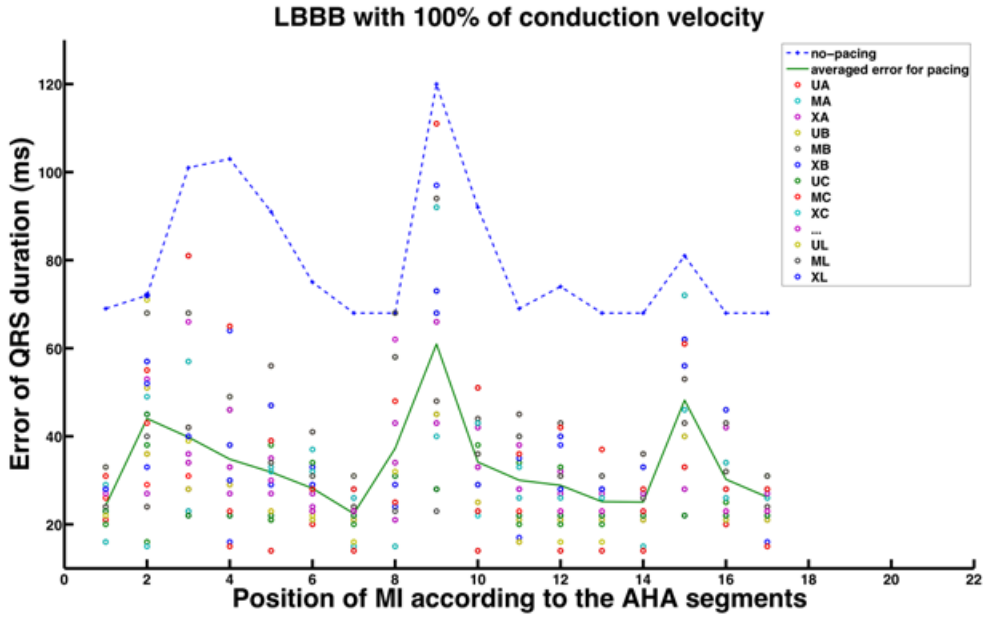

Figure 8.12. The minimal $Error_{QRS}$ achieved by the second optimization method versus AHA segments 1 to 17 corresponding to the 17 different infarction positions. (Each circular point is related to one pair of electrodes. The average of optimal electrode setups is demonstrated with a green line while the blue line shows the $Error_{QRS}$ pathology without pacing.)

Infarction position	$Error_{QRS}$ (phy-path) ms	$Error_{QRS}$ (phy-pac) ms	% $Error_{QRS}$ reduction	Opt. elec positions	Opt. A-V ms	Opt. V-V ms	Nr. of sim.
AHA1	94	37	60.64	UG	160.00	70.00	491
AHA2	99	38	61.61	UG	160.00	70.00	441
AHA3	137	42	69.34	UG	160.00	70.00	457
AHA4	140	25	82.14	UG	160.00	70.00	433
AHA5	122	27	77.86	UG	160.00	70.00	535
AHA6	103	27	73.78	UG	160.00	70.00	548
AHA7	93	22	76.34	UG	160.00	70.00	505
AHA8	94	25	73.40	UG	160.00	70.00	490
AHA9	164	50	69.51	UG	160.00	70.00	298
AHA10	127	30	76.37	UE	160.00	70.00	466
AHA11	94	22	76.59	ME	160.00	70.00	490
AHA12	99	22	77.77	UE	160.00	70.00	490
AHA13	93	22	76.34	UG	160.00	70.00	497
AHA14	93	22	76.34	UE	160.00	70.00	499
AHA15	116	42	63.79	UE	160.00	70.00	391
AHA16	93	30	67.74	UE	160.00	70.00	492
AHA17	93	29	68.82	UG	160.00	70.00	501

phy-path: between physiology and pathology, phy-pac: between physiology and pacing, Opt: optimal, elec: electrodes, Nr. of sim: number of simulations.

Table 8.11. Results of the second optimization method for Patient-2 with 80 % conduction velocity.

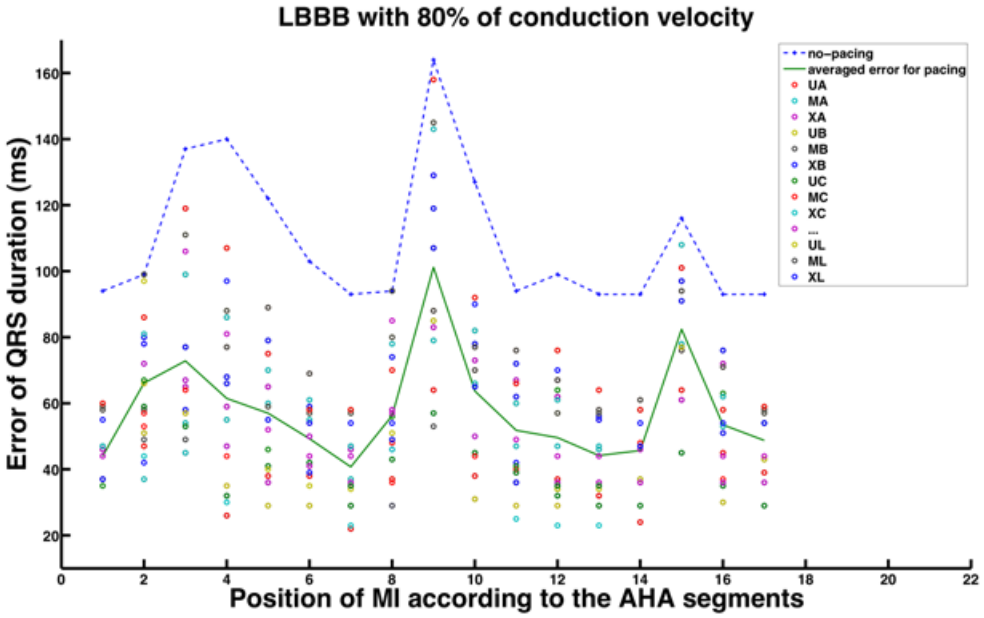

Figure 8.13. The minimal $Error_{QRS}$ achieved by the second optimization method versus AHA segments 1 to 17 corresponding to the 17 different infarction positions. (Each circular point is related to one pair of electrodes. The average of optimal electrode setups is demonstrated with a green line while the blue line shows the $Error_{QRS}$ pathology without pacing.)

Infarction position	$Error_{QRS}$ (phy-path) ms	$Error_{QRS}$ (phy-pac) ms	% $Error_{QRS}$ reduction	Opt. elec positions	Opt. A-V ms	Opt. V-V ms	Nr. of sim.
AHA1	134	57	56.20	UG	160.00	70.00	499
AHA2	138	65	52.89	UG	160.00	70.00	387
AHA3	194	82	57.73	UG	160.00	70.00	330
AHA4	199	72	63.81	UG	160.00	70.00	349
AHA5	173	70	59.53	UG	160.00	70.00	362
AHA6	147	58	60.54	UG	160.00	70.00	487
AHA7	133	49	63.15	UG	160.00	70.00	510
AHA8	133	62	53.38	UG	160.00	70.00	441
AHA9	230	110	52.17	UF	160.00	70.00	241
AHA10	186	80	56.98	UE	160.00	70.00	402
AHA11	140	59	57.85	UG	160.00	70.00	429
AHA12	138	51	63.04	UG	160.00	70.00	458
AHA13	133	50	62.40	UG	160.00	70.00	543
AHA14	133	60	54.88	UG	160.00	70.00	468
AHA15	171	86	49.70	UE	160.00	70.00	336
AHA16	133	70	47.36	UG	160.00	70.00	417
AHA17	133	63	52.63	UG	160.00	70.00	493

phy-path: between physiology and pathology, phy-pac: between physiology and pacing, Opt: optimal, elec: electrodes, Nr. of sim: number of simulations.

Table 8.12. Results of the second optimization method for Patient-2 with 60 % conduction velocity.

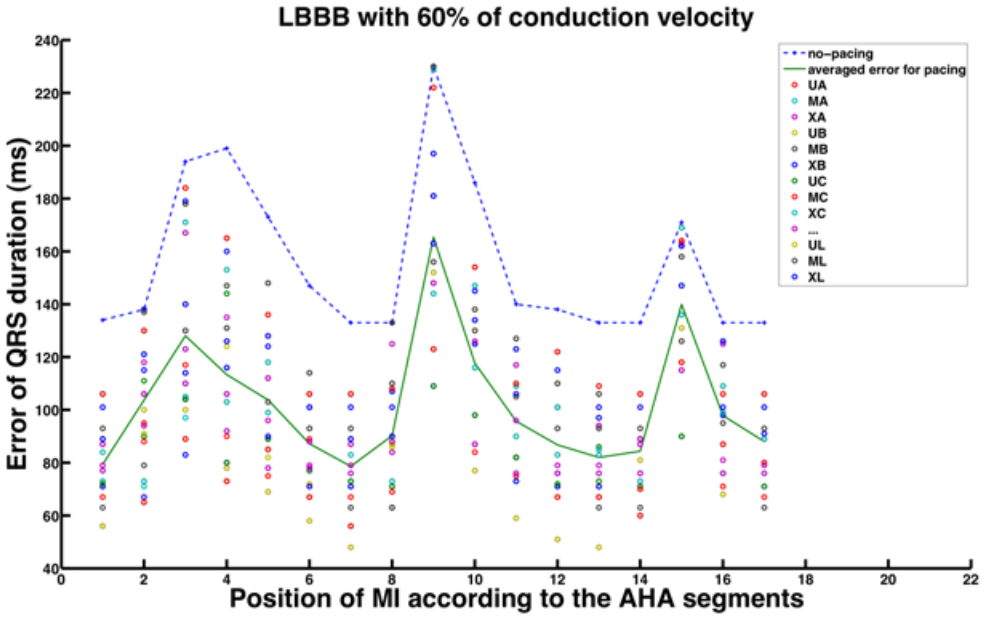

Figure 8.14. The minimal $Error_{QRS}$ achieved by the second optimization method versus AHA segments 1 to 17 corresponding to the 17 different infarction positions. (Each circular point is related to one pair of electrodes. The average of optimal electrode setups is demonstrated with a green line while the blue line shows the $Error_{QRS}$ pathology without pacing.)

8.1.3 Patient-3

The electrode positioning setup is demonstrated in figure 8.15. The results of both optimization methods are summarized in tables 8.13 - 8.18 for the several conduction velocities. The minimal errors associated with each electrode setup for each MI position are illustrated in figures 8.16 - 8.21. Both optimization methods mostly found the optimal left

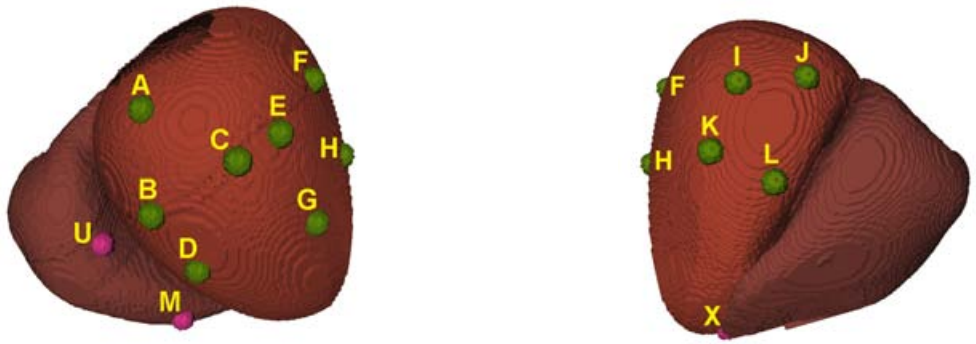

(a) (b)

Figure 8.15. The electrode positions chosen for the Patient-3 heart model. The electrodes A, B, C and D are referred to the anterior branches of coronary sinus. The electrodes I, J, K and L are referred to the posterior branches of coronary sinus. The electrodes E, F, G and H are located on the left ventricular free wall. The electrodes U, M and X are located at the right ventricular upper septum, middle septum and apex respectively.

electrode position in the lateral wall of the left ventricle (electrode G and H). The optimal right electrode position is mostly in the RV apex (electrode X) only in case of 60 % of conduction velocity, the position is changed to the middle septal (electrode M), which is attained with the first optimization method. The best timing delays range mostly achieved is 160 ms for the A-V delay and 70 ms for V-V delay. Merely the timing delays achieved by the first optimization method, vary between $120 - 140$ ms for A-V delay and $51 - 59$ ms for V-V delay once the conduction velocity is set to 60 %. In case of 80 % of the conduction velocity when the infarction is located in AHA8 and AHA9 the timing delays determined by the first algorithm is different $140 - 150$ ms for A-V delay and 64.57 ms, 60.70 ms for V-V delay.

DSA optimization delivers a number between 307 to 554 simulations for each pathological case. A maximum improvement of up to 59 %, the reduction percentage of E_{RMS} and an improvement of up to 89 %, the reduction percentage of $Error_{QRS}$, can be reached.

Infarction position	E_{RMS} (phy-path) ms	E_{RMS} (phy-pac) ms	% E_{RMS} reduction	Opt. elec positions	Opt. A-V ms	Opt. V-V ms	Nr. of sim.
AHA1	18.21	11.55	36.57	XG	160.00	70.00	483
AHA2	20.19	15.84	21.54	XG	160.00	70.00	463
AHA3	22.93	17.57	23.37	XH	160.00	70.00	465
AHA4	22.06	17.04	22.75	XG	160.00	70.00	456
AHA5	24.55	17.50	28.71	XG	160.00	70.00	461
AHA6	24.88	17.90	28.05	XG	160.00	70.00	456
AHA7	17.83	11.51	35.44	XG	160.00	70.00	480
AHA8	23.99	17.55	26.84	XH	160.00	70.00	420
AHA9	25.88	18.22	29.59	XH	160.00	70.00	441
AHA10	24.37	18.02	26.05	XG	160.00	70.00	434
AHA11	26.60	18.28	31.27	XG	160.00	70.00	451
AHA12	25.38	18.13	28.56	XG	160.00	70.00	454
AHA13	23.91	17.78	25.63	XG	160.00	70.00	455
AHA14	24.21	17.75	26.68	XH	160.00	70.00	438
AHA15	23.71	17.89	24.54	XG	160.00	70.00	451
AHA16	24.78	17.72	28.49	XH	160.00	70.00	451
AHA17	27.59	17.69	35.88	XG	160.00	70.00	444

phy-path: between physiology and pathology, phy-pac: between physiology and pacing, Opt: optimal, elec: electrodes, Nr. of sim: number of simulations.

Table 8.13. Results of the first optimization method for Patient-3 with 100 % conduction velocity.

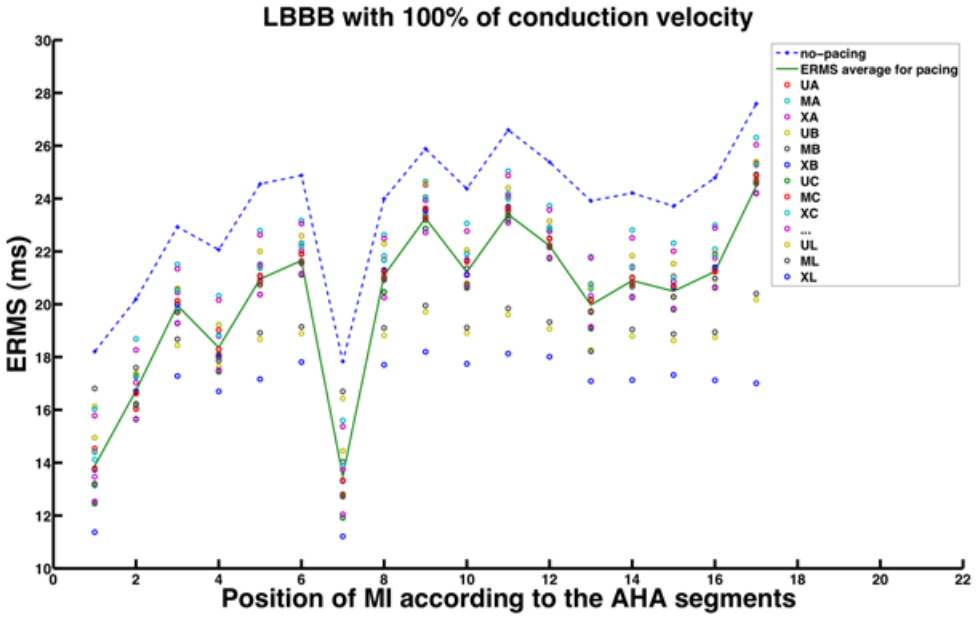

Figure 8.16. The minimal E_{RMS} achieved by the first optimization method versus AHA segments 1 to 17 corresponding to the 17 different infarction positions. (Each circular point is related to one pair of electrodes. The average of optimal electrode setups is demonstrated with a green line while the blue line shows the E_{RMS} pathology without pacing.)

Infarction position	E_{RMS} (phy-path) ms	E_{RMS} (phy-pac) ms	% E_{RMS} reduction	Opt. elec positions	Opt. A-V ms	Opt. V-V ms	Nr. of sim.
AHA1	21.93	11.09	47.61	XH	160.00	70.00	432
AHA2	23.36	12.02	48.63	XH	160.00	70.00	418
AHA3	25.70	17.05	33.65	XH	160.00	70.00	401
AHA4	25.23	16.25	35.59	XH	160.00	70.00	425
AHA5	27.49	17.35	36.88	XH	160.00	70.00	397
AHA6	27.69	17.23	37.77	XH	160.00	70.00	393
AHA7	21.57	11.01	48.95	XH	160.00	70.00	432
AHA8	26.57	17.55	33.94	XH	150.00	64.57	398
AHA9	28.28	18.53	34.47	XH	140.00	60.70	391
AHA10	27.22	17.29	36.48	XH	160.00	70.00	414
AHA11	29.30	17.99	38.60	XH	160.00	70.00	391
AHA12	28.12	17.81	36.66	XH	160.00	70.00	388
AHA13	27.04	16.94	37.35	XH	160.00	70.00	402
AHA14	27.00	17.33	35.81	XH	160.00	70.00	384
AHA15	26.64	17.20	35.43	XH	160.00	70.00	384
AHA16	27.74	17.25	37.81	XH	160.00	70.00	405
AHA17	30.14	16.91	43.89	XH	160.00	70.00	369

phy-path: between physiology and pathology, phy-pac: between physiology and pacing, Opt: optimal, elec: electrodes, Nr. of sim: number of simulations.

Table 8.14. Results of the first optimization method for Patient-3 with 80 % conduction velocity.

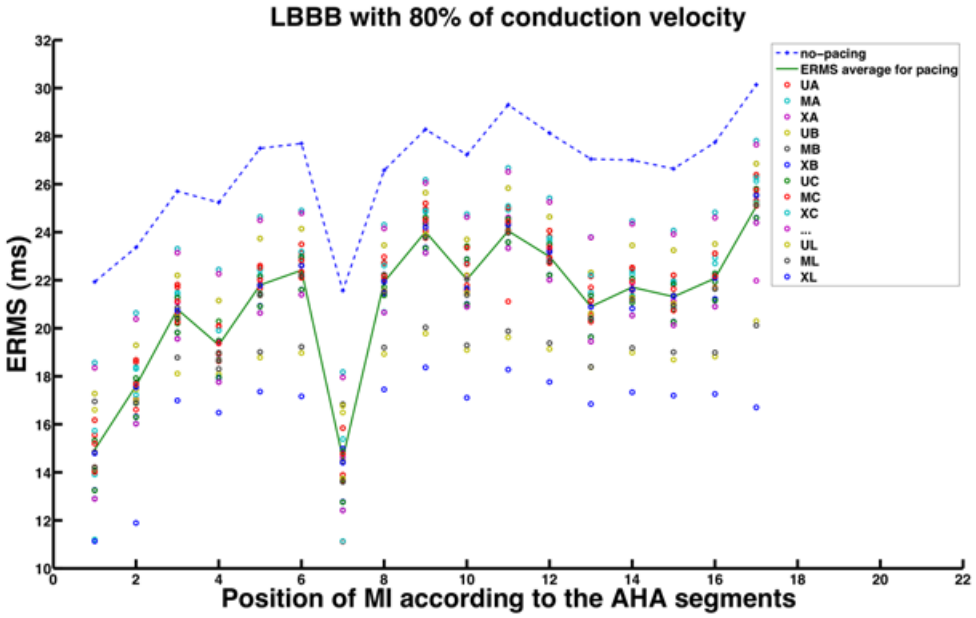

Figure 8.17. The minimal E_{RMS} achieved by the first optimization method versus AHA segments 1 to 17 corresponding to the 17 different infarction positions. (Each circular point is related to one pair of electrodes. The average of optimal electrode setups is demonstrated with a green line while the blue line shows the E_{RMS} pathology without pacing.)

Infarction position	E_{RMS} (phy-path) ms	E_{RMS} (phy-pac) ms	% E_{RMS} reduction	Opt. elec positions	Opt. A-V ms	Opt. V-V ms	Nr. of sim.
AHA1	28.36	11.04	61.07	XH	130.00	52.15	554
AHA2	29.05	12.06	58.48	XH	140.00	59.14	523
AHA3	30.86	13.55	56.09	XH	140.00	59.14	501
AHA4	30.98	12.37	60.07	XH	130.00	55.27	526
AHA5	32.92	17.23	47.66	XH	140.00	59.14	503
AHA6	32.97	17.35	47.37	XH	140.00	59.14	503
AHA7	27.96	11.80	57.79	XH	130.00	52.15	548
AHA8	31.40	17.29	44.93	MH	125.00	51.00	514
AHA9	32.90	17.84	45.77	MH	120.00	49.84	505
AHA10	32.58	17.47	46.37	XH	130.00	55.27	500
AHA11	34.43	17.84	48.18	XH	140.00	59.14	493
AHA12	33.28	17.54	47.29	XH	140.00	59.14	505
AHA13	32.73	13.37	59.15	MH	130.00	53.71	519
AHA14	32.18	17.68	45.33	XH	140.00	59.14	496
AHA15	32.10	17.59	45.20	XH	120.00	49.84	505
AHA16	33.21	17.45	47.45	XH	140.00	59.14	502
AHA17	35.02	17.53	49.94	XH	140.00	59.14	469

phy-path: between physiology and pathology, phy-pac: between physiology and pacing, Opt: optimal, elec: electrodes, Nr. of sim: number of simulations.

Table 8.15. Results of the first optimization method for Patient-3 with 60 % conduction velocity.

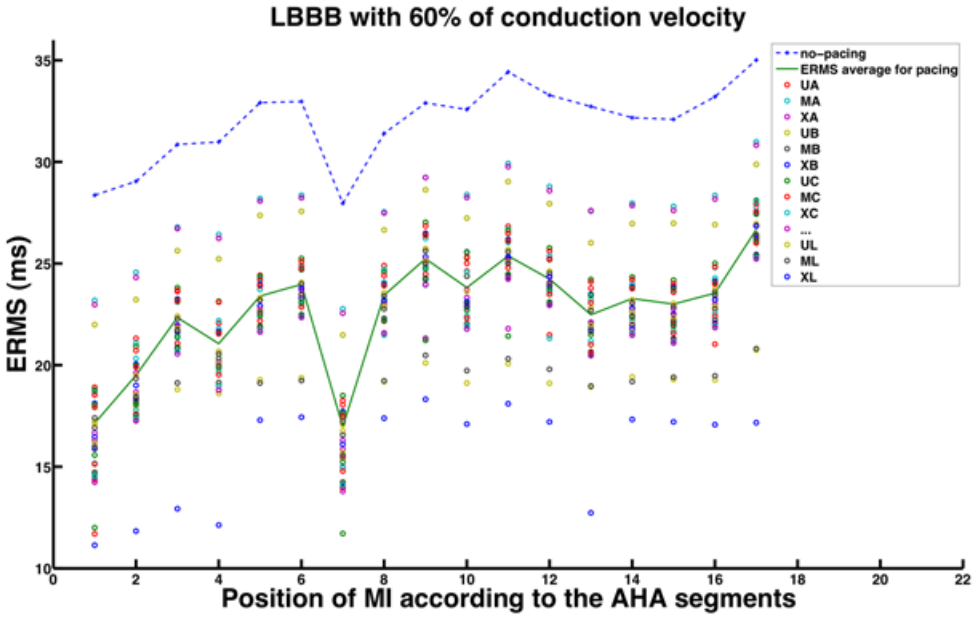

Figure 8.18. The minimal E_{RMS} achieved by the first optimization method versus AHA segments 1 to 17 corresponding to the 17 different infarction positions. (Each circular point is related to one pair of electrodes. The average of optimal electrode setups is demonstrated with a green line while the blue line shows the E_{RMS} pathology without pacing.)

Infarction position	$Error_{QRS}$ (phy-path) ms	$Error_{QRS}$ (phy-pac) ms	% $Error_{QRS}$ reduction	Opt. elec positions	Opt. A-V ms	Opt. V-V ms	Nr. of sim.
AHA1	93	10	89.24	XG	160.00	70.00	437
AHA2	108	22	79.62	XG	160.00	70.00	463
AHA3	106	12	88.67	XH	160.00	70.00	393
AHA4	100	30	70.00	XG	160.00	70.00	448
AHA5	91	28	69.23	XG	160.00	70.00	431
AHA6	92	10	72.82	XG	160.00	70.00	483
AHA7	90	10	88.88	XG	160.00	70.00	439
AHA8	104	20	80.76	XH	160.00	70.00	489
AHA9	107	12	88.78	XH	160.00	70.00	401
AHA10	90	30	66.66	XG	160.00	70.00	441
AHA11	92	25	72.82	XG	160.00	70.00	465
AHA12	98	20	79.59	XG	160.00	70.00	488
AHA13	93	22	76.34	XG	160.00	70.00	473
AHA14	97	22	77.31	XH	160.00	70.00	426
AHA15	98	24	77.51	XG	160.00	70.00	409
AHA16	99	22	77.77	XH	160.00	70.00	456
AHA17	100	22	78.00	XG	160.00	70.00	436

phy-path: between physiology and pathology, phy-pac: between physiology and pacing, Opt: optimal, elec: electrodes, Nr. of sim: number of simulations.

Table 8.16. Results of the second optimization method for Patient-3 with 100 % conduction velocity.

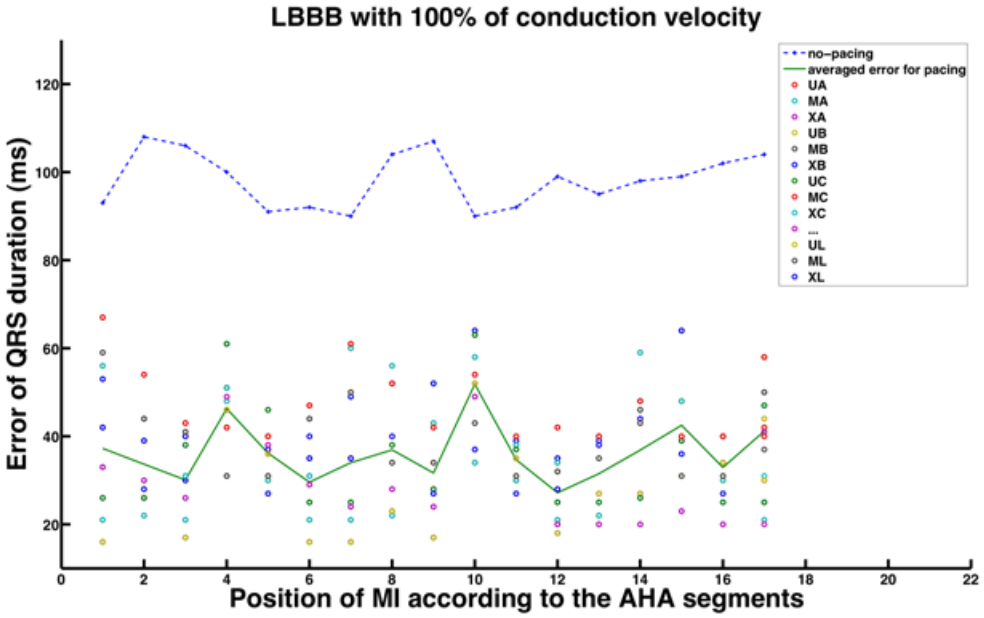

Figure 8.19. The minimal $Error_{QRS}$ achieved by the second optimization method versus AHA segments 1 to 17 corresponding to the 17 different infarction positions. (Each circular point is related to one pair of electrodes. The average of optimal electrode setups is demonstrated with a green line while the blue line shows the $Error_{QRS}$ pathology without pacing.)

Infarction position	$Error_{QRS}$ (phy-path) ms	$Error_{QRS}$ (phy-pac) ms	% $Error_{QRS}$ reduction	Opt. elec positions	Opt. A-V ms	Opt. V-V ms	Nr. of sim.
AHA1	127	35	72.44	XH	160.00	70.00	457
AHA2	145	45	68.96	XH	160.00	70.00	454
AHA3	143	38	73.42	XH	160.00	70.00	377
AHA4	130	55	57.69	XH	160.00	70.00	440
AHA5	121	50	58.67	XH	160.00	70.00	449
AHA6	126	35	72.22	XH	160.00	70.00	463
AHA7	121	35	71.07	XH	160.00	70.00	451
AHA8	141	45	68.08	XH	160.00	70.00	459
AHA9	146	45	69.17	XH	160.00	70.00	344
AHA10	123	65	47.15	XH	160.00	70.00	432
AHA11	121	49	59.50	XH	160.00	70.00	459
AHA12	121	40	66.94	XH	160.00	70.00	470
AHA13	121	42	65.28	XH	160.00	70.00	454
AHA14	121	42	65.28	XH	160.00	70.00	435
AHA15	122	47	61.47	XH	160.00	70.00	458
AHA16	122	42	65.57	XH	160.00	70.00	483
AHA17	121	43	64.46	XH	160.00	70.00	421

phy-path: between physiology and pathology, phy-pac: between physiology and pacing, Opt: optimal, elec: electrodes, Nr. of sim: number of simulations.

Table 8.17. Results of the second optimization method for Patient-3 with 80 % conduction velocity.

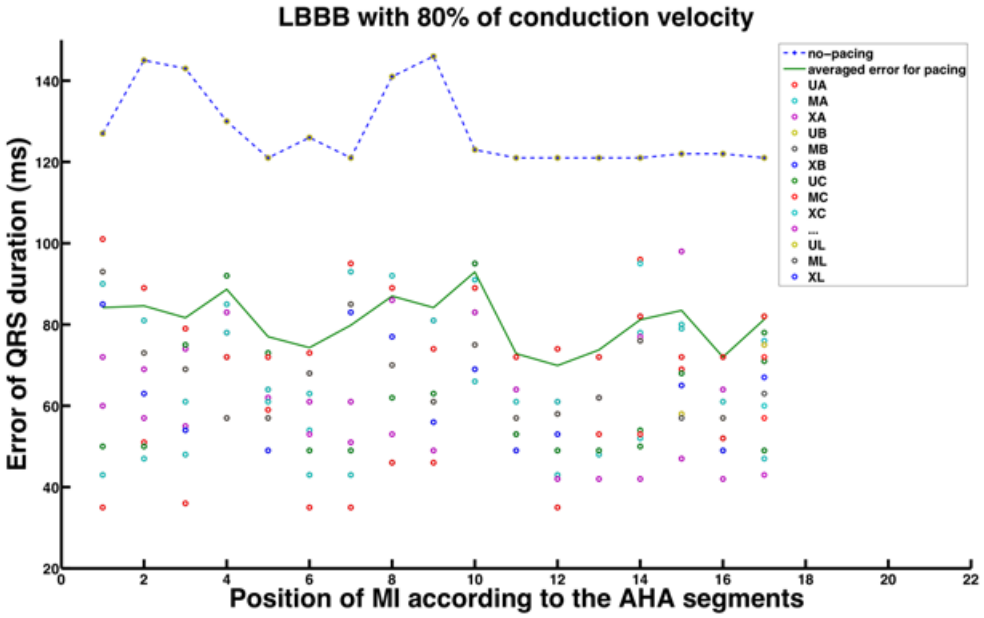

Figure 8.20. The minimal $Error_{QRS}$ achieved by the second optimization method versus AHA segments 1 to 17 corresponding to the 17 different infarction positions. (Each circular point is related to one pair of electrodes. The average of optimal electrode setups is demonstrated with a green line while the blue line shows the $Error_{QRS}$ pathology without pacing.)

Infarction position	$Error_{QRS}$ (phy-path) ms	$Error_{QRS}$ (phy-pac) ms	% $Error_{QRS}$ reduction	Opt. elec positions	Opt. A-V ms	Opt. V-V ms	Nr. of sim.
AHA1	183	70	61.74	XH	160.00	70.00	363
AHA2	205	90	56.09	XH	160.00	70.00	342
AHA3	201	85	57.71	XH	160.00	70.00	323
AHA4	182	100	45.05	XH	160.00	70.00	343
AHA5	173	90	47.97	XH	160.00	70.00	365
AHA6	179	70	60.89	XH	160.00	70.00	389
AHA7	172	70	59.30	XH	160.00	70.00	350
AHA8	199	90	54.77	XH	160.00	70.00	349
AHA9	208	95	54.32	XH	160.00	70.00	307
AHA10	176	125	28.97	XH	160.00	70.00	380
AHA11	175	78	55.42	XH	160.00	70.00	413
AHA12	174	75	53.44	XH	160.00	70.00	394
AHA13	175	81	53.71	XH	160.00	70.00	408
AHA14	174	81	53.44	XH	160.00	70.00	389
AHA15	175	85	51.42	XH	160.00	70.00	372
AHA16	176	79	55.11	XH	160.00	70.00	410
AHA17	175	84	52.00	XH	160.00	70.00	355

phy-path: between physiology and pathology, phy-pac: between physiology and pacing, Opt: optimal, elec: electrodes, Nr. of sim: number of simulations.

Table 8.18. Results of the second optimization method for Patient-3 with 60 % conduction velocity.

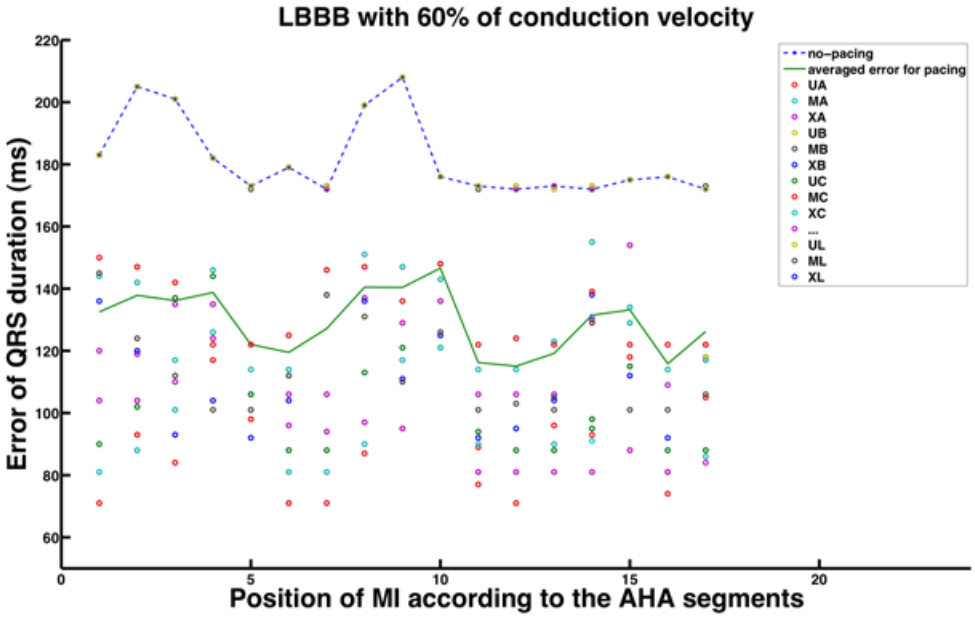

Figure 8.21. The minimal $Error_{QRS}$ achieved by the second optimization method versus AHA segments 1 to 17 corresponding to the 17 different infarction positions. (Each circular point is related to one pair of electrodes. The average of optimal electrode setups is demonstrated with a green line while the blue line shows the $Error_{QRS}$ pathology without pacing.)

8.1.4 Patient-4

The electrode positioning setup is demonstrated in figure 8.22. The results of both optimization methods are summarized in tables 8.19 - 8.24 for the several conduction velocities. The minimal errors associated with each electrode setup for each MI position are illustrated in figures 8.23 - 8.28.

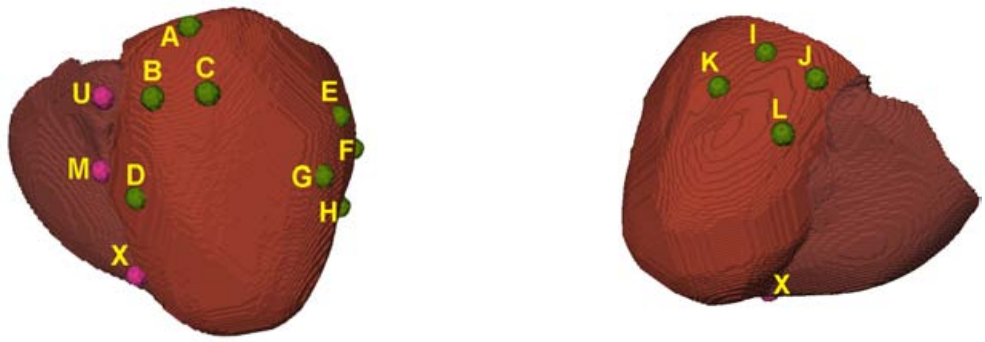

(a) (b)

Figure 8.22. The electrode positions chosen for the Patient-4 heart model. The electrodes A, B, C and D are referred to the anterior branches of coronary sinus. The electrodes I, J, K and L are referred to the posterior branches of coronary sinus. The electrodes E, F, G and H are located on the left ventricular free wall. The electrodes U, M and X are located at the right ventricular upper septum, middle septum and apex respectively.

Both optimization methods mostly found the optimal left electrode position in the lateral wall of the left ventricle (electrode G, H and rarely F). The optimal right electrode position is mostly in upper or middle septal area (electrode U and M). The best timing delays range assessed by the first optimization method is $110 - 160\ ms$ for the A-V delay and $46.72 - 70\ ms$ for V-V delay. The best timing delays range mostly achieved by the second optimization is overall 160 ms for the A-V delay and 70 ms for V-V delay.

DSA optimization delivers a number between 313 to 551 simulations for each pathological case. A maximum improvement of up to 36 %, the reduction percentage of E_{RMS} and an improvement of up to 76 %, the reduction percentage of $Error_{QRS}$, can be reached.

Infarction position	E_{RMS} (phy-path) ms	E_{RMS} (phy-pac) ms	% E_{RMS} reduction	Opt. elec positions	Opt. A-V ms	Opt. V-V ms	Nr. of sim.
AHA1	24.26	20.62	15.02	UG	160.00	70.00	395
AHA2	25.61	21.63	15.54	UG	160.00	70.00	408
AHA3	25.33	21.64	14.57	UG	160.00	70.00	395
AHA4	24.82	21.67	12.69	UG	160.00	70.00	398
AHA5	26.71	23.29	12.79	UG	160.00	70.00	371
AHA6	27.90	24.37	12.64	UG	160.00	70.00	385
AHA7	25.52	22.09	13.46	UG	160.00	70.00	388
AHA8	28.54	25.12	11.98	UG	160.00	70.00	413
AHA9	28.08	24.89	11.38	UG	160.00	70.00	383
AHA10	28.53	25.99	8.92	UH	160.00	70.00	371
AHA11	29.65	26.75	9.80	UG	160.00	70.00	370
AHA12	30.01	26.94	10.22	UG	160.00	70.00	367
AHA13	29.24	26.07	10.85	UH	160.00	70.00	376
AHA14	26.73	22.67	15.19	UG	160.00	70.00	398
AHA15	29.26	26.45	9.60	UH	160.00	70.00	375
AHA16	29.51	26.44	10.41	UG	160.00	70.00	392
AHA17	31.15	27.99	10.14	UG	160.00	70.00	386

phy-path: between physiology and pathology, phy-pac: between physiology and pacing, Opt: optimal, elec: electrodes, Nr. of sim: number of simulations.

Table 8.19. Results of the first optimization method for Patient-4 with 100 % conduction velocity.

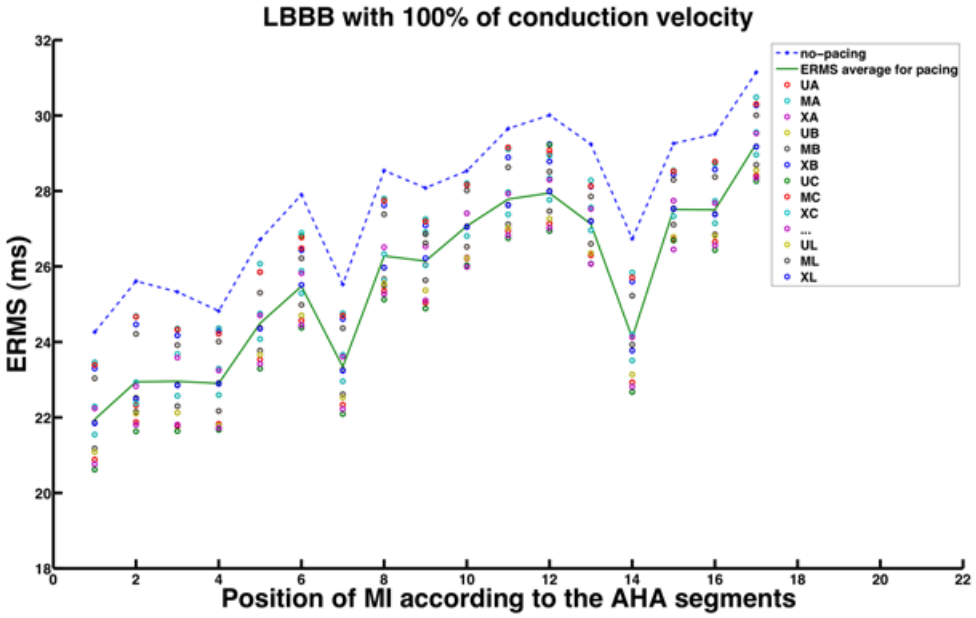

Figure 8.23. The minimal E_{RMS} achieved by the first optimization method versus AHA segments 1 to 17 corresponding to the 17 different infarction positions. (Each circular point is related to one pair of electrodes. The average of optimal electrode setups is demonstrated with a green line while the blue line shows the E_{RMS} pathology without pacing.)

Infarction position	E_{RMS} (phy-path) ms	E_{RMS} (phy-pac) ms	% E_{RMS} reduction	Opt. elec positions	Opt. A-V ms	Opt. V-V ms	Nr. of sim.
AHA1	28.31	21.36	24.56	UH	150.00	66.13	407
AHA2	29.89	22.56	24.52	UH	160.00	70.00	416
AHA3	29.34	22.39	23.70	UH	150.00	66.13	414
AHA4	28.57	22.41	21.57	UH	160.00	70.00	427
AHA5	30.52	23.96	21.50	UH	150.00	66.13	424
AHA6	31.82	25.12	21.08	UH	160.00	70.00	419
AHA7	29.40	22.78	22.51	UH	150.00	66.13	406
AHA8	32.27	25.89	19.78	UH	160.00	70.00	414
AHA9	31.62	25.68	18.78	UG	130.00	55.27	408
AHA10	31.73	26.81	15.52	UF	120.00	46.72	384
AHA11	33.07	27.42	17.09	UH	160.00	70.00	414
AHA12	33.56	27.59	17.79	UH	160.00	70.00	418
AHA13	32.94	26.68	19.02	UH	160.00	70.00	419
AHA14	30.80	23.47	23.81	UH	160.00	70.00	415
AHA15	32.61	27.41	15.93	MH	120.00	49.84	359
AHA16	33.01	26.60	19.41	UH	160.00	70.00	388
AHA17	34.42	28.82	16.27	UH	160.00	70.00	383

phy-path: between physiology and pathology, phy-pac: between physiology and pacing, Opt: optimal, elec: electrodes, Nr. of sim: number of simulations.

Table 8.20. Results of the first optimization method for Patient-4 with 80 % conduction velocity.

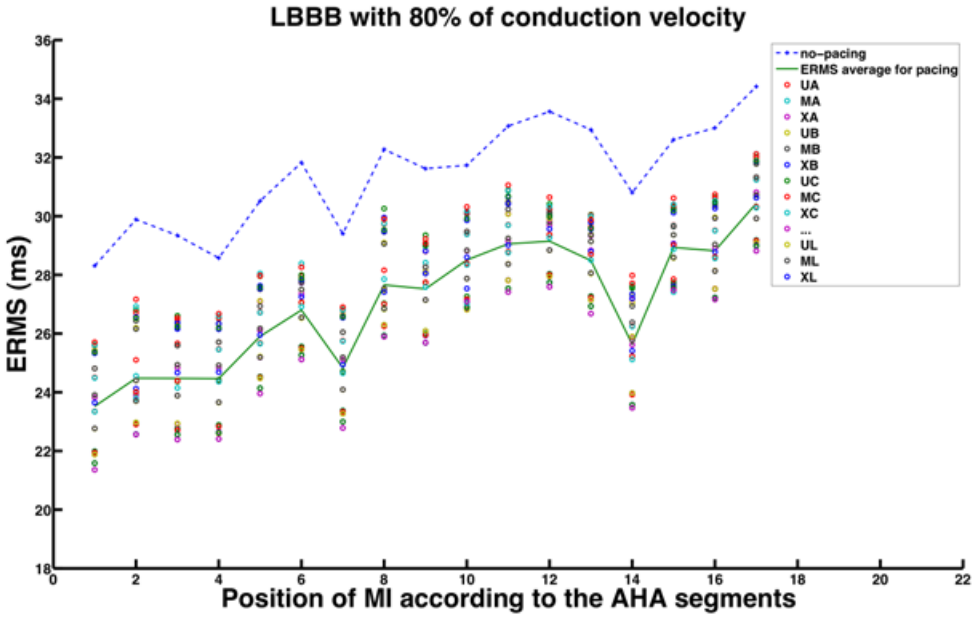

Figure 8.24. The minimal E_{RMS} achieved by the first optimization method versus AHA segments 1 to 17 corresponding to the 17 different infarction positions. (Each circular point is related to one pair of electrodes. The average of optimal electrode setups is demonstrated with a green line while the blue line shows the E_{RMS} pathology without pacing.)

Infarction position	E_{RMS} (phy-path) ms	E_{RMS} (phy-pac) ms	% E_{RMS} reduction	Opt. elec positions	Opt. A-V ms	Opt. V-V ms	Nr. of sim.
AHA1	36.08	22.91	36.49	MH	120.00	46.72	550
AHA2	38.12	24.03	36.96	MH	120.00	46.72	540
AHA3	37.11	23.89	35.61	MH	120.00	46.72	555
AHA4	35.90	23.81	33.67	MH	120.00	46.72	551
AHA5	37.97	25.36	33.19	MH	120.00	46.72	529
AHA6	39.44	26.43	32.99	MH	120.00	46.72	521
AHA7	36.94	24.25	34.36	MH	120.00	46.72	539
AHA8	39.65	27.19	31.44	MH	120.00	46.72	523
AHA9	38.65	26.97	30.21	UH	120.00	46.72	522
AHA10	38.23	27.95	26.89	MH	110.00	42.85	524
AHA11	39.94	28.69	28.19	MH	120.00	46.72	509
AHA12	40.71	28.81	29.23	MH	120.00	46.72	521
AHA13	40.25	27.90	30.68	MH	120.00	46.72	508
AHA14	38.58	24.80	35.72	UH	120.00	46.72	531
AHA15	39.36	28.27	28.19	MH	110.00	42.85	545
AHA16	40.03	28.54	28.71	MH	120.00	46.72	481
AHA17	41.09	29.98	27.04	MH	120.00	46.72	506

phy-path: between physiology and pathology, phy-pac: between physiology and pacing, Opt: optimal, elec: electrodes, Nr. of sim: number of simulations.

Table 8.21. Results of the first optimization method for Patient-4 with 60 % conduction velocity.

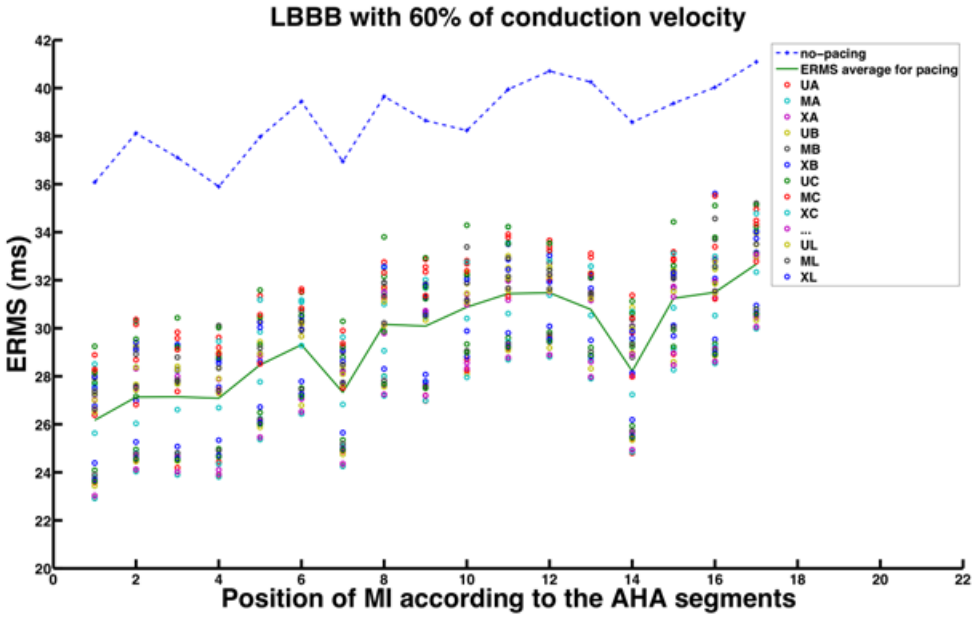

Figure 8.25. The minimal E_{RMS} achieved by the first optimization method versus AHA segments 1 to 17 corresponding to the 17 different infarction positions. (Each circular point is related to one pair of electrodes. The average of optimal electrode setups is demonstrated with a green line while the blue line shows the E_{RMS} pathology without pacing.)

Infarction position	$Error_{QRS}$ (phy-path) ms	$Error_{QRS}$ (phy-pac) ms	% $Error_{QRS}$ reduction	Opt. elec positions	Opt. A-V ms	Opt. V-V ms	Nr. of sim.
AHA1	81	30	62.95	UG	160.00	70.00	530
AHA2	88	29	67.04	UG	160.00	70.00	541
AHA3	88	28	68.18	UG	160.00	70.00	491
AHA4	107	25	76.63	UG	160.00	70.00	502
AHA5	100	40	60.00	UG	160.00	70.00	415
AHA6	90	38	57.71	UG	160.00	70.00	465
AHA7	81	30	62.96	UG	160.00	70.00	524
AHA8	81	25	69.13	UG	160.00	70.00	495
AHA9	86	31	63.95	UG	160.00	70.00	484
AHA10	104	32	69.23	UH	160.00	70.00	453
AHA11	93	42	54.83	UG	160.00	70.00	388
AHA12	81	40	50.61	UG	160.00	70.00	493
AHA13	81	38	53.08	UH	160.00	70.00	528
AHA14	81	30	62.96	UG	160.00	70.00	513
AHA15	88	35	60.22	UH	160.00	70.00	538
AHA16	87	42	51.72	UG	160.00	70.00	464
AHA17	80	32	60.00	UG	160.00	70.00	514

phy-path: between physiology and pathology, phy-pac: between physiology and pacing, Opt: optimal, elec: electrodes, Nr. of sim: number of simulations.

Table 8.22. Results of the second optimization method for Patient-4 with 100 % conduction velocity.

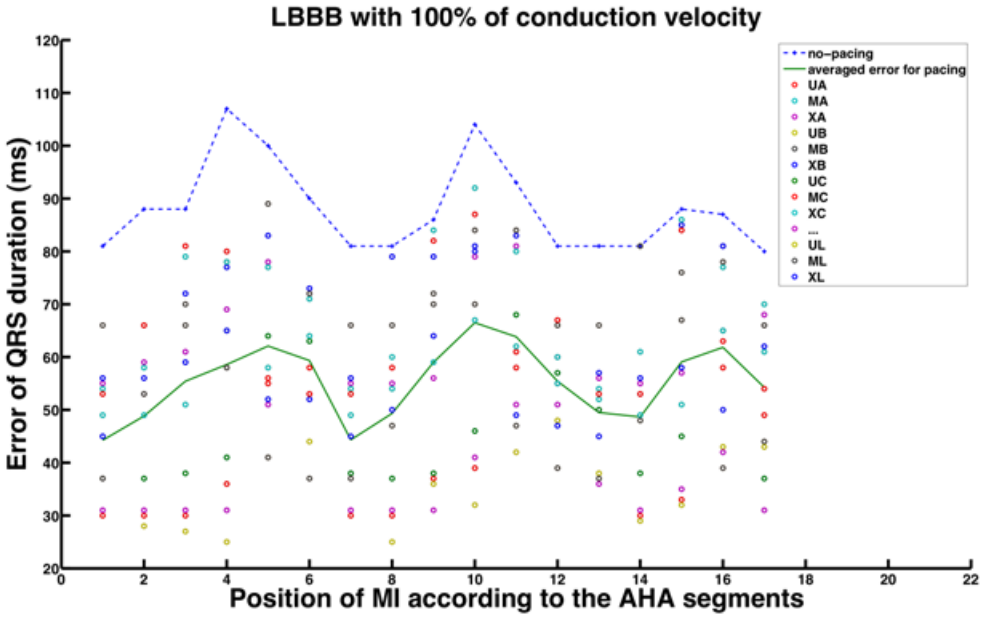

Figure 8.26. The minimal $Error_{QRS}$ achieved by the second optimization method versus AHA segments 1 to 17 corresponding to the 17 different infarction positions. (Each circular point is related to one pair of electrodes. The average of optimal electrode setups is demonstrated with a green line while the blue line shows the $Error_{QRS}$ pathology without pacing.)

Infarction position	$Error_{QRS}$ (phy-path) ms	$Error_{QRS}$ (phy-pac) ms	% $Error_{QRS}$ reduction	Opt. elec positions	Opt. A-V ms	Opt. V-V ms	Nr. of sim.
AHA1	112	42	62.50	UH	160.00	70.00	450
AHA2	124	58	53.22	UH	160.00	70.00	460
AHA3	123	57	53.65	UH	160.00	70.00	400
AHA4	148	56	62.16	UH	160.00	70.00	423
AHA5	137	78	43.06	UH	160.00	70.00	388
AHA6	125	75	40.00	UH	160.00	70.00	413
AHA7	112	40	64.28	UH	160.00	70.00	452
AHA8	112	50	55.35	UH	160.00	70.00	452
AHA9	124	60	51.61	UH	160.00	70.00	381
AHA10	144	58	59.72	UH	160.00	70.00	386
AHA11	131	75	42.74	UH	160.00	70.00	366
AHA12	115	73	36.52	UH	160.00	70.00	398
AHA13	112	65	41.96	UH	160.00	70.00	441
AHA14	112	60	46.42	UH	160.00	70.00	454
AHA15	128	62	51.56	UH	160.00	70.00	380
AHA16	125	76	39.20	UH	160.00	70.00	398
AHA17	112	60	46.42	UH	160.00	70.00	402

phy-path: between physiology and pathology, phy-pac: between physiology and pacing, Opt: optimal, elec: electrodes, Nr. of sim: number of simulations.

Table 8.23. Results of the second optimization method for Patient-4 with 80 % conduction velocity.

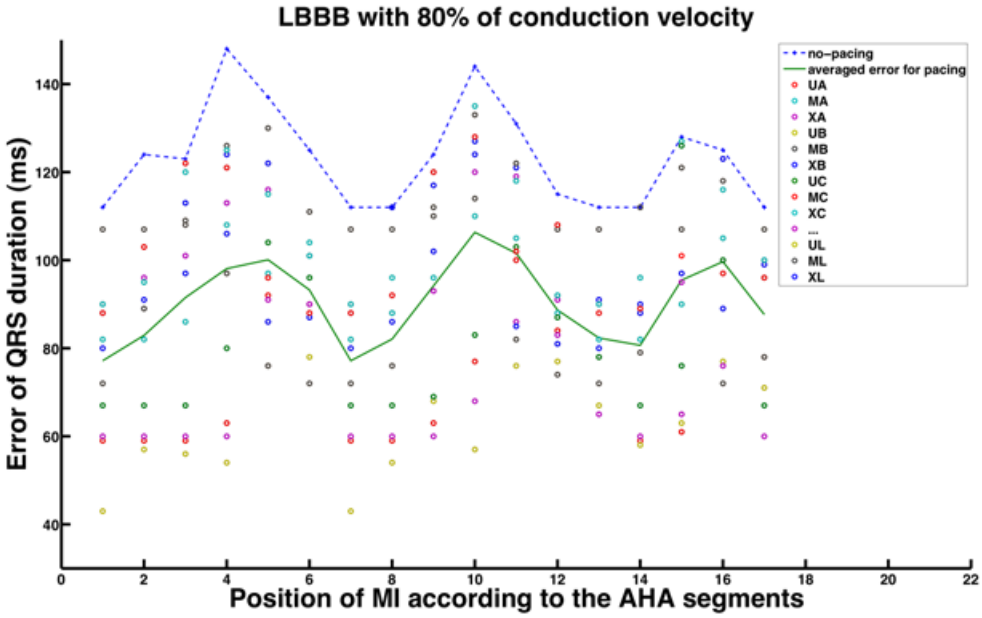

Figure 8.27. The minimal $Error_{QRS}$ achieved by the second optimization method versus AHA segments 1 to 17 corresponding to the 17 different infarction positions. (Each circular point is related to one pair of electrodes. The average of optimal electrode setups is demonstrated with a green line while the blue line shows the $Error_{QRS}$ pathology without pacing.)

Infarction position	$Error_{QRS}$ (phy-path) ms	$Error_{QRS}$ (phy-pac) ms	% $Error_{QRS}$ reduction	Opt. elec positions	Opt. A-V ms	Opt. V-V ms	Nr. of sim.
AHA1	166	90	45.78	UH	160.00	70.00	429
AHA2	183	100	45.35	UH	160.00	70.00	452
AHA3	185	100	45.94	UH	160.00	70.00	387
AHA4	215	98	54.41	UH	160.00	70.00	334
AHA5	198	128	35.35	UH	160.00	70.00	361
AHA6	185	125	48.00	UH	160.00	70.00	433
AHA7	166	89	46.38	UH	160.00	70.00	418
AHA8	166	100	66.00	UH	160.00	70.00	435
AHA9	184	108	41.30	UH	160.00	70.00	348
AHA10	212	110	48.11	UH	160.00	70.00	313
AHA11	194	137	29.38	UH	160.00	70.00	365
AHA12	170	129	24.12	UH	160.00	70.00	396
AHA13	168	113	32.74	UH	160.00	70.00	444
AHA14	166	103	37.95	UH	160.00	70.00	424
AHA15	195	106	45.64	UF	160.00	70.00	385
AHA16	188	131	30.32	UH	160.00	70.00	370
AHA17	166	108	34.94	UH	160.00	70.00	409

phy-path: between physiology and pathology, phy-pac: between physiology and pacing, Opt: optimal, elec: electrodes, Nr. of sim: number of simulations.

Table 8.24. Results of the second optimization method for Patient-4 with 60 % conduction velocity.

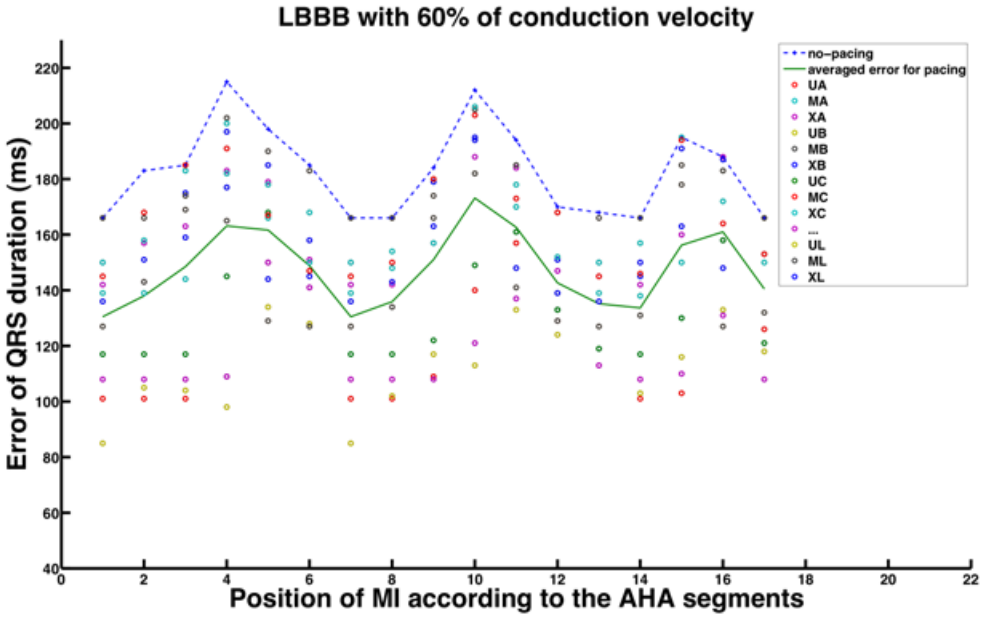

Figure 8.28. The minimal $Error_{QRS}$ achieved by the second optimization method versus AHA segments 1 to 17 corresponding to the 17 different infarction positions. (Each circular point is related to one pair of electrodes. The average of optimal electrode setups is demonstrated with a green line while the blue line shows the $Error_{QRS}$ pathology without pacing.)

8.1.5 Patient-5

The electrode positioning setup is demonstrated in figure 8.29. The results of both optimization methods, specific to several conduction velocities are summarized in tables 8.25 - 8.30. The minimal errors associated with each electrode setup for each MI position are illustrated in figures 8.30 - 8.35.

(a) (b)

Figure 8.29. The electrode positions chosen for the Patient-5 heart model. The electrodes A, B, C and D are referred to the anterior branches of coronary sinus. The electrodes I, J, K and L are referred to the posterior branches of coronary sinus. The electrodes E, F, G and H are located on the left ventricular free wall. The electrodes U, M and X are located at the right ventricular upper septum, middle septum and apex respectively.

Both optimization methods found the optimal left electrode position in the lateral wall of the left ventricle (electrode E). The optimal right electrode position is mostly in upper septal area or in the RV apex (electrode U and X). The best timing delays range evaluated by the first optimization method is $120 - 160\ ms$ for the A-V delay and $46.72 - 70\ ms$ for V-V delay. The best timing delays range achieved by the second optimization is overall $160\ ms$ for the A-V delay and $70\ ms$ for V-V delay. It is noticeable that the all resulted parameters from second optimization method are the same, independent of conduction velocities and MI locations.

DSA optimization delivers a number between 250 to 565 simulations for each pathological case. A maximum improvement of up to 39 %, the reduction percentage of E_{RMS} and an improvement of up to 96 %, the reduction percentage of $Error_{QRS}$, can be reached.

Infarction position	E_{RMS} (phy-path) ms	E_{RMS} (phy-pac) ms	% E_{RMS} reduction	Opt. elec positions	Opt. A-V ms	Opt. V-V ms	Nr. of sim.
AHA1	26.60	20.38	23.37	UE	160.00	70.00	440
AHA2	25.68	19.68	23.35	UE	160.00	70.00	436
AHA3	25.21	19.47	22.78	XE	140.00	60.70	414
AHA4	25.47	20.34	20.13	ME	140.00	60.70	427
AHA5	24.79	18.20	26.57	UE	160.00	70.00	421
AHA6	23.59	17.03	27.81	UE	160.00	70.00	436
AHA7	29.79	23.51	21.07	UE	140.00	60.70	454
AHA8	29.26	23.66	19.14	UE	160.00	70.00	392
AHA9	26.73	21.73	18.73	ME	120.00	49.84	454
AHA10	31.10	27.09	12.88	UE	150.00	64.57	418
AHA11	29.52	24.05	18.52	UE	160.00	70.00	400
AHA12	28.61	22.88	20.00	ME	140.00	60.70	477
AHA13	27.99	22.60	19.27	UE	160.00	70.00	456
AHA14	29.12	23.43	19.54	UE	160.00	70.00	443
AHA15	31.34	27.06	13.66	ME	140.00	57.58	414
AHA16	30.05	25.10	16.46	UE	160.00	70.00	446
AHA17	33.18	28.53	14.01	UE	160.00	70.00	427

phy-path: between physiology and pathology, phy-pac: between physiology and pacing, Opt: optimal, elec: electrodes, Nr. of sim: number of simulations.

Table 8.25. Results of the first optimization method for Patient-5 with 100 % conduction velocity.

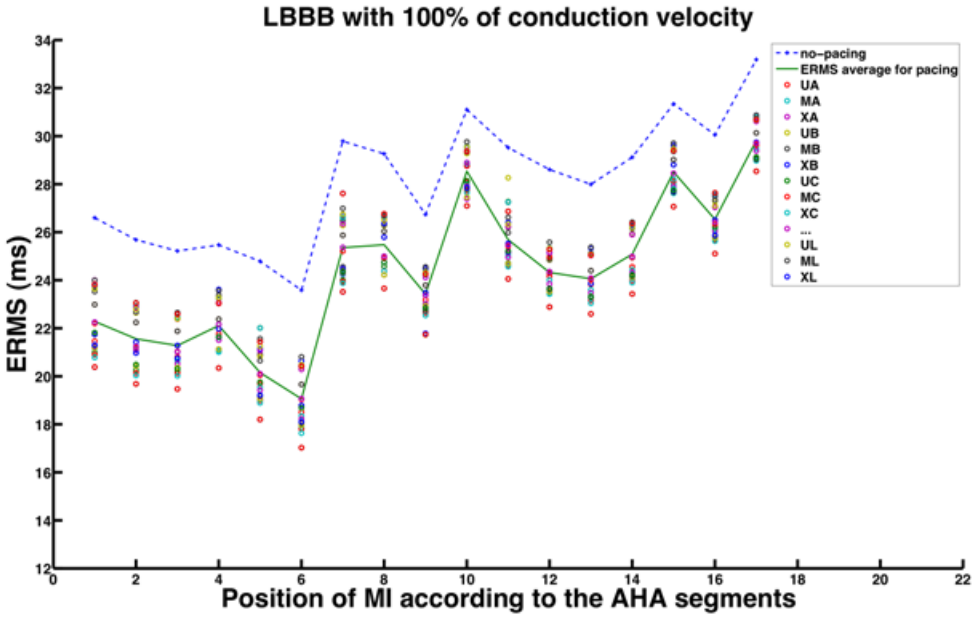

Figure 8.30. The minimal E_{RMS} achieved by the first optimization method versus AHA segments 1 to 17 corresponding to the 17 different infarction positions. (Each circular point is related to one pair of electrodes. The average of optimal electrode setups is demonstrated with a green line while the blue line shows the E_{RMS} pathology without pacing.)

Infarction position	E_{RMS} (phy-path) ms	E_{RMS} (phy-pac) ms	% E_{RMS} reduction	Opt. elec positions	Opt. A-V ms	Opt. V-V ms	Nr. of sim.
AHA1	20.51	16.34	20.33	UE	160.00	70.00	381
AHA2	20.93	17.31	17.29	UE	160.00	70.00	383
AHA3	21.14	17.65	16.50	UE	160.00	70.00	395
AHA4	20.57	16.50	19.78	UE	160.00	70.00	384
AHA5	20.32	16.29	19.83	UE	160.00	70.00	402
AHA6	21.01	17.15	18.37	UE	160.00	70.00	387
AHA7	22.63	18.67	17.49	UE	160.00	70.00	360
AHA8	21.94	18.28	16.68	UE	160.00	70.00	384
AHA9	21.02	17.20	18.01	UE	140.00	57.58	386
AHA10	22.80	18.64	18.24	UE	160.00	70.00	330
AHA11	22.98	19.47	15.27	UE	160.00	70.00	422
AHA12	24.15	20.72	14.20	UE	160.00	70.00	383
AHA13	22.85	18.60	18.59	UE	160.00	70.00	391
AHA14	21.86	18.29	16.33	UE	160.00	70.00	382
AHA15	18.14	13.23	28.50	UE	160.00	70.00	322
AHA16	18.31	13.52	26.16	UE	160.00	70.00	374
AHA17	21.29	17.46	17.98	UE	160.00	70.00	364

phy-path: between physiology and pathology, phy-pac: between physiology and pacing, Opt: optimal, elec: electrodes, Nr. of sim: number of simulations.

Table 8.26. Results of the first optimization method for Patient-5 with 80 % conduction velocity.

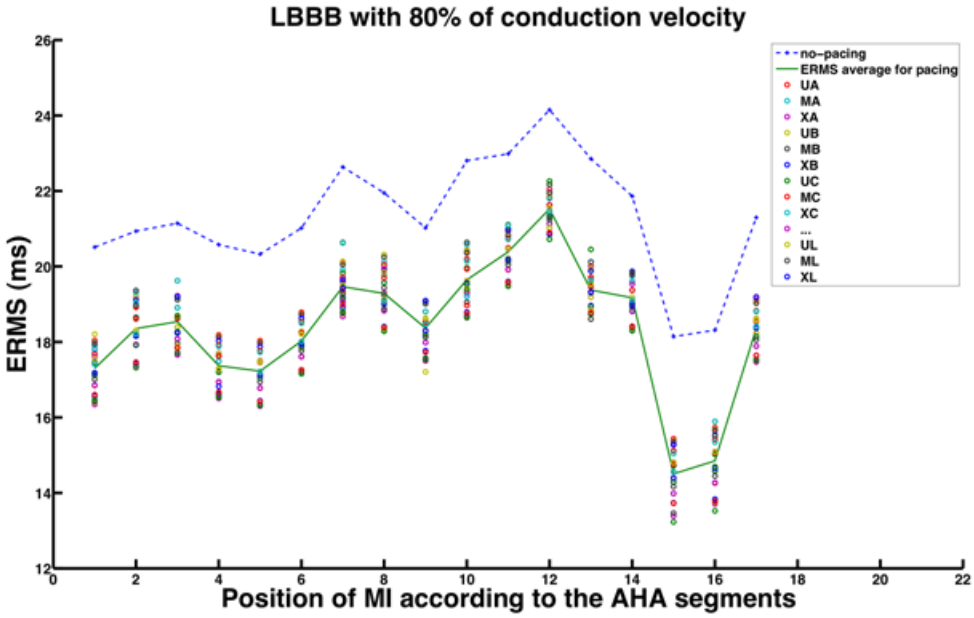

Figure 8.31. The minimal E_{RMS} achieved by the first optimization method versus AHA segments 1 to 17 corresponding to the 17 different infarction positions. (Each circular point is related to one pair of electrodes. The average of optimal electrode setups is demonstrated with a green line while the blue line shows the E_{RMS} pathology without pacing.)

Infarction position	E_{RMS} (phy-path) ms	E_{RMS} (phy-pac) ms	% E_{RMS} reduction	Opt. elec positions	Opt. A-V ms	Opt. V-V ms	Nr. of sim.
AHA1	31.94	20.87	34.67	XE	120.00	49.84	534
AHA2	30.91	20.19	34.67	XE	120.00	49.84	525
AHA3	30.26	19.94	34.12	XE	120.00	49.84	508
AHA4	30.05	20.80	30.79	XE	120.00	49.84	542
AHA5	30.26	18.74	38.06	XE	120.00	49.84	554
AHA6	28.92	17.57	39.27	XE	120.00	46.72	565
AHA7	34.87	23.91	31.44	XE	120.00	46.72	489
AHA8	34.10	24.08	29.39	XE	120.00	49.84	505
AHA9	31.28	22.93	26.68	UE	100.00	38.98	526
AHA10	34.83	27.53	20.95	XE	120.00	49.84	509
AHA11	34.31	24.48	28.66	XE	120.00	49.84	500
AHA12	33.80	23.31	31.03	XE	120.00	46.72	497
AHA13	32.78	22.98	29.88	XE	120.00	46.72	520
AHA14	33.92	23.81	29.81	XE	120.00	49.84	503
AHA15	35.22	27.42	22.15	XE	120.00	46.72	497
AHA16	34.47	25.51	26.00	XE	125.00	51.00	470
AHA17	37.46	28.87	22.94	XE	120.00	46.72	485

phy-path: between physiology and pathology, phy-pac: between physiology and pacing, Opt: optimal, elec: electrodes, Nr. of sim: number of simulations.

Table 8.27. Results of the first optimization method for Patient-5 with 60 % conduction velocity.

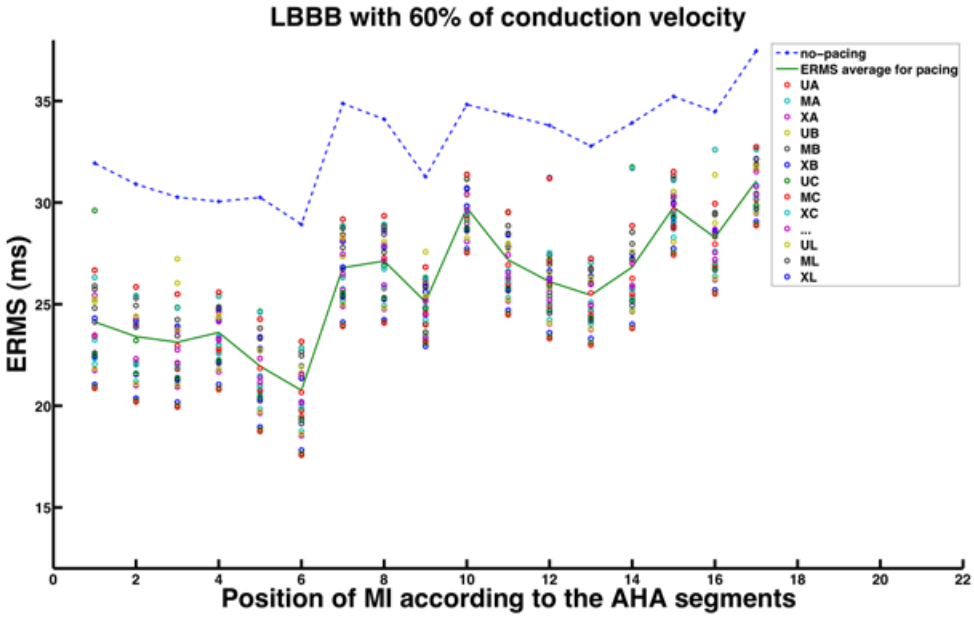

Figure 8.32. The minimal E_{RMS} achieved by the first optimization method versus AHA segments 1 to 17 corresponding to the 17 different infarction positions. (Each circular point is related to one pair of electrodes. The average of optimal electrode setups is demonstrated with a green line while the blue line shows the E_{RMS} pathology without pacing.)

Infarction position	$Error_{QRS}$ (phy-path) ms	$Error_{QRS}$ (phy-pac) ms	% $Error_{QRS}$ reduction	Opt. elec positions	Opt. A-V ms	Opt. V-V ms	Nr. of sim.
AHA1	61	2	96.72	UE	160.00	70.00	549
AHA2	61	11	81.97	UE	160.00	70.00	487
AHA3	81	9	88.89	UE	160.00	70.00	460
AHA4	88	11	87.50	UE	160.00	70.00	424
AHA5	61	13	78.68	UE	160.00	70.00	500
AHA6	58	13	77.58	UE	160.00	70.00	533
AHA7	64	10	84.37	UE	160.00	70.00	513
AHA8	58	12	79.31	UE	160.00	70.00	517
AHA9	80	20	75.00	UE	160.00	70.00	467
AHA10	83	18	78.31	UE	160.00	70.00	464
AHA11	69	18	73.91	UE	160.00	70.00	528
AHA12	63	10	76.19	UE	160.00	70.00	458
AHA13	57	10	82.45	UE	160.00	70.00	561
AHA14	57	11	80.70	UE	160.00	70.00	509
AHA15	60	3	85.96	UE	160.00	70.00	471
AHA16	57	8	95.00	UE	160.00	70.00	536
AHA17	57	3	94.74	UE	160.00	70.00	497

phy-path: between physiology and pathology, phy-pac: between physiology and pacing, Opt: optimal, elec: electrodes, Nr. of sim: number of simulations.

Table 8.28. Results of the second optimization method for Patient-5 with 100 % conduction velocity.

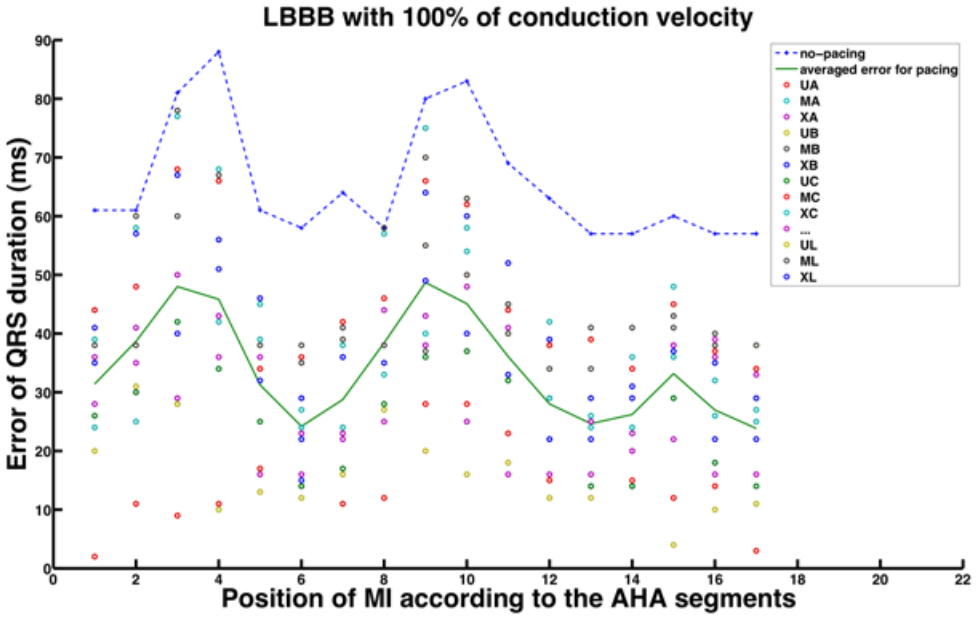

Figure 8.33. The minimal $Error_{QRS}$ achieved by the second optimization method versus AHA segments 1 to 17 corresponding to the 17 different infarction positions. (Each circular point is related to one pair of electrodes. The average of optimal electrode setups is demonstrated with a green line while the blue line shows the $Error_{QRS}$ pathology without pacing.)

Infarction position	$Error_{QRS}$ (phy-path) ms	$Error_{QRS}$ (phy-pac) ms	% $Error_{QRS}$ reduction	Opt. elec positions	Opt. A-V ms	Opt. V-V ms	Nr. of sim.
AHA1	92	25	72.83	UE	160.00	70.00	536
AHA2	93	36	61.29	UE	160.00	70.00	444
AHA3	116	39	66.38	UE	160.00	70.00	297
AHA4	124	42	66.13	UE	160.00	70.00	408
AHA5	89	38	57.30	UE	160.00	70.00	490
AHA6	86	10	88.37	UE	160.00	70.00	565
AHA7	95	20	78.94	UE	160.00	70.00	538
AHA8	89	37	58.42	UE	160.00	70.00	475
AHA9	116	51	56.03	UF	160.00	70.00	374
AHA10	120	40	66.66	UE	160.00	70.00	386
AHA11	100	42	58.00	UE	160.00	70.00	434
AHA12	92	39	57.60	UE	160.00	70.00	502
AHA13	86	14	83.72	UE	160.00	70.00	534
AHA14	86	20	76.74	UE	160.00	70.00	535
AHA15	93	29	68.81	UE	160.00	70.00	480
AHA16	85	38	55.29	UE	160.00	70.00	536
AHA17	86	20	76.74	UE	160.00	70.00	500

phy-path: between physiology and pathology, phy-pac: between physiology and pacing, Opt: optimal, elec: electrodes, Nr. of sim: number of simulations.

Table 8.29. Results of the second optimization method for Patient-5 with 80 % conduction velocity.

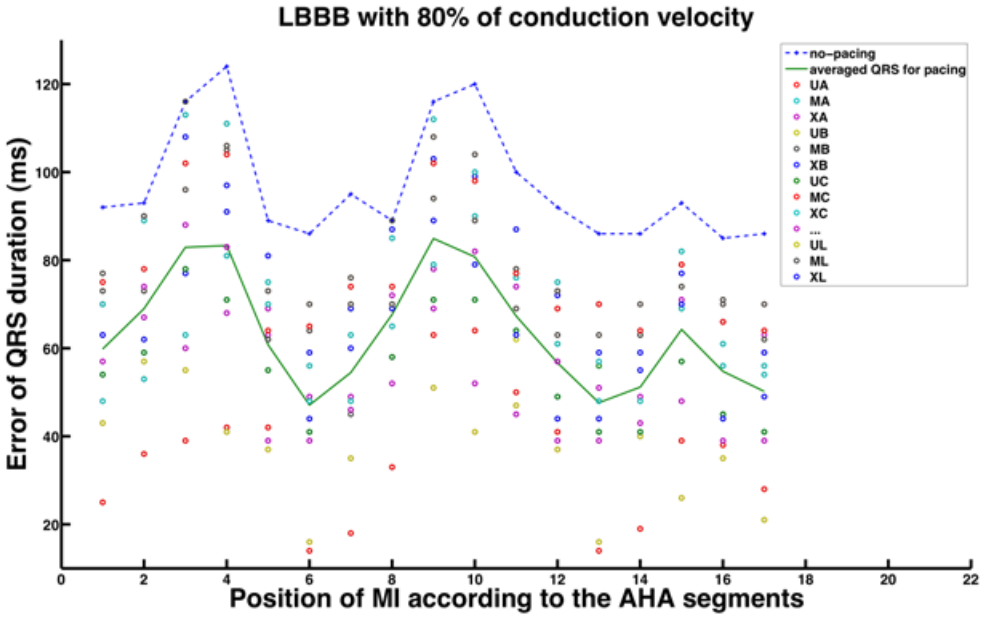

Figure 8.34. The minimal $Error_{QRS}$ achieved by the second optimization method versus AHA segments 1 to 17 corresponding to the 17 different infarction positions. (Each circular point is related to one pair of electrodes. The average of optimal electrode setups is demonstrated with a green line while the blue line shows the $Error_{QRS}$ pathology without pacing.)

Infarction position	$Error_{QRS}$ (phy-path) ms	$Error_{QRS}$ (phy-pac) ms	% $Error_{QRS}$ reduction	Opt. elec positions	Opt. A-V ms	Opt. V-V ms	Nr. of sim.
AHA1	144	59	59.03	UE	160.00	70.00	398
AHA2	144	75	47.92	UE	160.00	70.00	326
AHA3	173	91	47.40	UE	160.00	70.00	250
AHA4	185	83	55.13	UE	160.00	70.00	308
AHA5	137	80	41.60	UE	160.00	70.00	400
AHA6	131	50	61.83	UE	160.00	70.00	436
AHA7	143	52	63.64	UE	160.00	70.00	431
AHA8	136	71	47.79	UE	160.00	70.00	356
AHA9	174	97	44.25	UF	160.00	70.00	346
AHA10	181	83	54.14	UE	160.00	70.00	402
AHA11	152	84	41.44	UE	160.00	70.00	389
AHA12	142	82	42.25	UE	160.00	70.00	402
AHA13	130	50	61.54	UE	160.00	70.00	444
AHA14	131	53	59.54	UE	160.00	70.00	413
AHA15	148	61	58.78	UE	160.00	70.00	340
AHA16	130	78	40.00	UE	160.00	70.00	422
AHA17	130	60	53.84	UE	160.00	70.00	433

phy-path: between physiology and pathology, phy-pac: between physiology and pacing, Opt: optimal, elec: electrodes, Nr. of sim: number of simulations.

Table 8.30. Results of the second optimization method for Patient-5 with 60 % conduction velocity.

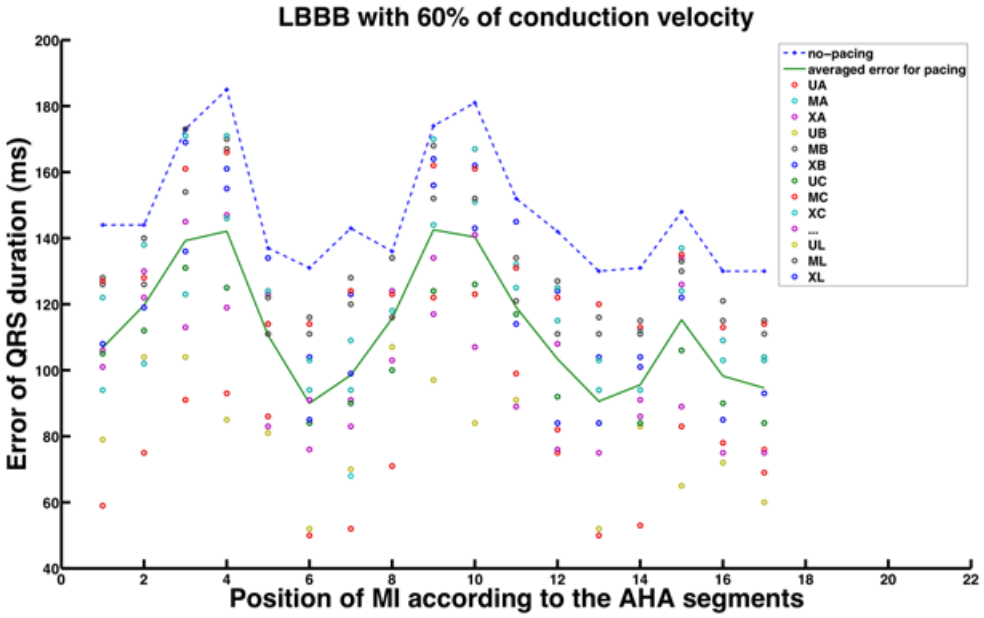

Figure 8.35. The minimal $Error_{QRS}$ achieved by the second optimization method versus AHA segments 1 to 17 corresponding to the 17 different infarction positions. (Each circular point is related to one pair of electrodes. The average of optimal electrode setups is demonstrated with a green line while the blue line shows the $Error_{QRS}$ pathology without pacing.)

8.1.6 Patient-6

The electrode positioning setup is demonstrated in figure 8.36. The results of both optimization methods are summarized in tables 8.31 - 8.36 for the several conduction velocities. The minimal errors associated with each electrode setup for each MI position are illustrated in figures 8.37 - 8.42.

(a) (b)

Figure 8.36. The electrode positions chosen for the Patient-6 heart model. The electrodes A, B, C and D are referred to the anterior branches of coronary sinus. The electrodes I, J, K and L are referred to the posterior branches of coronary sinus. The electrodes E, F, G and H are located on the left ventricular free wall. The electrodes U, M and X are located at the right ventricular upper septum, middle septum and apex respectively.

The first optimization methods mostly found the optimal left electrode position in the posterolateral or lateral wall of the left ventricle (electrode K and G). However the second optimization method found the optimal left electrode position in anterior, posterolateral and lateral wall (electrode B, K, G). The optimal right electrode position is mostly in upper or middle septal area (electrode U and M). The best timing delays range evaluated by the first optimization method is either 120 ms for the A-V delay and 49.84 ms for V-V delay or 160 ms and 70 ms respectively. The best timing delays range achieved by the second optimization is overall 160 ms for the A-V delay and 70 ms for V-V delay.

DSA optimization delivers a number between 326 to 514 simulations for each pathological case. A maximum improvement of up to 39 %, the reduction percentage of E_{RMS} and an improvement of up to 84 %, the reduction percentage of $Error_{QRS}$, can be reached.

Infarction position	E_{RMS} (phy-path) ms	E_{RMS} (phy-pac) ms	% E_{RMS} reduction	Opt. elec positions	Opt. A-V ms	Opt. V-V ms	Nr. of sim.
AHA1	18.00	15.80	12.20	MK	120.00	49.84	514
AHA2	19.00	16.65	12.36	MK	120.00	49.84	510
AHA3	19.50	17.01	12.76	MK	120.00	49.84	510
AHA4	18.07	15.55	13.94	MK	120.00	49.84	502
AHA5	17.80	15.30	14.04	MK	120.00	49.84	484
AHA6	19.02	16.04	15.66	MK	120.00	49.84	505
AHA7	20.41	17.81	12.73	UK	125.00	50.61	516
AHA8	20.03	17.10	14.62	MK	120.00	49.84	502
AHA9	19.06	16.55	13.16	MK	120.00	49.84	497
AHA10	20.63	17.33	15.99	MK	120.00	49.84	507
AHA11	21.02	18.00	14.36	MK	120.00	49.84	499
AHA12	22.30	19.60	12.10	MK	120.00	49.84	505
AHA13	20.70	17.59	15.02	MK	120.00	49.84	508
AHA14	19.50	17.33	11.12	MK	120.00	49.84	506
AHA15	15.05	12.31	18.20	MK	120.00	49.84	510
AHA16	15.22	12.88	15.37	MK	120.00	49.84	510
AHA17	19.08	16.00	16.14	MK	120.00	49.84	499

phy-path: between physiology and pathology, phy-pac: between physiology and pacing, Opt: optimal, elec: electrodes, Nr. of sim: number of simulations.

Table 8.31. Results of the first optimization method for Patient-6 with 100 % conduction velocity.

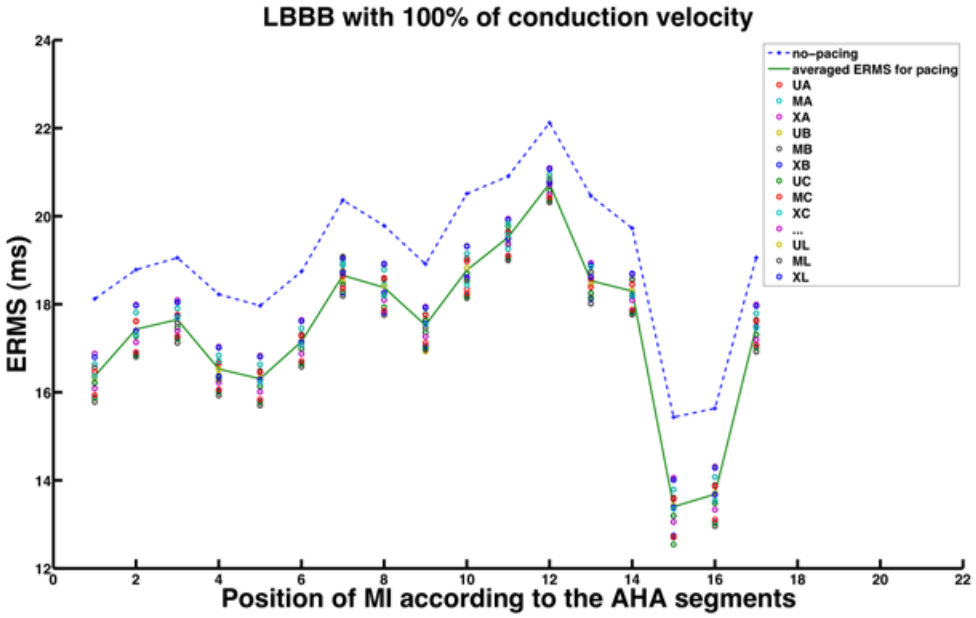

Figure 8.37. The minimal E_{RMS} achieved by the first optimization method versus AHA segments 1 to 17 corresponding to the 17 different infarction positions. (Each circular point is related to one pair of electrodes. The average of optimal electrode setups is demonstrated with a green line while the blue line shows the E_{RMS} pathology without pacing.)

Infarction position	E_{RMS} (phy-path) ms	E_{RMS} (phy-pac) ms	% E_{RMS} reduction	Opt. elec positions	Opt. A-V ms	Opt. V-V ms	Nr. of sim.
AHA1	20.50	16.22	20.87	UG	160.00	70.00	458
AHA2	20.81	17.01	18.26	UG	160.00	70.00	461
AHA3	21.01	17.32	17.56	UG	160.00	70.00	461
AHA4	20.36	16.25	9.62	UG	160.00	70.00	460
AHA5	20.05	16.29	18.75	UG	160.00	70.00	456
AHA6	20.95	17.12	18.28	UG	160.00	70.00	459
AHA7	22.45	18.23	18.79	UG	160.00	70.00	432
AHA8	21.88	18.14	17.09	UG	160.00	70.00	450
AHA9	20.34	17.00	16.42	UG	160.00	70.00	454
AHA10	22.22	18.21	18.04	UG	160.00	70.00	456
AHA11	22.36	19.52	12.70	UG	160.00	70.00	456
AHA12	24.15	20.44	15.36	UG	160.00	70.00	458
AHA13	22.27	18.21	18.23	UG	160.00	70.00	459
AHA14	21.00	18.14	13.61	UG	160.00	70.00	445
AHA15	17.89	13.36	25.32	UG	160.00	70.00	459
AHA16	17.94	13.80	23.07	UG	160.00	70.00	456
AHA17	20.55	17.51	14.79	UG	160.00	70.00	458

phy-path: between physiology and pathology, phy-pac: between physiology and pacing, Opt: optimal, elec: electrodes, Nr. of sim: number of simulations.

Table 8.32. Results of the first optimization method for Patient-6 with 80 % conduction velocity.

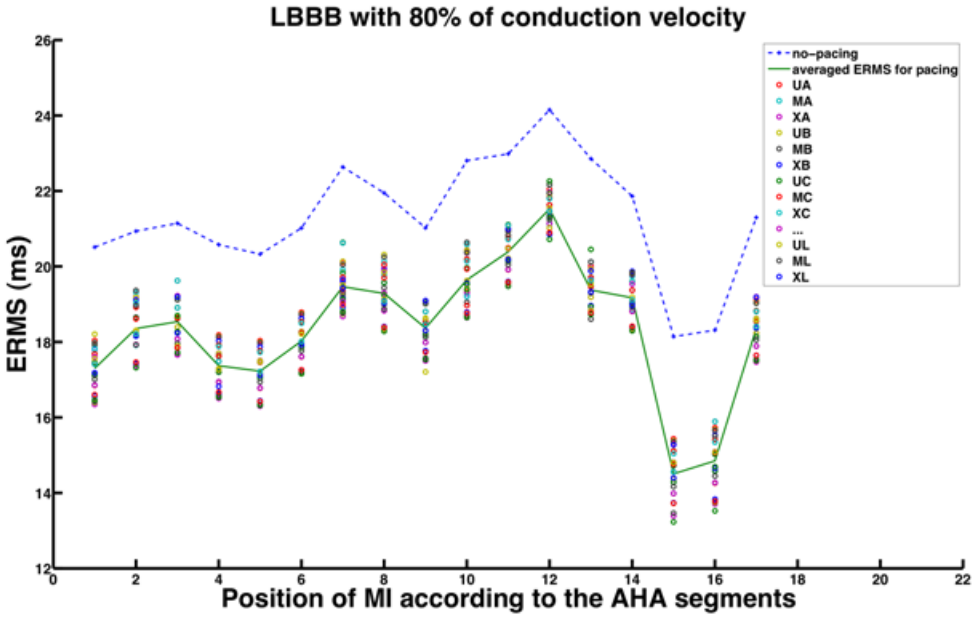

Figure 8.38. The minimal E_{RMS} achieved by the first optimization method versus AHA segments 1 to 17 corresponding to the 17 different infarction positions. (Each circular point is related to one pair of electrodes. The average of optimal electrode setups is demonstrated with a green line while the blue line shows the E_{RMS} pathology without pacing.)

Infarction position	E_{RMS} (phy-path) ms	E_{RMS} (phy-pac) ms	% E_{RMS} reduction	Opt. elec positions	Opt. A-V ms	Opt. V-V ms	Nr. of sim.
AHA1	25.20	17.78	29.44	UK	120.00	49.84	498
AHA2	25.25	17.92	29.02	UK	120.00	49.84	487
AHA3	25.25	18.00	28.71	UK	120.00	49.84	493
AHA4	25.00	17.72	32.00	UK	120.00	49.84	486
AHA5	24.85	16.92	31.91	UK	120.00	49.84	485
AHA6	25.32	17.72	30.01	UK	120.00	49.84	488
AHA7	27.22	18.71	31.26	UK	160.00	70.00	489
AHA8	26.60	18.30	31.20	UK	120.00	49.84	485
AHA9	24.36	18.25	25.08	UK	120.00	49.84	484
AHA10	27.54	18.80	31.73	UK	120.00	49.84	481
AHA11	27.25	19.27	29.28	UK	120.00	49.84	483
AHA12	27.98	20.12	28.09	UK	120.00	49.84	486
AHA13	27.11	18.53	31.64	UK	120.00	49.84	491
AHA14	25.75	18.02	30.01	UK	120.00	49.84	490
AHA15	23.12	14.05	39.23	UK	120.00	49.84	490
AHA16	23.24	14.20	38.89	UK	120.00	49.84	495
AHA17	25.19	17.80	29.33	UK	120.00	49.84	482

phy-path: between physiology and pathology, phy-pac: between physiology and pacing, Opt: optimal, elec: electrodes, Nr. of sim: number of simulations.

Table 8.33. Results of the first optimization method for Patient-6 with 60 % conduction velocity.

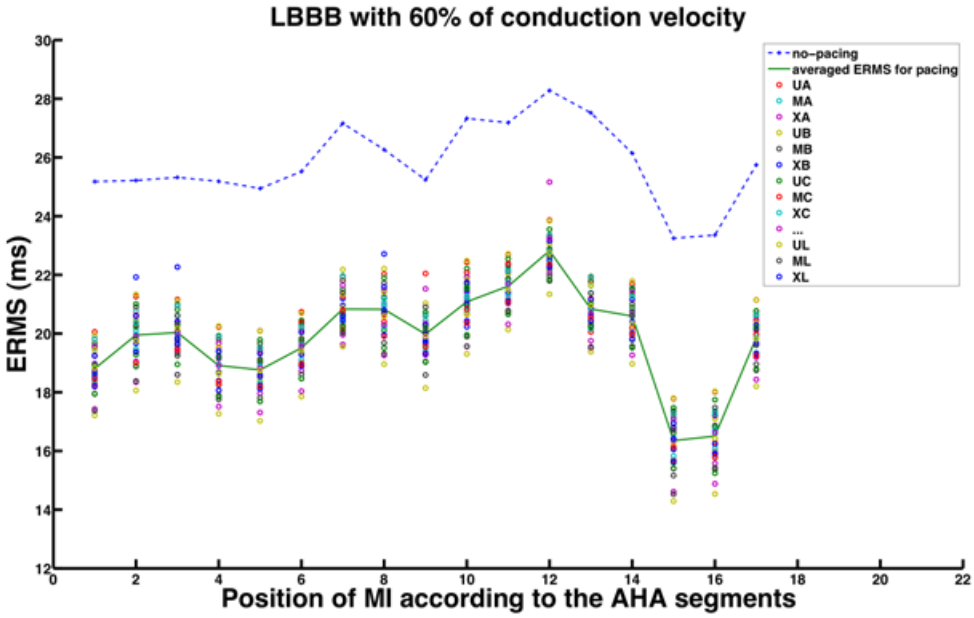

Figure 8.39. The minimal E_{RMS} achieved by the first optimization method versus AHA segments 1 to 17 corresponding to the 17 different infarction positions. (Each circular point is related to one pair of electrodes. The average of optimal electrode setups is demonstrated with a green line while the blue line shows the E_{RMS} pathology without pacing.)

Infarction position	$Error_{QRS}$ (phy-path) ms	$Error_{QRS}$ (phy-pac) ms	% $Error_{QRS}$ reduction	Opt. elec positions	Opt. A-V ms	Opt. V-V ms	Nr. of sim.
AHA1	105	20	80.95	UK	160.00	70.00	484
AHA2	124	35	71.77	UK	160.00	70.00	467
AHA3	217	71	67.28	UK	160.00	70.00	469
AHA4	156	62	60.26	UK	160.00	70.00	505
AHA5	146	58	60.27	UK	160.00	70.00	510
AHA6	113	52	53.98	UK	160.00	70.00	479
AHA7	110	20	81.82	UK	160.00	70.00	477
AHA8	121	37	69.42	UK	160.00	70.00	485
AHA9	158	59	62.66	UK	160.00	70.00	476
AHA10	151	45	70.20	UK	160.00	70.00	456
AHA11	121	48	60.33	UK	160.00	70.00	480
AHA12	116	36	68.97	UK	160.00	70.00	489
AHA13	105	20	80.95	UK	160.00	70.00	483
AHA14	105	35	66.67	UK	160.00	70.00	489
AHA15	121	47	61.16	UK	160.00	70.00	489
AHA16	105	30	71.43	UK	160.00	70.00	480
AHA17	105	42	60.00	UK	160.00	70.00	476

phy-path: between physiology and pathology, phy-pac: between physiology and pacing, Opt: optimal, elec: electrodes, Nr. of sim: number of simulations.

Table 8.34. Results of the second optimization method for Patient-6 with 100 % conduction velocity.

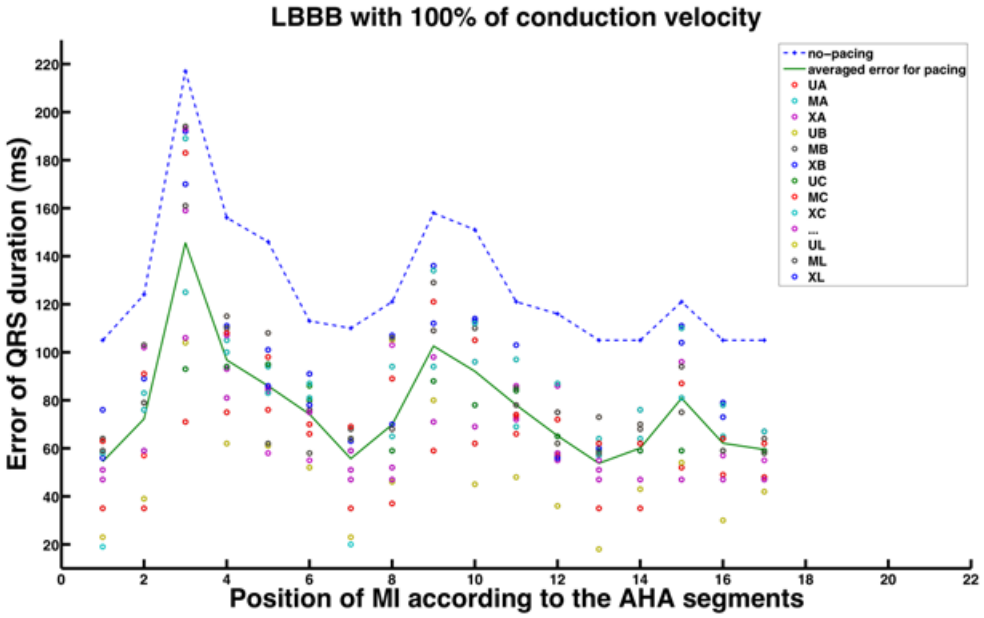

Figure 8.40. The minimal $Error_{QRS}$ achieved by the second optimization method versus AHA segments 1 to 17 corresponding to the 17 different infarction positions. (Each circular point is related to one pair of electrodes. The average of optimal electrode setups is demonstrated with a green line while the blue line shows the $Error_{QRS}$ pathology without pacing.)

Infarction position	$Error_{QRS}$ (phy-path) ms	$Error_{QRS}$ (phy-pac) ms	% $Error_{QRS}$ reduction	Opt. elec positions	Opt. A-V ms	Opt. V-V ms	Nr. of sim.
AHA1	90	15	83.33	UB	160.00	70.00	473
AHA2	109	30	72.47	UB	160.00	70.00	451
AHA3	202	66	67.32	UB	160.00	70.00	461
AHA4	141	57	59.57	UB	160.00	70.00	452
AHA5	131	53	59.54	UB	160.00	70.00	411
AHA6	98	47	52.04	UB	160.00	70.00	465
AHA7	95	15	84.21	UB	160.00	70.00	462
AHA8	106	32	69.81	UB	160.00	70.00	441
AHA9	143	54	62.23	UB	160.00	70.00	452
AHA10	136	40	70.58	UB	160.00	70.00	432
AHA11	106	43	59.43	UL	160.00	70.00	439
AHA12	101	31	69.30	UB	160.00	70.00	422
AHA13	90	15	83.33	UB	160.00	70.00	437
AHA14	90	30	66.66	UB	160.00	70.00	442
AHA15	106	42	60.37	UB	160.00	70.00	446
AHA16	90	25	72.22	UB	160.00	70.00	445
AHA17	90	37	54.63	UB	160.00	70.00	498

phy-path: between physiology and pathology, phy-pac: between physiology and pacing, Opt: optimal, elec: electrodes, Nr. of sim: number of simulations.

Table 8.35. Results of the second optimization method for Patient-6 with 80 % conduction velocity.

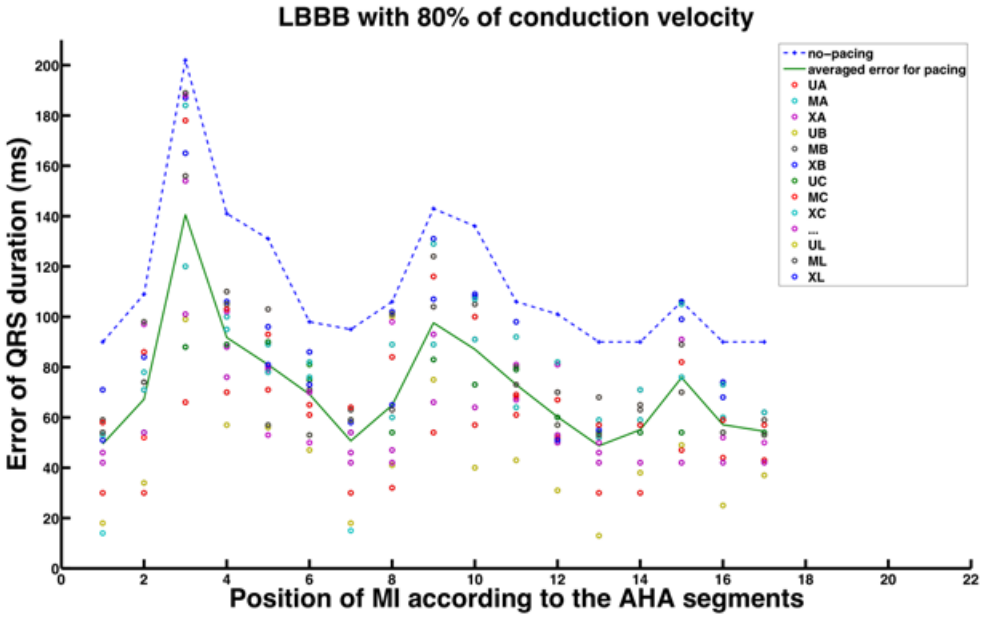

Figure 8.41. The minimal $Error_{QRS}$ achieved by the second optimization method versus AHA segments 1 to 17 corresponding to the 17 different infarction positions. (Each circular point is related to one pair of electrodes. The average of optimal electrode setups is demonstrated with a green line while the blue line shows the $Error_{QRS}$ pathology without pacing.)

Infarction position	$Error_{QRS}$ (phy-path) ms	$Error_{QRS}$ (phy-pac) ms	% $Error_{QRS}$ reduction	Opt. elec positions	Opt. A-V ms	Opt. V-V ms	Nr. of sim.
AHA1	125	49	60.80	UG	160.00	70.00	429
AHA2	144	65	54.86	UG	160.00	70.00	429
AHA3	237	101	57.38	UG	160.00	70.00	453
AHA4	176	92	47.72	UG	160.00	70.00	385
AHA5	166	88	46.98	UG	160.00	70.00	460
AHA6	133	82	38.34	UG	160.00	70.00	422
AHA7	130	50	61.53	UG	160.00	70.00	402
AHA8	141	67	52.48	UG	160.00	70.00	326
AHA9	178	89	50.00	UG	160.00	70.00	442
AHA10	171	75	56.14	UG	160.00	70.00	419
AHA11	141	78	44.68	UG	160.00	70.00	413
AHA12	136	66	51.47	UG	160.00	70.00	416
AHA13	125	48	61.60	UG	160.00	70.00	408
AHA14	125	65	48.00	UG	160.00	70.00	446
AHA15	141	77	45.39	UG	160.00	70.00	425
AHA16	125	60	52.00	UG	160.00	70.00	418
AHA17	125	72	42.40	UG	160.00	70.00	420

phy-path: between physiology and pathology, phy-pac: between physiology and pacing, Opt: optimal, elec: electrodes, Nr. of sim: number of simulations.

Table 8.36. Results of the second optimization method for Patient-6 with 60 % conduction velocity.

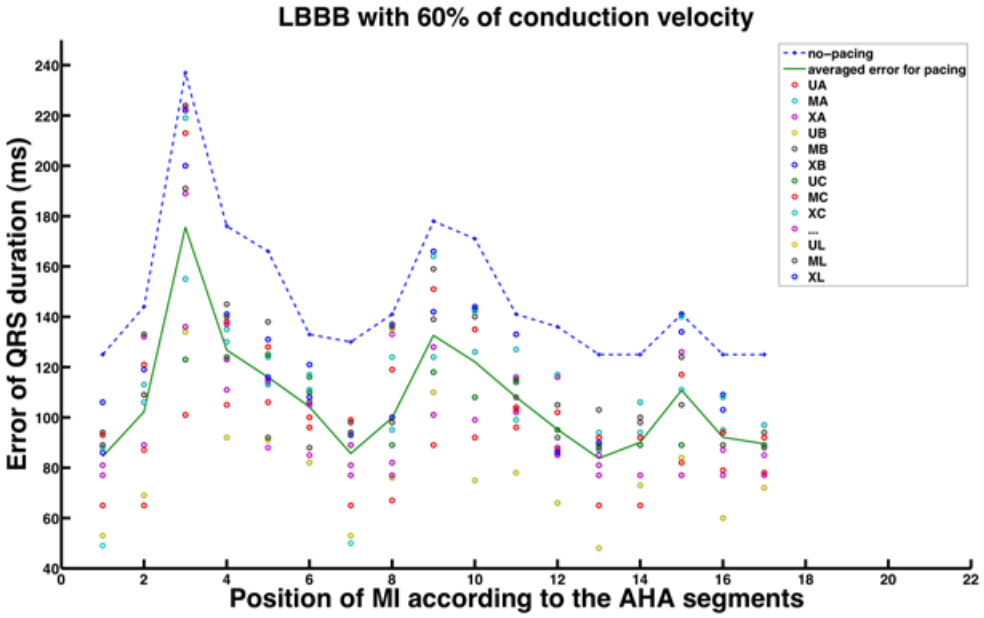

Figure 8.42. The minimal $Error_{QRS}$ achieved by the second optimization method versus AHA segments 1 to 17 corresponding to the 17 different infarction positions. (Each circular point is related to one pair of electrodes. The average of optimal electrode setups is demonstrated with a green line while the blue line shows the $Error_{QRS}$ pathology without pacing.)

8.1.7 Patient-7

The electrode positioning setup is demonstrated in figure 8.43. The results of both optimization methods are summarized in tables 8.37 - 8.42 for the several conduction velocities. The minimal errors associated with each electrode setup for each MI position are illustrated in figures 8.44 - 8.49.

(a) (b)

Figure 8.43. The electrode positions chosen for the Patient-7 heart model. The electrodes A, B, C and D are referred to the anterior branches of coronary sinus. The electrodes I, J, K and L are referred to the posterior branches of coronary sinus. The electrodes E, F, G and H are located on the left ventricular free wall. The electrodes U, M and X are located at the right ventricular upper septum, middle septum and apex respectively.

Both optimization methods mostly found the optimal left electrode position in the lateral wall of the left ventricle (electrode E and F). The optimal right electrode position is mostly in upper or middle septal area (electrode U and M) expect in the case of 60 % of conduction velocity the best position is in RV apex (electrode X). The best timing delays range evaluated by the first optimization method is between $120 - 160$ ms for the A-V delay and $49.81 - 70$ ms for the V-V delay. The best timing delays range achieved by the second optimization is overall 160 ms for the A-V delay and 70 ms for V-V delay.

DSA optimization delivers a number between 301 to 540 simulations for each pathological case. The maximum possible improvement is of 39 %, for the reduction of E_{RMS} and 82 %, for the decrease in $Error_{QRS}$.

Infarction position	E_{RMS} (phy-path) ms	E_{RMS} (phy-pac) ms	% E_{RMS} reduction	Opt. elec positions	Opt. A-V ms	Opt. V-V ms	Nr. of sim.
AHA1	23.67	17.92	24.30	UE	160.00	70.00	404
AHA2	21.01	14.23	32.29	UE	160.00	70.00	438
AHA3	20.75	14.60	29.63	UE	160.00	70.00	410
AHA4	22.18	16.50	25.63	UE	160.00	70.00	377
AHA5	26.09	20.70	20.65	UE	160.00	70.00	381
AHA6	24.91	19.38	22.21	UE	160.00	70.00	396
AHA7	24.18	18.12	25.07	UE	160.00	70.00	365
AHA8	24.60	18.96	22.92	UE	160.00	70.00	364
AHA9	22.97	17.63	23.22	ME	130.00	55.27	411
AHA10	26.23	21.70	17.27	UE	160.00	70.00	354
AHA11	27.15	22.18	18.33	UE	160.00	70.00	404
AHA12	26.73	21.28	20.41	UE	160.00	70.00	359
AHA13	26.67	21.78	18.33	UE	160.00	70.00	347
AHA14	24.28	18.64	23.25	UE	160.00	70.00	374
AHA15	26.78	22.09	17.51	UE	160.00	70.00	389
AHA16	26.43	21.51	18.60	UE	160.00	70.00	364
AHA17	26.34	21.27	19.27	UE	160.00	70.00	358

phy-path: between physiology and pathology, phy-pac: between physiology and pacing, Opt: optimal, elec: electrodes, Nr. of sim: number of simulations.

Table 8.37. Results of the first optimization method for Patient-7 with 100 % conduction velocity.

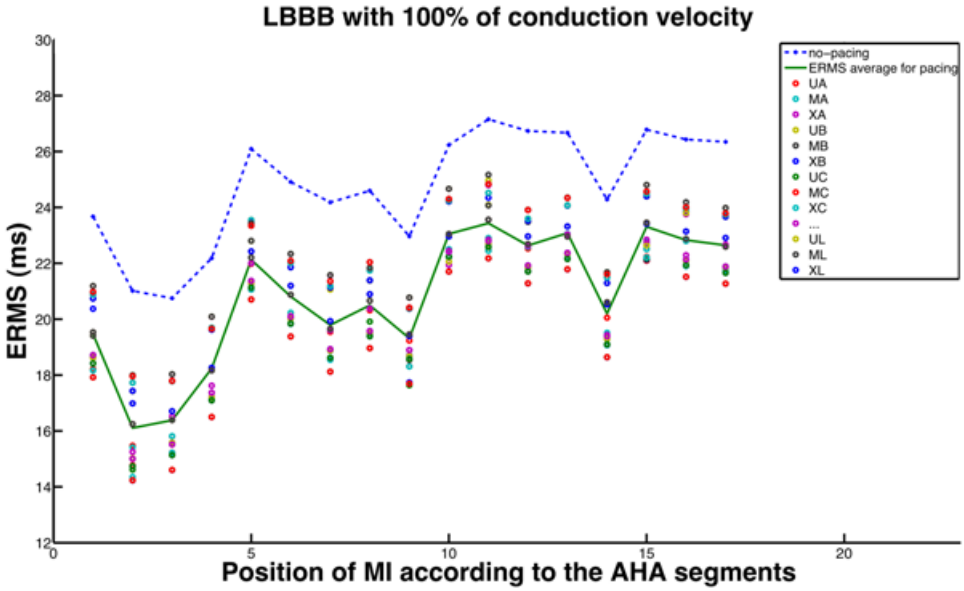

Figure 8.44. The minimal E_{RMS} achieved by the first optimization method versus AHA segments 1 to 17 corresponding to the 17 different infarction positions. (Each circular point is related to one pair of electrodes. The average of optimal electrode setups is demonstrated with a green line while the blue line shows the E_{RMS} pathology without pacing.)

Infarction position	E_{RMS} (phy-path) ms	E_{RMS} (phy-pac) ms	% E_{RMS} reduction	Opt. elec positions	Opt. A-V ms	Opt. V-V ms	Nr. of sim.
AHA1	26.54	18.33	30.92	ME	140.00	60.70	455
AHA2	24.22	14.71	39.27	UE	140.00	57.58	501
AHA3	23.77	15.02	36.80	UE	140.00	57.58	464
AHA4	24.99	16.91	32.31	UE	140.00	57.58	467
AHA5	28.87	21.06	27.07	ME	140.00	57.58	435
AHA6	27.71	19.75	28.74	UE	140.00	57.58	462
AHA7	27.10	18.52	31.66	UE	140.00	57.58	407
AHA8	27.49	19.32	29.70	UE	140.00	57.58	438
AHA9	25.68	18.26	28.91	ME	120.00	52.97	458
AHA10	28.59	22.01	23.00	XE	130.00	49.81	405
AHA11	29.74	22.53	24.27	UE	140.00	57.58	426
AHA12	29.49	21.63	26.66	UE	140.00	57.58	442
AHA13	29.26	22.15	24.28	ME	140.00	57.58	434
AHA14	27.10	19.02	29.80	UE	140.00	57.58	429
AHA15	29.18	22.43	23.13	UE	140.00	57.58	420
AHA16	28.96	21.84	24.60	UE	140.00	57.58	436
AHA17	28.95	21.60	25.38	ME	140.00	57.58	420

phy-path: between physiology and pathology, phy-pac: between physiology and pacing, Opt: optimal, elec: electrodes, Nr. of sim: number of simulations.

Table 8.38. Results of the first optimization method for Patient-7 with 80 % conduction velocity.

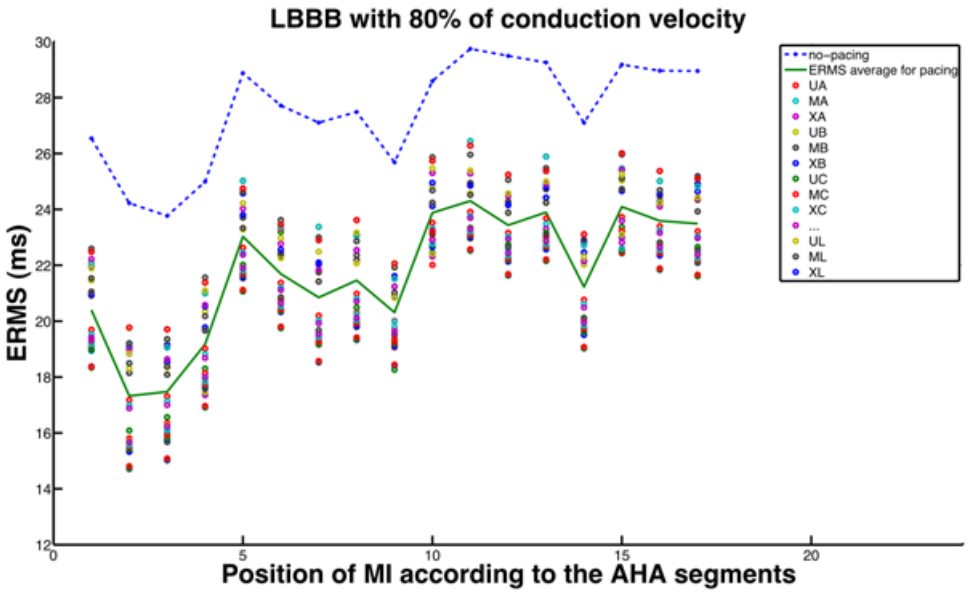

Figure 8.45. The minimal E_{RMS} achieved by the first optimization method versus AHA segments 1 to 17 corresponding to the 17 different infarction positions. (Each circular point is related to one pair of electrodes. The average of optimal electrode setups is demonstrated with a green line while the blue line shows the E_{RMS} pathology without pacing.)

Infarction position	E_{RMS} (phy-path) ms	E_{RMS} (phy-pac) ms	% E_{RMS} reduction	Opt. elec positions	Opt. A-V ms	Opt. V-V ms	Nr. of sim.
AHA1	31.83	19.13	39.91	XE	120.00	49.84	519
AHA2	29.97	15.54	48.15	XE	125.63	51.63	540
AHA3	29.20	15.96	45.34	XE	123.75	52.27	504
AHA4	30.12	17.77	41.01	XE	125.00	51.00	493
AHA5	34.09	21.75	36.20	XE	120.00	49.84	504
AHA6	32.94	20.43	37.97	XE	125.00	51.00	516
AHA7	32.47	19.28	40.62	XE	125.00	51.00	514
AHA8	32.77	20.01	38.94	XE	125.00	51.00	492
AHA9	30.71	19.75	35.69	MF	120.00	49.84	506
AHA10	33.05	22.78	31.07	ME	120.00	52.97	503
AHA11	34.57	23.15	33.03	XE	120.00	49.84	488
AHA12	34.63	22.31	35.57	XE	125.00	51.00	508
AHA13	34.14	22.79	33.25	XE	120.00	49.84	501
AHA14	32.32	19.76	38.86	ME	125.00	51.00	493
AHA15	33.71	23.04	31.66	XE	125.00	51.00	458
AHA16	33.73	22.47	33.37	XE	120.00	49.84	480
AHA17	33.85	22.26	34.24	XE	125.00	51.00	486

phy-path: between physiology and pathology, phy-pac: between physiology and pacing, Opt: optimal, elec: electrodes, Nr. of sim: number of simulations.

Table 8.39. Results of the first optimization method for Patient-7 with 60 % conduction velocity.

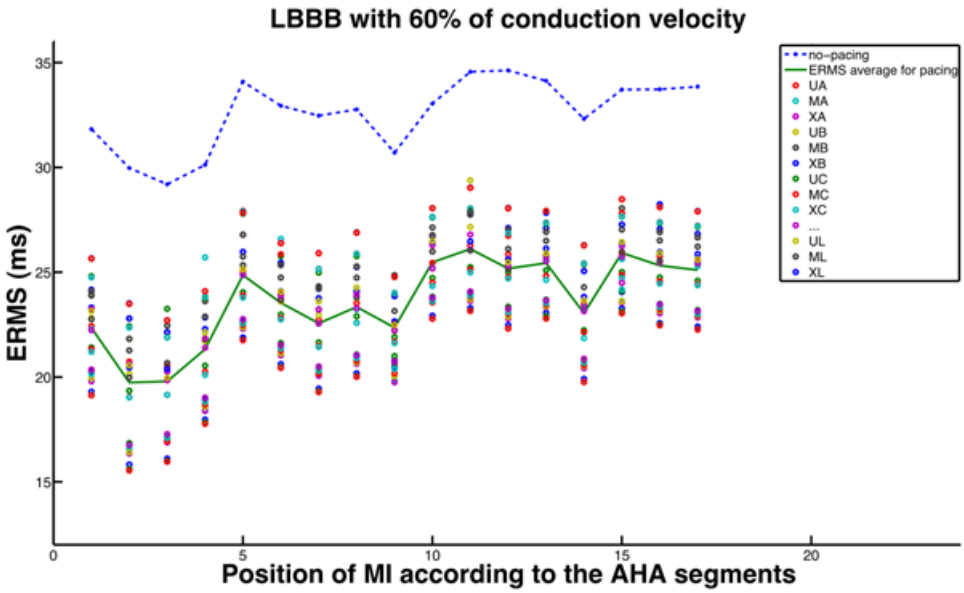

Figure 8.46. The minimal E_{RMS} achieved by the first optimization method versus AHA segments 1 to 17 corresponding to the 17 different infarction positions. (Each circular point is related to one pair of electrodes. The average of optimal electrode setups is demonstrated with a green line while the blue line shows the E_{RMS} pathology without pacing.)

Infarction position	$Error_{QRS}$ (phy-path) ms	$Error_{QRS}$ (phy-pac) ms	% $Error_{QRS}$ reduction	Opt. elec positions	Opt. A-V ms	Opt. V-V ms	Nr. of sim.
AHA1	96	38	60.42	UE	160.00	70.00	488
AHA2	100	29	71.00	UE	160.00	70.00	490
AHA3	123	21	82.93	UE	160.00	70.00	482
AHA4	126	23	81.75	UE	160.00	70.00	356
AHA5	106	39	63.20	UE	160.00	70.00	487
AHA6	97	38	60.82	UE	160.00	70.00	488
AHA7	96	20	79.16	UE	160.00	70.00	512
AHA8	95	25	73.68	UE	160.00	70.00	471
AHA9	114	38	66.66	MC	160.00	70.00	425
AHA10	124	30	75.80	UE	160.00	70.00	373
AHA11	102	38	62.74	UE	160.00	70.00	526
AHA12	101	38	62.37	UE	160.00	70.00	465
AHA13	95	30	68.42	UE	160.00	70.00	508
AHA14	94	20	78.72	UE	160.00	70.00	489
AHA15	95	30	68.42	UE	160.00	70.00	409
AHA16	95	35	63.15	UE	160.00	70.00	523
AHA17	95	24	74.73	UE	160.00	70.00	502

phy-path: between physiology and pathology, phy-pac: between physiology and pacing, Opt: optimal, elec: electrodes, Nr. of sim: number of simulations.

Table 8.40. Results of the second optimization method for Patient-7 with 100 % conduction velocity.

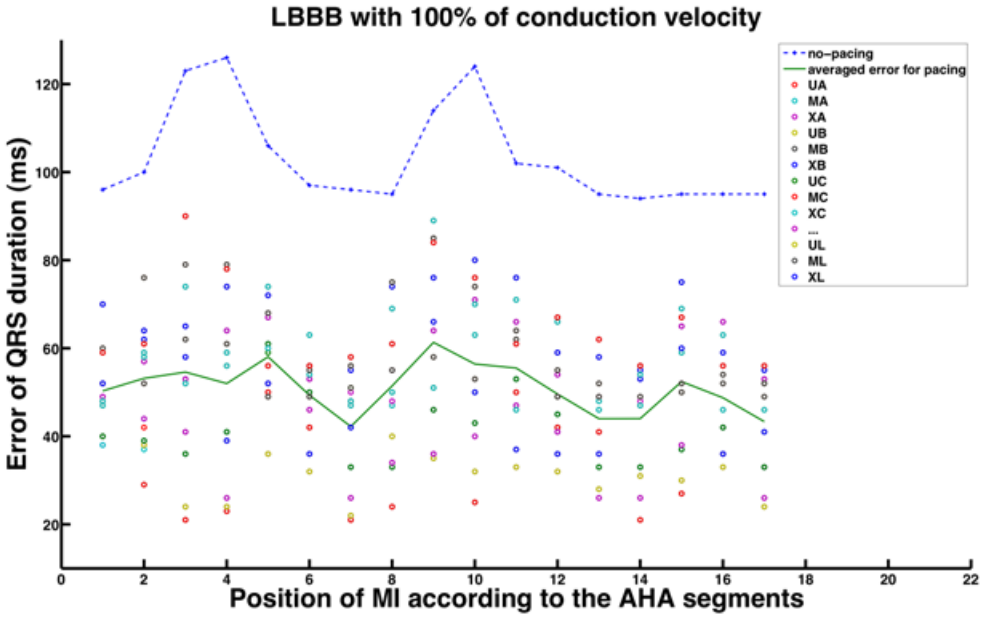

Figure 8.47. The minimal $Error_{QRS}$ achieved by the second optimization method versus AHA segments 1 to 17 corresponding to the 17 different infarction positions. (Each circular point is related to one pair of electrodes. The average of optimal electrode setups is demonstrated with a green line while the blue line shows the $Error_{QRS}$ pathology without pacing.)

Infarction position	$Error_{QRS}$ (phy-path) ms	$Error_{QRS}$ (phy-pac) ms	% $Error_{QRS}$ reduction	Opt. elec positions	Opt. A-V ms	Opt. V-V ms	Nr. of sim.
AHA1	128	48	62.50	UE	160.00	70.00	423
AHA2	133	51	61.65	UE	160.00	70.00	409
AHA3	164	45	72.56	UE	160.00	70.00	419
AHA4	166	49	70.48	UE	160.00	70.00	370
AHA5	140	70	50.00	UE	160.00	70.00	386
AHA6	130	58	55.38	UE	160.00	70.00	475
AHA7	128	45	64.84	UE	160.00	70.00	432
AHA8	126	53	57.94	UE	160.00	70.00	426
AHA9	151	70	53.64	UF	160.00	70.00	390
AHA10	164	59	64.02	UE	160.00	70.00	301
AHA11	133	70	47.36	UE	160.00	70.00	432
AHA12	132	62	53.03	UE	160.00	70.00	479
AHA13	126	58	53.96	UE	160.00	70.00	438
AHA14	126	46	63.49	UE	160.00	70.00	475
AHA15	130	53	59.23	UE	160.00	70.00	389
AHA16	126	68	46.03	UE	160.00	70.00	421
AHA17	126	50	60.31	UE	160.00	70.00	455

phy-path: between physiology and pathology, phy-pac: between physiology and pacing, Opt: optimal, elec: electrodes, Nr. of sim: number of simulations.

Table 8.41. Results of the second optimization method for Patient-7 with 80 % conduction velocity.

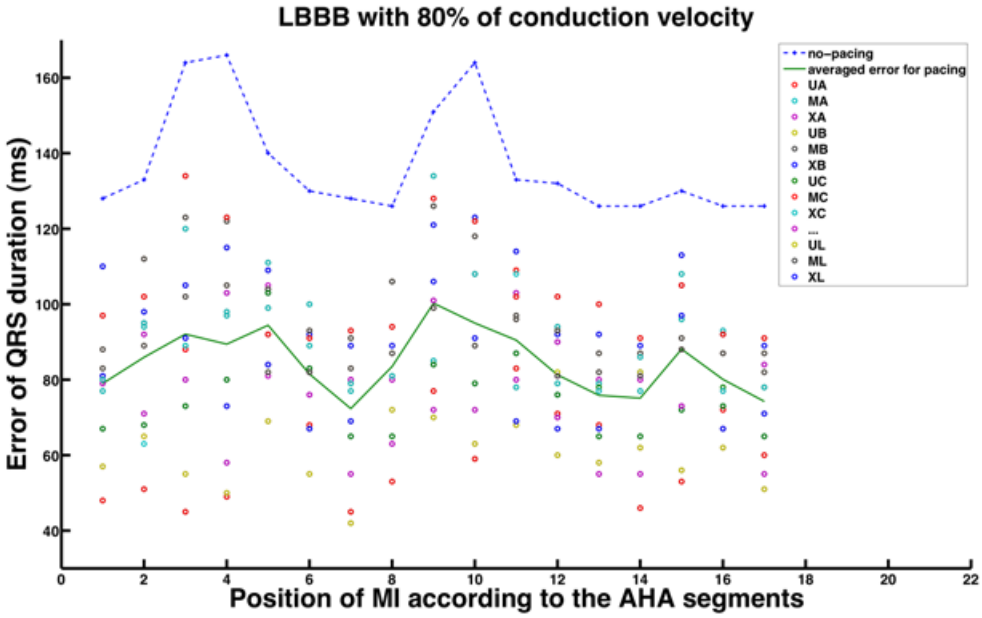

Figure 8.48. The minimal $Error_{QRS}$ achieved by the second optimization method versus AHA segments 1 to 17 corresponding to the 17 different infarction positions. (Each circular point is related to one pair of electrodes. The average of optimal electrode setups is demonstrated with a green line while the blue line shows the $Error_{QRS}$ pathology without pacing.)

Infarction position	$Error_{QRS}$ (phy-path) ms	$Error_{QRS}$ (phy-pac) ms	% $Error_{QRS}$ reduction	Opt. elec positions	Opt. A-V ms	Opt. V-V ms	Nr. of sim.
AHA1	182	87	52.20	UE	160.00	70.00	399
AHA2	189	88	53.44	UE	160.00	70.00	385
AHA3	225	87	61.33	UE	160.00	70.00	393
AHA4	231	102	55.84	UE	160.00	70.00	401
AHA5	196	120	38.77	UE	160.00	70.00	372
AHA6	183	98	46.44	UE	160.00	70.00	381
AHA7	179	70	60.89	UE	160.00	70.00	415
AHA8	179	97	45.81	UE	160.00	70.00	358
AHA9	216	121	43.98	UF	160.00	70.00	359
AHA10	231	117	49.35	UE	160.00	70.00	303
AHA11	185	120	35.13	UE	160.00	70.00	371
AHA12	183	110	39.89	UE	160.00	70.00	362
AHA13	178	110	38.20	UE	160.00	70.00	387
AHA14	178	90	49.43	UE	160.00	70.00	414
AHA15	191	98	48.69	UE	160.00	70.00	372
AHA16	150	110	26.66	UE	160.00	70.00	385
AHA17	178	98	44.94	UE	160.00	70.00	393

phy-path: between physiology and pathology, phy-pac: between physiology and pacing, Opt: optimal, elec: electrodes, Nr. of sim: number of simulations.

Table 8.42. Results of the second optimization method for Patient-7 with 60 % conduction velocity.

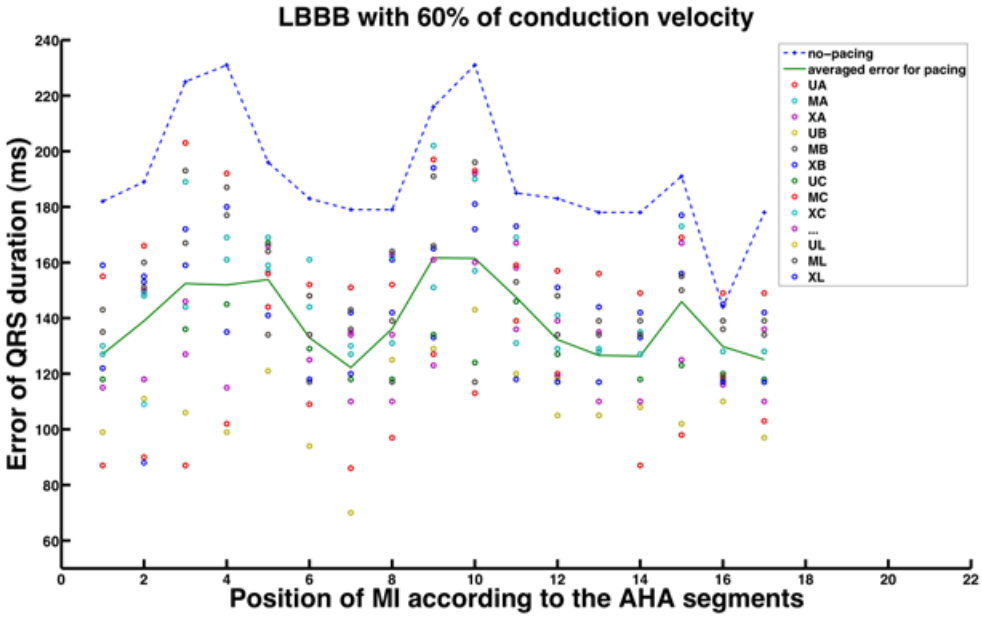

Figure 8.49. The minimal $Error_{QRS}$ achieved by the second optimization method versus AHA segments 1 to 17 corresponding to the 17 different infarction positions. (Each circular point is related to one pair of electrodes. The average of optimal electrode setups is demonstrated with a green line while the blue line shows the $Error_{QRS}$ pathology without pacing.)

8.1.8 Patient-8

The electrode positioning setup is demonstrated in figure 8.50. The results of both optimization methods are summarized in tables 8.43 - 8.48 for the several conduction velocities. The minimal errors associated with each electrode setup for each MI position are illustrated in figures 8.51 - 8.56.

(a) (b)

Figure 8.50. The electrode positions chosen for the Patient-8 heart model. The electrodes A, B, C and D are referred to the anterior branches of coronary sinus. The electrodes I, J, K and L are referred to the posterior branches of coronary sinus. The electrodes E, F, G and H are located on the left ventricular free wall. The electrodes U, M and X are located at the right ventricular upper septum, middle septum and apex respectively.

Both optimization methods mostly found the optimal left electrode position in the lateral wall of the left ventricle (electrode E, F ,G and H). The optimal right electrode position achieved by the first optimization method is in middle septal area or RV apex (electrode M and X) however the position is changed to the upper septal area (electrode U) with the second optimization method. The best timing delays range evaluated by the first optimization method is in the range of $120 - 160\ ms$ for the A-V delay and $49.84 - 70\ ms$. The best timing delays range achieved by the second optimization is overall $160\ ms$ for the A-V delay and $70\ ms$ for V-V delay.

DSA optimization delivers a number between 245 to 554 simulations for each pathological case. A maximum improvement of up to 62 %, the reduction percentage of E_{RMS} and an improvement of up to 88 %, the reduction percentage of $Error_{QRS}$, can be reached.

Infarction position	E_{RMS} (phy-path) ms	E_{RMS} (phy-pac) ms	% E_{RMS} reduction	Opt. elec positions	Opt. A-V ms	Opt. V-V ms	Nr. of sim.
AHA1	18.21	11.50	36.84	XG	160.00	70.00	483
AHA2	20.19	15.64	22.53	XG	160.00	70.00	463
AHA3	22.93	17.00	25.86	XH	160.00	70.00	465
AHA4	22.06	16.50	25.20	XG	160.00	70.00	456
AHA5	24.55	17.00	30.75	XG	160.00	70.00	461
AHA6	24.88	18.00	27.65	XG	160.00	70.00	456
AHA7	17.83	11.00	38.30	XG	160.00	70.00	480
AHA8	23.99	18.00	24.96	XH	160.00	70.00	420
AHA9	25.88	18.00	30.44	XH	160.00	70.00	441
AHA10	24.37	18.00	26.13	XG	160.00	70.00	434
AHA11	26.60	18.50	30.45	XG	160.00	70.00	451
AHA12	25.38	18.50	27.10	XG	160.00	70.00	454
AHA13	23.91	16.80	29.73	XG	160.00	70.00	455
AHA14	24.21	16.80	30.60	XH	160.00	70.00	438
AHA15	23.71	18.11	23.61	XG	160.00	70.00	451
AHA16	24.78	18.00	27.36	XH	160.00	70.00	451
AHA17	27.59	17.00	38.38	XG	160.00	70.00	444

phy-path: between physiology and pathology, phy-pac: between physiology and pacing, Opt: optimal, elec: electrodes, Nr. of sim: number of simulations.

Table 8.43. Results of the first optimization method for Patient-8 with 100 % conduction velocity.

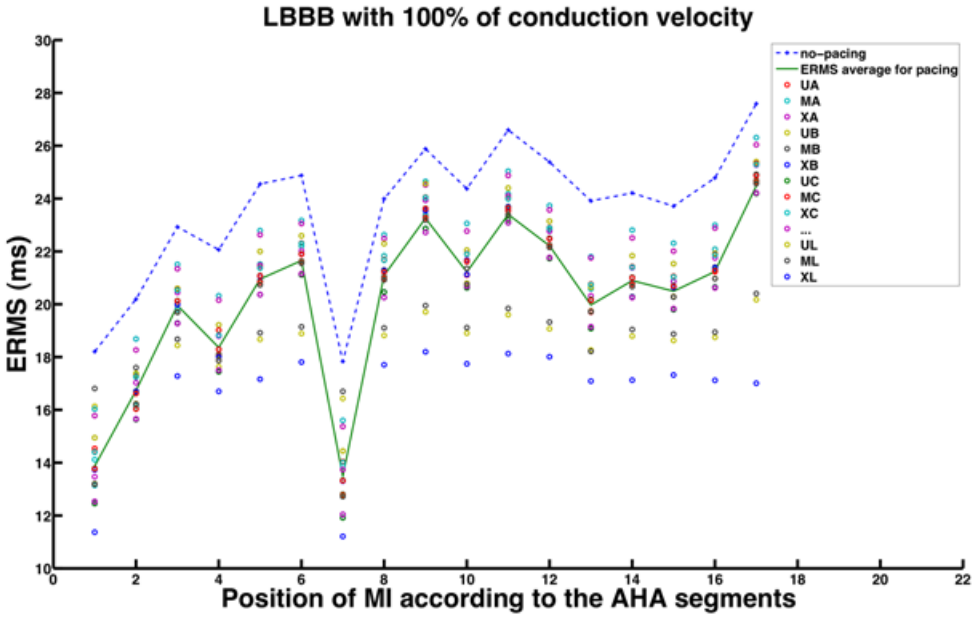

Figure 8.51. The minimal E_{RMS} achieved by the first optimization method versus AHA segments 1 to 17 corresponding to the 17 different infarction positions. (Each circular point is related to one pair of electrodes. The optimal electrode setups is demonstrated with a green line while the blue line shows the E_{RMS} pathology without pacing.)

Infarction position	E_{RMS} (phy-path) ms	E_{RMS} (phy-pac) ms	% E_{RMS} reduction	Opt. elec positions	Opt. A-V ms	Opt. V-V ms	Nr. of sim.
AHA1	21.93	11.89	45.78	XH	160.00	70.00	432
AHA2	23.36	12.00	48.63	XH	160.00	70.00	418
AHA3	25.70	17.00	33.85	XH	160.00	70.00	401
AHA4	25.23	16.60	34.20	XH	160.00	70.00	425
AHA5	27.49	17.70	35.61	XH	160.00	70.00	397
AHA6	27.69	17.50	36.80	XH	160.00	70.00	393
AHA7	21.57	11.00	49.00	XH	160.00	70.00	432
AHA8	26.57	17.70	33.38	XH	150.00	64.57	398
AHA9	28.28	18.30	34.65	XH	140.00	60.70	391
AHA10	27.22	17.80	34.60	XH	160.00	70.00	414
AHA11	29.30	18.30	37.54	XH	160.00	70.00	391
AHA12	28.12	18.00	35.98	XH	160.00	70.00	388
AHA13	27.04	17.00	37.13	XH	160.00	70.00	402
AHA14	27.00	17.50	35.18	XH	160.00	70.00	384
AHA15	26.64	17.50	34.30	XH	160.00	70.00	384
AHA16	27.74	17.50	36.91	XH	160.00	70.00	405
AHA17	30.14	17.00	43.59	XH	160.00	70.00	369

phy-path: between physiology and pathology, phy-pac: between physiology and pacing, Opt: optimal, elec: electrodes, Nr. of sim: number of simulations.

Table 8.44. Results of the first optimization method for Patient-8 with 80 % conduction velocity.

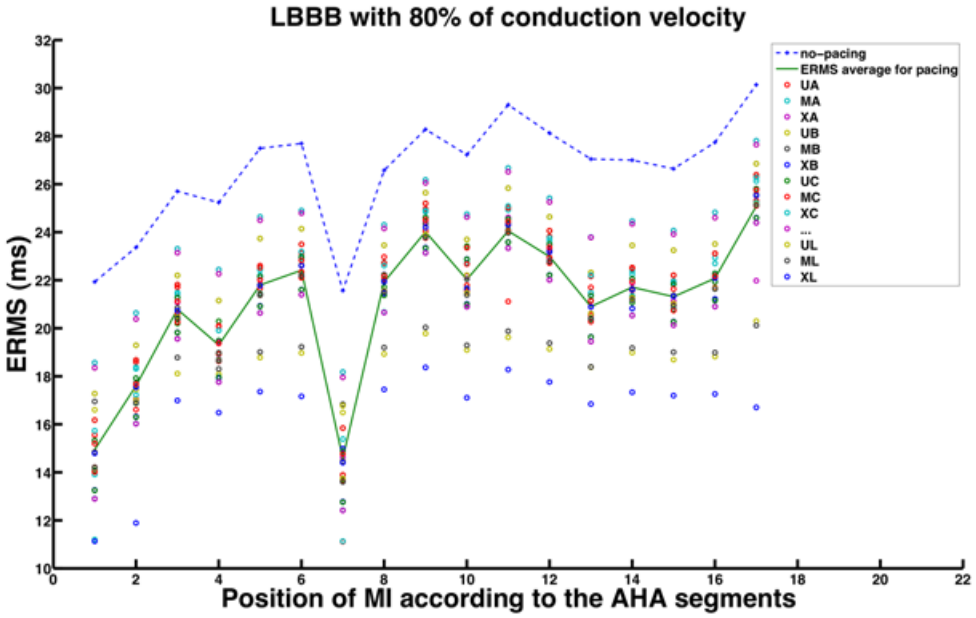

Figure 8.52. The minimal E_{RMS} achieved by the first optimization method versus AHA segments 1 to 17 corresponding to the 17 different infarction positions. (Each circular point is related to one pair of electrodes. The optimal electrode setups is demonstrated with a green line while the blue line shows the E_{RMS} pathology without pacing.)

Infarction position	E_{RMS} (phy-path) ms	E_{RMS} (phy-pac) ms	% E_{RMS} reduction	Opt. elec positions	Opt. A-V ms	Opt. V-V ms	Nr. of sim.
AHA1	28.36	11.11	60.82	XH	130.00	52.15	554
AHA2	29.05	12.26	57.79	XH	140.00	59.14	523
AHA3	30.86	13.00	57.87	XH	140.00	59.14	501
AHA4	30.98	12.50	59.65	XH	130.00	55.27	526
AHA5	32.92	17.20	47.75	XH	140.00	59.14	503
AHA6	32.97	17.30	47.52	XH	140.00	59.14	503
AHA7	27.96	12.22	56.29	XH	130.00	52.15	548
AHA8	31.40	17.25	45.06	MH	125.00	51.00	514
AHA9	32.90	18.80	42.85	MH	120.00	49.84	505
AHA10	32.58	17.25	47.05	XH	130.00	55.27	500
AHA11	34.43	18.80	45.39	XH	140.00	59.14	493
AHA12	33.28	17.30	48.01	XH	140.00	59.14	505
AHA13	32.73	12.50	61.80	MH	130.00	53.71	519
AHA14	32.18	17.50	45.61	XH	140.00	59.14	496
AHA15	32.10	17.50	45.48	XH	120.00	49.84	505
AHA16	33.21	17.45	47.45	XH	140.00	59.14	502
AHA17	35.02	17.51	50.00	XH	140.00	59.14	469

phy-path: between physiology and pathology, phy-pac: between physiology and pacing, Opt: optimal, elec: electrodes, Nr. of sim: number of simulations.

Table 8.45. Results of the first optimization method for Patient-8 with 60 % conduction velocity.

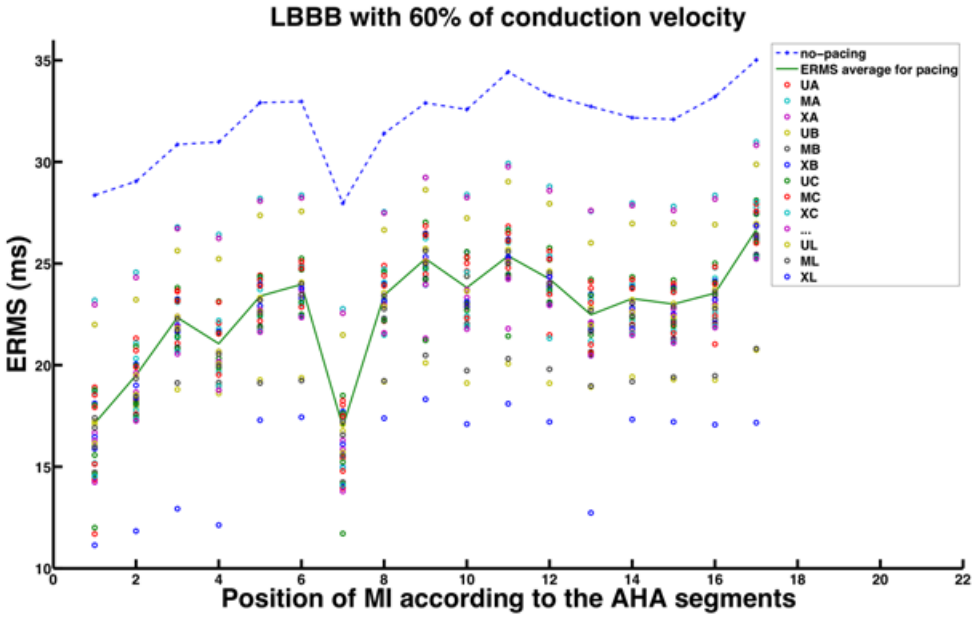

Figure 8.53. The minimal E_{RMS} achieved by the first optimization method versus AHA segments 1 to 17 corresponding to the 17 different infarction positions. (Each circular point is related to one pair of electrodes. The optimal electrode setups is demonstrated with a green line while the blue line shows the E_{RMS} pathology without pacing.)

Infarction position	$Error_{QRS}$ (phy-path) ms	$Error_{QRS}$ (phy-pac) ms	% $Error_{QRS}$ reduction	Opt. elec positions	Opt. A-V ms	Opt. V-V ms	Nr. of sim.
AHA1	56	18	67.85	UE	160.00	70.00	526
AHA2	67	10	85.07	UG	160.00	70.00	527
AHA3	121	19	84.29	UG	160.00	70.00	304
AHA4	87	10	88.50	UE	160.00	70.00	428
AHA5	81	19	76.54	UE	160.00	70.00	457
AHA6	61	18	70.49	UE	160.00	70.00	484
AHA7	58	18	68.96	UE	160.00	70.00	480
AHA8	67	10	85.07	UE	160.00	70.00	499
AHA9	83	18	78.31	UF	160.00	70.00	464
AHA10	82	10	87.80	UE	160.00	70.00	486
AHA11	65	12	81.53	UE	160.00	70.00	470
AHA12	70	15	78.57	UE	160.00	70.00	512
AHA13	56	10	82.14	UG	160.00	70.00	486
AHA14	56	10	82.14	UE	160.00	70.00	528
AHA15	61	10	83.60	UG	160.00	70.00	482
AHA16	56	10	82.14	UE	160.00	70.00	492
AHA17	56	10	82.14	UE	160.00	70.00	487

phy-path: between physiology and pathology, phy-pac: between physiology and pacing, Opt: optimal, elec: electrodes, Nr. of sim: number of simulations.

Table 8.46. Results of the second optimization method for Patient-8 with 100 % conduction velocity.

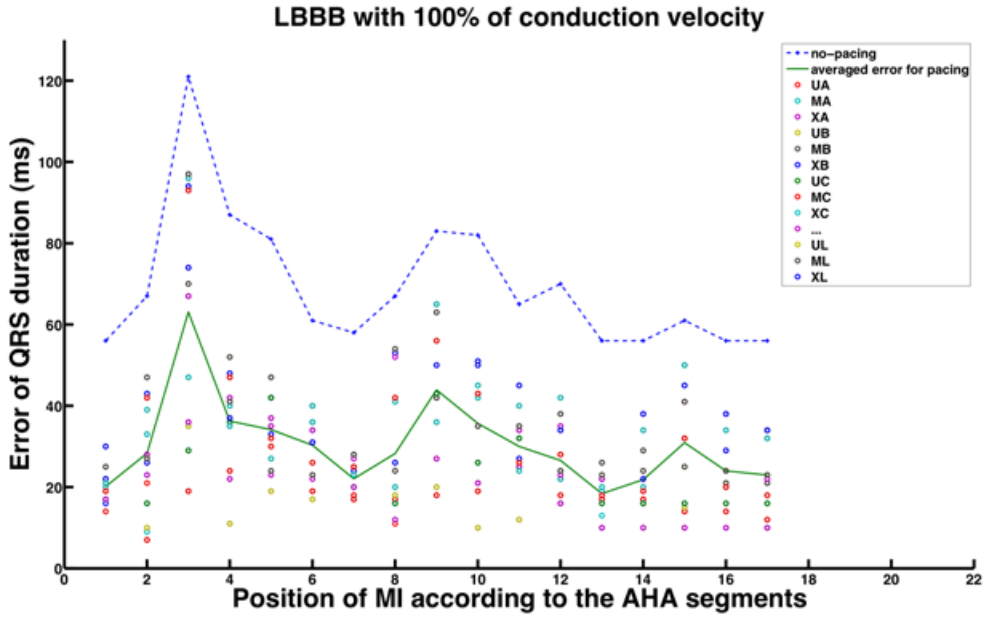

Figure 8.54. The minimal $error_{QRS}$ achieved by the second optimization method versus AHA segments 1 to 17 corresponding to the 17 different infarction positions. (Each circular point is related to one pair of electrodes. The optimal electrode setups is demonstrated with a green line while the blue line shows the $error_{QRS}$ pathology without pacing.)

Infarction position	$Error_{QRS}$ (phy-path) ms	$Error_{QRS}$ (phy-pac) ms	% $Error_{QRS}$ reduction	Opt. elec positions	Opt. A-V ms	Opt. V-V ms	Nr. of sim.
AHA1	82	29	64.63	UE	160.00	70.00	528
AHA2	96	30	68.75	UH	160.00	70.00	512
AHA3	165	44	73.33	UG	160.00	70.00	273
AHA4	120	40	66.66	UE	160.00	70.00	418
AHA5	114	44	61.40	UE	160.00	70.00	510
AHA6	88	38	56.81	UE	160.00	70.00	504
AHA7	85	30	64.70	UE	160.00	70.00	487
AHA8	94	28	70.21	UE	160.00	70.00	471
AHA9	118	42	64.40	UF	160.00	70.00	455
AHA10	115	35	69.56	UE	160.00	70.00	498
AHA11	93	39	58.06	UE	160.00	70.00	496
AHA12	92	25	72.82	UF	160.00	70.00	512
AHA13	82	10	87.80	UE	160.00	70.00	501
AHA14	82	25	69.51	UE	160.00	70.00	467
AHA15	91	29	68.13	UE	160.00	70.00	459
AHA16	82	20	75.60	UE	160.00	70.00	458
AHA17	82	29	64.63	UE	160.00	70.00	483

phy-path: between physiology and pathology, phy-pac: between physiology and pacing, Opt: optimal, elec: electrodes, Nr. of sim: number of simulations.

Table 8.47. Results of the second optimization method for Patient-8 with 80 % conduction velocity.

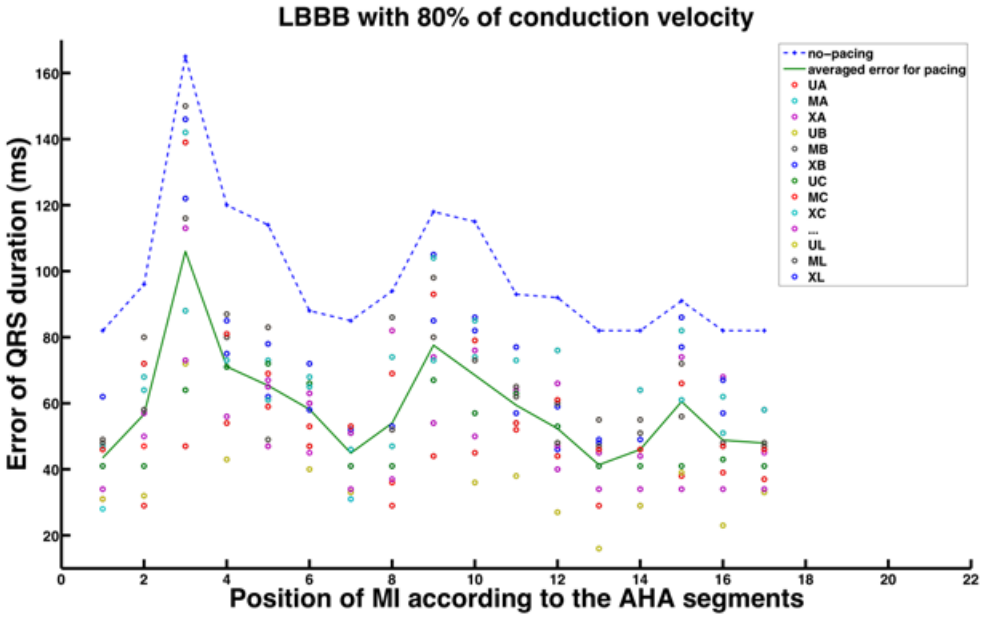

Figure 8.55. The minimal $error_{QRS}$ achieved by the second optimization method versus AHA segments 1 to 17 corresponding to the 17 different infarction positions. (Each circular point is related to one pair of electrodes. The optimal electrode setups is demonstrated with a green line while the blue line shows the $error_{QRS}$ pathology without pacing.)

Infarction position	$Error_{QRS}$ (phy-path) ms	$Error_{QRS}$ (phy-pac) ms	% $Error_{QRS}$ reduction	Opt. elec positions	Opt. A-V ms	Opt. V-V ms	Nr. of sim.
AHA1	125	45	64.00	UF	160.00	70.00	440
AHA2	144	65	55.55	UF	160.00	70.00	394
AHA3	237	100	57.80	UH	160.00	70.00	245
AHA4	176	95	46.02	UH	160.00	70.00	412
AHA5	166	94	43.37	UF	160.00	70.00	362
AHA6	133	93	30.07	UF	160.00	70.00	393
AHA7	130	45	65.38	UF	160.00	70.00	448
AHA8	141	65	53.90	UF	160.00	70.00	381
AHA9	178	85	52.24	UF	160.00	70.00	377
AHA10	171	75	56.14	UE	160.00	70.00	416
AHA11	141	79	43.97	UF	160.00	70.00	373
AHA12	136	70	48.52	UF	160.00	70.00	384
AHA13	125	45	64.00	UF	160.00	70.00	408
AHA14	125	70	44.00	UF	160.00	70.00	386
AHA15	141	75	46.80	UF	160.00	70.00	305
AHA16	125	55	56.00	UF	160.00	70.00	398
AHA17	125	70	44.00	UF	160.00	70.00	428

phy-path: between physiology and pathology, phy-pac: between physiology and pacing, Opt: optimal, elec: electrodes, Nr. of sim: number of simulations.

Table 8.48. Results of the second optimization method for Patient-8 with 60 % conduction velocity.

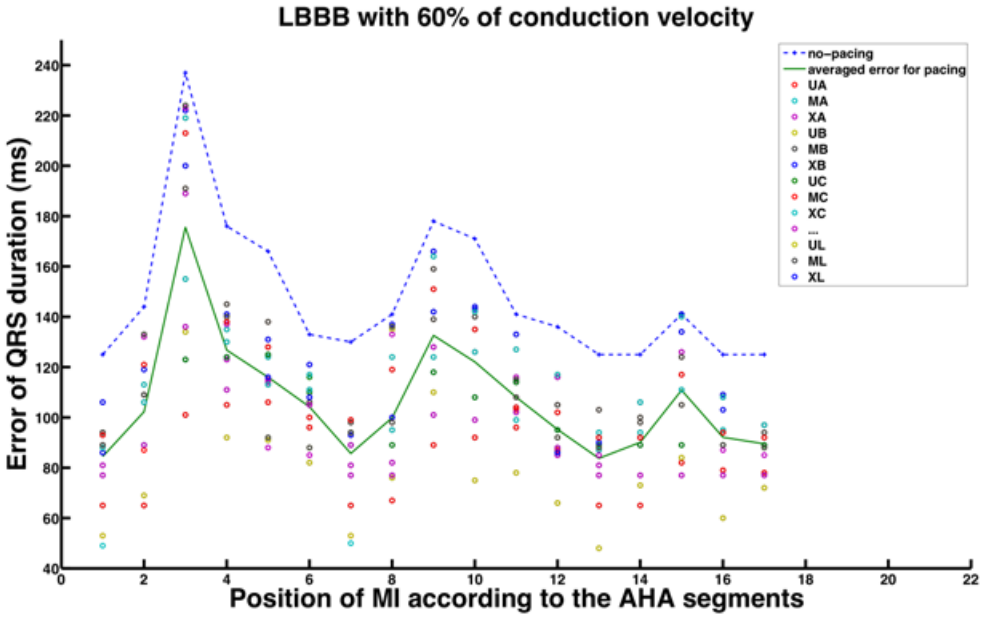

Figure 8.56. The minimal $error_{QRS}$ achieved by the second optimization method versus AHA segments 1 to 17 corresponding to the 17 different infarction positions. (Each circular point is related to one pair of electrodes. The optimal electrode setups is demonstrated with a green line while the blue line shows the $error_{QRS}$ pathology without pacing.)

8.1.9 Patient-9

The electrode positioning setup is demonstrated in figure 8.57. The results of both optimization methods are summarized in tables 8.49 - 8.54 for the several conduction velocities. The minimal errors associated with each electrode setup for each MI position are illustrated in figures 8.58 - 8.63.

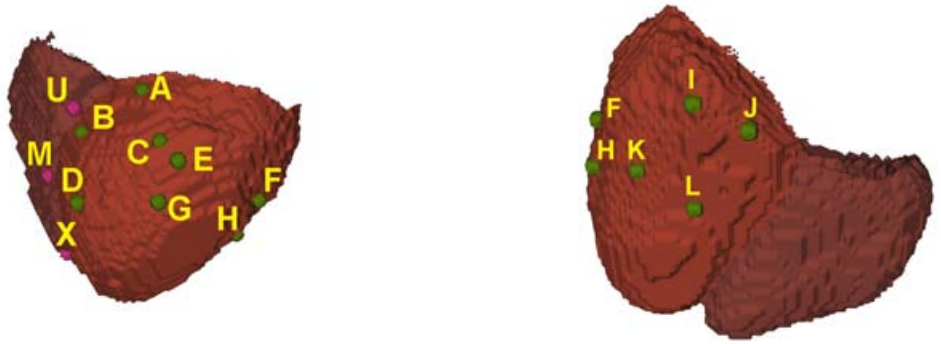

(a) (b)

Figure 8.57. The electrode positions chosen for the Patient-9 heart model. The electrodes A, B, C and D are referred to the anterior branches of coronary sinus. The electrodes I, J, K and L are referred to the posterior branches of coronary sinus. The electrodes E, F, G and H are located on the left ventricular free wall. The electrodes U, M and X are located at the right ventricular upper septum, middle septum and apex respectively.

Both optimization methods mostly found the optimal left electrode position in the lateral wall or posterolateral of the left ventricle (electrode E, F, G, H and K). The optimal right electrode position achieved by the first optimization method is mostly in upper or middle septal area (electrode U and M) however the position is fixed in the upper septal area (electrode U) with the second optimization method. The best timing delays range evaluated by the first optimization method is in the range of $110 - 160\ ms$ for the A-V delay and $42.85 - 70\ ms$. The best timing delays range achieved by the second optimization is overall $160\ ms$ for the A-V delay and $70\ ms$ for V-V delay.

DSA optimization delivers a number between 326 to 555 simulations for each pathological case. A maximum improvement of up to 36 %, the reduction percentage of E_{RMS} and an improvement of up to 83 %, the reduction percentage of $Error_{QRS}$, can be reached.

Infarction position	E_{RMS} (phy-path) ms	E_{RMS} (phy-pac) ms	% E_{RMS} reduction	Opt. elec positions	Opt. A-V ms	Opt. V-V ms	Nr. of sim.
AHA1	24.26	20.62	15.02	UG	160.00	70.00	395
AHA2	25.61	21.63	15.54	UG	160.00	70.00	408
AHA3	25.33	21.64	14.57	UG	160.00	70.00	395
AHA4	24.82	21.67	12.69	UG	160.00	70.00	398
AHA5	26.71	23.29	12.79	UG	160.00	70.00	371
AHA6	27.90	24.37	12.64	UG	160.00	70.00	385
AHA7	25.52	22.09	13.46	UG	160.00	70.00	388
AHA8	28.54	25.12	11.98	UG	160.00	70.00	413
AHA9	28.08	24.89	11.38	UG	160.00	70.00	383
AHA10	28.53	25.99	8.92	UH	160.00	70.00	371
AHA11	29.65	26.75	9.80	UG	160.00	70.00	370
AHA12	30.01	26.94	10.22	UG	160.00	70.00	367
AHA13	29.24	26.07	10.85	UH	160.00	70.00	376
AHA14	26.73	22.67	15.19	UG	160.00	70.00	398
AHA15	29.26	26.45	9.60	UH	160.00	70.00	375
AHA16	29.51	26.44	10.41	UG	160.00	70.00	392
AHA17	31.15	27.90	10.43	UG	160.00	70.00	386

phy-path: between physiology and pathology, phy-pac: between physiology and pacing, Opt: optimal, elec: electrodes, Nr. of sim: number of simulations.

Table 8.49. Results of the first optimization method for Patient-9 with 100 % conduction velocity.

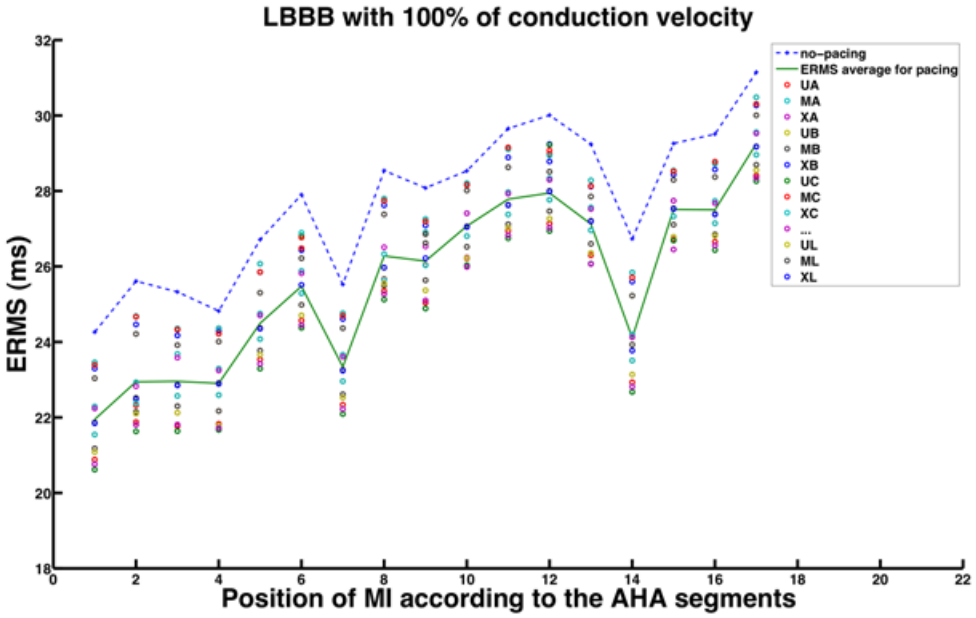

Figure 8.58. The minimal E_{RMS} achieved by the first optimization method versus AHA segments 1 to 17 corresponding to the 17 different infarction positions. (Each circular point is related to one pair of electrodes. The optimal electrode set up is demonstrated with a green line while the blue line shows the E_{RMS} pathology without pacing.)

Infarction position	E_{RMS} (phy-path) ms	E_{RMS} (phy-pac) ms	% E_{RMS} reduction	Opt. elec positions	Opt. A-V ms	Opt. V-V ms	Nr. of sim.
AHA1	28.31	21.36	24.56	UH	150.00	66.13	407
AHA2	29.89	22.56	24.52	UH	160.00	70.00	416
AHA3	29.34	22.39	23.70	UH	150.00	66.13	414
AHA4	28.57	22.41	21.57	UH	160.00	70.00	427
AHA5	30.52	23.96	21.50	UH	150.00	66.13	424
AHA6	31.82	25.12	21.08	UH	160.00	70.00	419
AHA7	29.40	22.78	22.51	UH	150.00	66.13	406
AHA8	32.27	25.89	19.78	UH	160.00	70.00	414
AHA9	31.62	25.68	18.78	UG	130.00	55.27	408
AHA10	31.73	26.81	15.52	XF	120.00	46.72	384
AHA11	33.07	27.42	17.09	UH	160.00	70.00	414
AHA12	33.56	27.59	17.79	UH	160.00	70.00	418
AHA13	32.94	26.68	19.02	UH	160.00	70.00	419
AHA14	30.80	23.47	23.81	UH	160.00	70.00	415
AHA15	32.61	27.41	15.93	MH	120.00	49.84	359
AHA16	33.01	27.16	17.71	UH	160.00	70.00	388
AHA17	34.42	28.82	16.27	UH	160.00	70.00	383

phy-path: between physiology and pathology, phy-pac: between physiology and pacing, Opt: optimal, elec: electrodes, Nr. of sim: number of simulations.

Table 8.50. Results of the first optimization method for Patient-9 with 80 % conduction velocity.

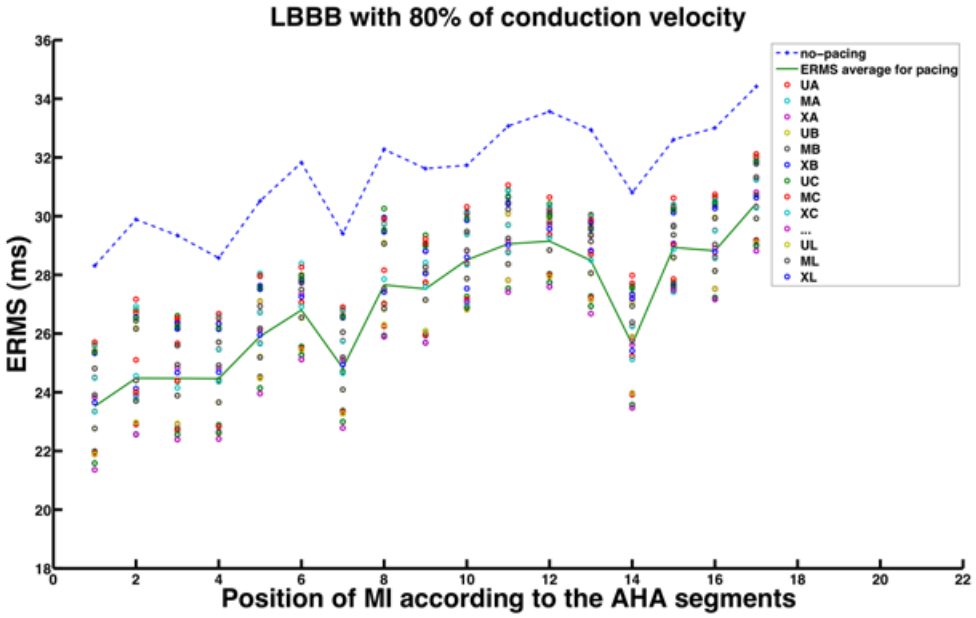

Figure 8.59. The minimal E_{RMS} achieved by the first optimization method versus AHA segments 1 to 17 corresponding to the 17 different infarction positions. (Each circular point is related to one pair of electrodes. The optimal electrode set up is demonstrated with a green line while the blue line shows the E_{RMS} pathology without pacing.)

Infarction position	E_{RMS} (phy-path) ms	E_{RMS} (phy-pac) ms	% E_{RMS} reduction	Opt. elec positions	Opt. A-V ms	Opt. V-V ms	Nr. of sim.
AHA1	36.08	22.91	36.49	MH	120.00	46.72	550
AHA2	38.12	24.03	36.96	MH	120.00	46.72	540
AHA3	37.11	23.89	35.61	MH	120.00	46.72	555
AHA4	35.90	23.81	33.67	MH	120.00	46.72	551
AHA5	37.97	25.36	33.19	MH	120.00	46.72	529
AHA6	39.44	26.43	32.99	MH	120.00	46.72	521
AHA7	36.94	24.25	34.36	MH	120.00	46.72	539
AHA8	39.65	27.19	31.44	MH	120.00	46.72	523
AHA9	38.65	26.97	30.21	UH	120.00	46.72	522
AHA10	38.23	27.95	26.89	MH	110.00	42.85	524
AHA11	39.94	28.69	28.19	MH	120.00	46.72	509
AHA12	40.71	28.81	29.23	MH	120.00	46.72	521
AHA13	40.25	27.90	30.68	MH	120.00	46.72	508
AHA14	38.58	24.80	35.72	UH	120.00	46.72	531
AHA15	39.36	28.27	28.19	MH	110.00	42.85	545
AHA16	40.03	28.54	28.71	MH	120.00	46.72	481
AHA17	41.09	29.98	27.04	MH	120.00	46.72	506

phy-path: between physiology and pathology, phy-pac: between physiology and pacing, Opt: optimal, elec: electrodes, Nr. of sim: number of simulations.

Table 8.51. Results of the first optimization method for Patient-9 with 60 % conduction velocity.

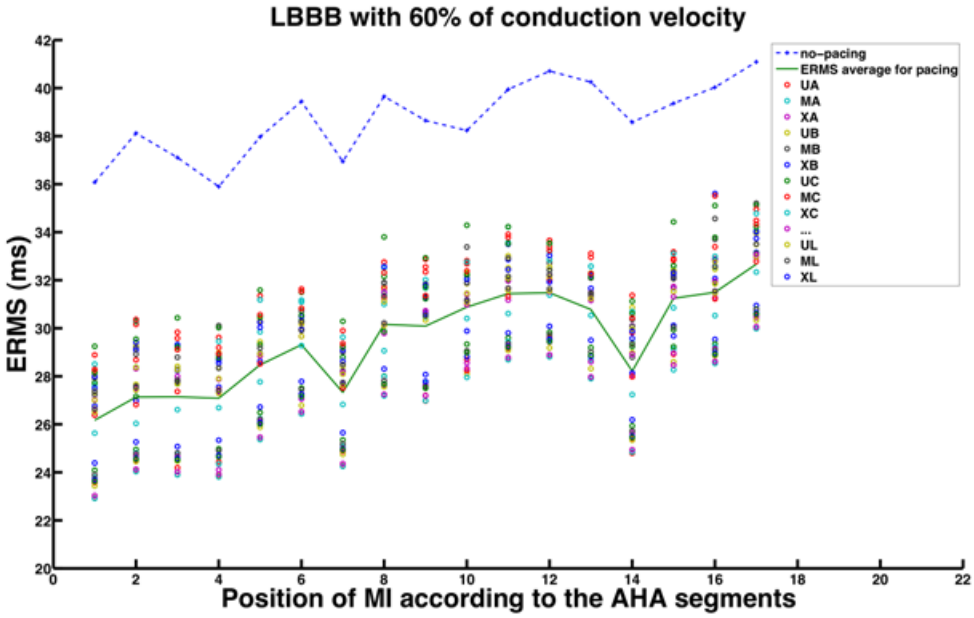

Figure 8.60. The minimal E_{RMS} achieved by the first optimization method versus AHA segments 1 to 17 corresponding to the 17 different infarction positions. (Each circular point is related to one pair of electrodes. The optimal electrode set up is demonstrated with a green line while the blue line shows the E_{RMS} pathology without pacing.)

Infarction position	$Error_{QRS}$ (phy-path) ms	$Error_{QRS}$ (phy-pac) ms	% $Error_{QRS}$ reduction	Opt. elec positions	Opt. A-V ms	Opt. V-V ms	Nr. of sim.
AHA1	44	15	65.90	UK	160.00	70.00	479
AHA2	64	12	81.25	UH	160.00	70.00	420
AHA3	68	12	82.35	UK	160.00	70.00	399
AHA4	70	18	74.28	UK	160.00	70.00	455
AHA5	55	18	67.27	UK	160.00	70.00	473
AHA6	37	13	64.86	UK	160.00	70.00	590
AHA7	39	15	61.53	UK	160.00	70.00	394
AHA8	59	12	79.66	UK	160.00	70.00	451
AHA9	66	22	66.66	UK	160.00	70.00	490
AHA10	74	22	70.27	UH	160.00	70.00	501
AHA11	62	10	83.87	UK	160.00	70.00	418
AHA12	39	8	79.48	UK	160.00	70.00	383
AHA13	34	15	55.88	UG	160.00	70.00	455
AHA14	48	10	79.16	UK	160.00	70.00	492
AHA15	50	18	64.00	UE	160.00	70.00	526
AHA16	79	20	74.68	UH	160.00	70.00	505
AHA17	39	10	74.35	UH	160.00	70.00	511

phy-path: between physiology and pathology, phy-pac: between physiology and pacing, Opt: optimal, elec: electrodes, Nr. of sim: number of simulations.

Table 8.52. Results of the second optimization method for Patient-9 with 100 % conduction velocity.

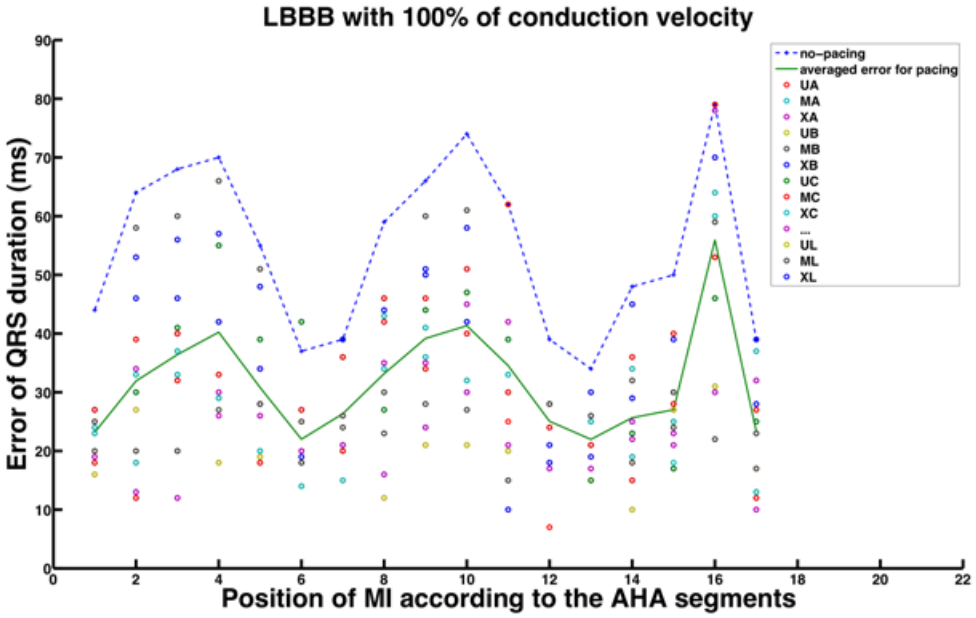

Figure 8.61. The minimal $error_{QRS}$ achieved by the second optimization method versus AHA segments 1 to 17 corresponding to the 17 different infarction positions. (Each circular point is related to one pair of electrodes. The optimal electrode set up is demonstrated with a green line while the blue line shows the $error_{QRS}$ pathology without pacing.)

Infarction position	$Error_{QRS}$ (phy-path) ms	$Error_{QRS}$ (phy-pac) ms	% $Error_{QRS}$ reduction	Opt. elec positions	Opt. A-V ms	Opt. V-V ms	Nr. of sim.
AHA1	76	18	76.31	UK	160.00	70.00	492
AHA2	103	30	70.87	UK	160.00	70.00	372
AHA3	105	32	59.52	UK	160.00	70.00	368
AHA4	108	38	64.81	UK	160.00	70.00	382
AHA5	87	37	57.47	UK	160.00	70.00	411
AHA6	67	16	76.11	UK	160.00	70.00	496
AHA7	70	45	35.71	UK	160.00	70.00	352
AHA8	95	40	57.89	UK	160.00	70.00	488
AHA9	104	50	51.92	UK	160.00	70.00	441
AHA10	111	48	56.75	UE	160.00	70.00	482
AHA11	88	32	63.63	UK	160.00	70.00	404
AHA12	70	36	48.57	UK	160.00	70.00	326
AHA13	63	34	46.03	UK	160.00	70.00	425
AHA14	82	20	75.60	UK	160.00	70.00	492
AHA15	85	34	60.00	UE	160.00	70.00	502
AHA16	120	50	58.33	UK	160.00	70.00	428
AHA17	71	34	52.11	UK	160.00	70.00	490

phy-path: between physiology and pathology, phy-pac: between physiology and pacing, Opt: optimal, elec: electrodes, Nr. of sim: number of simulations.

Table 8.53. Results of the second optimization method for Patient-9 with 80 % conduction velocity.

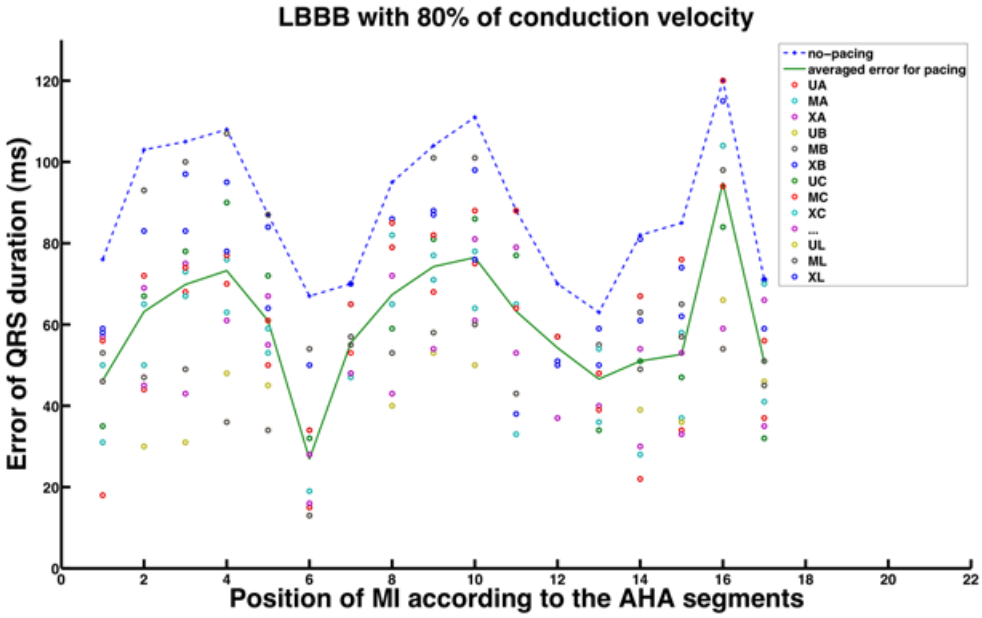

Figure 8.62. The minimal E_{RMS} achieved by the first optimization method versus AHA segments 1 to 17 corresponding to the 17 different infarction positions. (Each circular point is related to one pair of electrodes. The optimal electrode set up is demonstrated with a green line while the blue line shows the E_{RMS} pathology without pacing.)

Infarction position	$Error_{QRS}$ (phy-path) ms	$Error_{QRS}$ (phy-pac) ms	% $Error_{QRS}$ reduction	Opt. elec positions	Opt. A-V ms	Opt. V-V ms	Nr. of sim.
AHA1	126	60	52.38	UK	160.00	70.00	444
AHA2	166	78	53.01	UK	160.00	70.00	360
AHA3	170	78	54.11	UK	160.00	70.00	367
AHA4	170	84	50.58	UF	160.00	70.00	353
AHA5	141	81	42.55	UK	160.00	70.00	354
AHA6	116	42	63.79	UK	160.00	70.00	417
AHA7	120	90	25.00	UK	160.00	70.00	329
AHA8	156	80	48.71	UK	160.00	70.00	389
AHA9	167	110	34.13	UK	160.00	70.00	379
AHA10	175	100	42.85	UE	160.00	70.00	407
AHA11	142	80	43.66	UK	160.00	70.00	365
AHA12	119	84	29.41	UK	160.00	70.00	293
AHA13	112	82	26.78	UK	160.00	70.00	381
AHA14	140	65	53.57	UF	160.00	70.00	390
AHA15	142	76	46.47	UE	160.00	70.00	405
AHA16	189	110	41.79	UK	160.00	70.00	367
AHA17	122	78	36.06	UK	160.00	70.00	406

phy-path: between physiology and pathology, phy-pac: between physiology and pacing, Opt: optimal, elec: electrodes, Nr. of sim: number of simulations.

Table 8.54. Results of the second optimization method for Patient-9 with 60 % conduction velocity.

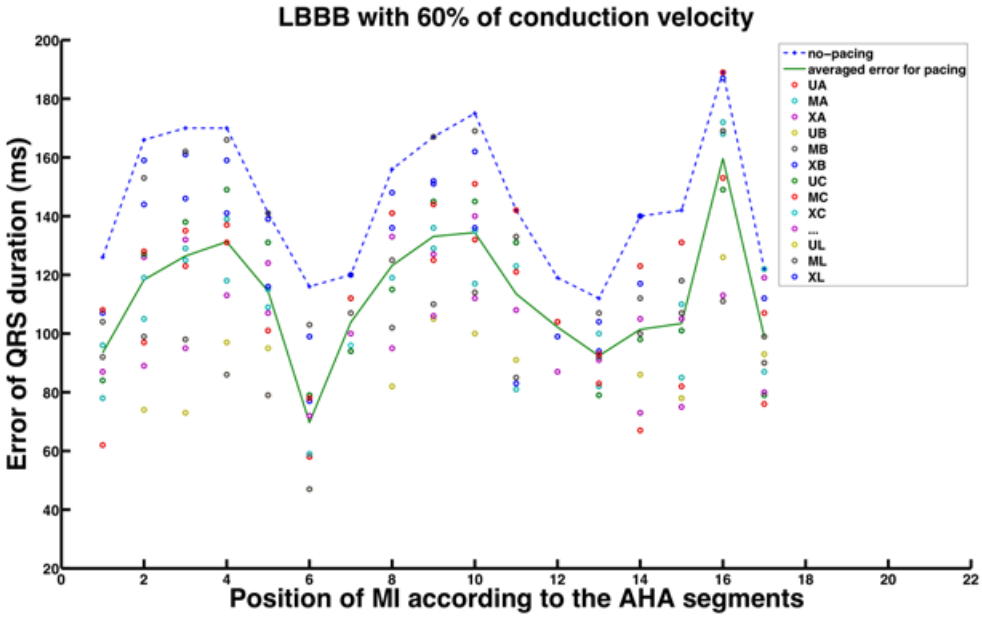

Figure 8.63. The minimal E_{RMS} achieved by the first optimization method versus AHA segments 1 to 17 corresponding to the 17 different infarction positions. (Each circular point is related to one pair of electrodes. The optimal electrode set up is demonstrated with a green line while the blue line shows the E_{RMS} pathology without pacing.)

8.1.10 Patient-10

The electrode positioning setup is demonstrated in figure 8.64. The results of both optimization methods are summarized in tables 8.55 - 8.60 for the several conduction velocities. The minimal errors associated with each electrode setup for each MI position are illustrated in figures 8.65 - 8.70.

(a) (b)

Figure 8.64. The electrode positions chosen for the Patient-10 heart model. The electrodes A, B, C and D are referred to the anterior branches of coronary sinus. The electrodes I, J, K and L are referred to the posterior branches of coronary sinus. The electrodes E, F, G and H are located on the left ventricular free wall. The electrodes U, M and X are located at the right ventricular upper septum, middle septum and apex respectively.

Both optimization methods mostly found the optimal left electrode position in the lateral wall or posterolateral of the left ventricle (electrode H, K and L). The optimal right electrode position is mostly in upper or middle septal area (electrode U and M). The best timing delays range evaluated by the first optimization method is in the range of $105 - 160\ ms$ for the A-V delay and $38.18 - 70\ ms$. The best timing delays range achieved by the second optimization is overall $160\ ms$ for the A-V delay and $70\ ms$ for V-V delay.

DSA optimization delivers a number between 323 to 604 simulations for each pathological case. A maximum improvement of up to 38 %, the reduction percentage of E_{RMS} and an improvement of up to 73 %, the reduction percentage of $Error_{QRS}$, can be reached.

Infarction position	E_{RMS} (phy-path) ms	E_{RMS} (phy-pac) ms	% E_{RMS} reduction	Opt. elec positions	Opt. A-V ms	Opt. V-V ms	Nr. of sim.
AHA1	18.12	15.87	12.43	ML	140.00	57.58	413
AHA2	18.78	16.85	10.30	ML	140.00	57.58	412
AHA3	19.05	17.21	9.67	ML	140.00	57.58	426
AHA4	18.22	16.00	12.20	ML	140.00	57.58	418
AHA5	17.97	15.77	12.21	ML	140.00	57.58	426
AHA6	18.74	16.65	11.17	ML	140.00	57.58	420
AHA7	20.36	18.26	10.34	UL	140.00	57.58	362
AHA8	19.78	17.80	10.00	UL	140.00	57.58	414
AHA9	18.91	16.92	10.51	MK	140.00	57.58	473
AHA10	20.51	18.18	11.33	ML	140.00	57.58	446
AHA11	20.91	19.01	9.06	UK	160.00	70.00	441
AHA12	22.12	20.32	8.14	UK	160.00	70.00	438
AHA13	20.46	18.01	11.97	MK	160.00	70.00	443
AHA14	19.72	17.81	9.71	ML	140.00	57.58	418
AHA15	15.43	12.54	18.74	ML	130.00	52.15	446
AHA16	15.63	13.03	16.66	ML	140.00	57.58	438
AHA17	19.06	17.01	10.76	ML	140.00	57.58	420

phy-path: between physiology and pathology, phy-pac: between physiology and pacing, Opt: optimal, elec: electrodes, Nr. of sim: number of simulations.

Table 8.55. Results of the first optimization method for Patient-10 for 100 % conduction velocity.

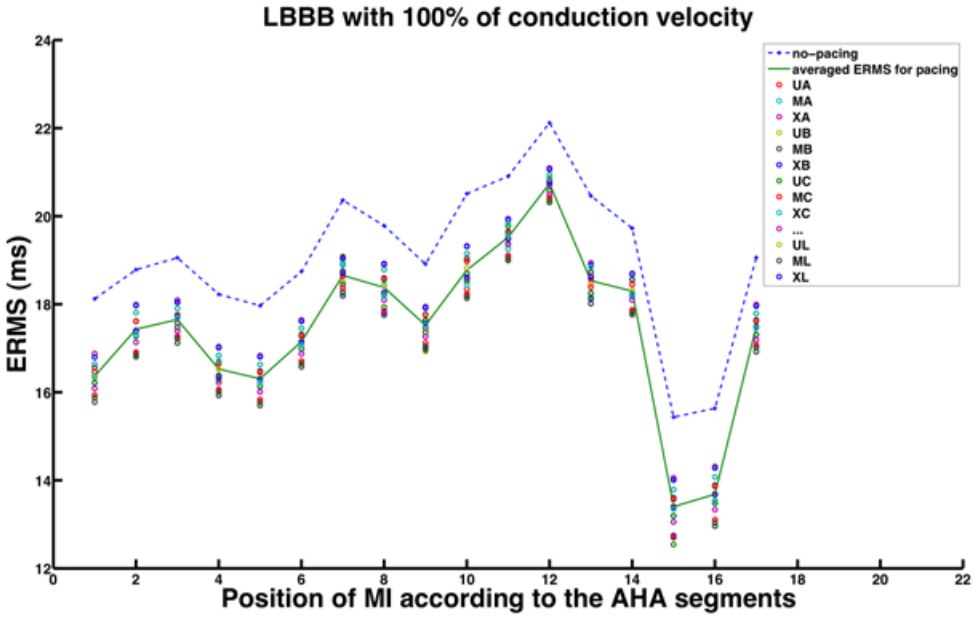

Figure 8.65. The minimal E_{RMS} achieved by the first optimization method versus AHA segments 1 to 17 corresponding to the 17 different infarction positions. (Each circular point is related to one pair of electrodes. The optimal electrode set up is demonstrated with a green line while the blue line shows the E_{RMS} pathology without pacing.)

Infarction position	E_{RMS} (phy-path) ms	E_{RMS} (phy-pac) ms	% E_{RMS} reduction	Opt. elec positions	Opt. A-V ms	Opt. V-V ms	Nr. of sim.
AHA1	20.51	16.34	20.33	UK	140.00	57.58	378
AHA2	20.94	17.32	17.28	ML	130.00	53.71	377
AHA3	21.14	17.65	16.50	UK	140.00	60.70	362
AHA4	20.58	16.50	19.80	UK	140.00	57.58	412
AHA5	20.33	16.30	19.82	UK	140.00	60.70	388
AHA6	21.02	17.16	18.38	ML	120.00	46.72	387
AHA7	22.64	18.67	17.50	UK	140.00	60.70	421
AHA8	21.95	18.28	16.70	ML	120.00	46.72	437
AHA9	21.02	17.21	18.15	MK	120.00	46.72	369
AHA10	22.80	18.64	18.26	UK	140.00	57.58	398
AHA11	22.98	19.47	15.27	ML	120.00	46.72	389
AHA12	24.15	20.72	14.20	ML	120.00	46.72	357
AHA13	22.85	18.60	18.60	XK	140.00	57.58	416
AHA14	21.86	18.30	16.31	ML	120.00	46.72	345
AHA15	18.14	13.23	27.07	ML	120.00	46.72	412
AHA16	18.31	13.53	26.14	ML	127.50	46.89	389
AHA17	21.30	17.47	17.98	UK	140.00	57.58	371

phy-path: between physiology and pathology, phy-pac: between physiology and pacing, Opt: optimal, elec: electrodes, Nr. of sim: number of simulations.

Table 8.56. Results of the first optimization method for Patient-10 for 80 % conduction velocity.

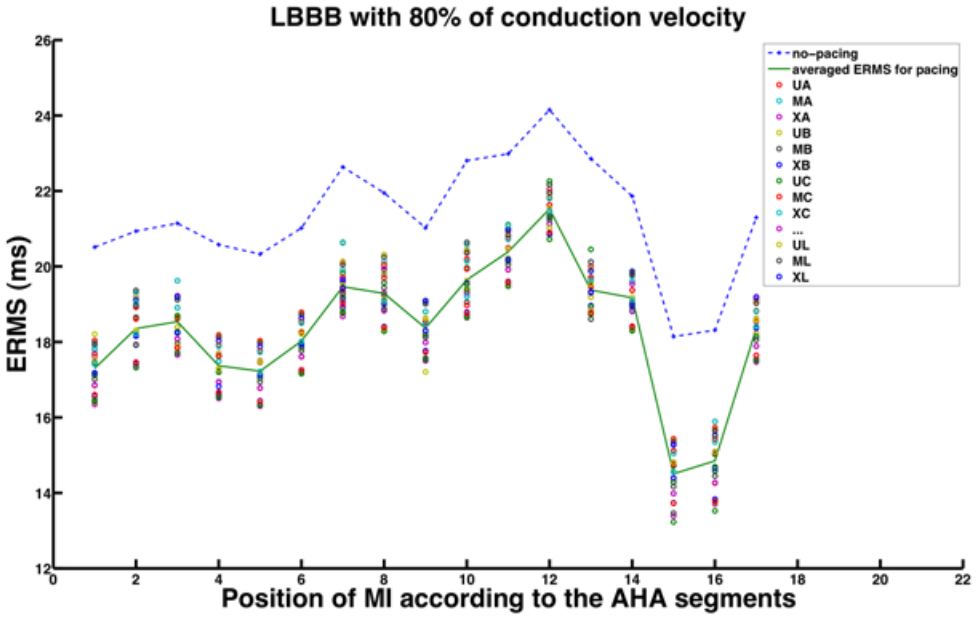

Figure 8.66. The minimal E_{RMS} achieved by the first optimization method versus AHA segments 1 to 17 corresponding to the 17 different infarction positions. (Each circular point is related to one pair of electrodes. The optimal electrode set up is demonstrated with a green line while the blue line shows the E_{RMS} pathology without pacing.)

Infarction position	E_{RMS} (phy-path) ms	E_{RMS} (phy-pac) ms	% E_{RMS} reduction	Opt. elec positions	Opt. A-V ms	Opt. V-V ms	Nr. of sim.
AHA1	25.18	17.21	31.64	MK	110.00	42.85	587
AHA2	25.22	18.06	28.38	MK	115.00	44.00	578
AHA3	25.32	18.35	27.53	MK	115.00	44.00	528
AHA4	25.18	17.27	31.43	MK	110.00	42.85	566
AHA5	24.94	17.03	31.74	MK	115.00	44.00	582
AHA6	25.52	17.85	30.05	MK	115.00	44.00	562
AHA7	27.16	19.56	27.99	MK	115.00	44.00	560
AHA8	26.27	18.96	27.83	MK	115.00	44.00	586
AHA9	25.24	18.14	28.12	MK	110.00	41.29	544
AHA10	27.33	19.31	29.36	MK	115.00	44.00	604
AHA11	27.18	20.13	25.93	MK	115.00	44.00	575
AHA12	28.28	21.34	24.55	MK	112.50	42.26	555
AHA13	27.52	19.38	29.58	MK	105.00	38.18	577
AHA14	26.14	18.97	27.44	MK	115.00	44.00	552
AHA15	23.25	14.29	38.53	MK	115.00	44.00	587
AHA16	23.35	14.54	37.75	MK	115.00	44.00	596
AHA17	25.75	18.20	29.29	MK	110.00	42.85	537

phy-path: between physiology and pathology, phy-pac: between physiology and pacing, Opt: optimal, elec: electrodes, Nr. of sim: number of simulations.

Table 8.57. Results of the first optimization method for Patient-10 for 60 % conduction velocity.

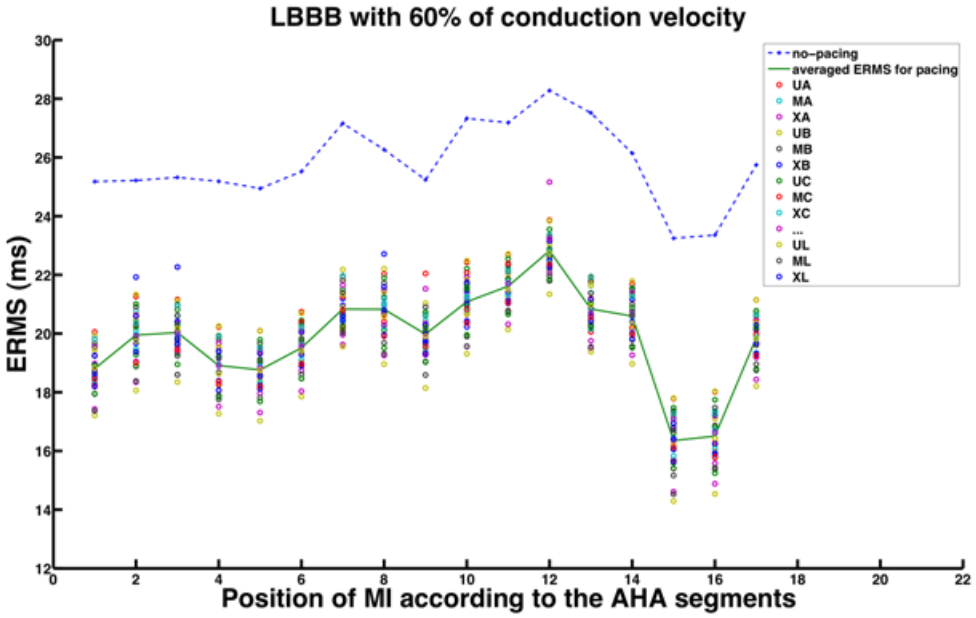

Figure 8.67. The minimal E_{RMS} achieved by the first optimization method versus AHA segments 1 to 17 corresponding to the 17 different infarction positions. (Each circular point is related to one pair of electrodes. The optimal electrode set up is demonstrated with a green line while the blue line shows the E_{RMS} pathology without pacing.)

Infarction position	$Error_{QRS}$ (phy-path) ms	$Error_{QRS}$ (phy-pac) ms	% $Error_{QRS}$ reduction	Opt. elec positions	Opt. A-V ms	Opt. V-V ms	Nr. of sim.
AHA1	71	19	73.23	UK	160.00	70.00	517
AHA2	92	26	71.73	UK	160.00	70.00	405
AHA3	87	30	65.52	UK	160.00	70.00	542
AHA4	70	29	58.57	MK	160.00	70.00	524
AHA5	69	38	44.92	MK	160.00	70.00	446
AHA6	70	33	52.86	UK	160.00	70.00	496
AHA7	72	22	69.44	UK	160.00	70.00	490
AHA8	88	25	71.59	UK	160.00	70.00	495
AHA9	84	30	64.28	UK	160.00	70.00	519
AHA10	79	29	63.29	UK	160.00	70.00	528
AHA11	69	20	71.01	UK	160.00	70.00	485
AHA12	69	20	71.01	UK	160.00	70.00	461
AHA13	75	20	73.33	MK	160.00	70.00	491
AHA14	70	25	64.28	MK	160.00	70.00	471
AHA15	69	29	57.97	UK	160.00	70.00	480
AHA16	69	20	71.01	UK	160.00	70.00	493
AHA17	70	29	58.57	MK	160.00	70.00	497

phy-path: between physiology and pathology, phy-pac: between physiology and pacing, Opt: optimal, elec: electrodes, Nr. of sim: number of simulations.

Table 8.58. Results of the second optimization method for Patient-10 with 100 % conduction velocity.

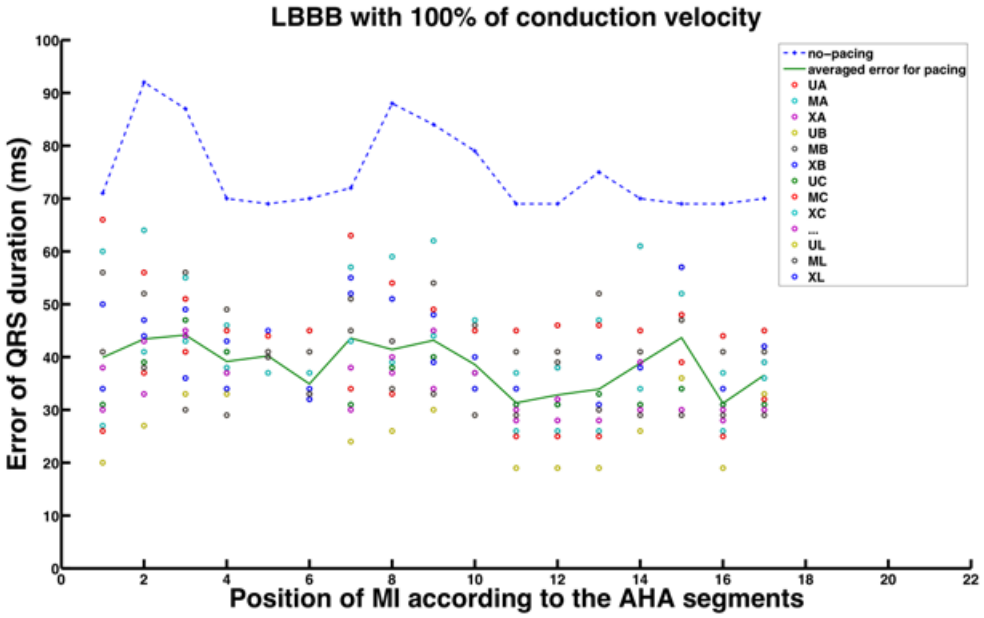

Figure 8.68. The minimal E_{RMS} achieved by the first optimization method versus AHA segments 1 to 17 corresponding to the 17 different infarction positions. (Each circular point is related to one pair of electrodes. The optimal electrode set up is demonstrated with a green line while the blue line shows the E_{RMS} pathology without pacing.)

Infarction position	$Error_{QRS}$ (phy-path) ms	$Error_{QRS}$ (phy-pac) ms	% $Error_{QRS}$ reduction	Opt. elec positions	Opt. A-V ms	Opt. V-V ms	Nr. of sim.
AHA1	102	45	55.88	UK	160.00	70.00	505
AHA2	128	58	54.68	UK	160.00	70.00	333
AHA3	125	56	55.20	MK	160.00	70.00	480
AHA4	103	55	46.60	UK	160.00	70.00	502
AHA5	102	64	37.26	MK	160.00	70.00	484
AHA6	102	55	46.07	MK	160.00	70.00	504
AHA7	104	52	50.00	MK	160.00	70.00	452
AHA8	125	58	53.60	MK	160.00	70.00	479
AHA9	121	58	52.06	MH	160.00	70.00	489
AHA10	112	55	50.89	UK	160.00	70.00	515
AHA11	102	52	49.01	UK	160.00	70.00	486
AHA12	102	52	49.01	UK	160.00	70.00	475
AHA13	108	52	51.85	MK	160.00	70.00	494
AHA14	102	56	45.09	UK	160.00	70.00	471
AHA15	102	55	46.07	UK	160.00	70.00	446
AHA16	102	52	49.01	MK	160.00	70.00	490
AHA17	102	55	46.07	UK	160.00	70.00	489

phy-path: between physiology and pathology, phy-pac: between physiology and pacing, Opt: optimal, elec: electrodes, Nr. of sim: number of simulations.

Table 8.59. Results of the second optimization method for Patient-10 with 80 % conduction velocity.

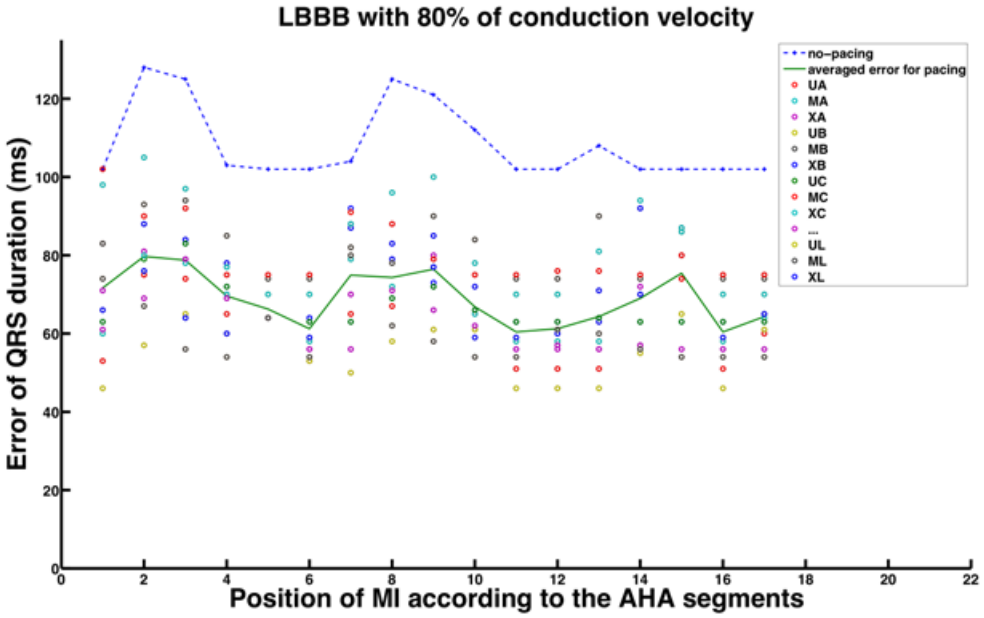

Figure 8.69. The minimal E_{RMS} achieved by the first optimization method versus AHA segments 1 to 17 corresponding to the 17 different infarction positions. (Each circular point is related to one pair of electrodes. The optimal electrode set up is demonstrated with a green line while the blue line shows the E_{RMS} pathology without pacing.)

Infarction position	$Error_{QRS}$ (phy-path) ms	$Error_{QRS}$ (phy-pac) ms	% $Error_{QRS}$ reduction	Opt. elec positions	Opt. A-V ms	Opt. V-V ms	Nr. of sim.
AHA1	154	90	41.55	UK	160.00	70.00	436
AHA2	190	114	40.00	UK	160.00	70.00	323
AHA3	184	100	45.65	MH	160.00	70.00	443
AHA4	156	100	35.90	UK	160.00	70.00	373
AHA5	154	104	32.47	MK	160.00	70.00	445
AHA6	154	90	41.55	UK	160.00	70.00	461
AHA7	158	95	39.87	UH	160.00	70.00	377
AHA8	183	108	40.98	UK	160.00	70.00	397
AHA9	180	102	43.33	UH	160.00	70.00	459
AHA10	168	95	43.45	MK	160.00	70.00	409
AHA11	154	90	41.55	UK	160.00	70.00	464
AHA12	154	90	44.78	UH	160.00	70.00	440
AHA13	163	90	44.78	MH	160.00	70.00	439
AHA14	155	95	38.70	MK	160.00	70.00	422
AHA15	154	95	38.31	MH	160.00	70.00	386
AHA16	154	90	41.55	MK	160.00	70.00	465
AHA17	154	95	38.31	UK	160.00	70.00	448

phy-path: between physiology and pathology, phy-pac: between physiology and pacing, Opt: optimal, elec: electrodes, Nr. of sim: number of simulations.

Table 8.60. Results of the second optimization method for Patient-10 with 60 % conduction velocity.

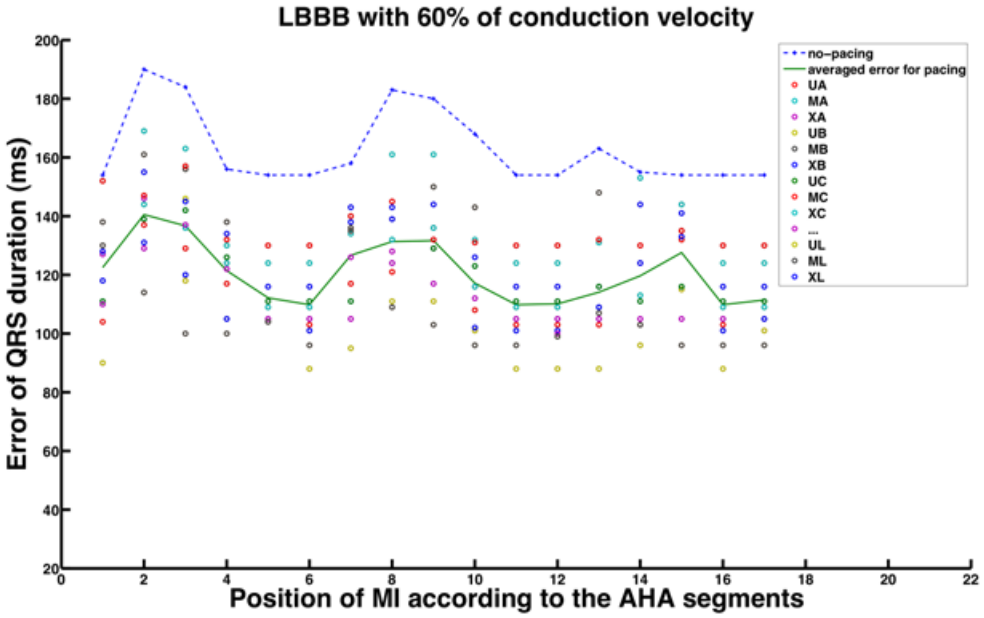

Figure 8.70. The minimal E_{RMS} achieved by the first optimization method versus AHA segments 1 to 17 corresponding to the 17 different infarction positions. (Each circular point is related to one pair of electrodes. The optimal electrode set up is demonstrated with a green line while the blue line shows the E_{RMS} pathology without pacing.)

8.2 Discussion on the Results

Several key observations can be made from this investigation: The influence of pacing locations on reducing electrical dyssynchrony. Placing the LV pacing tip on the lateral or postero lateral section of LV and pacing leads sequentially with a delay of $40 - 70$ ms helps to reduce dyssynchrony.

The optimal pacemaker setups achieved by both optimization methods for all patients (E_{RMS} and QRS based) are demonstrated in figures 8.71 - 8.76. It can be observed that the most optimal A-V delay achieved by the E_{RMS} based optimization is in the range of $120 - 160$ ms and by the QRS based method only 160 ms. The range of V-V delay for the the first method is $45 - 70$ ms and in the second method only 70 ms. The most frequent position of the left electrode is the LV lateral and posterolateral area.

For obtaining a global view upon the E_{RMS} based optimization method, the 10 patients data including the 17 infarction positions and the 3 different conduction velocities creating a sample space of 510 sample points are investigated. The distribution of the calculated values over the population is illustrated in the plotted histograms in figures (8.77 - 8.78). It is noticeable that the most frequent A-V delay is 160 ms and V-V delay is 70 ms. For each case, the most dominant value covered almost half of the population. In addition, it is interesting to note that A-V and V-V are not normally distributed, neither are they following a specific trend, which underlines the necessity of patient specific data analysis for establishing the optimal electrodes positions. The patient specific agreement between the timing delays and the electrode setups were calculated for determining if the analyzed optimization methods deliver equal results. The results are included in table 8.61 and they indicate that the agreement range of timing delays are varying between 5.9 % and 98 % . The agreement range of the electrode positions varies widely, somethimes the results are not equal while some results are 96 % identical. The association between the physiological, pathological and reduction errors of the two optimization methods were analyzed with Pearson correlation method [184]. For all three sets of data, the level of association is significant:

1. Correlation coefficients of QRS error and E_{RMS} between physiological and pathological cases: r=0.46, p<0.001.
2. Correlation coefficients of QRS error and E_{RMS} between physiological and pacing cases: r=0.25, p<0.001.
3. Correlation coefficients of QRS and E_{RMS} for reduction errors: r=-0.24, p<0.001.

The relation between the parameters of the two optimization methods is depicted in figures 8.79 - 8.81. The large variations of agreement ranges and the correlation coefficients prove that even though the two optimization methods are significantly associated, one cannot

be used as a confounder of the other. The r value and the frequent number of cases per analysis deliver the p values.

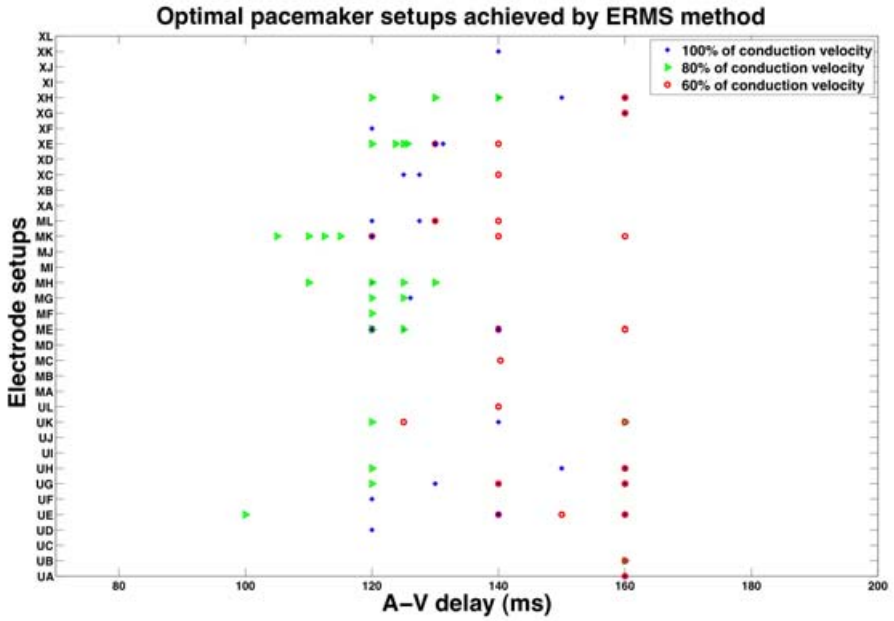

Figure 8.71. The optimal pacing parameters achieved by the first optimization method for all patients with different conduction velocities (The electrode setups versus A-V delays).

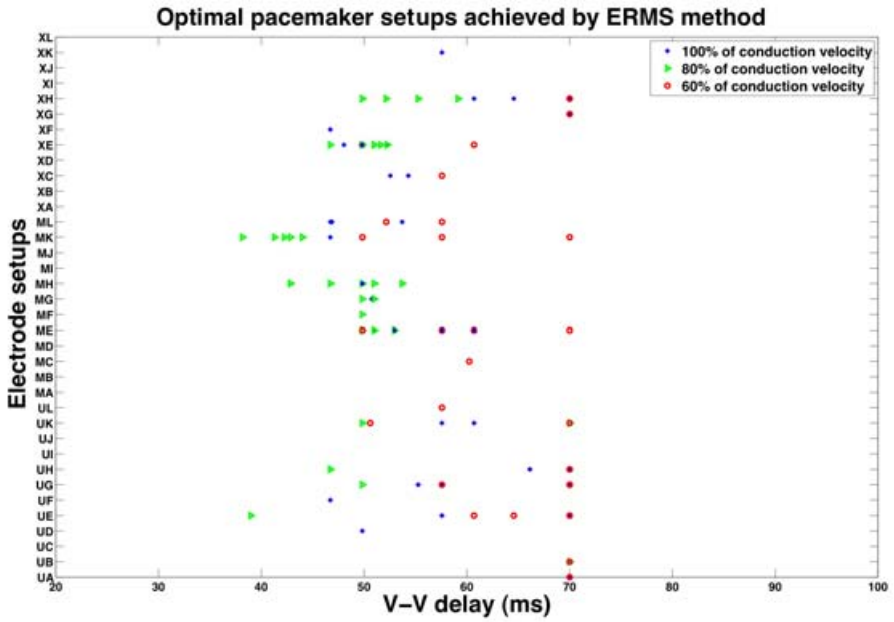

Figure 8.72. The optimal pacing parameters achieved by the first optimization method for all patients with different conduction velocities (The electrode setups versus V-V delays).

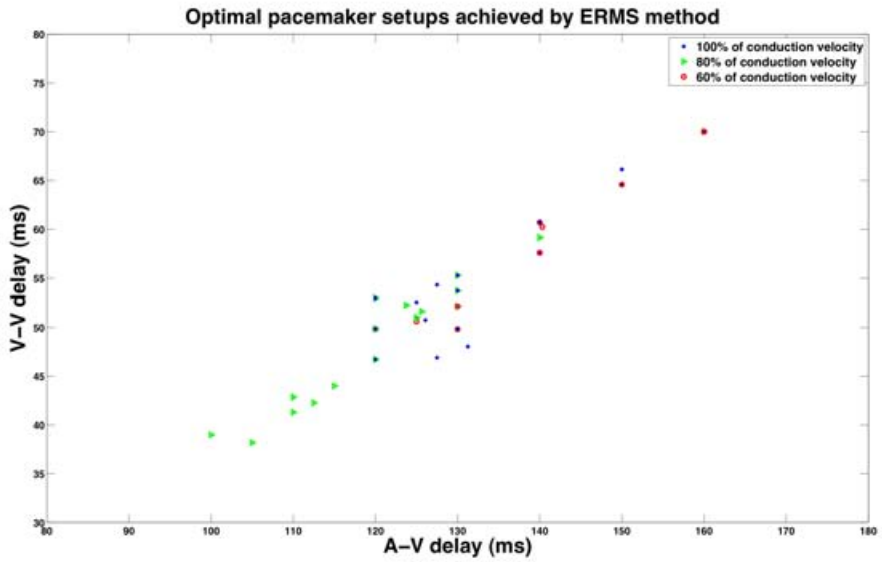

Figure 8.73. The optimal pacing parameters achieved by the first optimization method for all patients with different conduction velocities (The V-V delays versus A-V delays).

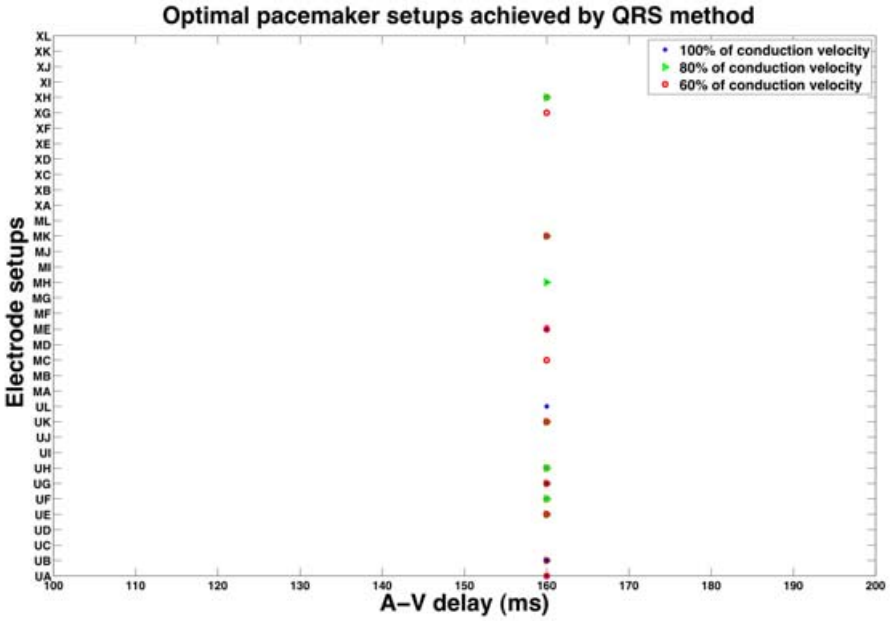

Figure 8.74. The optimal pacing parameters achieved by the second optimization method for all patients with different conduction velocities (The electrode setups versus A-V delays).

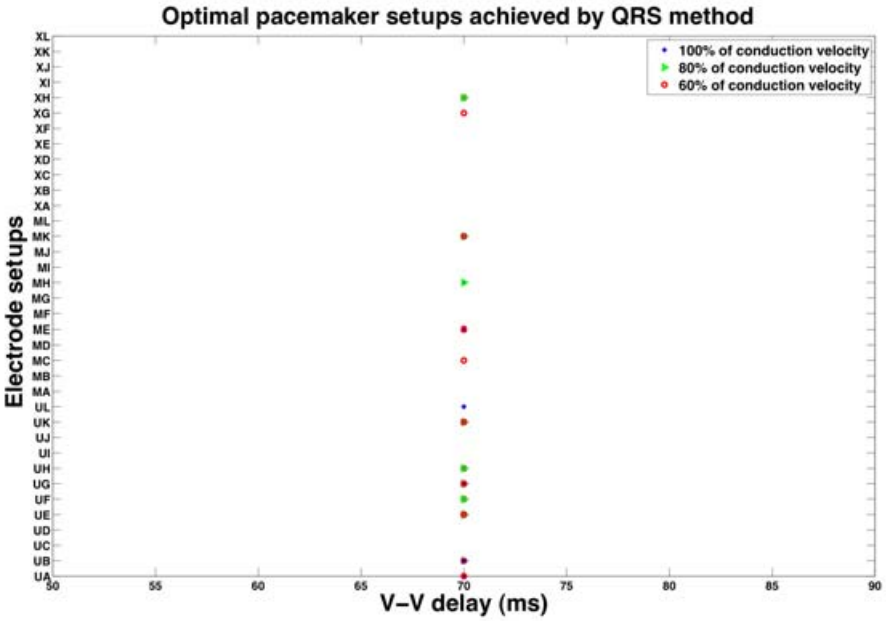

Figure 8.75. The optimal pacing parameters achieved by the second optimization method for all patients with different conduction velocities (The electrode setups versus V-V delays).

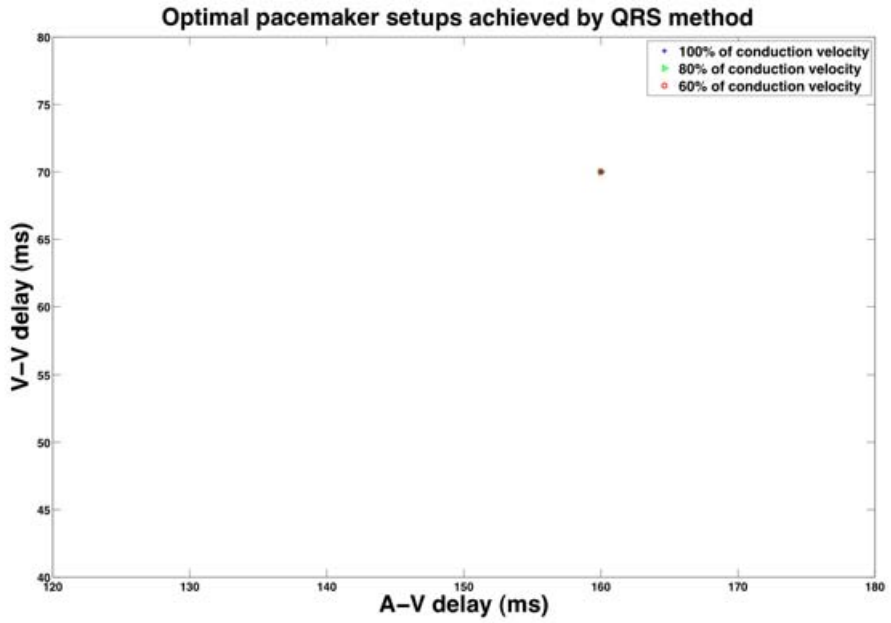

Figure 8.76. The optimal pacing parameters achieved by the second optimization method for all patients with different conduction velocities (The V-V delays versus A-V delays).

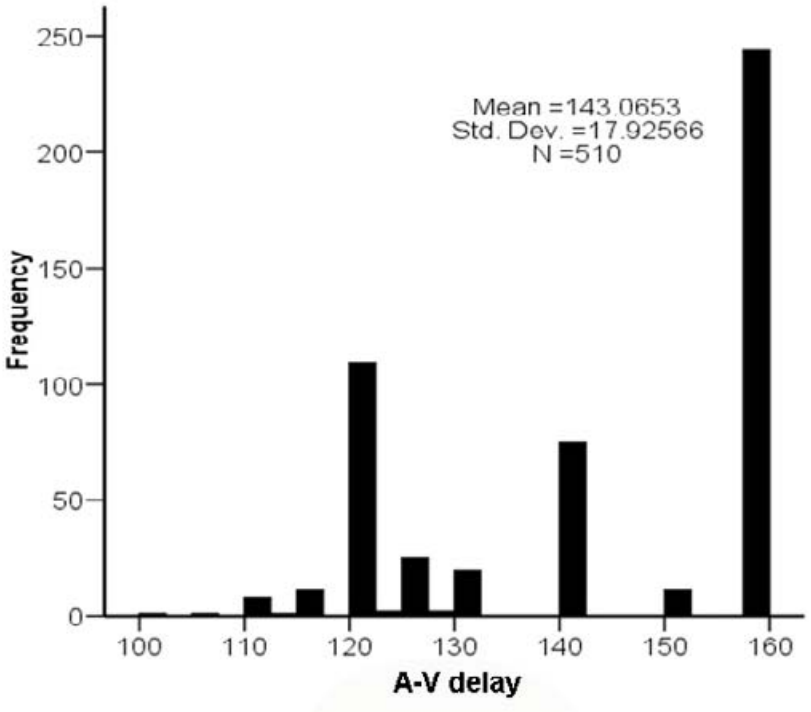

Figure 8.77. Histogram of the optimal A-V delays achieved by the first optimization method. The sample space N, mean value and standard deviation are 510, 143.06 and 17.92, respectively.

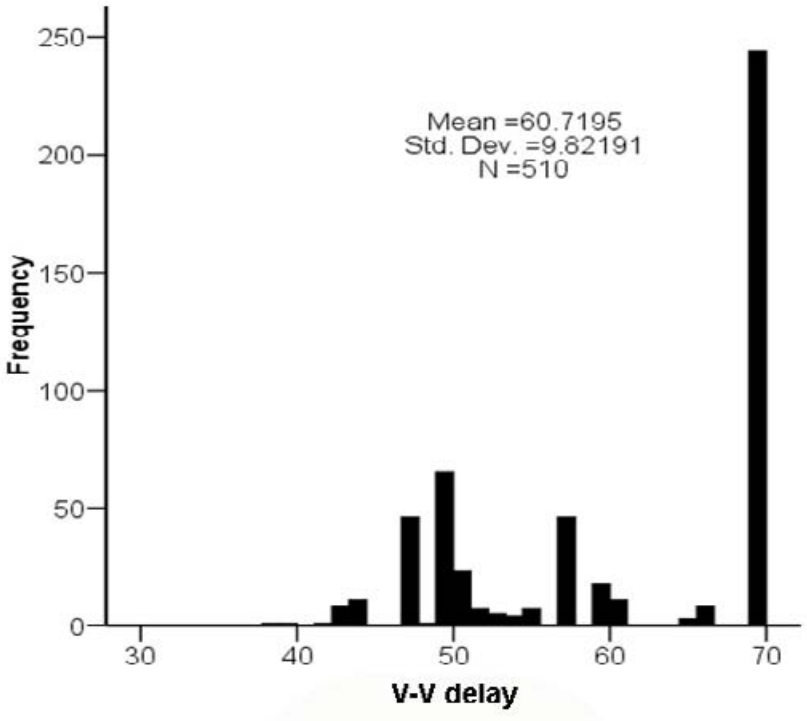

Figure 8.78. Histogram of the optimal V-V delays achieved by the first optimization method. The sample space N, mean value and standard deviation are 510, 60.71 and 9.82, respectively.

Patient ID	Equal A-V delay (%)	Equal V-V delay (%)	Equal electrode setups (%)
1	98	98	96.1
2	25.5	25.5	31.4
3	62.7	62.7	94.1
4	52.9	52.9	64.7
5	51	51	54.9
6	35.3	35.3	2
7	31.4	31.4	52.9
8	62.7	62.7	0
9	52.9	52.9	2
10	5.9	5.9	21.6
all	47.84	47.84	41.96

Table 8.61. Percentage range of agreement of timing delays and electrode setups for both optimization methods in all patients. All optimal pacing setups achieved from both optimization methods in 32.35 % of cases are equal.

The values corresponding to the electrodes positions, identified over all 10 patients including 17 infarction positions and 3 different conduction velocities were pooled and statistically tested according to the error. The descriptive statistics of the obtained distributions for each electrode position are incorporated in table 8.62.

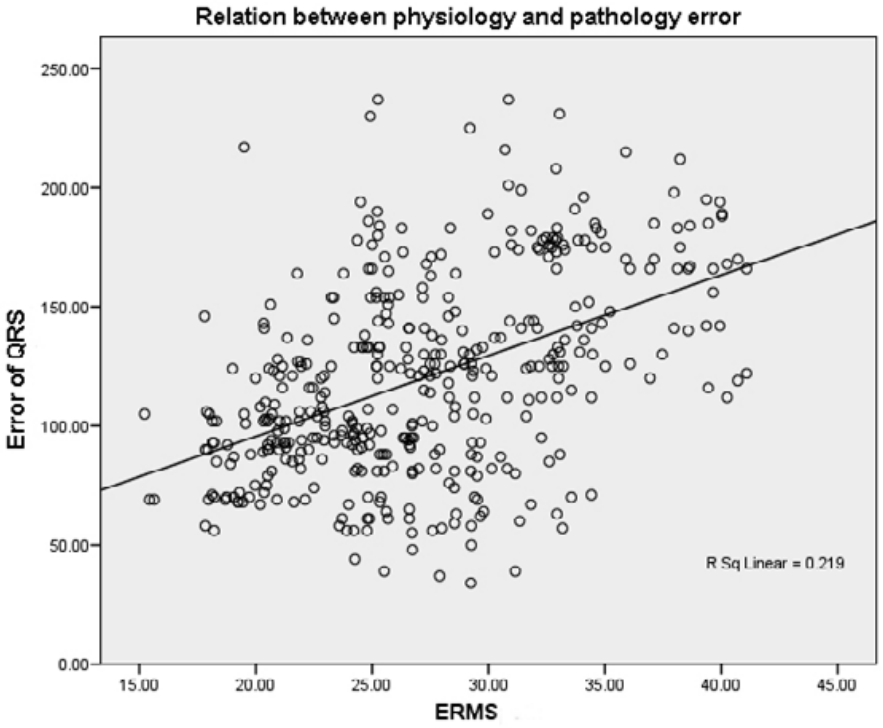

Figure 8.79. Regression line demonstrating the relation between both optimization methods in terms of physiological-pathological error.

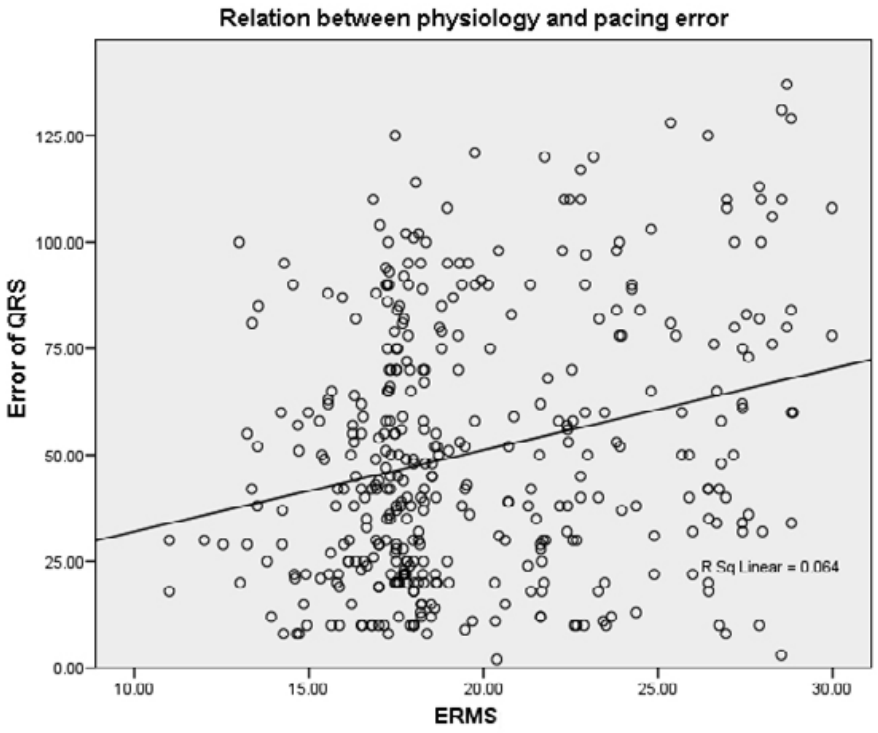

Figure 8.80. Regression line demonstrating the relation between both optimization methods for in terms of physiological-pacing error.

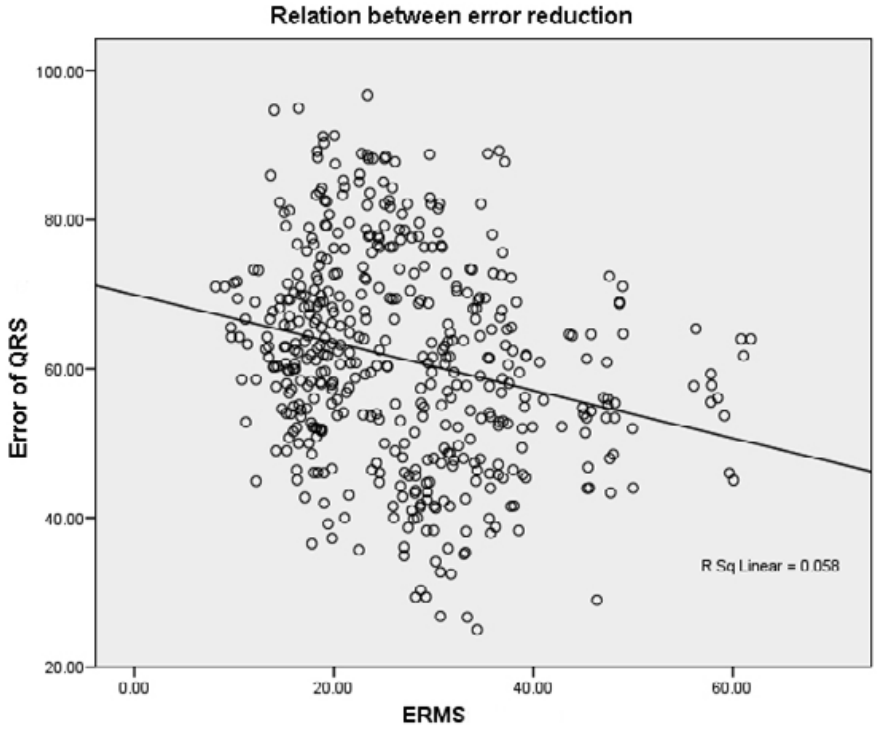

Figure 8.81. Regression line demonstrating the relation between both optimization methods for in terms of reduction error percentage.

Effect	Mean	Standard error
MC	84.28	36.07
ME	82.35	17.38
MH	167.33	21.19
MK	121.39	15.26
UA	62.58	16.16
UB	107.51	13.70
UE	111.86	11.46
UF	165.58	13.02
UG	126.30	11.44
UH	164.62	12.60
UK	121.37	11.79
UL	79.58	26.95
XG	95.41	32.21
XH	148.38	31.16

Effect is electrode position setups.

Table 8.62. Descriptive statistics of the obtained distributions for each electrode position.

The variables corresponding to the pacing electrodes were tested for normality using Shapiro-Wilk, Kolmogorov-Smirnov, Cramer-von-Mises and Anderson-Darling tests. The results of the tests are included in table 8.63.

In these tests, the null hypothesis is that the data is normally distributed and if the p value is small (<0.05) the hypothesis is being rejected. Therefore, all four tests underline that the data is normally distributed, which allow further statistical analysis. The chosen level of significance was 0.05. For the first two tests, the probability is larger than this value, meaning that the hypothesis of a normal distribution is correct. For the second two test, the probability is only a little bit smaller than 0.05, meaning that there is no significant evidence for rejecting the hypothesis. With two tests confirming the normal distribution and two tests very closely not confirming, it can be assumed that the data is normally distributed.

Tests for Normality				
Test	Statistic		p Value	
Shapiro-Wilk	W	0.995020	Pr < W	0.0995
Kolmogorov-Smirnov	D	0.032847	Pr > D	>0.1500
Cramer-von Mises	W-Sq	0.132227	Pr > W-Sq	0.0428
Anderson-Darling	A-Sq	0.781781	Pr > A-Sq	0.0436

Table 8.63. Tests of normality.

Following the difference in mean physiological-pacing values between electrode positions were globally evaluated with multiple regression analysis. The Null Hypothesis is that the means physiological-pathological levels are the same between electrode positions. The p-value <0.0001 indicates there is a significant difference in mean response levels between electrodes. From the results, illustrated in table 8.64. It can be concluded that there is a significant difference in mean physiological-pacing levels between electrodes.

Tests of Fixed Effects				
Effect	Num. DF	Den. DF	F Value	Pr >F
Electrode position setups	13	219	10.05	<.0001

Num: numerator, DF: degree of freedom, Den: denominator

Table 8.64. Tests of fixed effects between electrode position setups.

9

Clinical Verification of the Methods

Multichannel ECG measurements (BSPM) and MRI data acquisition are carried out on three patients at University Hospital Mannheim in order to gain the individual pathology by solving the inverse problem of electrocardiography. The models resulting from MRI data sets based on geometries described in section 6.2 are implemented together with the 64 ECG channels measurements to solve the inverse problem. The inverse solver is based on optimization approach discussed in section 5.3. An electrophysiological cardiac model is created in which the parameters are varied until the simulated ECG is as similar as possible to the measured one. The solution of inverse problem enables the simulation of excitation propagation in the ventricular myocardium and conduction system. After optimizing the pacing setups, the BSPM is simulated by solving the forward problem of electrocardiography. The resulting simulated ECG signals are compared with the measured ECG signals after implantation in order to verify the results of the optimization procedure.

9.1 Verification of the Optimization Method for Patient-11

The general information of Patient-11 about the pathologies and geometries is shown in tables 6.1 - 6.2. The demonstration of the heart and torso are in figures 6.12 and 6.16, respectively.

9.1.1 ECG Measurements of Patient-11

The measured ECGs before and after pacemaker implantation are demonstrated in figure 9.1 - 9.2. The signal processing steps including baseline wander cancellation, denoising, averaging of multiple ECG cycles in each channel were performed. For the signals after implantation, an additional signal processing step was performed in order to suppress the stimulus artifacts.

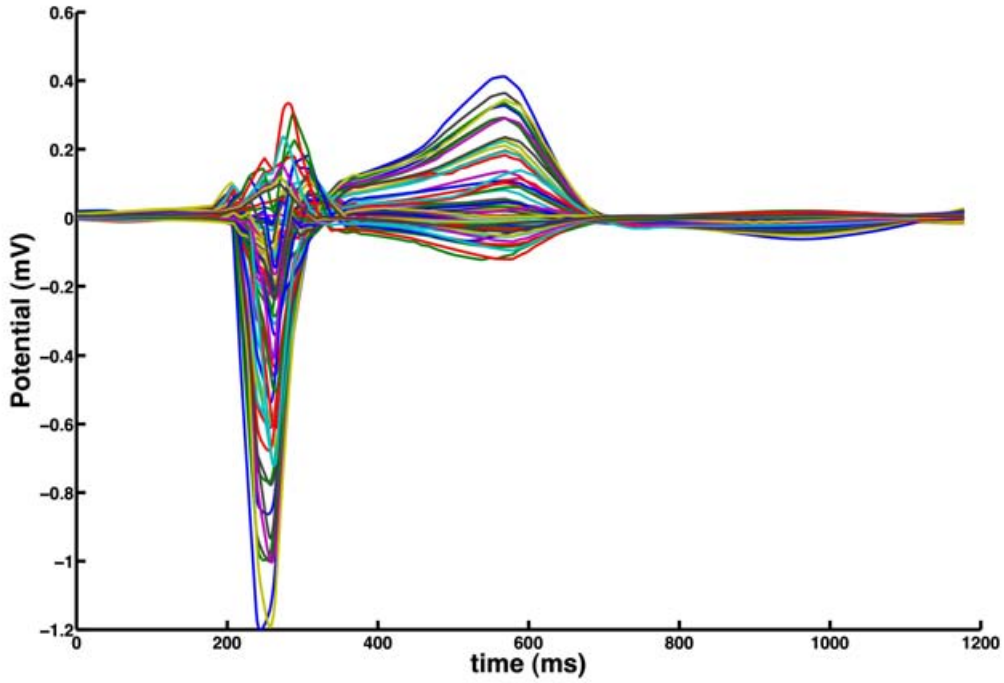

Figure 9.1. The measured 64 channels ECG before implantation for Patient-11.

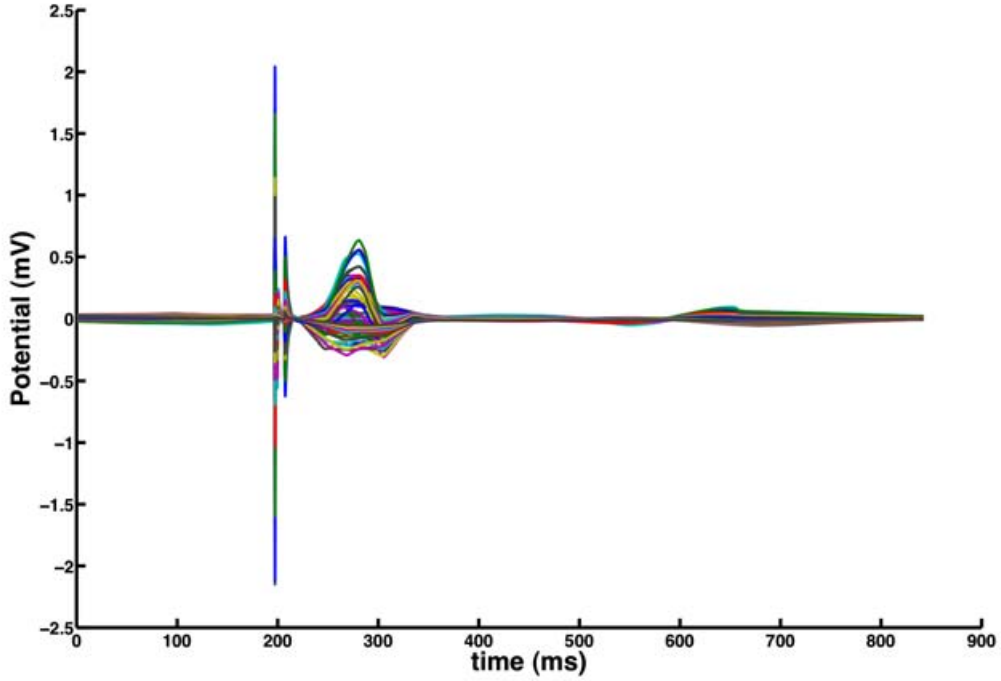

Figure 9.2. The measured 64 channels ECG after implantation for Patient-11.

9.1.2 Parameter Optimization of Patient-11

The inverse problem of electrocardiography was solved at least 8 times to achieve the optimal results. The best results including the optimal parameters based on the least E_{RMS} between measured and simulated ECG were selected. The initial and optimized values for excitation conduction velocity in different tissues and the location of myocardial infarction are demonstrated in table 9.1. The initial values are the first estimation of the pathological parameters and were extracted from the previous studies [94, 216]. The 12 standard ECG channels were extracted from the measured 64 channels ECG. These signals are compared to the simulated ECG for 12 standard channels based on optimized parameters of inverse solver before implantation. The simulated and measured 12 channels ECG pre-implantation are demonstrated in figures 9.3 and 9.4, detailed in figures 9.5 to 9.8. The correlation coefficients between the simulated and measured ECGs are demonstrated in figure 9.9. The signals are highly correlated (up to 0.8) in the interval of QRS complex.

Tissue class	**Initial values**	**Optimized values**
Infarction position (x, y, z)	157 132 100 (AHA10)	155 102 108 (AHA15)
Infarction size (voxels)	20	18.90
ECV in LV myocardium	1065 mm/s	1315.70 mm/s
ECV in RV myocardium	1065 mm/s	1675.40 mm/s
ECV in RV Purkinje fibers	4862.02 mm/s	3762.15 mm/s
E_{RMS}	0.136043	0.123527

ECV: the excitation conduction velocity (mm/s). Number of iterations: 272.

Table 9.1. Initial and optimized values for infarction location and excitation conduction velocity in different tissues.

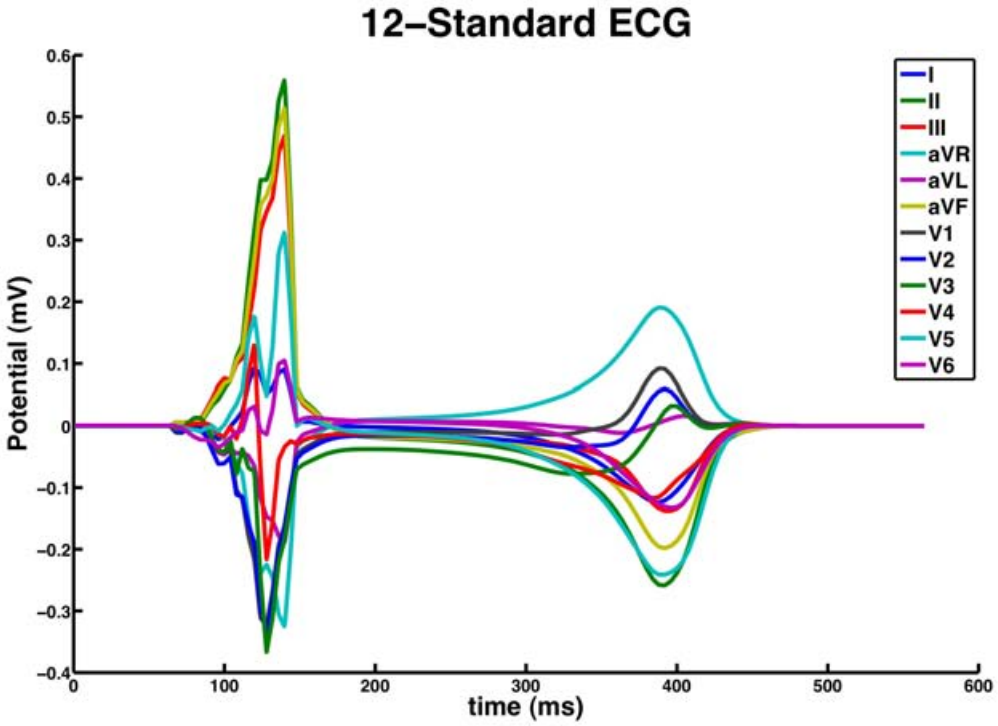

Figure 9.3. The simulated ECG channels of Patient-11 pre-implantation.

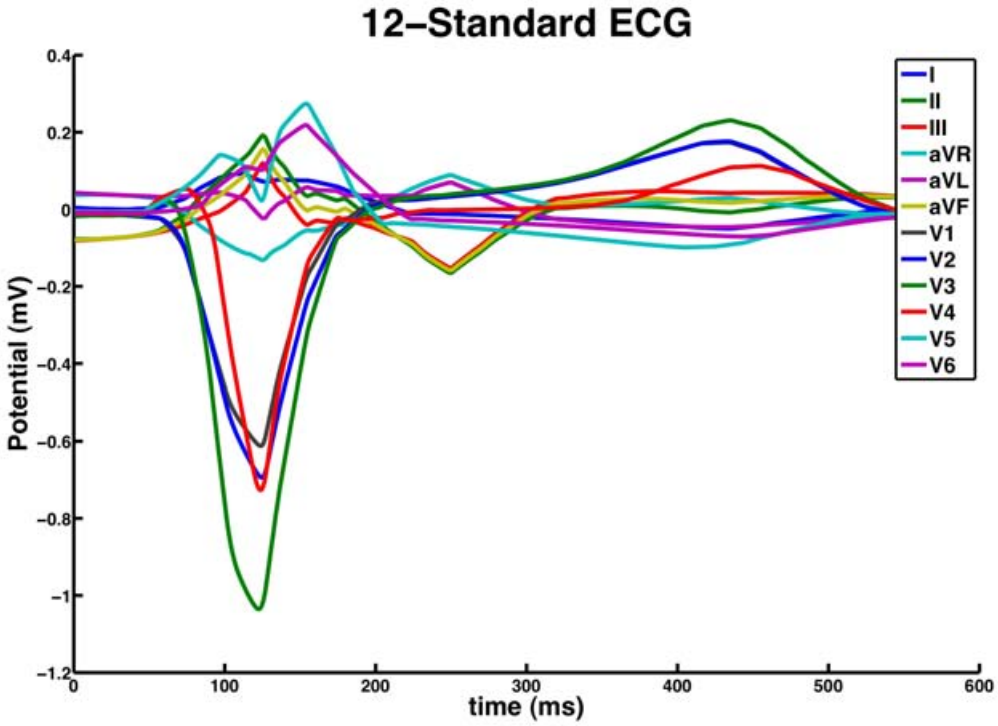

Figure 9.4. The measured ECG channels of Patient-11 pre-implantation.

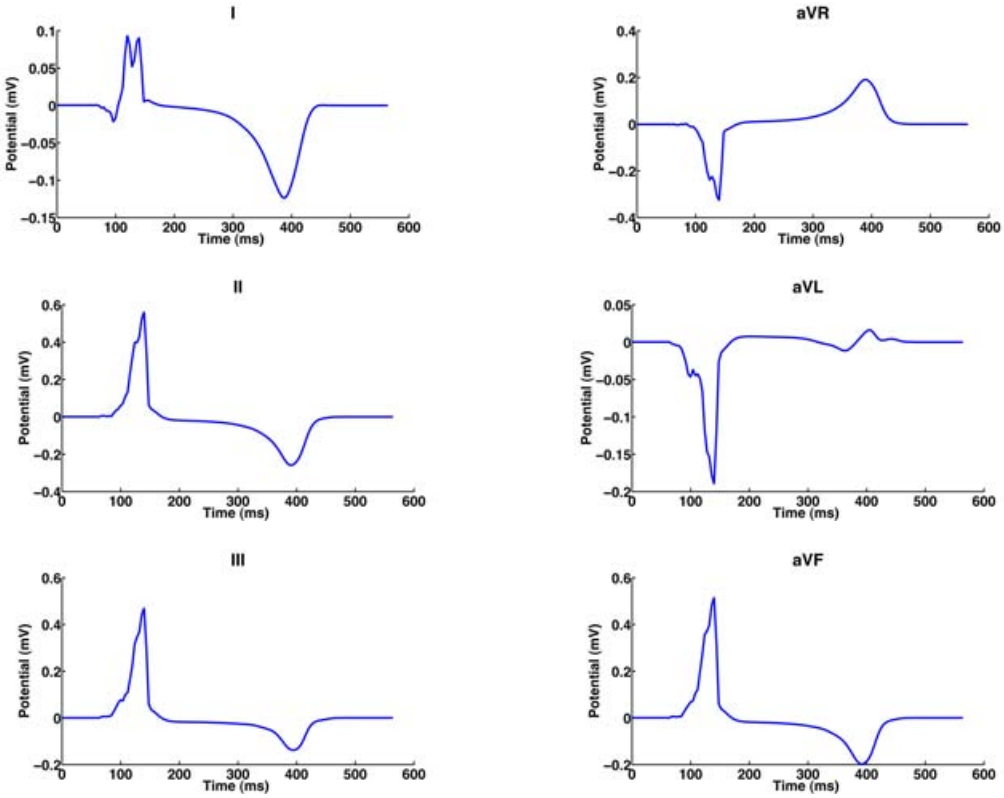

Figure 9.5. The simulated ECG channels of Patient-11 pre-implantation (Einthoven and Goldberger).

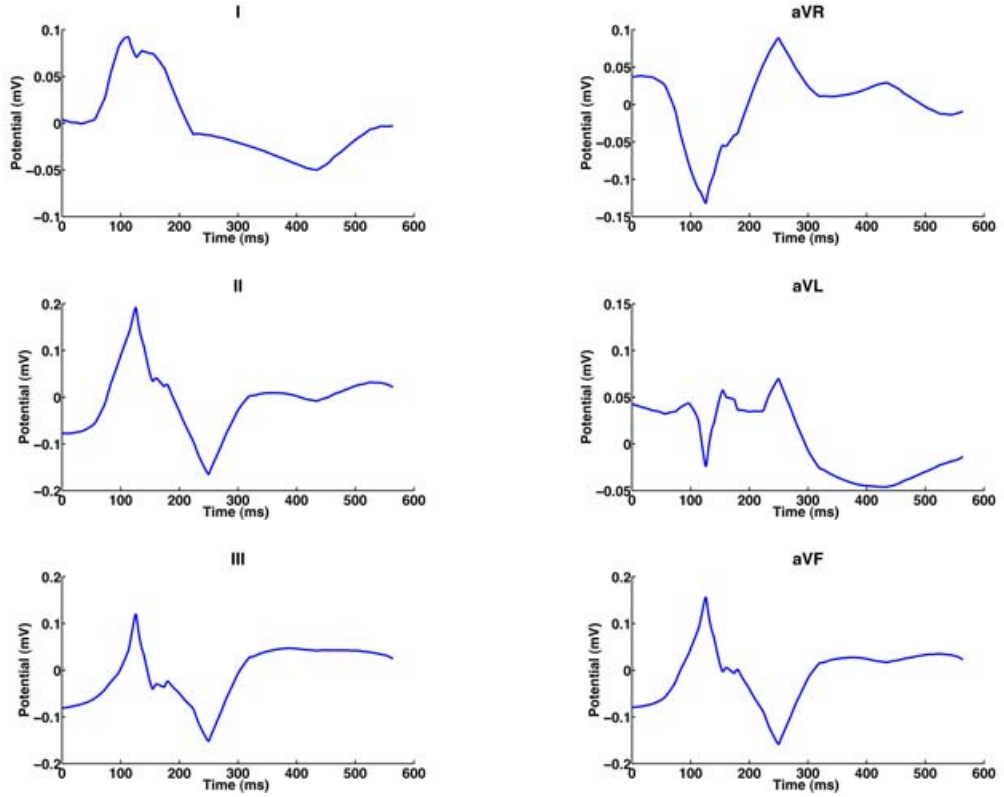

Figure 9.6. The measured ECG channels of Patient-11 pre-implantation (Einthoven and Goldberger).

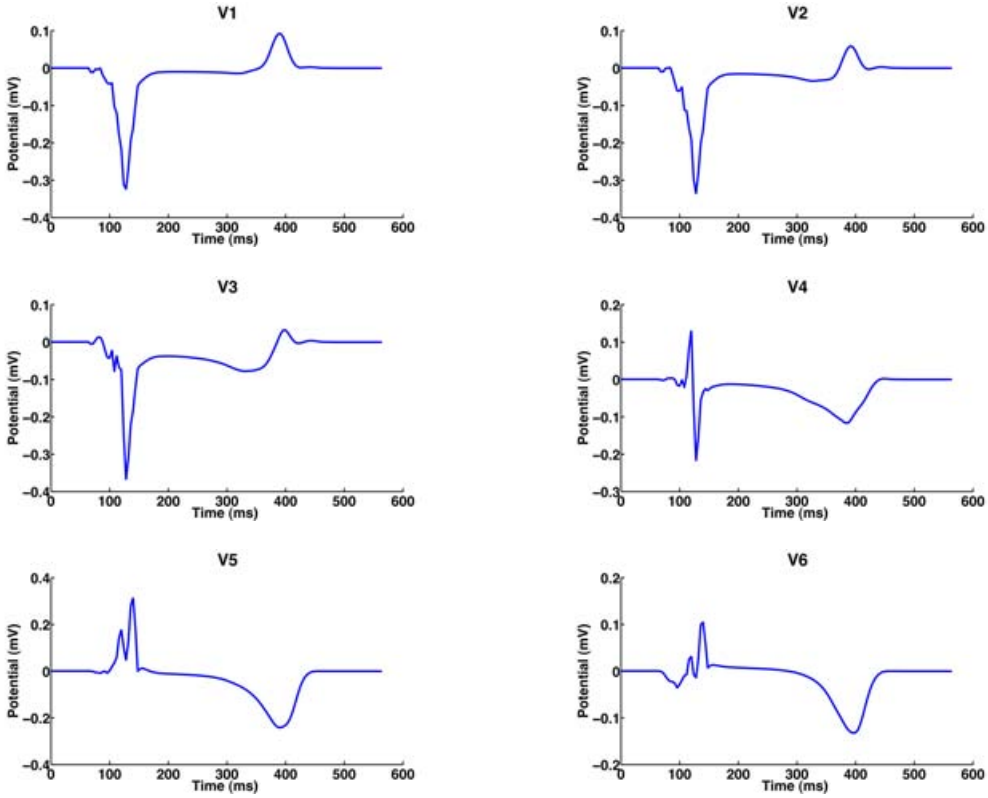

Figure 9.7. The simulated ECG channels of Patient-11 pre-implantation (Wilson).

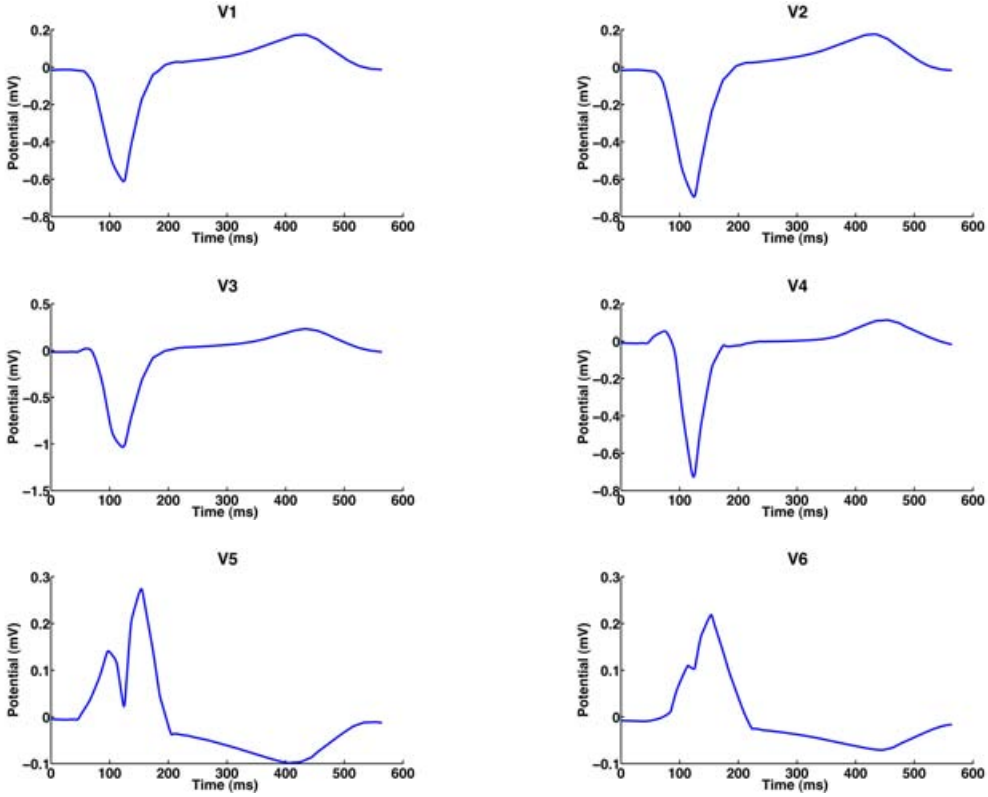

Figure 9.8. The measured ECG channels of Patient-11 pre-implantation (Wilson).

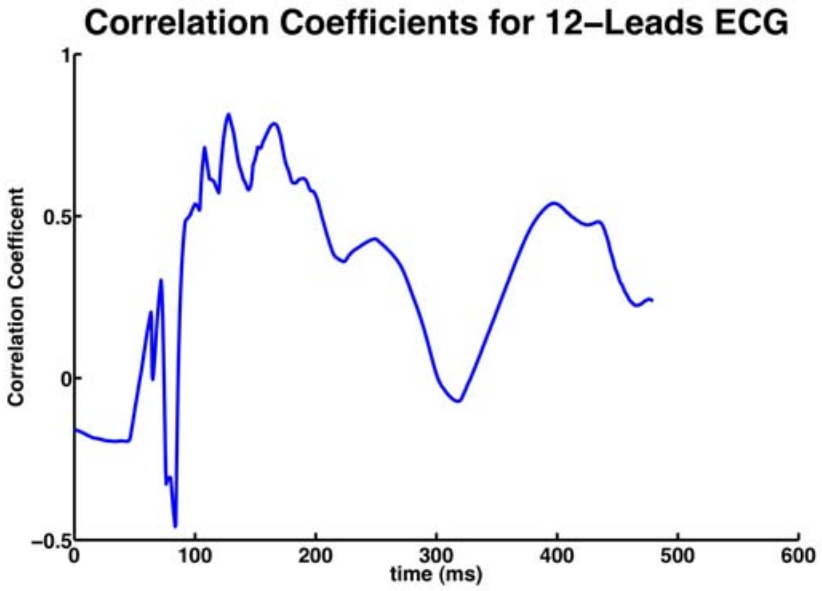

(a)

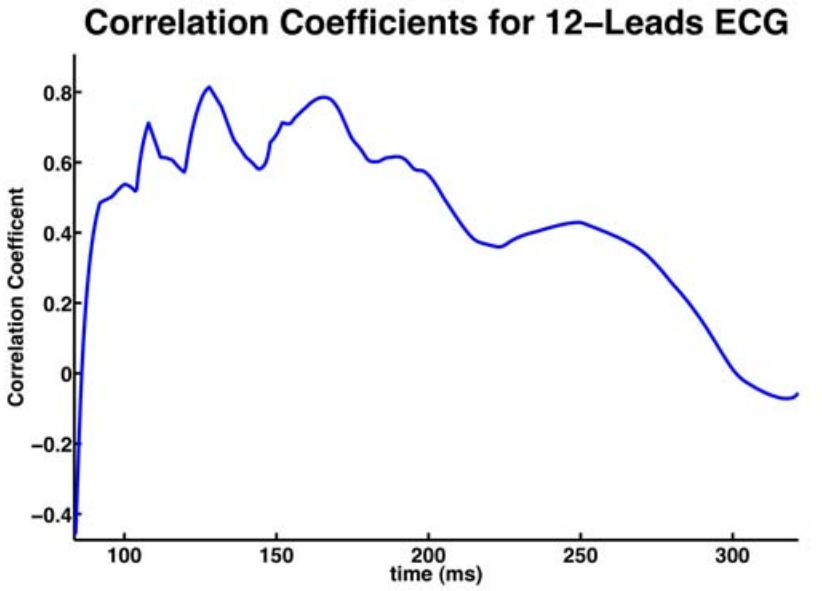

(b)

Figure 9.9. Correlation coefficients between simulated and measured 12 standard ECG channels before implantation: (a) Heart cycle. (b) QRS complex.

9.1.3 CRT Optimization of Patient-11

The pathological heart is simulated based on the optimized parameters achieved with the inverse solver. Furthermore, the optimal setup parameters were discovered using the optimization methods for CRT developed in this work. The electrode positions are demonstrated in figure 9.10. The optimal results of both optimization methods based on E_{RMS}

and QRS duration were achieved and a trade off between the results leads to following consideration:

- Pacing the leads in RV apex (X) and the LV posterolateral area (J).
- Setting the timing delays to 140 ms for A-V delay and 58 ms for V-V delay.

(a) (b)

Figure 9.10. The electrode positions chosen for the Patient-11 heart model. The electrodes A, B, C and D are referred to the anterior branches of coronary sinus. The electrodes I, J, K and L are referred to the posterior branches of coronary sinus. The electrodes E, F, G and H are located on the left ventricular free wall. The electrodes U, M and X are located at the upper septum, middle septum and apex of the right ventricle respectively.

9.1.4 Forward Calculation of Simulated ECG for Patient-11 after Pacing

The BSPM of the patient model based on the optimal BVP setup was simulated. The 12 standard ECG leads system were extracted (see figure 9.11) and compared to the corresponding channels in measured ECG after implantation (see figure 9.12) in terms of QRS durations.

9.1.5 Discussion on the Results

The QRS duration before and after implantation are calculated in both measured and simulated ECG based on the automatic QRS detection method described in chapter 7. The QRS duration before and after implantation are compared together and demonstrated in figure 9.13. It can be observed that QRS durations are reduced both in measured and simulated ECG after implantation.

The simulated optimized electrode positions are comparable to the ones used in hospital. The timing delays used in hospital are 130 ms for A-V and 0 ms for V-V delay, while the values obtained in this work are slightly larger.

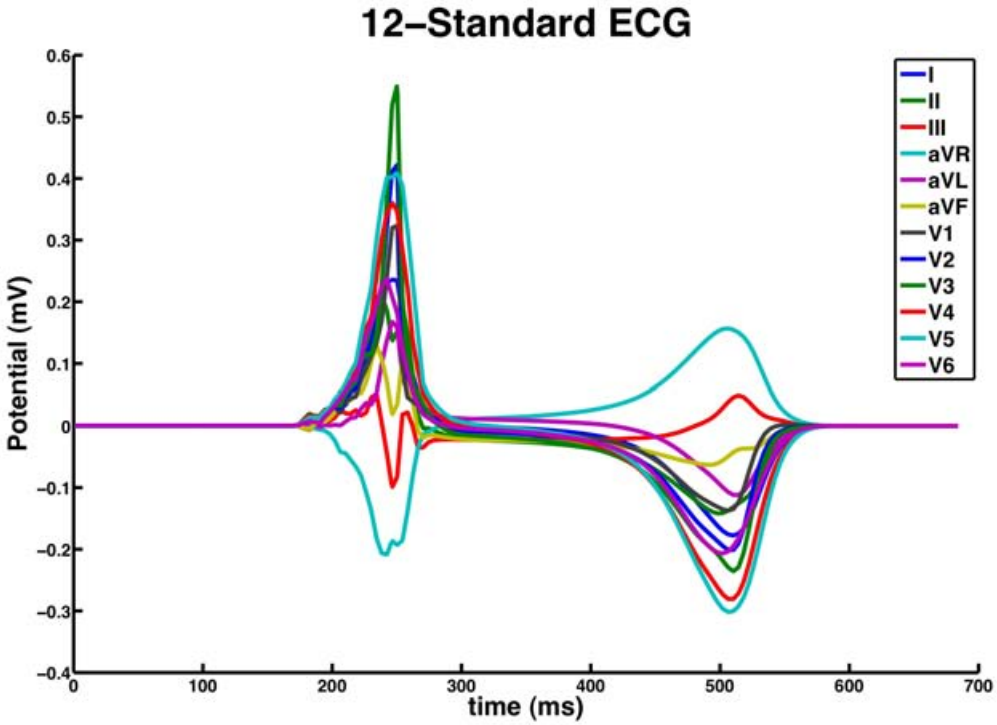

Figure 9.11. The simulated ECG channels of Patient-11 post-implantation.

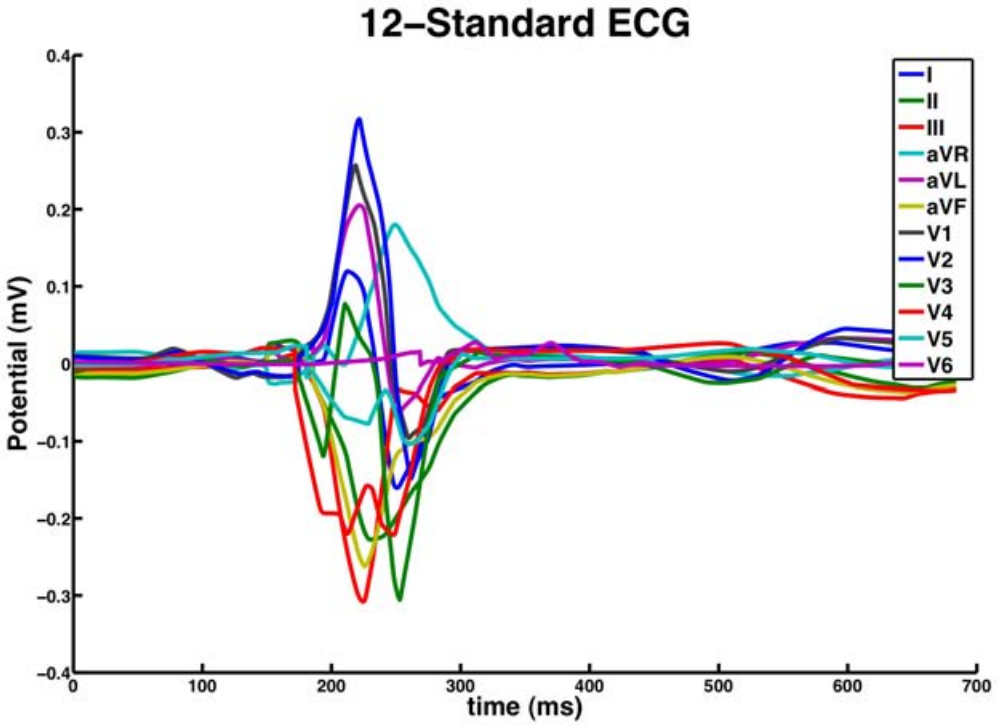

Figure 9.12. The measured ECG channels of Patient-11 post-implantation.

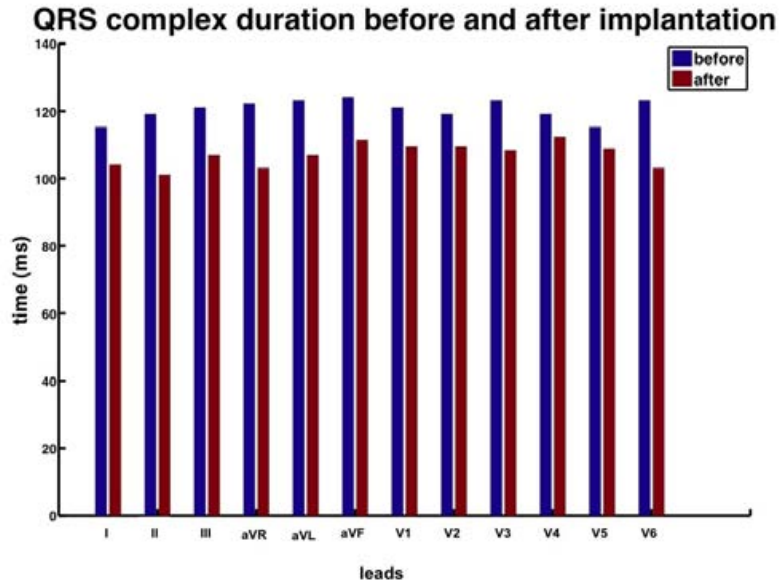

(a)

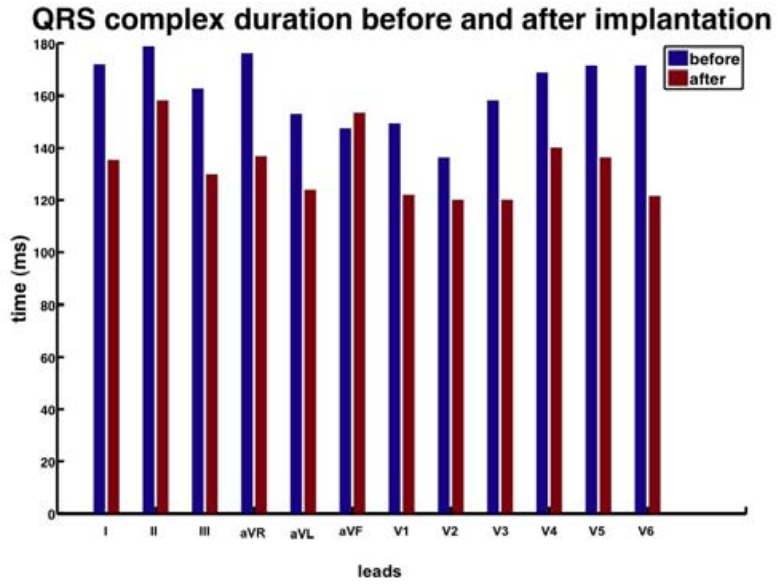

(b)

Figure 9.13. QRS duration of the 12 channels ECG before and after implantation: (a) Simulated. (b) Measured.

9.2 Verification of the Optimization Method for Patient-12

The general information of Patient-12 about the pathologies and geometries is shown in tables 6.1 - 6.2. The demonstration of the heart and torso are in figures 6.13 and 6.17, respectively.

9.2.1 ECG Measurements of Patient-12

The measured ECGs before and after pacemaker implantation are demonstrated in figures 9.14 - 9.15. The signal processing steps including baseline wander cancellation, denoising, averaging of multiple ECG cycles in each channel were performed.

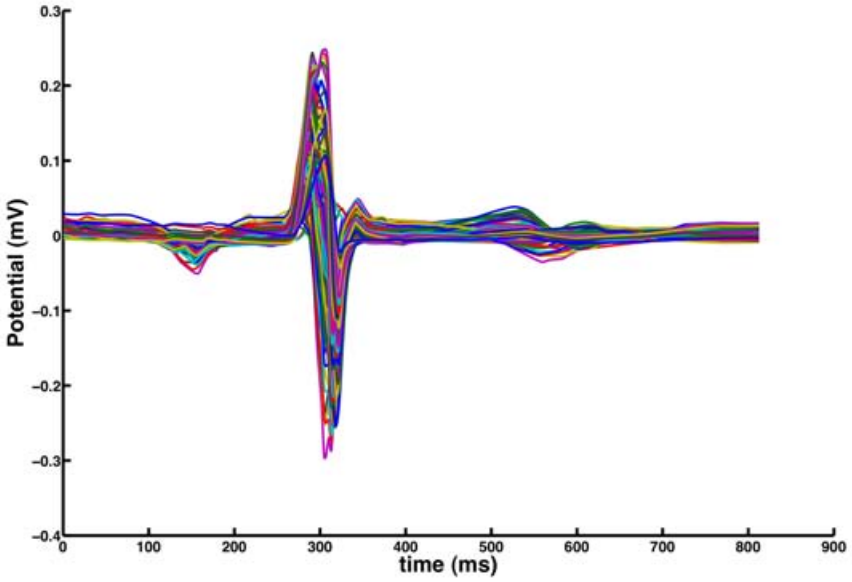

Figure 9.14. The measured 64 channels ECG before implantation for Patient-12.

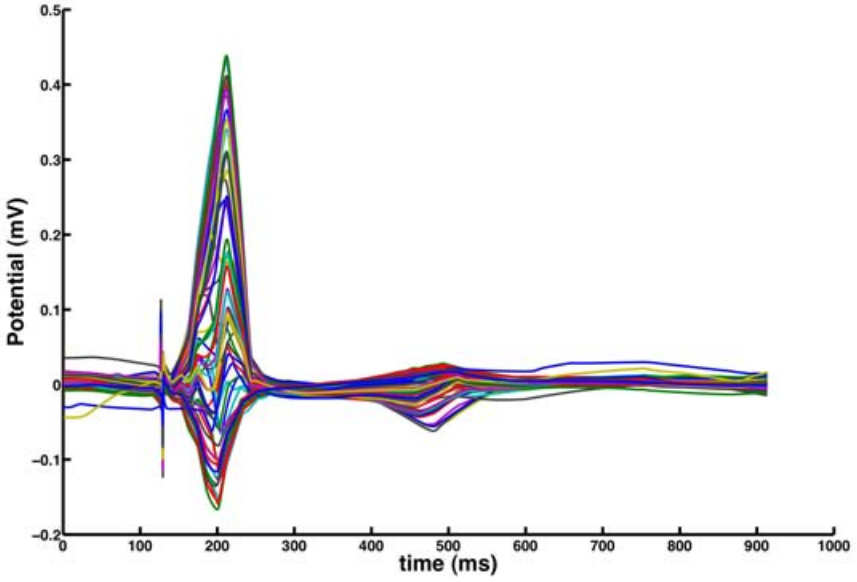

Figure 9.15. The measured 64 channels ECG after implantation for Patient-12.

For the signals after implantation an additional signal processing step was performed in order to suppress the stimulation artifacts.

9.2.2 Parameter Optimization of Patient-12

The inverse problem of electrocardiography was solved at least 8 times to achieve the optimal results. The best results including the optimal parameters based on the least E_{RMS} between measured and simulated ECG were selected. The initial and optimized values for excitation conduction velocity in different tissues are demonstrated in table 9.2. The initial values are the first estimation of the pathological parameters and were extracted from the literature. The 12 standard ECG channels were extracted from the measured 64 channels ECG. These signals are compared to the simulated ECG for 12 standard channels based on optimized parameters of inverse solver before implantation. The simulated and measured 12 channels ECG pre-implantation are demonstrated in figures 9.16 and 9.17, detailed in figures 9.18 - 9.21.

Tissue class	**Initial values**	**Optimized values**
ECV in the left bundle branch	800 mm/s	796.55 mm/s
ECV in LV myocardium	852 mm/s	856.80 mm/s
ECV in RV myocardium	958 mm/s	983.70 mm/s
ECV in RV Purkinje fibers	3889.62 mm/s	3824.55 mm/s
E_{RMS}	0.138776	0.12934

ECV: the excitation conduction velocity (mm/s). Number of iterations: 185.

Table 9.2. Initial and optimized values for excitation conduction velocity in different tissues.

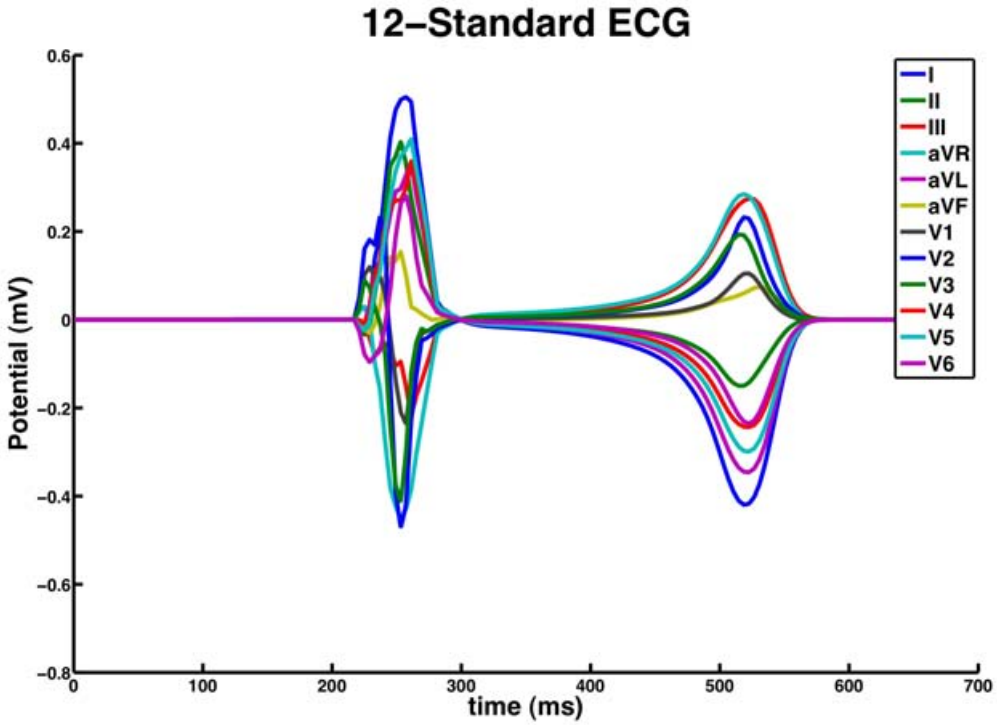

Figure 9.16. The simulated ECG channels of Patient-12 pre-implantation.

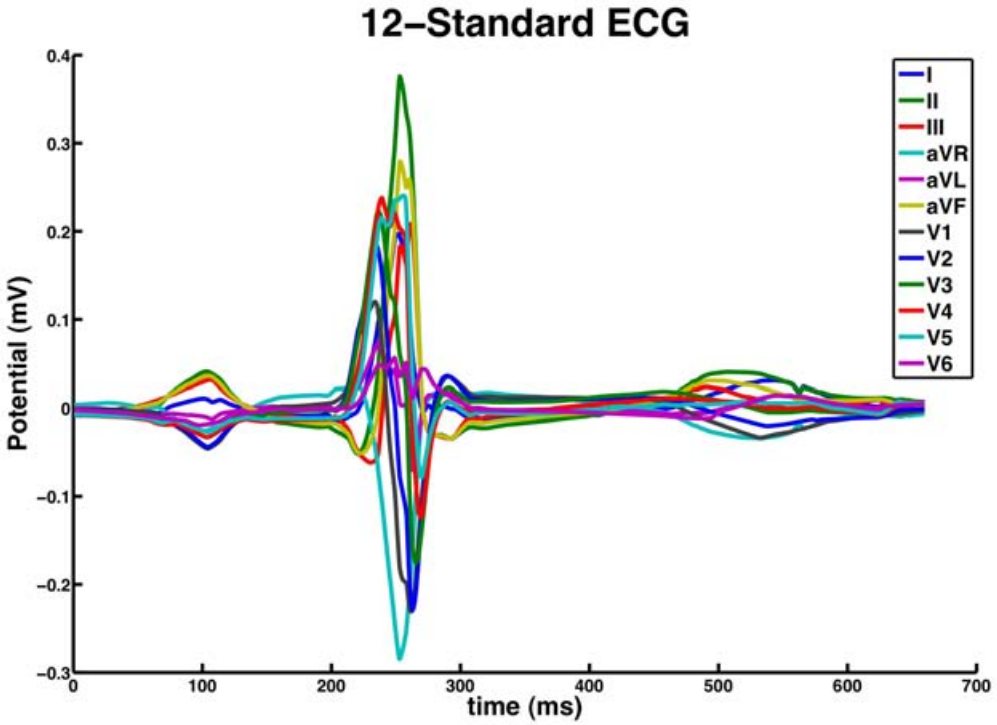

Figure 9.17. The measured ECG channels of Patient-12 pre-implantation.

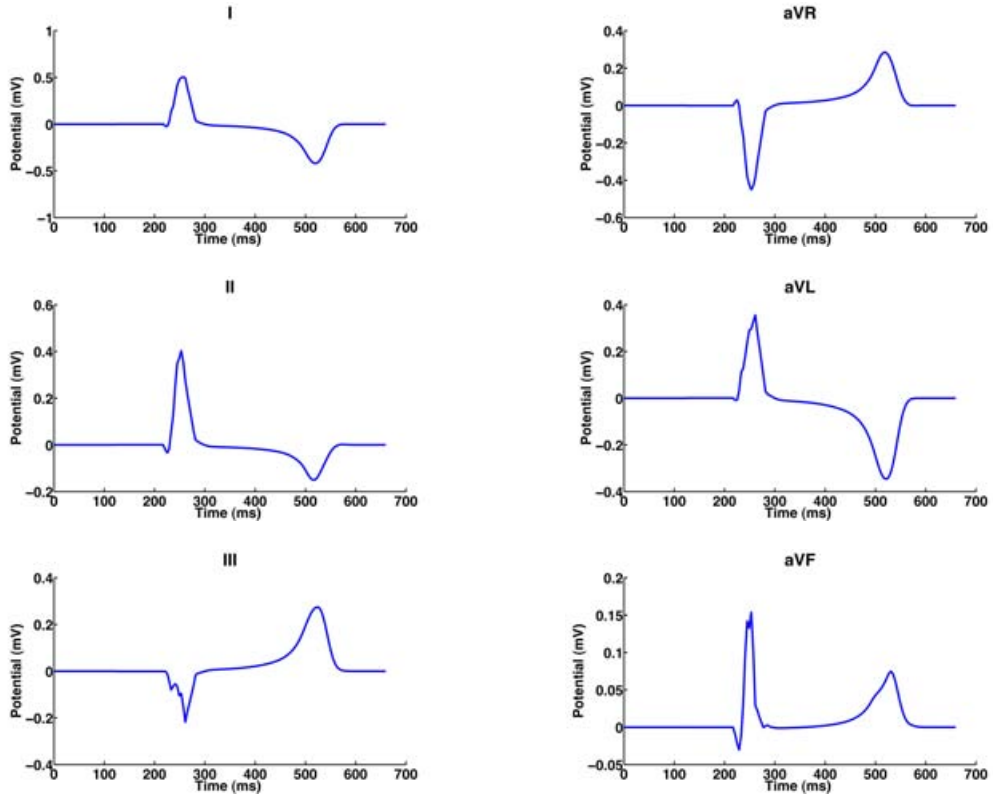

Figure 9.18. The simulated ECG channels of Patient-12 pre-implantation (Einthoven and Goldberger).

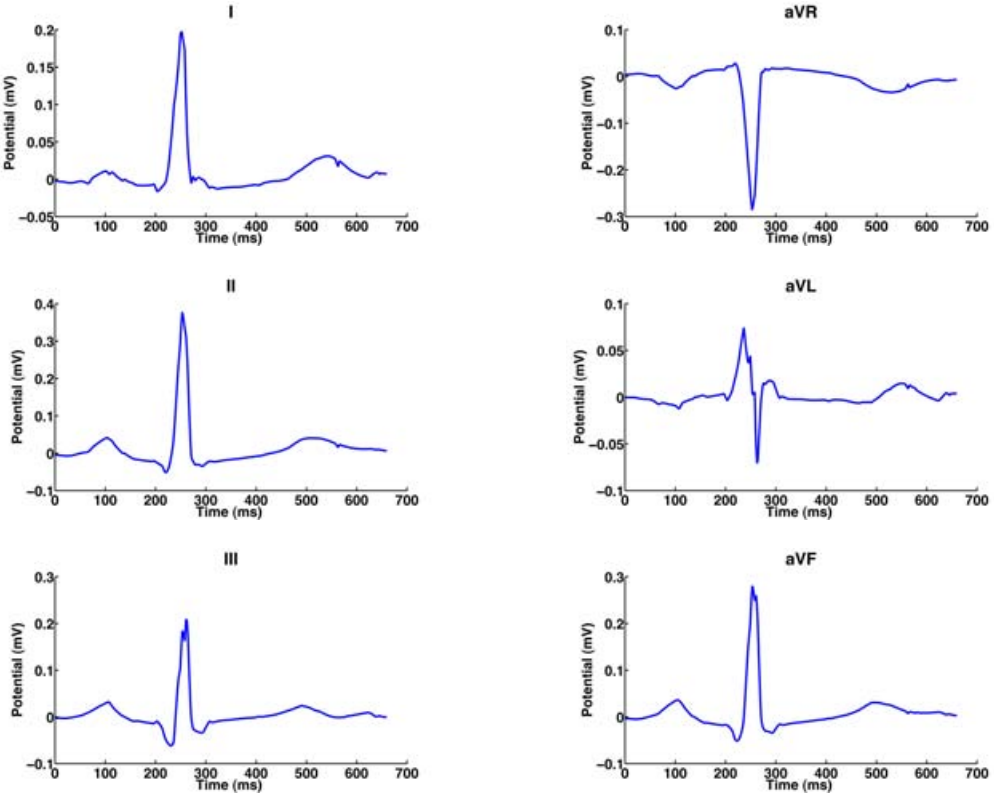

Figure 9.19. The measured ECG channels of Patient-12 pre-implantation (Einthoven and Goldberger).

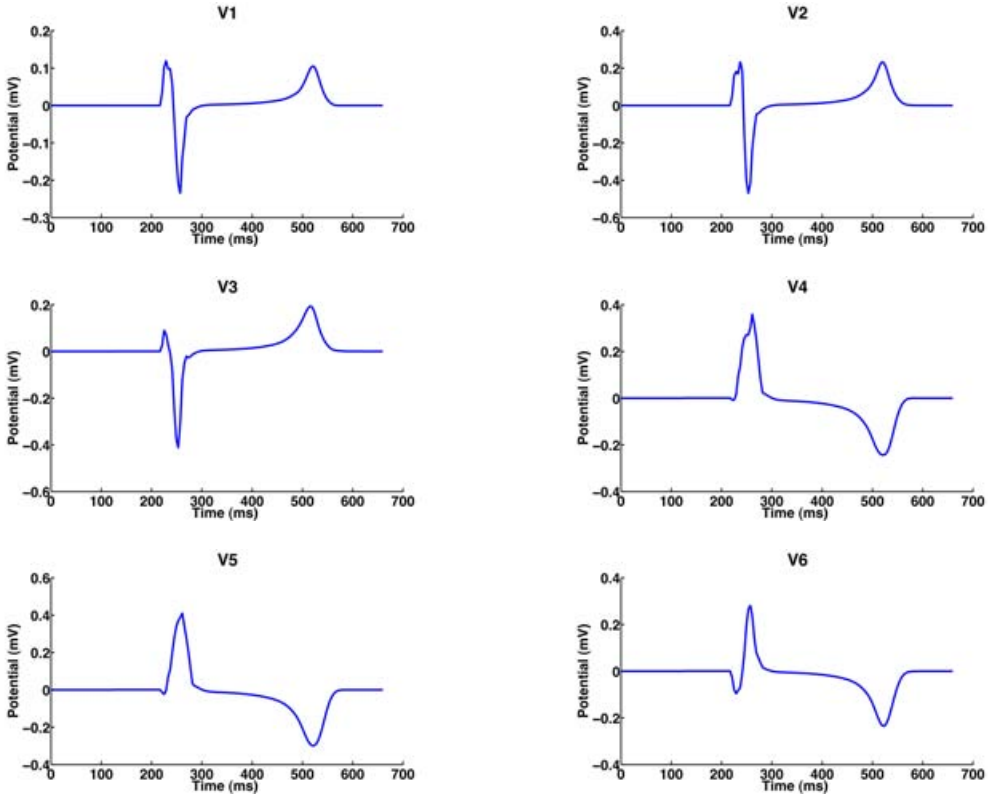

Figure 9.20. The simulated ECG channels of Patient-12 pre-implantation (Wilson).

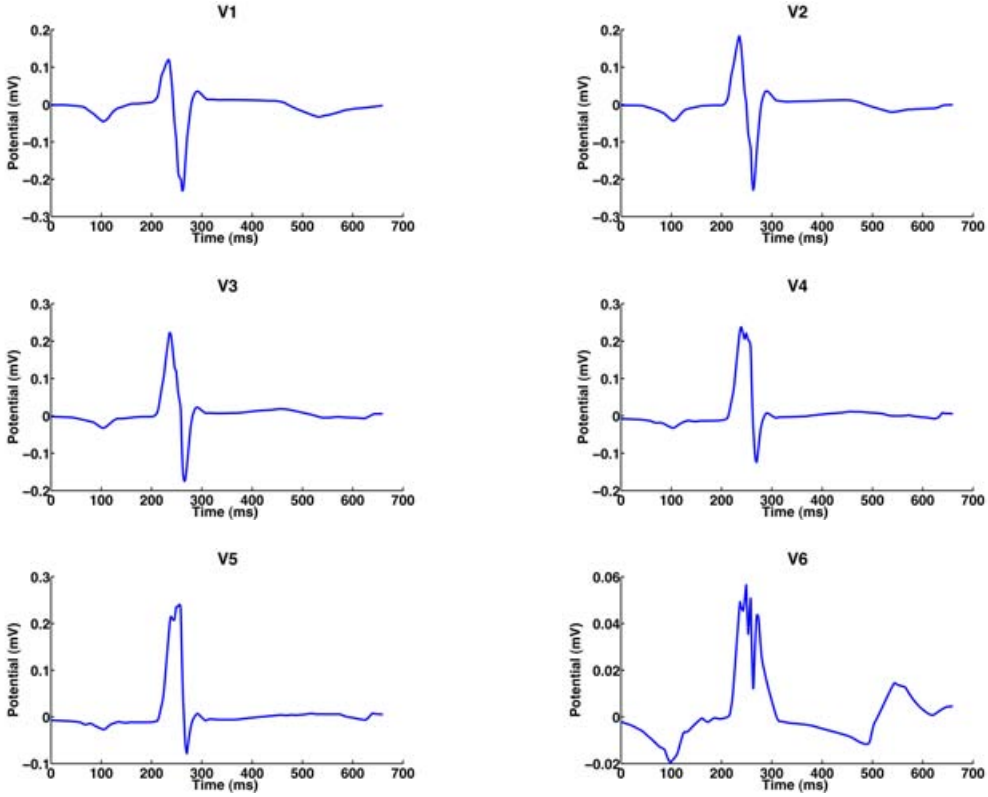

Figure 9.21. The measured ECG channels of Patient-12 pre-implantation (Wilson).

The correlation coefficients between the simulated and measured ECGs are demonstrated in figure 9.22. The signals are highly correlated (up to 0.8) in the interval of QRS complex.

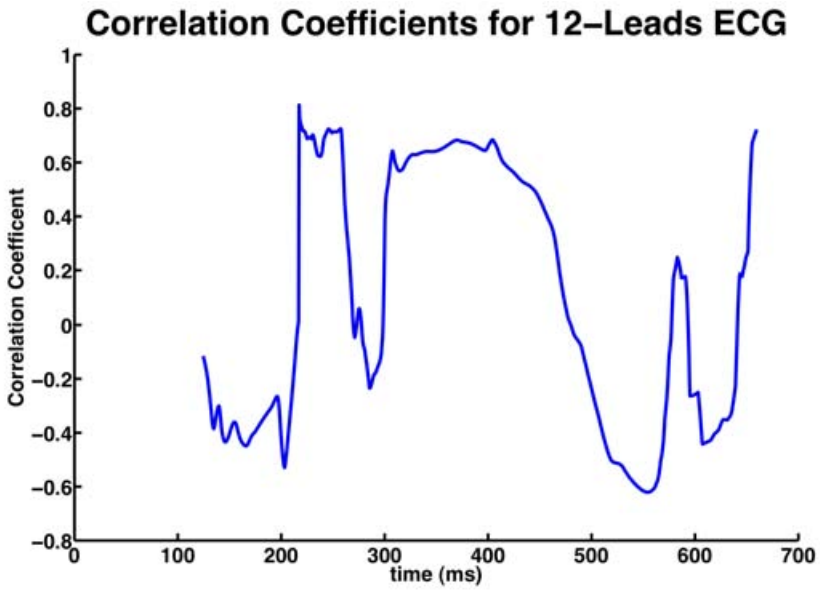

(a)

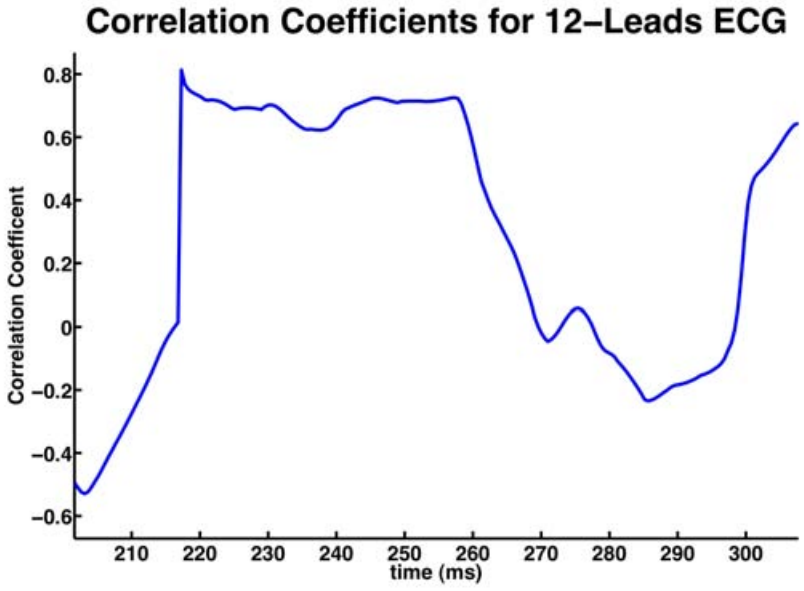

(b)

Figure 9.22. Correlation coefficients between simulated and measured 12 standard ECG channels before implantation: (a) Heart cycle. (b) QRS complex.

9.2.3 CRT Optimization of Patient-12

The pathological heart is simulated based on the optimized parameters achieved with the inverse solver. Furthermore, the optimal setup parameters were discovered using the

optimization methods for CRT developed in this work. The electrode positions are demonstrated in figure 9.23. The optimal results of both optimization methods based on E_{RMS} and QRS duration were achieved and a trade off between the results leads to following consideration:

- Pacing the leads in RV upper septal area (U) and the LV posterolateral area (J).
- Setting the timing delays as 130 ms for A-V delay and 49 ms for V-V delay.

(a) (b)

Figure 9.23. The electrode positions chosen for the Patient-12 heart model. The electrodes A, B, C and D are referred to the anterior branches of coronary sinus. The electrodes I, J, K and L are referred to the posterior branches of coronary sinus. The electrodes E, F, G and H are located on the left ventricular free wall. The electrodes U, M and X are located at the right ventricular upper septum, middle septum and apex respectively.

9.2.4 Forward Calculation of Simulated ECG for Patient-12 after Pacing

The BSPM of the patient model based on the optimal BVP setup was simulated. The 12 standard ECG leads system were extracted (see figure 9.24) and compared to the corresponding channels in measured ECG after implantation (see figure 9.25) in terms of QRS duration.

9.2.5 Discussion on the Results

The QRS durations before and after implantation are calculated in both measured and simulated ECG based on the automatic QRS detection method described in chapter 7. The QRS duration before and after implantation are compared together and demonstrated in figure 9.26. It can be observed that QRS duration are increased both in measured and simulated ECG after implantation.

The simulated optimized electrode positions are comparable to the ones used in hospital. The timing delays used in hospital are 130 ms for A-V and 0 ms for V-V delay, while the V-V delay obtained in this work is slightly larger.

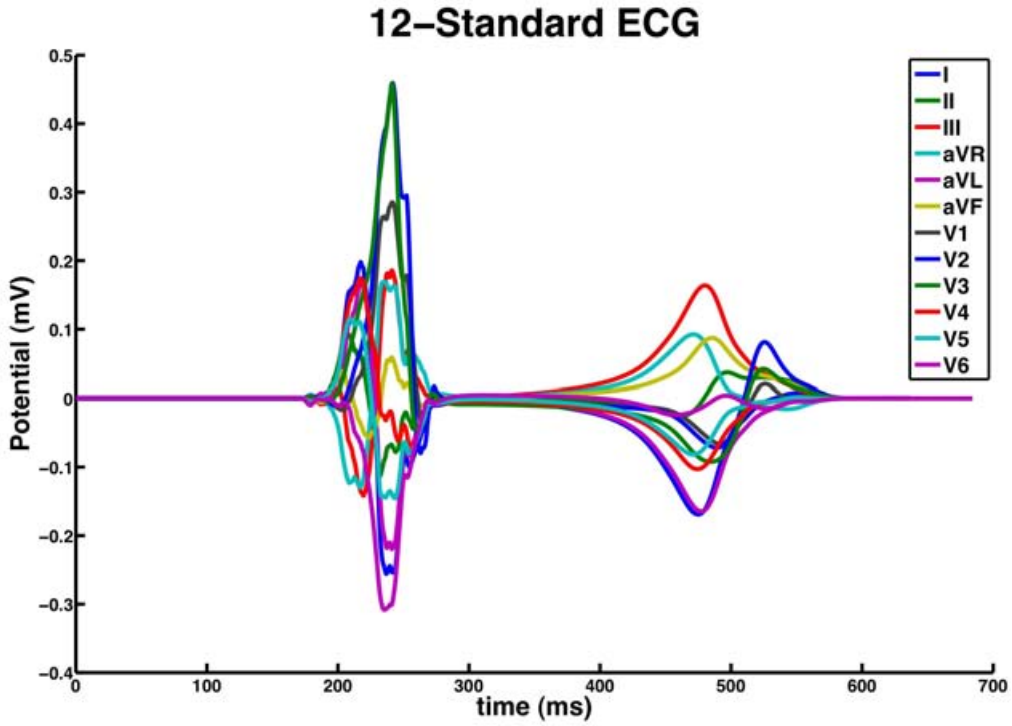

Figure 9.24. The simulated ECG channels of Patient-12 post-implantation.

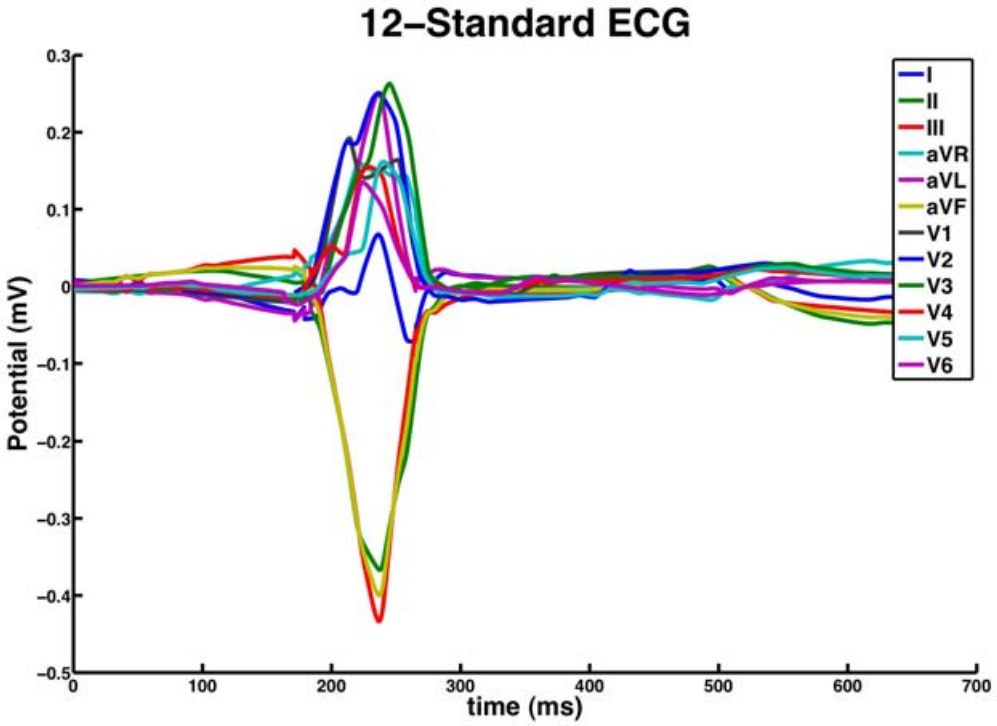

Figure 9.25. The measured ECG channels of Patient-12 post-implantation.

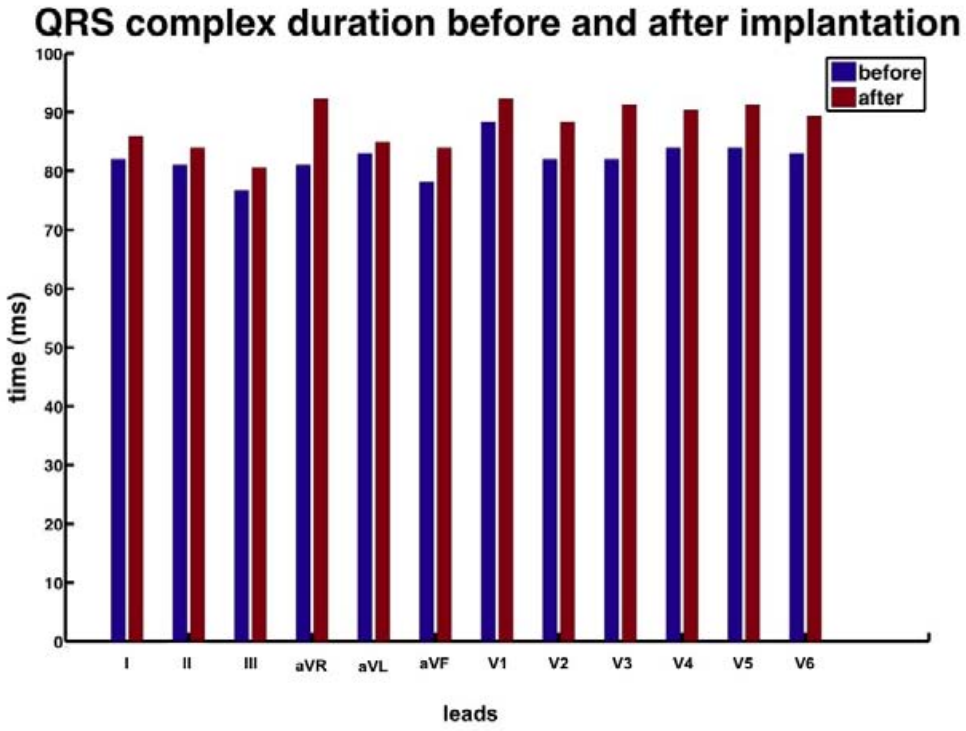

(a)

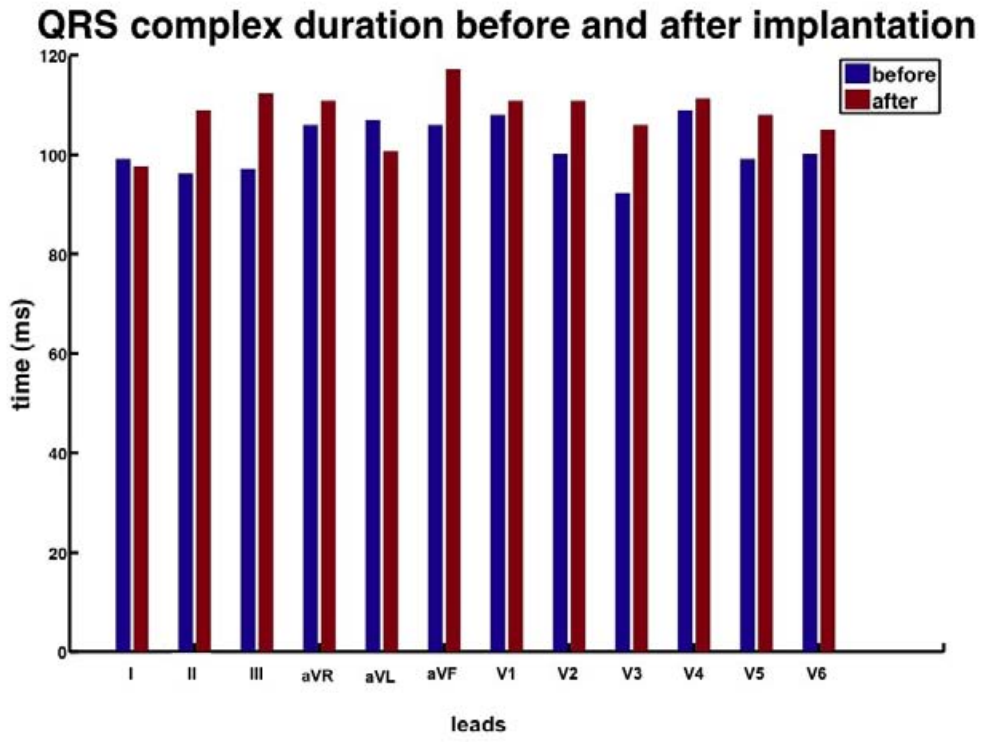

(b)

Figure 9.26. QRS duration of the 12 channels ECG before and after implantation: (a) Simulated. (b) Measured.

9.3 Verification of the Optimization Method for Patient-13

The general information of Patient-13 about the pathologies and geometries is shown in tables 6.1 - 6.2. The demonstration of the heart and torso are in figures 6.14 and 6.18, respectively.

9.3.1 ECG Measurements of Patient-13

The measured ECGs before therapy is demonstrated in figure 9.27. The signal processing steps including baseline wander cancellation, denoising, averaging of multiple ECG cycles in each channel were performed.

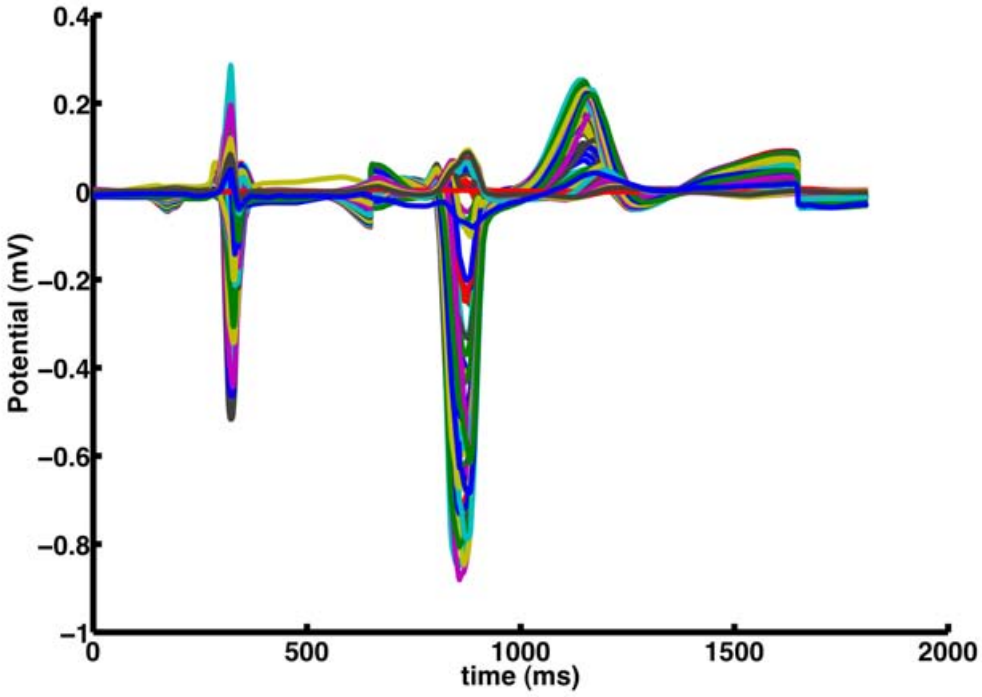

Figure 9.27. The measured 64 channels ECG before therapy for Patient-13 showing 2 heart cycles with an extrasystole.

9.3.2 Parameter Optimization of Patient-13

The inverse problem of electrocardiography was solved at least 3 times to achieve the optimal results. The best results including the optimal parameters based on the least E_{RMS} between measured and simulated ECG were selected. The initial and optimized values for excitation conduction velocity in different tissues and the location of extrasystole are demonstrated in table 9.3. The initial values are the first estimation of the pathological parameters and were extracted from the literature. The 12 standard ECG channels were extracted from the measured 64 channels ECG. These signals are compared to the simulated ECG for 12 standard channels based on optimized parameters of inverse solver before implantation. The simulated and measured 12 channels ECG pre-implantation are demonstrated in figures 9.28 and 9.29, detailed in 9.30 to 9.33 .

Tissue class	**Initial values**	**Optimized values**
Extrasystole location	127 53 80 (AHA17)	104 83 112 (AHA7)
ECV in RV myocardium	479.25 mm/s	653.70 mm/s
ECV in LV myocardium	479.25 mm/s	646.96 mm/s
ECV in RV Purkinje fibers	1983.47 mm/s	2299.87 mm/s
ECV in LV Purkinje fibers	2917.21 mm/s	1229.56 mm/s
E_{RMS}	0.155873	0.0960135

ECV: the excitation conduction velocity (mm/s).

Table 9.3. Initial and optimized values for extrasystole location and excitation conduction velocity in different tissues.

The correlation coefficients between the simulated and measured ECGs are demonstrated in figure 9.34. The signals are highly correlated (up to 0.8) in the interval of QRS complex.

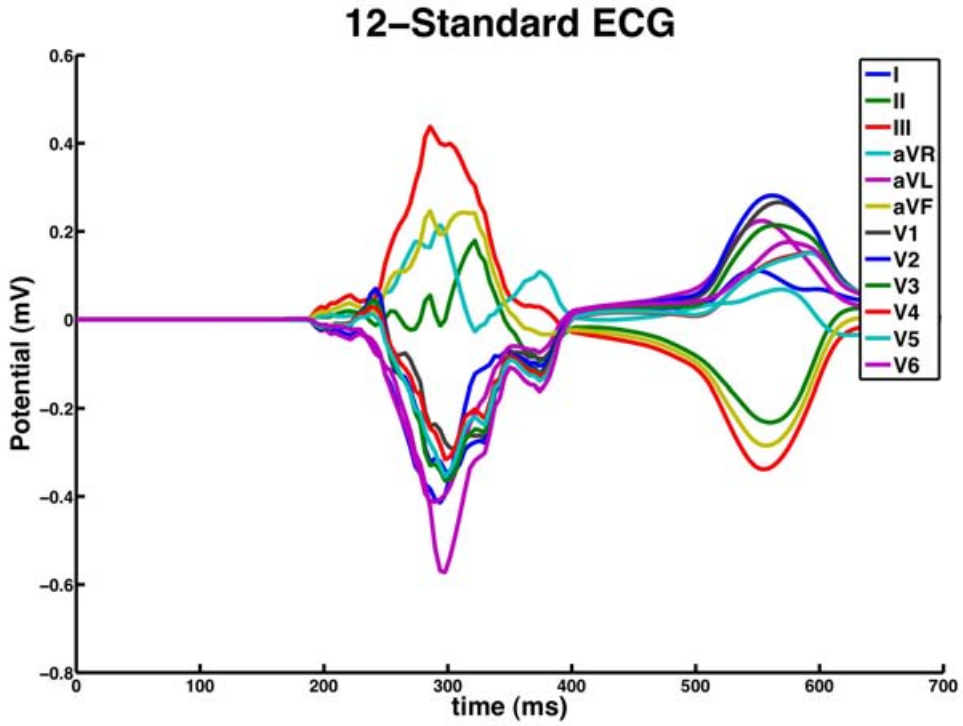

Figure 9.28. The simulated ECG channels of Patient-13 (extrasystolic beat).

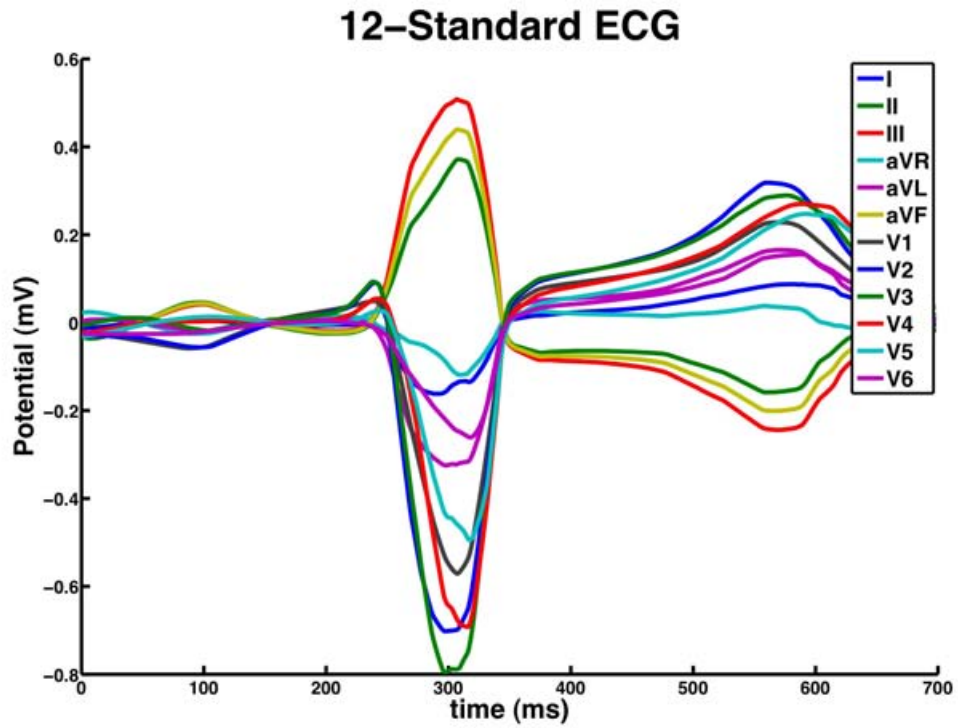

Figure 9.29. The measured ECG channels of Patient-13 (extrasystolic beat).

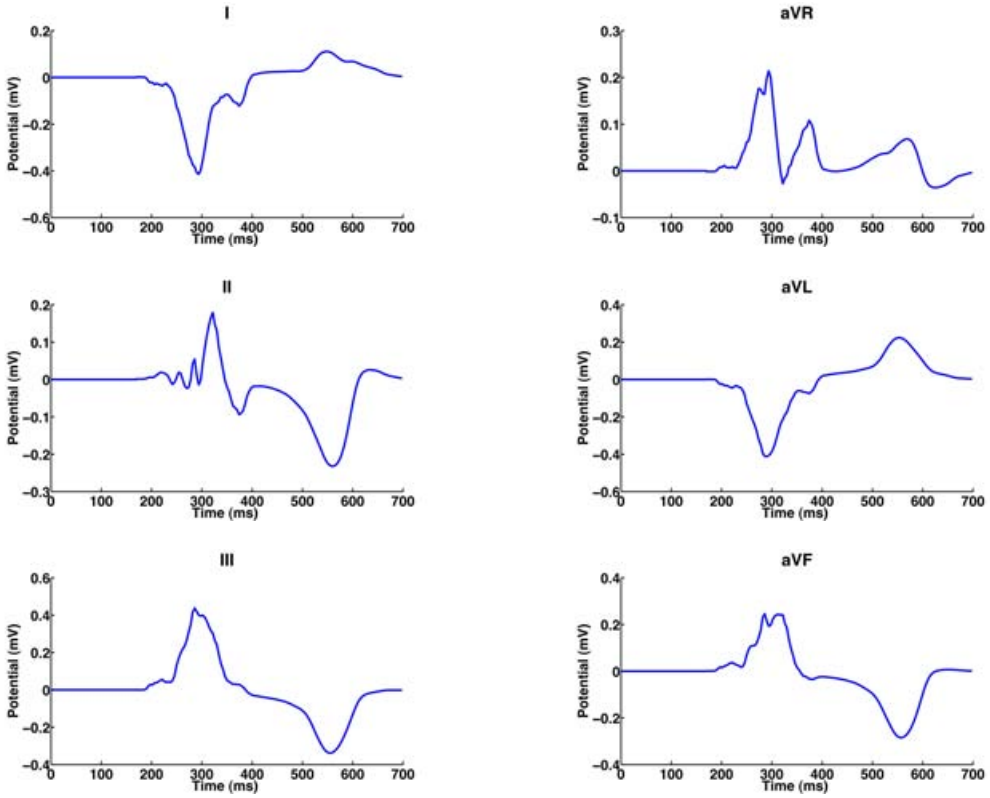

Figure 9.30. The simulated ECG channels of Patient-13 (Einthoven and Goldberger).

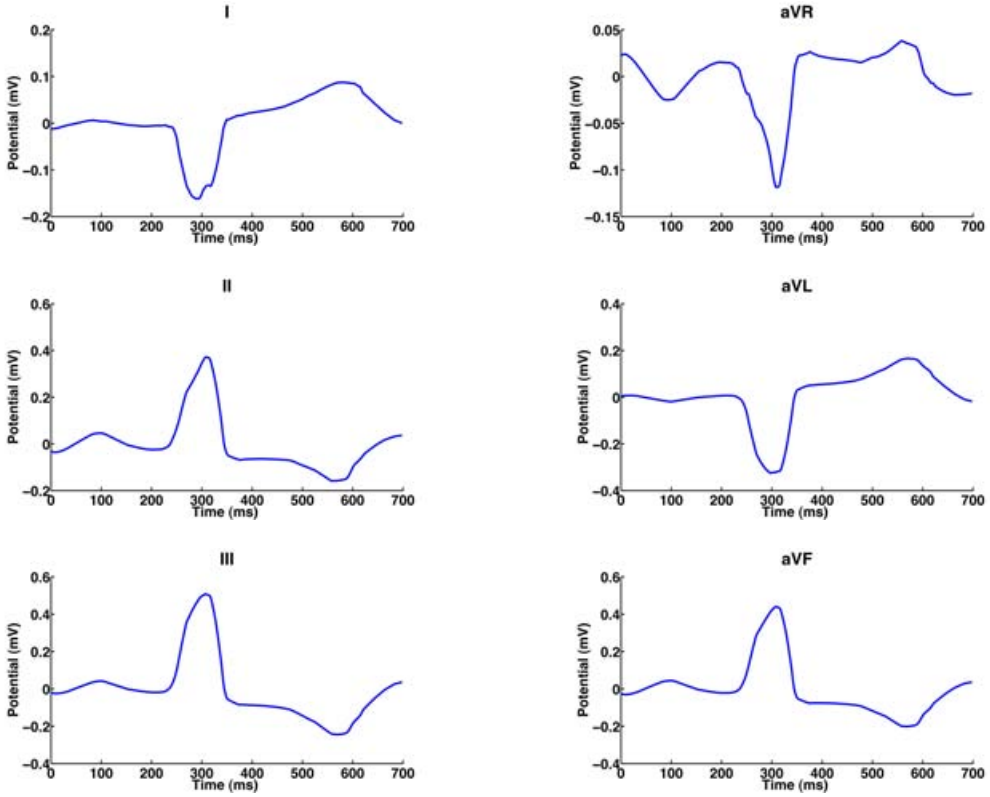

Figure 9.31. The measured ECG channels of Patient-13 (Einthoven and Goldberger).

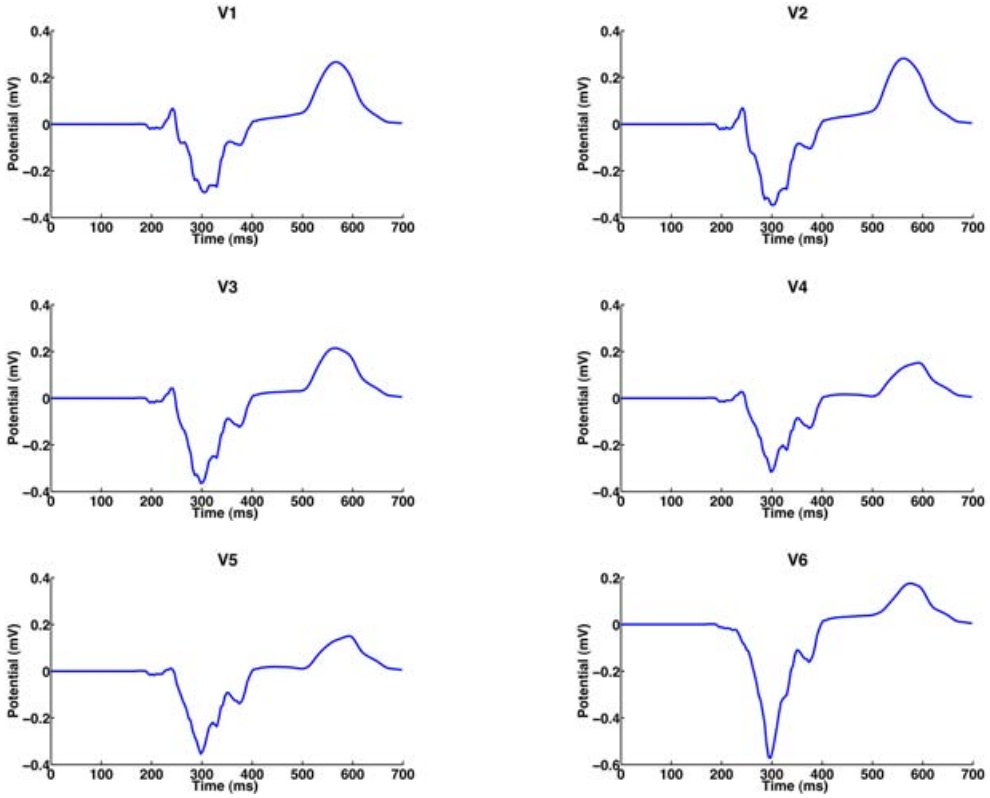

Figure 9.32. The simulated ECG channels of Patient-13 (Wilson).

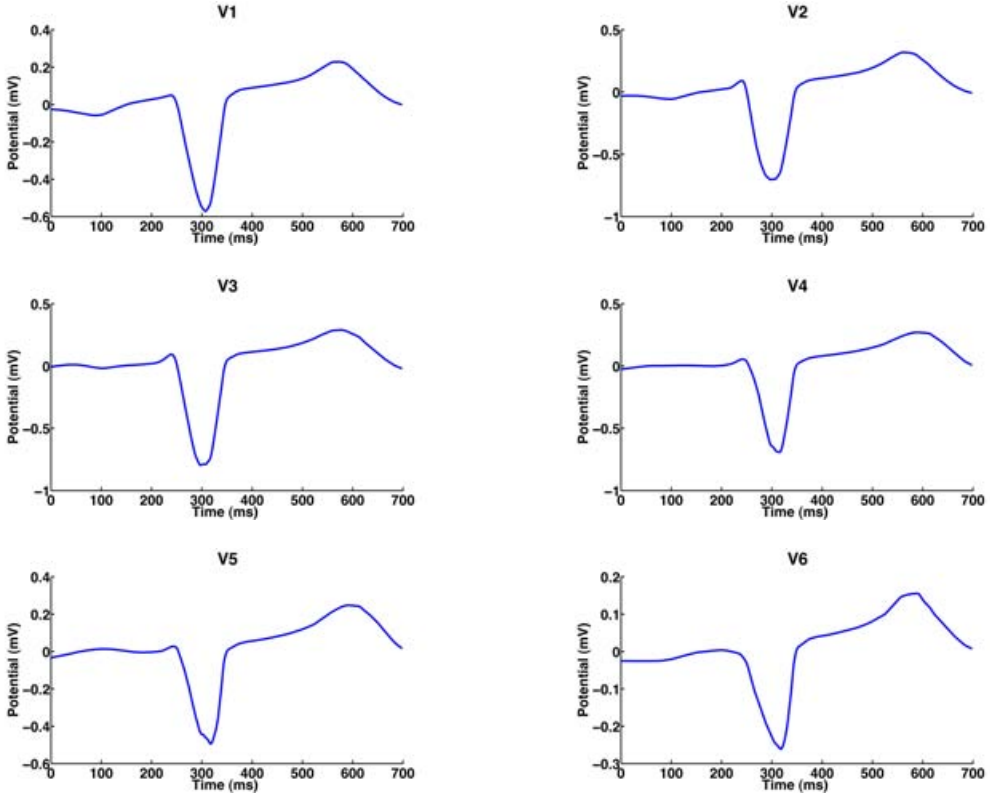

Figure 9.33. The measured ECG channels of Patient-13 (Wilson).

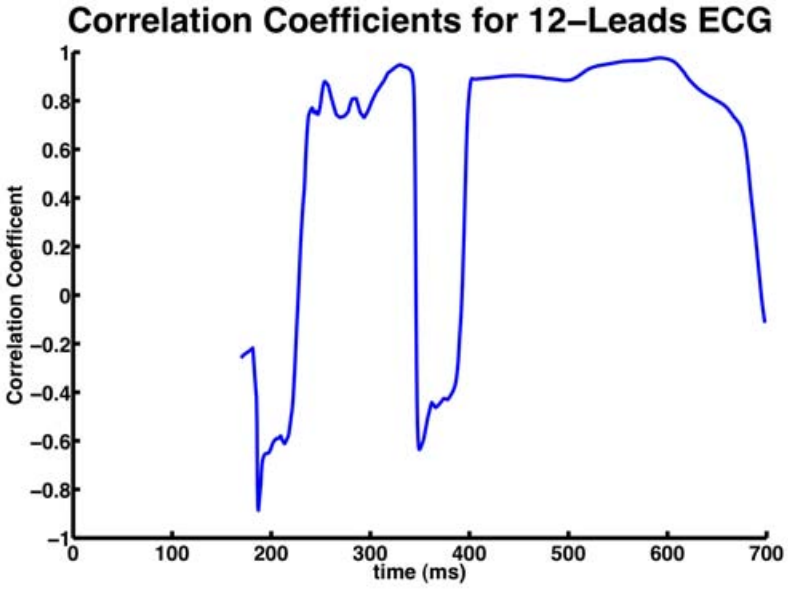

(a)

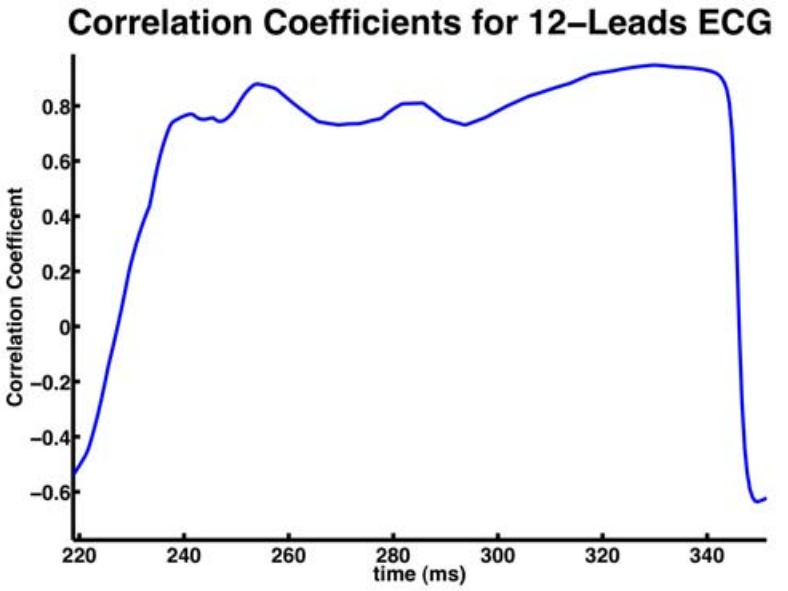

(b)

Figure 9.34. Correlation coefficients between simulated and measured 12 standard ECG channels with extrasystole: (a) Heart cycle. (b) QRS complex.

9.3.3 Discussion on the Results

An extrasystolic beat can be modeled by defining a spontaneous excitation in the myocardium near epicardium. The excitation is conducted through the myocardium until it reaches the excitation conduction system. Afterwards the excitation is spread over the endocardium by the conduction system [94]. The estimated position of the extrasystole and the optimized location after solving the inverse problem is demonstrated in isochrones

of figure 9.35. The first activated areas are demonstrated by dark blue color. More information about this patient after the therapy was not available at this time.

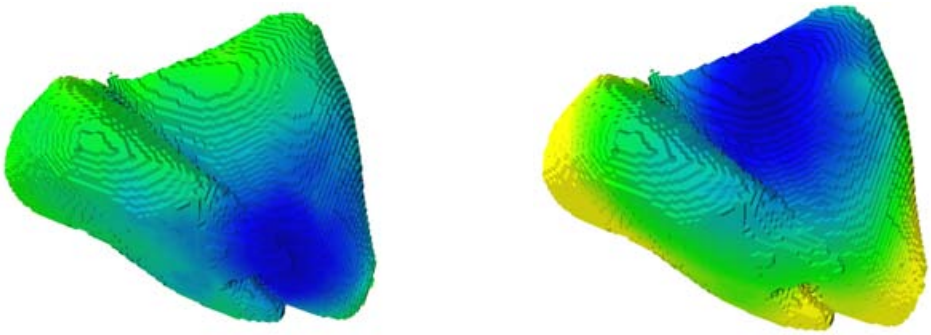

(a) (b)

Figure 9.35. Location of extrasystole (dark blue area) in Patient-13: (a) Estimated. (b) Optimized.

10

Discussion

The presented data bring evidence that correlating the heart model results with the clinical recordings is an effortful procedure. Heart failure is a complex condition and capturing the variations in conduction block and ischemia for each patient is a hard process [227]. Extracting BSPMs to evaluate the optimal setting for CRT devices is clinically relevant. The results presented in this work constitute an important step toward the goal of clinical use of BSPMs and are a good indicator of the potential of the present approach. It would be premature at this time to speculate how successful this technique would be at improving patient response. Clearly, there are several factors that need to be considered before this method can be applied in daily clinical practice. However, with a careful approach in future research projects, it seems feasible that both the BSPM and the heart model simulations could be valuable tools to help optimize resynchronization therapy.

10.1 Comparison with Clinical Studies from Literature

The simulation results of both optimization methods presented in this work on the 10 data sets demonstrated that a minimal root mean square error and QRS duration error between the physiological and therapeutic excitation could be achieved with respect to a proper pacing se tup. Using DSA as a fast computational algorithm to find the optimal timing delays saves the time in comparison with the clinical practice optimization methods. However, the DSA still needs validation and adjustment in order to avoid suboptimal results. The optimization algorithms can be applied for individual patients either pre-operatively to find the optimal lead positions and timing parameters or post-operatively for optimal adjustment of the timing delays. The major advantage of the presented method is that it is non-invasive and pre-operative.

Most studies of CRT involve simultaneous pacing of right and left ventricle. However, the results of this paper agree with the results of the study of Perego et al. [204], supporting the hypothesis that the best efficiency is not necessarily obtained by simultaneous delivery of stimulus in both ventricles. In our work, since the left stimulation electrode is placed

virtually transvenously through the coronary sinus leading to an epicardial implantation, a delay in the transmission of the stimulus occured. The effect would decline with stimulating the left ventricular electrode before right pacing electrode.

The review paper of Bax et al. [24] investigated different echocardiographic approaches to predict the response to CRT and demonstrated that the latest mechanical activity is frequently located in the lateral wall followed by anterior and posterior regions, whereas the inferior wall infrequently had latest mechanical activity. It is also shown that Tissue Doppler Imaging (TDI) may allow precise assessment of inter-ventricular dyssynchrony. In the presented work, the LV lateral wall and posterolateral positions were used to place the stimulus electrodes comparing well with the results presented in several research papers [24, 139, 252, 264, 273]. The optimal timing delays achieved in this work are similar to the studies of Perego et al. [204] and Whinnett et al. [287].

Moreover, based on the AHA model for the left ventricle in the patient model, TDI can be used for estimation of excitation conduction velocity for each segment [24]. The inter-ventricular dyssynchrony in different regions of TDI images corresponding to AHA segments should be taken into account in order to model the reduction of the excitation conduction velocity for each individual patient by adaptation of a conduction velocity factor. In clinical practice, multiple lead positioning for the evaluation of different lead positions and related optimization of timing is inapplicable due to the time consumption. The presented computer algorithms can be run automatically in order to determine the optimal pacing parameters including electrode positioning pre-operatively. By running the algorithm post-operatively, the timing delays for a fixed electrode positioning can be adjusted.

10.2 Comparison with Clinical Trials in University Hospital Mannheim

The results presented in chapter 8 and 9 mostly show an optimal parameter set up when the right electrode is placed in the RV apex or septal area and the left electrode is in lateral or posterolateral positions of left ventricle. The LV electrode position agrees with the clinical practices in University Hospital Mannheim. For the RV electrode, the surgeons would also prefer to use the septal position as they believe that a larger distance between electrodes results in a better coverage of the ventricular area. However, achieving the septal position is a difficult process and to avoid the risk of injuries, usually the apical positions in right ventricle is selected. The method we used can be adopted to any individual anatomy and pathology. Additionally, due to the pre-operative advantage, our method in comparison to clinical optimization, leads to a less invasive procedure for the patient and is time efficient, both aspects being essentially beneficial for the patient. The timing delays used in hospital

were $100 - 130$ ms for A-V delay and 0 ms for V-V delay, while the values obtained in this work are slightly larger.

10.3 Study Limitation

The results of optimization show a reliable improvement in cardiac activation. However, activation time alone does not reflect directly the cardiac contraction, hence the results of this work need clinical validation. The optimization would be better evaluated in terms of cardiac output and aortic (beat to beat) blood pressure measurements. Changing the timing parameters affects the rate of pressure variation in left ventricle, which results in aortic differential pressure and cardiac output changes [17, 139, 204]. The aortic pressure and the cardiac output could be calculated with an electromechanical heart model. Since this model is still under development, the present work depends on the assumption that the cardiac output is correlated to a physiological excitation propagation. Hence, if the excitation propagation of a diseased heart is corrected to the physiological excitation propagation by means of pacing, it is assumed that the optimal cardiac output of the diseased heart also approximates to the output of the physiological heart. Considering that the mechanical activation will follow the electrical activation with a constant delay, the simulation results are all valid. In order to validate the results, an extended electromechanical model based on the paper of Sermesant [243] can be developed.

The relationship between electrical dyssynchrony and mechanical performance needs to be established. Based on the results, CRT pacing induces an electrical pattern of activation, which can be used to reduce the electrical dyssynchrony between the ventricles, but on the other hand the BSPM do not provide any information about how these patterns improve cardiac output, which is the right goal of CRT. Echocardiographic studies will be required to measure the dyssynchrony to find the link between cardiac performance and optimized CRT [99, 183, 217].

A recent review of Kerckhoffs et al. [141] investigating an electromechanical model for different pacing parameters in CRT showed that the best results are achieved when the electromechanical function was optimized. By measuring the cardiac output as ejection fraction (EF) and stroke work (SW), it was noticeable that always if the electromechanical parameters were optimized also the QRS duration was minimal; this supports the approach that optimization of electrophysiological function leads to an optimization of electromechanical function.

The inverse solution algorithm yields an estimate of the epicardial potential distribution. The estimation inaccuracy can be influenced by lead position, segmentation error, inaccurate geometry and recorded noise [126]. For a better segmentation of the coronary sinus,

it is necessary to acquire higher resolution MR images or to use registered MR/CT images. A better segmentation of the coronary sinus would also increase the accuracy of left ventricular electrode positioning.

Finally, given the inapplicability of invasive, expensive and time consuming protocols in clinical practices, further efforts on enhancement of the heart model such as including the cardiac motion would be devoted to a non-invasive parameter optimization which simplifies the therapeutic strategy for the individual patient.

11

Conclusions and Future Work

This work offers an optimization strategy to find the best pacing sites and timing delays in CRT for patients suffering from LBBB and MI. Different reduced conduction velocities to 80 % or 60 % of the physiological value and different allocation of infarction are considered to implement several pathologies. Two optimization methods based on calculation of the activation times and QRS duration are implemented to achieve the best parameter setups.

A close cooperation with University Hospital Mannheim provides the opportunity of measuring 64 channels ECG of patients which is used to solve the inverse problem of electrocardiography. This leads to a better parameterization of the pathological model and therefore to an optimization of the cellular automaton parameters such as conduction velocity in different parts and detecting approximately the infarction position. The aim of this parameter optimization is to simulate a realistic model of the pathology, in which the simulated 64 ECG channels will be as similar as possible to the measured one. The similar QRS duration between measured and simulated ECG channel is a good indicator of the method success. Both optimization methods are implemented and the BSPM is calculated due to the optimal pacing parameters. The simulated ECG extracted from BSPM is compared with the measured ECG of the patient after implantation. The results of the comparison in terms of E_{RMS} and correlation coefficient are determined and the efficacy of the optimization algorithm is investigated. It is planned to measure the influence of pacemaker timing changes on the BSPM of the patient after implantation, which provides valuable information to validate the CRT optimization method. Since a clinical validation of the results would require a careful consideration of the ethical aspects and preceding animal studies, the results were verified in this work by pre-implatative and post-implantative measurements of the BSPM. Both measurements were compared and the success of the method was established.

In the future, it will be necessary to get an improved parameterization of the computer model. This could be done with Tissue Doppler Imaging (TDI), which can be used to determine areas of asynchronous contraction of the heart. As mentioned above, the opti-

mization method will have to be validated in experimental and clinical studies. For clinical optimization, the current optimization methods like blood pressure measurements, cardiac output measurements and ultrasound measurements can be used and compared with the results from the method presented in this work. Additionally, an implementation of the cardiac contraction into the computer model would allow the straight-forward determination of cardiac output. The optimization method would optimize directly the cardiac output. Therefore, the presented investigation represents a crucial step in the biomedical engineering research of pacing optimization, being of future aid to patients with LBBB and MI.

A

Appendix

A.1 Abbreviations

2D	2 Dimensional
3D	3 Dimensional
ACA	Adaptive cellular automaton
ACE	Angiotensin converting enzyme
AF	Atrial fibrillation
AHA	American Heart Association
AP	Action potential
ATP	Adenosine triphosphat
AV	Atrio-ventricular node
AVB	Atrio-ventricular block
A-V	Atrio-ventricular
BE	Boundary element
BEM	Boundary element method
BSA	Body surface area
BSPM	Body surface potential map
BVP	Biventricular pacing
CHF	Congestive heart failure
CI	Cardiac index
CO	Cardiac output
COG	Center of gravity
CRT	Cardiac resynchronization therapy
CT	Computed tomography
CT	Crista terminalis
CURE	Circumferential uniformity ratio estimate
CV	Conduction velocity
DCMP	Dilated cardiomyopathy
DLC	Delayed longitudinal contraction
DSA	Downhill simplex algorithm

DWT	Discrete wavelet transform
ECG	Electrocardiogram
EDP	End diastolic pressure
EDV	End diastolic volume
EF	Ejection fraction
EMAT	Electromechanical activation time
ePAD	Estimate the pulmonary artery diastolic pressure
E_{RMS}	Root mean square error
ESV	End systolic volume
FDA	US food and drug administration
FDM	Finite difference method
FEM	Finite element method
FVM	Finite volume method
GSVD	Generalized singular value decomposition
HF	Heart failure
HR	Heart rate
IBT	Institut für Biomedizinische Technik
ICD	Implantable cardioverter defibrillator
IEGM	Intracardial Electrogram
IHM	Implantable hemodynamic monitor
IVCD	Intra-ventricular conduction delay
JSR	Junctional sarcoplasmic reticulum
LA	Left arm
LA	Left atrium
LAD	Left anterior descending artery
LBBB	Left bundle branch block
LCA	Left coronary artery
LCX	Left circumflex artery
LL	Left leg
LV	Left ventricular
LVA	Left ventricular apex
LVEDd	Left ventricular end diastolic diameter
LVEDV	Left ventricular end diastolic volume
LVEF	Left ventricular ejection fraction
LVESd	Left ventricular end systolic diameter
LVESV	Left ventricular end systolic volume
LVOT	Left ventricular outflow tract
MAD	Median absolute deviation
MI	Myocardial infarction
MPI	Myocardial performance index

MR	Mitral regurgitation
MRI	Magnetic resonance imaging
NYHA	New York heart association
Pdf	Probability density function
PEA	Peak endocardial accleration
RA	Right arm
RA	Right atrium
RBBB	Right bundle branch block
RCA	Right coronary artery
RV	Right ventricular
RVA	Right ventricular apex
RVOT	Right ventricular outflow tract
SA	Sinoatrial node, sinus node
SD	Standard deviation
SP	Systolic pressure
SR	Sarcoplasmatic reticulum
SV	Stroke volume
SVD	Singular value decomposition
SVT	Supraventricular tachycardia
SW	Stroke work
TDI	Tissue doppler imaging
TMV	Transmembrane voltage
Ts	Time to peak myocardial sutained systolic
TSI	Tissue synchronization imaging
TT	Tissue tracking
VF	Ventricular fibrillation
VTI	Velocity time integral
V-V	Inter-ventricular
WCT	Wilson central terminal

A.2 Graphical User Interface for CRT

In order to make data processing more efficient, a graphical user interface (GUI) was developed. The GUI provides the user with an interactive tool, which automatically generates the parameter files and Perl scripts necessary for a simulation. The calculations are performed with C++ programs which are controlled by Perl scripts. The calculations could be done for E_{RMS} and QRS based optimization methods. Both calculations use mainly the BeatGTI program. For QRS calculation ASCIILatticeMMD is additionally required to find the minimal and maximal values of converted lattice file (ASCII). This toolset of different programs receives the parameters via the command line. A Perl script executes the programs and provides them with the respective command line parameters. The data for the calculations are stored in folders with a fixed structure. The IBT CRT application allows to enter parameters easily, to store them, to reload them and to start the Perl scripts. By selecting 'Start Job', the application creates a parameter file and a Perl script with all information needed for the calculation. When the selected computer is available, the calculation starts immediately. So, it is not necessary to edit parameter files or Perl scripts manually.

In figure A.1, the main window with the list of jobs is demonstrated. In figure A.2 the data entry window is shown. The user can enter data for the following parameters:

1. Simulation and data set description
2. Electrode positions
3. A-V and V-V delay values
4. Infarction position
5. Simulation mode: physiology, pathology and pacing (sequential/simplex)
6. Computer ID where the job should be executed
7. The path to the simulation data
8. The percentage of conduction velocity (*.mp files)
9. Optional start values for the simplex algorithm

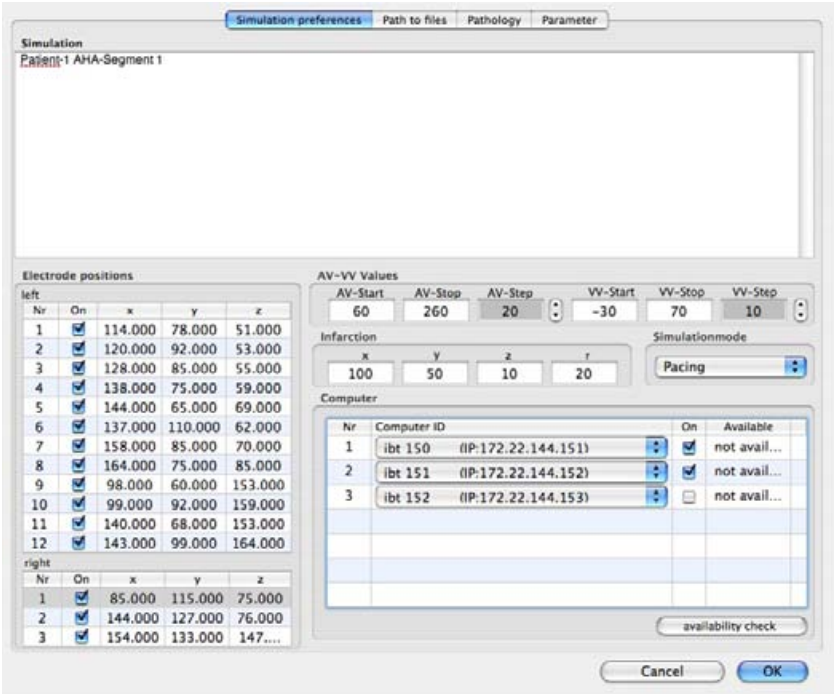

Figure A.1. Screenshot of the GUI data input (data entry window).

Depending on the selected simulation mode, different Perl scripts are generated. Furthermore, the project folder is renamed according to the simulation mode.

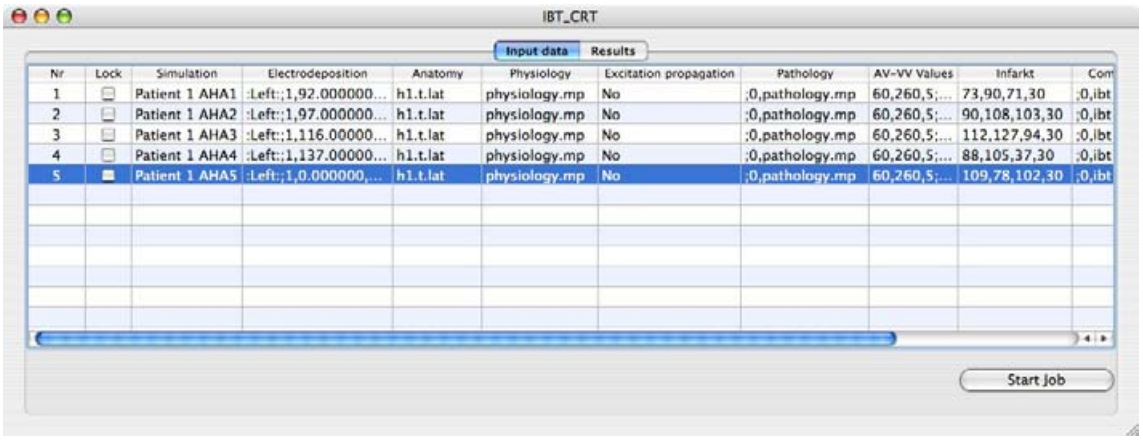

Figure A.2. Overview over simulation jobs.

A.3 Graphical User Interface for Clinical Application

This tool is used for clinical application. The user provides 3 pairs of A-V and V-V values as starting entries. For these values, the actual QRS duration is measured and entered in the third column labeled 'result'. Then, the DSA [213] calculates a new pair of timing values in which the QRS duration should be again measured. This step is repeated until the change in QRS duration is smaller than a predefined threshold and the criterion is fulfilled.

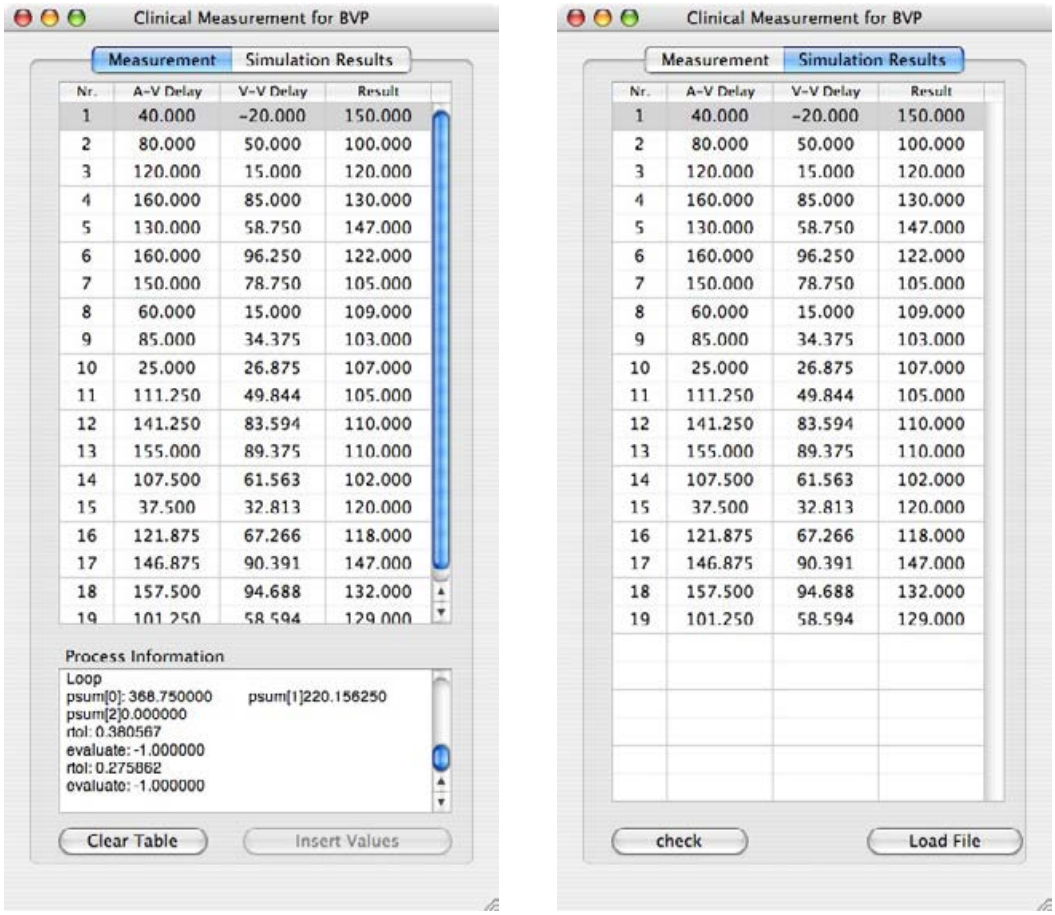

(a) (b)

Figure A.3. Simplex GUI for clinical application: (a) Data entry. (b) Calculated data from file.

List of Figures

2.1 The anatomy of the heart and the blood flow 8
2.2 View of the right atrium 9
2.3 View of the left ventricle 10
2.4 Heart in systole 10
2.5 Heart in diastole 11
2.6 Schematic drawing of the connection of the heart's major vessels 12
2.7 Heart and coronary arteries 12
2.8 A schematic overview of myocardium 14
2.9 A schematic representing the structure of the sarcomeres, myofibrilles and myofilaments 14
2.10 A microscopic photography of myocytes surrounded by capillary vessels . . 15
2.11 Schematic drawing of gap junctions providing electrical and mechanical coupling between the intercellular spaces of cardiac cells 16
2.12 A schematic showing the components of a cell membrane 17
2.13 Typical action potential of a myocyte with the 5 typical phases 20
2.14 Schematic of the cardiac excitation 22
2.15 The electrical depolarization-repolarization cycle of a cardiac pacemaker cell 23
2.16 Pacemaker and conduction system 23
2.17 Depolarization causes calcium to be released within a myocyte 24
2.18 Deploarization of atria 25
2.19 Excitation conduction system 26
2.20 Different configurations of the QRS complex 26
2.21 Repolarization of ventricles 27
2.22 Orientation angles of limb leads 29
2.23 Orientation angles of precordial leads 30
2.24 The IBT 64-channel ECG lead positions on the human torso 31
2.25 Several infarction positions 35
2.26 Ventricular remodeling after acute infarction 36

2.27 Ventricular remodeling in diastolic and systolic heart failure 37
2.28 ECG and transmitral flow velocity curve 39

3.1 BVP devices from Medtronic 45
3.2 Biventricular pacing device 46
3.3 Illustration of coronary sinus branches using angiography 47
3.4 Illustration of leads position using radiographs 48
3.5 Optimal LV pacing region with cost function 50
3.6 Techniques used for optimization of timing delays 54
3.7 Example of the impedance cardiography measurement acquired by the Task Force Monitor System 55
3.8 Chest X-ray of a patient under CRT with an IHM 58
3.9 Linear correlation between maximal systolic rate of LV pressure change and minimal diastolic rate of LV pressure change 59
3.10 Tissue tracking (TT) in a patient with LBBB 61
3.11 Apical long-axis view in patient with dilated cardiomyopathy and LBBB . 62
3.12 Short axis view of circumferential strain display prior to CRT 64
3.13 Short axis view of circumferential strain display during CRT 65
3.14 Example of the data acquired for measuring relative change in systolic blood pressure (SBP) for the tested atrio-ventricular and inter-ventricular delays 68
3.15 Pressure-volume loops measured with the conductance catheter 69
3.16 ECG morphology at different A-V intervals 71

4.1 Segmentation of left ventricle in short axis view 75
4.2 Cross section of segmented left ventricle in axial view. 76
4.3 A segmented ventricular model 77
4.4 Fiber orientation in ventricle 77
4.5 Subdivision of the left ventricle according to the AHA 78
4.6 AHA standard subdivision of the patient left ventricle 79
4.7 The electrical equivalent circuit representing the cell membrane of Hodgkin and Huxley 80
4.8 Schematic description of the ventricular cell model based on ten Tusscher 81
4.9 The simulated AP curves changing from endocardium to epicardium 83
4.10 Cellular automaton function 85
4.11 Simulated excitation conduction system of the ventricles starting from AV node to Purkinje fibers 86
4.12 Myocardium infarction 87

5.1 The Meet Man finite element model 92

6.1 The steps of generating the patient model 100
6.2 Ventricular model of patient-1 101
6.3 Ventricular model of patient-2 101
6.4 Ventricular model of patient-3 102
6.5 Ventricular model of patient-4 102
6.6 Ventricular model of patient-5 103
6.7 Ventricular model of patient-6 103
6.8 Ventricular model of patient-7 104
6.9 Ventricular model of patient-8 104
6.10 Ventricular model of patient-9 105
6.11 Ventricular model of patient-10 105
6.12 Ventricular model of patient-11 106
6.13 Ventricular model of patient-12 106
6.14 Ventricular model of patient-13 107
6.15 Torso model of patient-10 108
6.16 Torso model of patient-11 108
6.17 Torso model of patient-12 109
6.18 Torso model of patient-13 109
6.19 ECG of patient-13 110

7.1 The electrode positions chosen for the patient-4 heart model 115
7.2 Isochrones of the excitation for a cardiac model 115
7.3 QRS duration in the isochrones of the excitation for a cardiac model 117
7.4 Steps of performing DSA 119
7.5 Probability density functions of several distributions 121
7.6 Percentage points of the t distribution 121
7.7 Baseline wander cancellation in measured ECG 124
7.8 Block diagram of a simple wavelet shrinkage denoising system 125
7.9 Noise removal in measured ECG signal 125
7.10 Time averaging in measured ECG signal 127
7.11 Peak detection in ECG signal 128
7.12 Stimulus removal in ECG signal 129

8.1 The electrode positions chosen for the Patient-1 heart model 134
8.2 The minimal results achieved by the first optimization method for patient-1 with 100 % of conduction velocity 135
8.3 The minimal results achieved by the first optimization method for patient-1 with 80 % of conduction velocity 136
8.4 The minimal results achieved by the first optimization method for patient-1 with 60 % of conduction velocity 137

8.5 The minimal results achieved by the second optimization method for patient-1 with 100 % of conduction velocity 138
8.6 The minimal results achieved by the second optimization method for patient-1 with 80 % of conduction velocity 139
8.7 The minimal results achieved by the second optimization method for patient-1 with 60 % of conduction velocity 140
8.8 The electrode positions chosen for the Patient-2 heart model..... 141
8.9 The minimal results achieved by the first optimization method for patient-2 with 100 % of conduction velocity 142
8.10 The minimal results achieved by the first optimization method for patient-2 with 80 % of conduction velocity 143
8.11 The minimal results achieved by the first optimization method for patient-2 with 60 % of conduction velocity 144
8.12 The minimal results achieved by the second optimization method for patient-2 with 100 % of conduction velocity 145
8.13 The minimal results achieved by the second optimization method for patient-2 with 80 % of conduction velocity 146
8.14 The minimal results achieved by the second optimization method for patient-2 with 60 % of conduction velocity 147
8.15 The electrode positions chosen for the Patient-3 heart model..... 148
8.16 The minimal results achieved by the first optimization method for patient-3 with 100 % of conduction velocity 149
8.17 The minimal results achieved by the first optimization method for patient-3 with 80 % of conduction velocity 150
8.18 The minimal results achieved by the first optimization method for patient-3 with 60 % of conduction velocity 151
8.19 The minimal results achieved by the second optimization method for patient-3 with 100 % of conduction velocity 152
8.20 The minimal results achieved by the second optimization method for patient-3 with 80 % of conduction velocity 153
8.21 The minimal results achieved by the second optimization method for patient-3 with 60 % of conduction velocity 154
8.22 The electrode positions chosen for the Patient-4 heart model..... 155
8.23 The minimal results achieved by the first optimization method for patient-4 with 100 % of conduction velocity 156
8.24 The minimal results achieved by the first optimization method for patient-4 with 80 % of conduction velocity 157
8.25 The minimal results achieved by the first optimization method for patient-4 with 60 % of conduction velocity 158

8.26 The minimal results achieved by the second optimization method for patient-4 with 100 % of conduction velocity 159
8.27 The minimal results achieved by the second optimization method for patient-4 with 80 % of conduction velocity 160
8.28 The minimal results achieved by the second optimization method for patient-4 with 60 % of conduction velocity 161
8.29 The electrode positions chosen for the Patient-5 heart model..... 162
8.30 The minimal results achieved by the first optimization method for patient-5 with 100 % of conduction velocity 163
8.31 The minimal results achieved by the first optimization method for patient-5 with 80 % of conduction velocity 164
8.32 The minimal results achieved by the first optimization method for patient-5 with 60 % of conduction velocity 165
8.33 The minimal results achieved by the second optimization method for patient-5 with 100 % of conduction velocity 166
8.34 The minimal results achieved by the second optimization method for patient-5 with 80 % of conduction velocity 167
8.35 The minimal results achieved by the second optimization method for patient-5 with 60 % of conduction velocity 168
8.36 The electrode positions chosen for the Patient-6 heart model..... 169
8.37 The minimal results achieved by the first optimization method for patient-6 with 100 % of conduction velocity 170
8.38 The minimal results achieved by the first optimization method for patient-6 with 80 % of conduction velocity 171
8.39 The minimal results achieved by the first optimization method for patient-6 with 60 % of conduction velocity 172
8.40 The minimal results achieved by the second optimization method for patient-6 with 100 % of conduction velocity 173
8.41 The minimal results achieved by the second optimization method for patient-6 with 80 % of conduction velocity 174
8.42 The minimal results achieved by the second optimization method for patient-6 with 60 % of conduction velocity 175
8.43 The electrode positions chosen for the Patient-7 heart model..... 176
8.44 The minimal results achieved by the first optimization method for patient-7 with 100 % of conduction velocity 177
8.45 The minimal results achieved by the first optimization method for patient-7 with 80 % of conduction velocity 178
8.46 The minimal results achieved by the first optimization method for patient-7 with 60 % of conduction velocity 179

8.47 The minimal results achieved by the second optimization method for patient-7 with 100 % of conduction velocity 180
8.48 The minimal results achieved by the second optimization method for patient-7 with 80 % of conduction velocity 181
8.49 The minimal results achieved by the second optimization method for patient-7 with 60 % of conduction velocity 182
8.50 The electrode positions chosen for the Patient-8 heart model..... 183
8.51 The minimal results achieved by the first optimization method for patient-8 with 100 % of conduction velocity 184
8.52 The minimal results achieved by the first optimization method for patient-8 with 80 % of conduction velocity 185
8.53 The minimal results achieved by the first optimization method for patient-8 with 60 % of conduction velocity 186
8.54 The minimal results achieved by the second optimization method for patient-8 with 100 % of conduction velocity 187
8.55 The minimal results achieved by the second optimization method for patient-8 with 80 % of conduction velocity 188
8.56 The minimal results achieved by the second optimization method for patient-8 with 60 % of conduction velocity 189
8.57 The electrode positions chosen for the Patient-9 heart model..... 190
8.58 The minimal results achieved by the first optimization method for patient-9 with 100 % of conduction velocity 191
8.59 The minimal results achieved by the first optimization method for patient-9 with 80 % of conduction velocity 192
8.60 The minimal results achieved by the first optimization method for patient-9 with 60 % of conduction velocity 193
8.61 The minimal results achieved by the second optimization method for patient-9 with 100 % of conduction velocity 194
8.62 The minimal results achieved by the second optimization method for patient-9 with 80 % of conduction velocity 195
8.63 The minimal results achieved by the second optimization method for patient-9 with 60 % of conduction velocity 196
8.64 The electrode positions chosen for the Patient-10 heart model..... 197
8.65 The minimal results achieved by the first optimization method for patient-10 with 100 % of conduction velocity 198
8.66 The minimal results achieved by the first optimization method for patient-10 with 80 % of conduction velocity 199
8.67 The minimal results achieved by the first optimization method for patient-10 with 60 % of conduction velocity 200

8.68 The minimal results achieved by the second optimization method for patient-10 with 100 % of conduction velocity 201
8.69 The minimal results achieved by second optimization method for patient-10 with 80 % of conduction velocity 202
8.70 The minimal results achieved by second optimization method for patient-10 with 60 % of conduction velocity 203
8.71 The optimal pacing parameters achieved by the first optimization method for all patients with different conduction velocities 205
8.72 The optimal pacing parameters achieved by the first optimization method for all patients with different conduction velocities 205
8.73 The optimal pacing parameters achieved by the first optimization method for all patients with different conduction velocities 206
8.74 The optimal pacing parameters achieved by the second optimization method for all patients with different conduction velocities 206
8.75 The optimal pacing parameters achieved by the second optimization method for all patients with different conduction velocities 207
8.76 The optimal pacing parameters achieved by the second optimization method for all patients with different conduction velocities 207
8.77 Histogram of the optimal A-V delays achieved by the first optimization method 208
8.78 Histogram of the optimal V-V delays achieved by the first optimization method 208
8.79 Regression line demonstrating the relation between both optimization methods in terms of physiological-pathological error. 209
8.80 Regression line demonstrating the relation between both optimization methods for in terms of physiological-pacing error. 210
8.81 Regression line demonstrating the relation between both optimization methods for in terms of reduction error percentage. 210

9.1 The measured 64 channels ECG before implantation for Patient-11. 214
9.2 The measured 64 channels ECG after implantation for Patient-11. 214
9.3 The simulated ECG channels of Patient-11 pre-implantation. 216
9.4 The measured ECG channels of Patient-11 pre-implantation. 216
9.5 The simulated ECG channels of Patient-11 pre-implantation 217
9.6 The measured ECG channels of Patient-11 pre-implantation 217
9.7 The simulated ECG channels of Patient-11 pre-implantation 218
9.8 The measured ECG channels of Patient-11 pre-implantation 218
9.9 Correlation coefficients between simulated and measured 12 standard ECG channels 219
9.10 The electrode positions chosen for the Patient-11 heart model 220

9.11 The simulated ECG channels of Patient-11 post-implantation. 221
9.12 The measured ECG channels of Patient-11 post-implantation. 221
9.13 QRS duration of the 12 channels ECG before and after implantation in Patient-11 222
9.14 The measured 64 channels ECG before implantation for Patient-12. 223
9.15 The measured 64 channels ECG after implantation for Patient-12. 223
9.16 The simulated ECG channels of Patient-12 pre-implantation. 225
9.17 The measured ECG channels of Patient-12 pre-implantation. 225
9.18 The simulated ECG channels of Patient-12 pre-implantation 226
9.19 The measured ECG channels of Patient-12 pre-implantation 226
9.20 The simulated ECG channels of Patient-12 pre-implantation 227
9.21 The measured ECG channels of Patient-12 pre-implantation 227
9.22 Correlation coefficients between simulated and measured 12 standard ECG channels 228
9.23 The electrode positions chosen for the Patient-12 heart model 229
9.24 The simulated ECG channels of Patient-12 post-implantation. 230
9.25 The measured ECG channels of Patient-12 post-implantation. 230
9.26 QRS duration of the 12 channels ECG before and after implantation in Patient-12 231
9.27 The measured 64 channels ECG before therapy for Patient-13. 232
9.28 The simulated ECG channels of Patient-13 pre-implantation. 234
9.29 The measured ECG channels of Patient-13 pre-implantation. 234
9.30 The simulated ECG channels of Patient-13 pre-implantation 235
9.31 The measured ECG channels of Patient-13 pre-implantation 235
9.32 The simulated ECG channels of Patient-13 pre-implantation 236
9.33 The measured ECG channels of Patient-13 pre-implantation 236
9.34 Correlation coefficients between simulated and measured 12 standard ECG channels 237
9.35 Location of extrasystole in Patient-13 238

A.1 Data entry window 249
A.2 Screenshot of the GUI 249
A.3 Simplex GUI for clinical application 250

List of Tables

2.1 Intracellular and extracellular concentrations of several ions [216]. 18
2.2 Sequence of cardiac excitation with corresponding conduction velocities and intrinsic pacemaking frequencies [216]. 21

3.1 Some studies determining the CRT responders and non-responders due to the parameters change representing the efficacy. 44
3.2 Several studies since 1999 on CRT in which various positions of the electrodes have been investigated. 50
3.3 Several studies since 1999 on CRT in which different timing delays have been investigated. Bold values state the optimal values chosen by the authors. In some studies, no optimal values were achieved. 52
3.4 Clinical methods used for optimization of CRT parameters. 72

4.1 Ionic models of cardiac cells [241] 82
4.2 I components according to the ten Tusscher cell model [261]. 83

6.1 Overview of the 13 different data sets used in this study. 100
6.2 Overview of the 4 different volume conductor models used in this study. . . 107

7.1 Calculation of random variable T based on t test type. 122
7.2 Frequency contents of different levels with respect to the sample rate [41]. 126

8.1 Results of the first optimization method for Patient-1 with 100 % conduction velocity. 135
8.2 Results of the first optimization method for Patient-1 with 80 % conduction velocity. 136
8.3 Results of the first optimization method for Patient-1 with 60 % conduction velocity. 137
8.4 Results of the second optimization method for Patient-1 with 100 % conduction velocity. 138

8.5 Results of the second optimization method for Patient-1 with 80 % conduction velocity. 139
8.6 Results of the second optimization method for Patient-1 with 60 % conduction velocity. 140
8.7 Results of the first optimization method for Patient-2 with 100 % conduction velocity. 142
8.8 Results of the first optimization method for Patient-2 with 80 % conduction velocity. 143
8.9 Results of the first optimization method for Patient-2 with 60 % conduction velocity. 144
8.10 Results of the second optimization method for Patient-2 with 100 % conduction velocity. 145
8.11 Results of the second optimization method for Patient-2 with 80 % conduction velocity. 146
8.12 Results of the second optimization method for Patient-2 with 60 % conduction velocity. 147
8.13 Results of the first optimization method for Patient-3 with 100 % conduction velocity. 149
8.14 Results of the first optimization method for Patient-3 with 80 % conduction velocity. 150
8.15 Results of the first optimization method for Patient-3 with 60 % conduction velocity. 151
8.16 Results of the second optimization method for Patient-3 with 100 % conduction velocity. 152
8.17 Results of the second optimization method for Patient-3 with 80 % conduction velocity. 153
8.18 Results of the second optimization method for Patient-3 with 60 % conduction velocity. 154
8.19 Results of the first optimization method for Patient-4 with 100 % conduction velocity. 156
8.20 Results of the first optimization method for Patient-4 with 80 % conduction velocity. 157
8.21 Results of the first optimization method for Patient-4 with 60 % conduction velocity. 158
8.22 Results of the second optimization method for Patient-4 with 100 % conduction velocity. 159
8.23 Results of the second optimization method for Patient-4 with 80 % conduction velocity. 160
8.24 Results of the second optimization method for Patient-4 with 60 % conduction velocity. 161

8.25 Results of the first optimization method for Patient-5 with 100 % conduction velocity. 163
8.26 Results of the first optimization method for Patient-5 with 80 % conduction velocity. 164
8.27 Results of the first optimization method for Patient-5 with 60 % conduction velocity. 165
8.28 Results of the second optimization method for Patient-5 with 100 % conduction velocity. 166
8.29 Results of the second optimization method for Patient-5 with 80 % conduction velocity. 167
8.30 Results of the second optimization method for Patient-5 with 60 % conduction velocity. 168
8.31 Results of the first optimization method for Patient-6 with 100 % conduction velocity. 170
8.32 Results of the first optimization method for Patient-6 with 80 % conduction velocity. 171
8.33 Results of the first optimization method for Patient-6 with 60 % conduction velocity. 172
8.34 Results of the second optimization method for Patient-6 with 100 % conduction velocity. 173
8.35 Results of the second optimization method for Patient-6 with 80 % conduction velocity. 174
8.36 Results of the second optimization method for Patient-6 with 60 % conduction velocity. 175
8.37 Results of the first optimization method for Patient-7 with 100 % conduction velocity. 177
8.38 Results of the first optimization method for Patient-7 with 80 % conduction velocity. 178
8.39 Results of the first optimization method for Patient-7 with 60 % conduction velocity. 179
8.40 Results of the second optimization method for Patient-7 with 100 % conduction velocity. 180
8.41 Results of the second optimization method for Patient-7 with 80 % conduction velocity. 181
8.42 Results of the second optimization method for Patient-7 with 60 % conduction velocity. 182
8.43 Results of the first optimization method for Patient-8 with 100 % conduction velocity. 184
8.44 Results of the first optimization method for Patient-8 with 80 % conduction velocity. 185

8.45 Results of the first optimization method for Patient-8 with 60 % conduction velocity. 186
8.46 Results of the second optimization method for Patient-8 with 100 % conduction velocity. 187
8.47 Results of the second optimization method for Patient-8 with 80 % conduction velocity. 188
8.48 Results of the second optimization method for Patient-8 with 60 % conduction velocity. 189
8.49 Results of the first optimization method for Patient-9 with 100 % conduction velocity. 191
8.50 Results of the first optimization method for Patient-9 with 80 % conduction velocity. 192
8.51 Results of the first optimization method for Patient-9 with 60 % conduction velocity. 193
8.52 Results of the second optimization method for Patient-9 with 100 % conduction velocity. 194
8.53 Results of the second optimization method for Patient-9 with 80 % conduction velocity. 195
8.54 Results of the second optimization method for Patient-9 with 60 % conduction velocity. 196
8.55 Results of the first optimization method for Patient-10 for 100 % conduction velocity. 198
8.56 Results of the first optimization method for Patient-10 for 80 % conduction velocity. 199
8.57 Results of the first optimization method for Patient-10 for 60 % conduction velocity. 200
8.58 Results of the second optimization method for Patient-10 with 100 % conduction velocity. 201
8.59 Results of the second optimization method for Patient-10 with 80 % conduction velocity. 202
8.60 Results of the second optimization method for Patient-10 with 60 % conduction velocity. 203
8.61 Percentage range of agreement of timing delays and electrode setups for both optimization methods in all patients. 209
8.62 Descriptive statistics of the obtained distributions for each electrode position. 211
8.63 Tests of normality. 211
8.64 Tests of fixed effects between electrode position setups. 212

9.1 Initial and optimized values for infarction location and excitation conduction velocity in different tissues. 215
9.2 Initial and optimized values for excitation conduction velocity in different tissues. 224
9.3 Initial and optimized values for extrasystole location and excitation conduction velocity in different tissues. 233

References

[1] W. Abraham. Cardiac resynchronisation therapy: a review of clinical trials and criteria for identifying the appropriate patient. *Reviews in Cardiovascular Medicine*, 4(2):S30–S37, 2003.

[2] W. T. Abraham, W. G. Fisher, A. L. Smith, D. B. Delurgio, A. R. Leon, E. Loh, D. Z. Kocovic, M. Packer, A. L. Clavell, D. L. Hayes, M. Ellestad, R. J. Trupp, J. Underwood, F. Pickering, C. Truex, P. McAtee, and J. Messenger for the MIRACLE Study Group. Multicenter InSync Randomized Clinical Evaluation. Cardiac resynchronization in chronic heart failure. *N Engl J Med*, 346:1845–1853, 2002.

[3] W. T. Abraham and D. L. Hayes. Cardiac resynchronization therapy for heart failure. *Circulation*, 108:2596–2603, 2003.

[4] Z. Akalm Acar and N. G. Gencer. An advanced boundary element method (bem) implementation for the forward problem of electromagnetic source imaging. *Phys Med Biol*, 49:5011–5028, 2004.

[5] A. Achilli, M. Sassara, S. Ficilli, and et al. Long-term effectiveness of cardiac resynchronization therapy in patients with refractory heart failure and narrow qrs. *J Am Coll Cardiol*, 42:2117–2124, 2003.

[6] M. Sassaraand A. Achilli, S. Ficili, and et al. Efficacy of cardiac resynchronisation therapy in narrow qrs patients. *Europace*, 3:A29, 2002.

[7] Action potential. http://www.cvphysiology.com/Arrhythmias/A006.htm.

[8] P. B. Adamson, A. Magalski, F. Braunschweig, M. Bohm, and et al. Ongoing right ventricular hemodynamics in heart failure: clinical value of measurements derived from an implantable monitoring system. *J Am Coll Cardiol*, 41:565–571, 2003.

[9] Alford. http://alford.bios.uic.edu/Images/586 20images/circuit 20model.

[10] American Heart Association. http://www.americanheart.org/downloadable/heart/1072969 766940HS Stats2004Update.pdf.

[11] American Heart Association. http://www.americanheart.org/presenter.jhtml?identifier=11077.

[12] Anatomy. http://www.octc.kctcs.edu/gcaplan/anat/.

[13] Anatomy 1. http://umanitoba.ca/faculties/medicine/units/anatomy/images/.

[14] R. H. Anderson and A. E. Becker. *Anatomie des Herzens*. Georg Thieme Verlag, Stuttgart, 1982.

[15] G. Ansalone, P. Giannantoni, R. Ricci, P. Trambaiolo, F. Fedele, and M. Santini. Doppler myocardial imaging to evaluate the effectiveness of pacing sites in patients receiving biventricular pacing. *J Am Coll Cardiol*, 39:489–499, 2002.

[16] A. Auricchio and C. Fantoni. Cardiac resynchronization therapy in heart failure. *Ital Heart J*, 6(3):256–260, 2005.

[17] A. Auricchio, C. Stellbrink, M. Block, S. Sack, J. Vogt, P. Bakker, Klein, A. Kramer, J. Ding, R. Salo, Tockman, T. Pochet, and J. Spinelli. Effect of pacing chamber and atrioventricular delay on acute systolic function of paced patients with congestive heart failure. *Circulation*, 99:2993–3001, 1999.

[18] A. Auricchio, C. Stellbrink, and et al. Clinical efficacy of cardiac resynchronization therapy using left ventricular pacing in heart failure patients stratified by severity of ventricular conduction delay. *J Am Coll Cardiol*, 42:2109–2116, 2003.

[19] A. Auricchio, C. Stellbrink, S. Sack S, and et al. Long term clinical effect of haemodynamically optimised cardiac resynchronisation therapy in patients with heart failure and ventricular conduction delay. *J Am Coll Cardiol*, 39:2026–2033, 2002.

[20] A. Auricchio and C. M. Yu. Beyond the measurement of qrs complex toward mechanical dyssynchrony: cardiac resynchronisation therapy in heart failure patients with a normal qrs duration. *Heart*, 90:479–481, 2004.

[21] P. Banerjee, T. Banerjee, and et. al. Diastolic heart failure: neglected or misdiagnosed? *J Am Coll Cardiol*, 39:138–141, 2002.

[22] I. N. Bankman. *Handbook of Medical Imaging*. Academic Press, 2000.

[23] W. Bargmann. Bau des Herzens. In W. Bargmann and W. Doerr, editors, *Das Herz des Menschen*, pages 88–164. Georg Thieme Verlag, Stuttgart, 1963.

[24] J. J. Bax, G. Ansalone, O. A. Breithardt, G. Derumeaux, C. Leclercq, M. J. Schalij, P. Sogaard, M. St. John Sutton, and P. Nihoyannopoulos. Echocardiographic evaluation of cardiac resynchronization therapy: ready for routine clinical use? *J Am Coll Cardiol*, 44:1–9, 2004.

[25] J. J. Bax, E. E. Van der Wall, and M. J. Schalij. Left ventricular dyssynchrony predicts response and prognosis after cardiac resynchronization therapy. *J Am Coll Cardiol*, 44:1834–1840, 2004.

[26] J. J. Bax, S. G. Molhoek, L. van Erven, P. J. Voogd, S. Somer, E. Boersma, P. Steendijk, M. J. Schalij, and E. E. van der Wall. Usefulness of myocardial tissue doppler echocardiography to evaluate left ventricular dyssynchrony before and after ventricular pacing in patients with idiopathic dilated cardiomyopathy. *J Am Coll Cardiol*, 91:94–97, 2003.

[27] H. Bazett. An analysis of the time relation of electrocardiograms. *Heart*, 7:353–370, 1920.

[28] M. Becker, R. kramann, A. Franke, O. A. Breithardt, N. Heussen, C. Knackstedt, C. Stellbrink, P. Schauerte, M. Kelm, and R. Hoffman. Impact of left ventricular lead position in cardiac resynchronization therapy on left ventricular remodeling. a circumferential strain analysis based on 2-d echocardiography. *European Heart Journal*, 28:1211–1220, 2007.

[29] R. C. Becker. Biomarkers in atrial fibrillation: investigating biologic plausibility, cause, and effect. *J Thromb Thrombolysis*, 19(1):71–75, Feb 2005.

[30] G. W. Beeler and H. Reuter. Reconstruction of the action potential of ventricular myocardial fibres. *J. Physiol.*, 268:177–210, 1977.

[31] E. J. Benjamin, P. A. Wolf, and et al. Impact of atrial fibrillation on the risk of death: the framingham heart study. *Circulation*, 98(10):946–952, 1998.

[32] P. B. Bennett and H.-G. Shin. Biophysics of cardiac sodium channels. In D. P. Zipes and J. Jalife, editors, *Cardiac Electrophysiology. From Cell to Bedside*, chapter 8, pages 67–78. W. B. Saunders Company, Philadelphia, 3 edition, 1999.

[33] O. Bernus, R. Wilders, C. W. Zemlin, H. Verschelde, and A. V. Panfilov. A computationally efficient electrophysiological model of human ventricular cells. *Am. J. Physiol.*, 282:H2296–H2308, 2002.

[34] Biosemi. http://www.biosemi.com/.

[35] G. B. Bleeker, J. J. Bax, J. Wing-Hong Fung, E. E. Van der Wall, and et al. Clinical versus echocardiographic parameters to assess response to cardiac resynchronization therapy. *J Am Coll Cardiol*, 97:260–263, 2006.

[36] G. B. Bleeker, E. R. Holman, and et al. Cardiac resynchronization therapy in patients with a narrow qrs complex. *J Am Coll Cardiol*, 48:2243–2250, 2006.

[37] G. B. Bleeker, T. A. Kaandorp, H. J. Lamb, E. Boersma, P. Steendijk, A. de Roos, E. E. van der Wall, M. J. Schalij, and J. J. Bax. Effect of posterolateral scar tissue on clinical and echocardiographic improvement after cardiac resynchronization therapy. *Circulation*, 113:969–976, 2006.

[38] G. B. Bleeker, M. Schalij, E. Boersma, P. Steendijk, E. E. van der Wall, and J. J. Bax. Does a gender difference in response to cardiac resynchronization therapy exist? *Pacing Clin Electrophysiol*, 28:1271–1275, 2005.

[39] G. B. Bleeker, M. J. Schalij, S. G. Molhoek, and et al. Frequency of left ventricular dyssynchrony in patients with heart failure and a narrow qrs complex. *Am J Cardiol*, 95:140–142, 2005.

[40] G. B. Bleeker, M. J. Schalij, S. G. Molhoek, H. F. Verwey, E. R. Holman, E. Boersma, P. Steendijk, E. E. Van der Wall, and J. J. Bax. Relationship between qrs duration and left ventricular dyssynchrony in patients with end-stage heart failure. *J Cardiovasc Electrophysiol*, 15(5):544–549, May 2004.

[41] Julia Bohnert. ECG segmentation using wavelet transformation. Master's thesis, Universität Karlsruhe (TH), Institut für Biomedizinische Technik, 2007. Diploma Thesis.

[42] P. Bordachar, S. Lafitte, S. Reuter, P. Sanders, P. Jais, M. Haissaguerre, R. Roudaut, S. Garrigue, and J. Clementy. Echocardiographic parameters of ventricular dyssynchrony validation in patients with heart failure using sequential biventricular pacing. *J Am Coll Cardiol*, 44:2157–2165, 2004.

[43] G. Boriani, C. P. Müller, K. H. Seidl, and et al. Randomized comparison of simultaneous biventricular stimulation versus optimized interventricular delay in cardiac resynchronization therapy: The resynchronization for the hemodynamic treatment for heart failure management ii implantable cardioverter defibrillator (rhythm ii icd) study. *American Heart Journal*, 151(5):1050–1058, 2006.

[44] M. R. Boyett, H. Zhang, A. Garny, and A. V. Holden. Control of the pacemaker activity of the sinoatrial node by intracellular Ca^{2+}. Experiments and modelling. *Phil. Trans. R. Soc. London*, 359:1091–1110, 2001.

[45] M. U. Braun, A. Schnabel, and et al. Impedance cardiography as a noninvasive technique for atrioventricular interval optimization in cardiac resynchronization therapy. *J Interv Cardiac Electrophysiol*, 13:223–229, 2005.

[46] F. Braunschweig, B. Kjellstrom, F. Gadler, C. Linde, and et al. Optimization of cardiac resynchronization therapy by continuous hemodynamic monitoring. *Cardiovasc Electrophysiol*, 15:94–96, 2004.

[47] D. G. Bristow and J. W. Clark. A mathematical model of primary pacemaker cell in SA node of the heart. *Am. J. Physiol.*, 243(2):H207–H218, 1982.

[48] D. G. Bristow and J. W. Clark. A mathematical model of the vagally driven primary pacemaker. *Am. J. Physiol.*, 244(1):H150–H161, 1983.

[49] M. R. Bristow, E. M. Gilbert, W. T. Abraham W.T., and et al. Carvedilol produces dose-related improvements in left ventricular function and survival in subjects with chronic heart failure. *Circulation*, 94:2807–2816, 1996.

[50] M. R. Bristow, L. A. Saxon, J. Boehmer, S. Krueger, D. A. Kass, T. De Marco, P. Carson, L. DiCarlo, D. DeMets, B. G. White, and et al. Comparison of medical therapy, pacing and defibrillation in heart failure (companion) investigators. cardiac resynchronization therapy with or without an implantable defibrillator in advanced chronic heart failure. *N Engl J Med*, 250:2140–2150, 2004.

[51] H. J. Bruns, F. Braunschweig, D. Ersgard, M. Stalberg, P. Reiters, and et al. Opportunities for optimization of biventricular pacing using an implanted hemodynamic monitor. *Computers in cardiol*, 32:121–124, 2005.

[52] D. L. Brutsaert and S. U. Sys. Diastolic dysfunction in heart failure. *J Card Fail*, 3:225–242, 1997.

[53] E. Buch, N. Lellouche, C. D. Diego, M. Vaseghi, D. A. Cesario, O. Fujimura, I. Wiener, J. S. Child, N. G. Boyle, and K. Shivkumar. Left ventricular apical wall motion abnormality is associated with lack of response to cardiac resynchronization therapy in patients with ischemic cardiomyopathy. *Heart Rhythm*, 4(10):1300–1305, 2007.

[54] M. Buist and A. Pullan. Torso coupling techniques for the forward problem of electrocardiography. *Ann Biomed Eng*, 30:1187–1201, 2002.

[55] H. Burri, D. Shah, and R. Lerch. Optimization of device programming for cardiac resynchonization therapy. *Pacing Clin Electrophysiol*, 29:1416–1425, 2006.

[56] H. Burri, H. Sunthorn, and A. Somsen. Optimizing sequential biventricular pacing using radionuclide ventriculography. *Heart Rhythm*, 2:960–965, 2005.

[57] C. Butter, A. Auricchio, C. Stellbrink, and et al. Effect of resynchronisation therapy site on the systolic function of heart failure patients-on behalf of the pacing therapy for chronic heart failure ii (path-chf-ii) study group. *Circulation*, 104:3026–3029, 2001.

[58] C. Butter, C. Stellbrink, A. Belalcazar, D. Villalata, and et al. Cardiac resynchronization therapy optimization by finger plethysmography. *Heart Rhythm*, 1:568–575, 2004.

[59] C. Alonso C, C. Leclercq, F. Victor, and et al. Electrocardiographic predictive factors of long-term clinical improvement with multisite biventricular pacing in advanced heart failure. *Am J Cardiol*, 84:1417–1421, 1999.

[60] Cardiac index. http://www.medterms.com.

[61] Cardiac Resynchronization Therapy. http://my.clevelandclinic.org/heart/services/tests/.

[62] S. Caseau, P. Ritter, A. Lazarus, and et al. Multisite pacing for end stage heart failure: early experience. *Pacing Clin Electrophysiol*, 19:1748–1757, 1996.

[63] S. Cazeau, C. Alonso, G. Jauvert, A. Lazarus, and P. Ritter. Cardiac resynchronization therapy. *Europace*, 5 Suppl1:S42–S48, Sep 2004.

[64] S. Cazeau, C. Leclerq, T. Lavergne, S. Walker, C. Varma, C. Linde, S. Garrigue, L. Kappnberger, G. A: Haywood, M. Santini, and et al. Multisite stimulation in cardiomyopathies (mustic) study investigators. effects of multisite biventricular pacing in patients with heart failure and intraventricular conduction delay. *N Engl J Med*, 344:873–880, 2001.

[65] M. D. Cerqueira, N. J. Weissman, V. Dilsizian, and et al. Writing group on myocardial segmentation registration for cardiac imaging. standardized myocardial segmentation and nomenclature for tomographic imaging of the heart: a statement for healthcare professionals from the cardiac imaging committee of the council on clinical cardiology of the american heart association. *Circulation*, 105:539–542, 2002.

[66] J. G. Cleland, J. C. Daubert, E. Erdmann, and et al. The effect of cardiac resynchronization therapy on morbidity and mortality in heart failure. *N Engl J Med*, 352:1539–1549, 2005.

[67] Conduction system. http://butler.cc.tut.fi/ malmivuo/bem/bembook/06/06.htm.

[68] R. S. Cotran, V. Kumar, and T. Collins. *Robbins Pathologic Basis of Disease*. W. B. Saunders Company, 6 edition, 1999.

[69] M. Courtemanche, R. J. Ramirez, and S. Nattel. Ionic mechanisms underlying human atrial action potential properties: Insights from a mathematical model. *Am. J. Physiol.*, 275(44):H301–H321, 1998.

[70] J. L. Cox, J. P. Boineau, R. B. Schuessler, K. M. Kater, and D. G. Lappas DG. Five-year experience with the maze procedure for atrial fibrillation. *Ann Thorac Surg*, 56:814–824, 1994.

[71] J. M. Van Dantzig, B. J. Delemarre, and et. al. Pathogenesis of mitral regurgitation in acute myocardial infarction: importance of changes in left ventricular shape and regional function. *Am Heart J*, 131:865–871, 1996.

[72] J. C. Daubert, P. Ritter, H. Le Breton, and et al. Permanent left ventricular pacing with transvenous leads inserted into the coronary veins. *Pacing Clin Electrophysiol*, 21:239–245, 1998.

[73] N. R. Van de Veire, G. B. Bleeker, J. D. Sutter, and et al. Systolic dysfunction: correlation of acoustic cardiography with doppler echocardiography. *Heart*, 93:1034–1039, 2007.

[74] M. Delmar, H. S. Duffy, P. L. Sorgen, S. M. Taffet, and D. C. Spray. Molecular organization and regulation of the cardiac gap junction channel connexin43. In D. P. Zipes and J. Jalife, editors, *Cardiac Electrophysiology. From Cell to Bedside*, chapter 8, pages 66–76. W. B. Saunders Company, Philadelphia, 4 edition, 2004.

[75] M. Delmar, G. E. Morley, J. F. Ek-Vitorin, D. Francis, N. Homma, K. Stergiopoulos, A. Lau, and S. M. Taffet. Intracellular regulation of the cardiac gap junction channel connexin43. In D. P. Zipes and J. Jalife, editors, *Cardiac Electrophysiology. From Cell to Bedside*, chapter 15, pages 126–132. W. B. Saunders Company, Philadelphia, 3 edition, 1999.

[76] S. S. Demir, J. W. Clark, and W. R. Giles. Parasympatheticc modulation of sinoatrial node pacemaker activity in rabbit heart: A unifying model. *Am. J. Physiol.*, 276:H2221–H2244, 1999.

[77] S. S. Demir, J. W. Clark, C. R. Murphey, and W. R. Giles. A mathematical model of a rabbit sinoatrial node cell. *Am. J. Physiol.*, 35:832–852, 1994.

[78] S. S. Demir, B. O'Rourke, G. F. Tomaselli, E. Marbán, and R. L. Winslow. Action potential variation in canine ventricle: A modeling study. In *Proc. Computers in Cardiology*, volume 23, pages 221–224, 1996.

[79] D. DiFrancesco and D. Noble. A model of cardiac electrical activity incorporating ionic pumps and concentration changes. *Phil. Trans. R. Soc. Lond.*, 307:353–398, 1985.

[80] K. Dohi, M. S. Suffoletto, D. Schwartzman, L. Ganz, M. R. Pinsky, and J. Gorcsan. Utility of echocardiographic radial strain to quantify left ventricular dyssynchrony and predict acute response to cardiac resynchronization therapy. *Am J Cardiol*, 96:112–116, 2005.

[81] S. Dokos, B. G. Celler, and N. H. Lovell. Vagal control of sinoatrial rhythm: A mathematical model. *J. Theor. Biol.*, 182:21–44, Sep. 1996.

[82] D. Donnell, N. Nadurata, A. Hamer, and et al. Long-term variations in optimal programming of cardiac resynchronization therapy device. *PACE*, 28:S24–S26, 2005.

[83] D. L. Donoho. Denoising by soft thresholding. *IEEE Transactions on Information Theory*, 41, May 1995.

[84] O. Dössel. *Bildgebende Verfahren in der Medizin*. Springer, Berlin, 1999.

[85] O. Dössel. Inverse problem of electro- and magnetocardiography: Review and recent progress. *Bioelectromagnetism*, 2(2), 2000.

[86] O. Dössel and F. R. Schneider. The nullspace of electrocardiography. In *Biomedizinische Technik*, volume 42-1, pages 37–40, 1997.

[87] J. Dudel. Grundlagen der Zellphysiologie. In R. F. Schmidt, G. Thews, and F. Lang, editors, *Physiologie des Menschen*, chapter 1, pages 3–19. Springer, Berlin, Heidelberg, New York, 2000.

[88] J. Dudel. Informationsvermittlung durch elektrische Erregung. In R. F. Schmidt, G. Thews, and F. Lang, editors, *Physiologie des Menschen*, chapter 2, pages 20–42. Springer, Berlin, Heidelberg, New York, 2000.

[89] E-wave. http://www.fac.org.ar/scvc/llave/echo/roeland/roelandi.htm.

[90] Y. E. Earm and D. Noble. A model of single atrial cell: Relation between calcium current and calcium release. *Proc. R. Soc. Lond.*, 240:83–96, 1990.

[91] ECG trace. http://www.cvphysiology.com/Arrhythmias/ECG trace with grid.gif.

[92] E. J. Eichhorn and M. R. Bristow. Medical therapy can improve the biological properties of the chronically failing heart: a new era in the treatment of heart failure. *Circulation*, 94:2285–2296, 1996.

[93] D. Farina and O. Dössel. Influence of cardiac activity in midmyocardial cells on resulting ecg: simulation study. *In Biomedizinische Technik*, 2006.

[94] Dmytro. Farina. *Forward and Inverse Problems of Electrocardiography: Clinical Investigations*. PhD thesis, Institut für Biomedizinische Technik, Universitätsverlag Karlsruhe ISBN 978-3-86644-219-1, 2008.

[95] O. Faris, C. Leclercq, and R. Kato et al. Assessment of electrical and mechanical function in the paced lbbb failing heart using tagged mri and epicardial mapping. *J Electrocardiol suppl*, 35:205, 2002.

[96] G. Fischer and B. Tilg. Application of high order boundary elements to the electrocardiographic inverse problem. *Comput Meth Pro Biomed*, 58:119–131, 1999.

[97] D. J. Fox, A. P. Fitzpatrick, and N. C. Davidson. Optimization of cardiac resyncronisation therapy: addressing the problem of non-responders. *Heart*, 91:1001–1002, 2005.

[98] S. S. Galvao, C. M. Barcellos, and et al. Ventricular resynchronization through biventricular cardiac pacing for the treatment of refractory heart failure in dilated cardiomyopathy. *Arq Bras Cardiol*, 78(1):45–50, 2002.

[99] M. Gardner, J. Sapp, and et al. Electromechanical coupling in resynchronized heart failure: Empress study protocol. *EMPRESS study protocol Unpublished*, 2006.

[100] H. Ghanbari, B. Hassunizadeh, and C. Machado. Expanding cardiac resynchronization for systolic heart failure to patients with mechanical dyssynchrony and atrial fibrillation. *Rev Cardiovasc Med*, 6(3):140–151, 2005.

[101] S. Ghosh and Y. Rudy. Accuracy of quadratic versus linear interpolation in noninvasive electrocardiographic imaging (ecgi). *Ann Biomed Eng*, 33:1187–1201, 2005.

[102] L. Gianfranchi, K. Bettiol, and et al. The fusion band in v1: a simple ecg guide to optimal resynchronization? an echocardiographic case report. *Cardiovascular Ultrasound*, 3(29), 2005.

[103] D. E. Goldman. Potential, impedance, and rectification in membranes. *J. Gen. Physiol.*, 27:37–60, 1943.

[104] G. H. Golub and C. F. V. Loan. *Matrix Computations*. The Johns Hopkins University Press, 1996.

[105] B. D. Gonska and R. Heinecker. *EKG in Klinik und Praxis*. George Theme, 14 edition, 1999.

[106] J. Gorscan, H. Kanzaki, R. Bazaz, K. Dohi, and D. Schwartzman. Usefulness of echocardiogrphic tissue synchronization imaging to predict acute response to cardiac resynchronization therapy. *Am J Cardiol*, 93:1178–1181, 2004.

[107] K. Goscinska-Bis, B. Grzegorzewski, and et al. Intracardiac electrogram method of vv-delay optimization in biventricular pacemakers. *Cardiol J*, 14:305–310, 2007.

[108] H. Gray and W. H. Lewis. *Anatomy of the human body*. Lea & Febiger, Philadelphia, 20 edition, 1918.

[109] B. Greenberg, M. A. Quinones, C. Koilpillai, and et al. Effects of long-term enalapril therapy on cardiac structure and function in patients with left ventricular dysfunction: results of the solvd echocardiography substudy. *Circulation*, 91:2573–2581, 1995.

[110] R. M. Gulrajani. The forward problem of electrocardiography: from heart models to body surface potentials. In *Proceedings of 19th Intl IEEE/EMBS Conference, Oct 30 - Nov 2. 1997, Chicago, IL. USA*, pages 2604–2609. IEEE, 1997.

[111] A. C. Guyton and J. E. Hall. Human physiology and mechanisms of disease. In *The electrocardiogram and electrocardiographic interpretation of heart abnormalities*, chapter 10. W. B. Saunders Company, 1997.

[112] S. A. Hall, C. G. Cigarroa, and et al. Time course of improvement in left ventricular function, mass and geometry in patients with congestive heart failure treated with beta-adrenergic blockade. *J Am Coll Cardiol*, 25:1154–1161, 1995.

[113] D. M. Harrild and C. S. Henriquez. A finite volume model of cardiac propagation. *Ann Biomed Eng*, 25:315–334, 1997.

[114] S. He, A. A. Fontaine, and et. al. Integrated mechanism for functional mitral regurgitation: leaflet restriction versus coapting force: in vitro studies. *Circulation*,

96:1824–1834, 1997.

[115] Heart anatomy. http://www.pacemakerproject.com/.

[116] Heart interior. http://www.nhlbi.nih.gov/health/dci/images/.

[117] K. M. Heinroth, M. Elster, S. Nuding, and et al. Impedance cardiography: a useful and reliable tool in optimization of cardiac resynchronization devices. *Europace*, 9(9):744–750, 2007.

[118] R. H. Helm, M. Byrne, P. A. Helm, S. K. Daya, N. F. Osman, R. Tunin, H. R. Halperin, R. D. Berger, D. A. Kass, and A. C. Lardo. Three-dimensional mapping of optimal left ventricular pacing site for cardiac resynchronization. *Circulation*, 115:953–961, 2007.

[119] R. H. Helm, C. Leclercq, O. P. Faris, C. Ozturk, E. McVeigh, A. C. Lardo, and D. A. Kass. Cardiac dyssynchrony analysis using circumferential versus longitudinal strain: implications for assessing cardiac resynchronization. *Circulation*, 111:2760–2767, 2005.

[120] Herzschrittmacher und Defibrillator. http://www.uniklinikum−giessen.de/herz/Defi.html.

[121] S. L. Higgins, H. D. Hummel, I. K. Niazi, M. C. Guidici, S. J. Worley, L. A. Saxon, J. P. Boehmer, M. B. Higginbotham, T. De Marco, E. Foster, and et al. Cardiac resynchronization therapy for the treatment of heart failure in patients with intraventricular conduction delay and malignant ventricular tachyarrhythmias. *J Am Coll Cardiol*, 42:1454–1459, 2003.

[122] D. W. Hilgemann and D. Noble. Excitation-contraction coupling and extracellular calcium transients in rabbit atrium: Reconstruction of basic cellular mechanisms. *Proc. R. Soc. Lond.*, 230:163–205, 1987.

[123] M. Hochleitner, H. Hortnagl, and et al. Usefulness of physiologic dual chamber pacing in drug resistant idiopathic dilated cardiomyopathy. *Am J cardiol*, 66:198–202, 1990.

[124] A. L. Hodgkin and A. F. Huxley. A quantitative description of membrane current and its application to conduction and excitation in nerve. *J. Physiol.*, 177:500–544, 1952.

[125] A. L. Hodgkin and B. Katz. The effect of sodium ions on the electrical activity of the giant axon of a squid. *J. Physiol.*, 108:37–77, 1949.

[126] G. Huiskamp and A. van Oosterom. Tailored versus realistic geometry in the inverse problem of electrocardiography. *IEEE Trans Biomed Eng*, 36(8):827–835, 1989.

[127] Hypertensive HF. http://www.healthcentral.com/high−blood−pressure/complications−4766-108.html.

[128] InSync III-CRT-PDevice. http://www.medtronic.com/physician/hf/.

[129] V. Iyer, R. Mazhari, and R. L. Winslow. A computational model of the human left-ventricular epicardial myocyte. *Biophys. J.*, 87(3):1507–1525, 2004.

[130] M. S. Jafri, J. J. Rice, and R. L. Winslow. Cardiac Ca^{2+} dynamics: The roles of ryanodine receptor adapation and sarcoplasmic reticulum load. *Biophysical J.*,

74:1149–1168, Mar. 1998.

[131] T. N. James and L. Sherf. Fine structure of the his bundle. *Circulation*, 1971.

[132] A. H. Jansen, F. A. Bracke, J. M. Dantzig, A. Meijer, and et al. Correlation of echo-doppler optimization of atrioventricular delay in cardiac resynchronization therapy with invasive haemodynamics in patients with heart failure secondary to ischemic or idiopathic dilated cardiomyopathy. *Am J Cardiol*, 97:552–557, 2004.

[133] M. Jessup and S. Brozena. Heart failure. *N Engl J Med*, 348:2007–2018, May 2003.

[134] Y. Jiang, D. Farina, and et al. Modeling and reconstruction of myocardial infarction. *Proc BMT*, 2006.

[135] C. R. Johnson. Inverse problems in electrocardiology, advances in computational biomedicine, edited by peter johnston. *WIT Press*, 5:51–88.

[136] C. R. Johnson. Computational and numerical methods for bioelectric field problems. *Crit Rev Biomed Eng*, 25(1):1–81, 1997.

[137] H. J. Jongsma and M. B. Rook. Biophysics of cardiac gap junction channels. In D. P. Zipes and J. Jalife, editors, *Cardiac Electrophysiology. From Cell to Bedside*, chapter 14, pages 119–125. W. B. Saunders Company, Philadelphia, 3 edition, 1999.

[138] Justice. http://www.chemistry.emory.edu/.

[139] D. A. Kass, C. H. Chen, C. Curry, M. Talbot, R. Berger, B. Fetics, and E. Nevo. Improved left ventricular mechanics from acute vdd pacing in patients with dilated cardiomyopathy and ventricular conduction delay. *Circulation*, 99:1567–1573, 1999.

[140] D. J. U. Keller. Detailed anatomical and electrophysiological modeling of the human ventricles based on diffusion tensor MRI data. Master's thesis, Universität Karlsruhe (TH), Institut für Biomedizinische Technik, 2006. Diploma Thesis.

[141] R.C.P. Kerckhoffs, J. Lumens, K. Vernooy, and et al. Cardiac resynchronization: Insight from experimental and computational models. *Progress in Biophysics and Molecular Biology*, 97:543–561, 2008.

[142] J. E. kerlan, N. S. Sawhney, A. D. Waggoner, and et al. Prospective comparison of echocardiographic atrioventricular delay optimization methods for cardiac resynchronization therapy. *Heart Rhythm*, 3:148–154, 2006.

[143] W. F. Kerwin, E. H. Botvinick, and J. W. O'Connell et al. Ventricular contraction abnormalities in dilated cardiomyopathy: effect of biventricular pacing to correct interventricular dyssynchrony. *J Am Coll Cardiol*, 35:1221–1227, 2000.

[144] W. F. Kerwin and O. Paz. Cardiac resynchronisation therapy: Overcoming ventricular dyssynchrony in dilated heart failure. *Cardiology in Review*, 11(4):221–239, July/Aug. 2003.

[145] W. Y. Kim, P. Sogaard, P. T. Mortensen, and et al. Three dimensional echocardiography documents haemodynamic improvement by biventricular pacing in patients with severe heart failure. *Heart*, 85:514–520, 2001.

[146] M. Kindermann, G. Frolhig, T. Dörr, and et al. Optimizing the av delay in ddd pacemaker patients with high degree av block: mitral valve doppler versus impedance

cardiography. *Pacing Clin Electrophysiol*, 20:2435–2462, 1997.

[147] R. Klinke and S. Silbernagl. *Taschenatlas der Physiologie*. Georg Thieme Verlag, Stuttgart; New York, 5 edition, 2001.

[148] J. Kneller, R. J. Ramirez, D. Chartier, M. Courtemanche, and S. Nattel. Time-dependent transients in an ionically based mathematical model of the canine atrial action potential. *Am. J. Physiol.*, 282:H1437–H1451, 2002.

[149] W. Koglek. Eine einfache methode zur bestimmung des av-intervalls bei zweikammerschrittmacher. *Herzschr Elektrophys*, 11:244–253, 2000.

[150] J. Kron and J. B. Conti. Cardiac resynchronization therapy for treatment of heart failure in the eldery. *Clin Geriatr Med*, 23:193–203, 2007.

[151] Y. Kurata, I. Hisatome, S. Imanishi, and T. Shibamoto. Dynamical description of sinoatrial node pacemaking: Improved mathematical model for primary pacemaking cells. *Am. J. Physiol.*, 283:H2074–H2101, 2002.

[152] P. D. Lambiase, A. Rinaldi, Hauck, and et. al. Non-contact left ventricular endocardial mapping in cardiac resynchronisation therapy. *Heart*, 90:44–51, 2004.

[153] C. Leclercq, O. P. Faris, R. Tunin, J. Johnson, R. kato, F. Evans, J. Spinelliand H. Halperin, E. McVeigh, and D. A. Kass. Systolic improvement and mechanical resynchronization does not require electrical synchrony in the dilated failing heart with left bundle branch block. *Circulation*, 106:1760–1763, 2002.

[154] C. Leclercq and D. A. Kass. Retiming the failing heart: principles and current clinical status of cardiac resynchronization. *J Am Coll Cardiol*, 39:194–201, 2002.

[155] G. Lecoq, C. Leclercq, E. Leray, and et al. Clinical and electrocardiographic predictors of a positive response to cardiac resynchronization therapy in advanced heart failure. *Eur Heart J*, 26:1094–1100, 2005.

[156] M. Leitman, P. Lysyansky, S. Sidenko, V. Shir, E. Peleg, and et al. Two-dimensional strain-a novel software for real-time quantitative echocardiographic assessment of myocardial function. *J Am Soc Echocardiogr*, 17:1021–1029, 2004.

[157] R. Liberman, D. Grenz, H. G. Mond, and M. D. Gammage. Selective site pacing: defining and reaching the selected site. *PACE*, 27:883–886, 2004.

[158] D. S. Lindblad, C. R. Murphey, J. W. Clark, and W. R. Giles. A model of the action potential and underlying membrane currents in a rabbit atrial cell. *Am. J. Physiol.*, 271(4 Pt 2):H1666–H1696, 1996.

[159] N. H. Lovell, S. L. Cloherty, B. G. Celler, and S. Dokos. A gradient model of cardiac pacemaking myocytes. *Progress in Biophysics and Molecular Biology*, 85(2-3):301–323, 2004.

[160] M. Lunati, Y. poezevara, and A. Boncompagni. *Focus on optimization of cardiac resynchronization therapy techniques*, chapter 2, pages 119–124. Mediterranean cardiology meeting, 2007.

[161] C.-H. Luo and Y. Rudy. A model of the ventricular cardiac action potential. *Circ. Res.*, 68(6):1501–1526, 1991.

[162] C.-H. Luo and Y. Rudy. A dynamic model of the ventricular cardiac action potential: I. Simulations of ionic currents and concentration changes. *Circ. Res.*, 74(6):1071–1096, 1994.

[163] C.-H. Luo and Y. Rudy. A dynamic model of the ventricular cardiac action potential: II. afterdepolarizations, triggered activity, and potentiation. *Circ. Res.*, 74(6):1097–1113, 1994.

[164] R. L. Lux, A. K. Evans, and et al. Redundancy reduction for improved display and analysis of body surface potential map. i. spatial compression. *Circ Res*, 49:186–196, 1981.

[165] R. L. Lux, C. R. Smith, and et al. Limited lead selection for estimation of body surface potential maps in electrocardiography. *IEEE Trans Biomed Eng*, 25:270–276, 1978.

[166] A. Magalski, P. Adamson, F. Gadler, and et al. Continuous ambulatory right heart pressure measurements with an implantable hemodynamic monitor: a multicenter, 12-month follow-up study of patients with chronic heart failure. *J Card Fail*, 8:63–70, 2002.

[167] J. Malmivuo and R. Plonsey. 12 lead ecg system. *Bioelectromagnetism*, 15:159–168, 1995.

[168] G. Marcus, I. L. Gerber, and et al. The association between phonocardiographic third and fourth heart sounds and objective measures of left ventricular function. *JAMA*, 293:2238–2244, 2005.

[169] F. A. McAlister, J. A. Ezekowitz, N. Wiebe, B. Rowe, C. Spooner, E. Crumley, L. Hartling, T. Klassen, and W. Abraham. Systematic review: cardiac resynchronization in patients with symptomatic heart failure. *Ann Intern Med*, 141(5):381–390, 2004.

[170] R. E. McAllister, D. Noble, and R. W. Tsien. Reconstruction of the electrical activity of cardiac purkinje fibres. *J. Physiol.*, 251:1–59, 1975.

[171] W. A. McAlpine. *Heart and Coronary Arteries*. Springer, Berlin, 1976.

[172] Medline. http://www.nlm.nih.gov/medlineplus/.

[173] Medtronic. *Medtronic announces FDA approval of InSync marquis cardiac resynchronization therapy system. In*, 2002.

[174] M. Meine, X. Min, M. Paris, and E. Park. An intracardiac egm method for vv optimization during cardiac resynchronization therapy. *Heart Rhythm J*, 3:AB30–5, 2006.

[175] J. Meluzin, M. Novak, A. J. Mullerov, J. Krejici, and et al. A fast and simple echocardiographic method of determination of the optimal atrioventricular delay in patients after biventricular stimulation. *Pacing Clin Electrophysiol*, 27:58–64, 2004.

[176] J. V. Miller, D. E. Breen, W. E. Lorensen, and et. al. Geometrically deformed models: a method for extracting closed geometric models form volume data. *Comput Graph*, 25(4):217–226, 1991.

[177] R. Miri, M. Reumann, and et al. Computer based optimization of biventricular pacing according to the left ventricular 17 myocardial segments. In *Proceedings of The 29th Annual International Conference of the IEEE/EMBS, Aug 23-26. 2007, Lyon, France*, pages 1418–1421. IEEE, 2007.

[178] R. Miri, M. Reumann, D. Farina, B. Osswald, and O. Dössel. Computer assisted optimization of biventricular pacing assuming ventricular heterogeneity. In *IFMBE Proceedings of 11th Mediterranean Conference on Medical and Biomedical Engineering and Computing, June 26-30, Ljubljana, Slovenia*, volume 16, pages 541–544, 2007.

[179] R. Miri, M. Reumann, D. Farina, B. Osswald, and O. Dössel. Optimizing a-v and v-v delay in cardiac resynchronization therapy in simulations including ventricular heterogeneity. In *Proceedings of the fifth IASTED International Conference on Biomedical Enginerring, Feb 14-16, Innsbruck, Austria*, pages 20–25, 2007.

[180] R. Miri, M. Reumann, D. Keller, D. Farina, and O. Dössel. A non-invasive computer based optimization strategy of biventricular pacing. In *Proc. CURAC, Oct 11-13, Karlsruhe, Germany*, pages 133–136, 2007.

[181] R. Miri, M. Reumann, D. Keller, D. Farina, and O. Dössel. Comparison of the electrophysiologically based optimization methods with different pacing parameters in patient undergoing resynchronization treatment. In *Proceedings of The 30th Annual International Conference of the IEEE/EMBS, Aug 20-24, Vancouver, British Columbia, Canada*, pages 1741–1744, 2008.

[182] R. Miri, M. Reumann, D. Keller, D. Farina, C. Wolpert, and O. Dössel. Optimization of cardiac resynchronization therapy based on a computer heart model assuming 17 left ventricular segments. In *Proc. BMT, Sep 26-29, Aachen, Germany*, volume 52, 2007.

[183] R. Mohindra, J. L. Sapp, and et al. Use of body-surface potential mapping and computer model simulations for optimal programming of cardiac resynchronization therapy devices. *Computers in Cardiology*, 34:69–72, 2007.

[184] D. C. Montgomery and G. C. Runger. *Applied Statistics and probability for Engineers*. John Wiley & Sons, 3 edition, 2005.

[185] A. P. Moreno, V. Hayrapetyan, G. Zhong, A. D. Martinez, and E. C. Beyer. Homometric and heterometric gap junctions. In D. P. Zipes and J. Jalife, editors, *Cardiac Electrophysiology. From Cell to Bedside*, chapter 14, pages 120–126. W. B. Saunders Company, Philadelphia, 4 edition, 2004.

[186] C. A. Morillo, G. J Klein, and D. L. Jones. Chronic rapid atrial pacing. structural, functional, and electrophysiological characteristics of a new model of sustained atrial fibrillation. *Circulation*, 91:1588–1595, 1995.

[187] B. Mozaffary and M. A. Tinati. 3d computer model of atrial arrhythmias. In *Proceedings of World Academy of Science, Engineering and Technology, Jan 3*, volume 3, pages 22–24, 2005.

[188] Myocardial structure. http://www.mhhe.com/.

[189] National Institute for Health and Clinical Excellence. *Cardiac resynchronisation therapy (biventricular pacing) for the treatment of heart failure*, 2006.

[190] G. Ndrepepa, M. A. Schneider, and M. R. Karch. Pulmonary vein internal electrical activity does not contribute to the maintenance of atrial fibrillation. *PACE*, 26:1356–1362, 2003.

[191] F. H. Netter. *The CIBA collection of medical Illustration*, volume 5. CIBA Pharmaceutical Company, New York, 1971.

[192] F. H. Netter. Anatomie. In *Farbatlanten der Medizin*, volume 1, chapter 1, pages 2–33. Thieme, Stuttgart; New York, 3 edition, 1990.

[193] F. H. Netter. *Atlas der Anatomie des Menschen*. Novartis, 1995.

[194] J. B. Nixon, P. E. Rasser, and et al. Numerical model of electrical potential within the human head. *Int J Numer Methods Eng*, 56:2353–2366, 2003.

[195] D. Noble and S. J. Noble. A model of sino-atrial node electrical activity based on a modification of the DiFrancesco-Noble (1984) equations. *Proc. R. Soc. Lond. B. Biol. Sci.*, 222:295–304, 1984.

[196] D. Noble, A. Varghese, P. Kohl, and P. Noble. Improved guinea-pig ventricular cell model incorporating a diadic space, I_{Kr} and I_{Ks}, and length- and tension-dependend processes. *Can. J. Cardiol.*, 14(1):123–134, Jan. 1998.

[197] A. Noma and N. Tsuboi. Dependence of junctional conductance on proton, calcium and magnesium ions in cardiac paired cells of guinea-pig. *J. Physiol.*, 382:193–211, 1987.

[198] A. Nygren, C. Fiset, L. Firek, J. W. Clark, D. S. Lindblad, R. B. Clark, and W. R. Giles. Mathematical model of an adult human atrial cell. *Circ. Res.*, 82:63–81, 1998.

[199] Y. Otsuji, D. Gilon, L. Jiang, and et. al. Restricted diastolic opening of the mitral leaflets in patients with left ventricular dysfunction: evidence for increased valve tethering. *J Am Coll Cardiol*, 32:398–404, 1998.

[200] C. Pan, R. Hoffmann, H. Kuhl, and et al. Tissue tracking allows rapid and accurate visual evaluation of left ventricular function. *Eur J Echocardiogr*, 2:197–202, 2001.

[201] S. V. Pandit, R. B. Clark, W. R. Giles, and S. S. Demir. A mathematical model of action potential heterogeneity in adult left ventricular myocytes. *Biophys. J.*, 81:3029–3051, 2001.

[202] F. C. Patino. *Level Sets Applied to Inverse Problem in Electrocardiography* . 2004. Dissertation.

[203] M. Penicka, J. Bartunek, B. De Bryne, M. Vanderheyden, M. Goethals, M. De Zutter, P. Brugada, and P. Geelen. Improvement of left ventricular function alter cardiac resynchronization therapy is predicted by tissue doppler imaging echocardiography. *Circulation*, 109:978–983, 2004.

[204] G. B. Perego, R. Chianca, M. Facchini, A. Frattola, E. Balla, S. Zucchi, S. Cavaglia, I. Vicini, M. Negretto, and G. Osculati. Simultaneous vs sequential biventricular

pacing in dilated cardiomyopathy: an acute hemodynamic study. *Eur J Heart Fail*, 5(3):305–313, 2003.

[205] M. A. Pfeffer and E. Braunwald. Ventricular remodeling after myocardial infarction: experimental observations and clinical implications. *Circulation*, 81:1161–1172, 1990.

[206] F. Philippon. Cardiac resynchronization therapy: Device-based medicine for heart failure. *J Card Surg*, 19:270–274, 2004.

[207] M. V. Pitzales, M. Iacoviello, R. Romito, P. Guida, E. De Tommasi, G. Luzzi, M. Anaclerio, C. Forleo, and P. Rizzon. Ventricular asynchrony predicts better outcome in patients with chronic heart failure receiving cardiac resynchronization therapy. *J Am Coll Cardiol*, 45:65–69, 2005.

[208] M. V. Pitzalis, M. Iacoviello, R. Romito, and et al. Cardiac resynchronisation therapy tailored by echocardiographic evaluation of ventricular asynchrony. *J Am Coll Cardiol*, 40:1615–1622, 2002.

[209] G. Plicchi, E. Marcelli, and et al. Pea i and pea ii based implantable haemodynamics monitor: pre clinical studies in sheep. *Europace*, 4:49–54, 2002.

[210] Plötzlicher Herztod und Herzinsuffizienz. http://www.kardionet.de/.

[211] M. Potse, B. Dube, and et al. A comparison of monodomain and bidomain reaction-diffusion models for action potential propagation in the human heart. *IEEE Trans Biomed Eng*, 53:2425–2435, 2006.

[212] W. H. Press, S. A. Teukolsky, W. T. Vetterling, and B. P. Flannery. *Numerical Recipes in C.* Cambridge University Press, Cambridge, New York, Melbourne, 2 edition, 1992.

[213] W. H. Press, S. A. Teukolsky, W. T. Vetterling, and B. P. Flannery. *Numerical Recipes in C. The art of scientific computing.* Cambridge University Press, 2 edition, 2002.

[214] L. Priebe and D. J. Beuckelmann. Simulation study of cellular electric properties in heart failure. *Circ. Res.*, 82:1206–1223, 1998.

[215] J. L. Puglisi and D. M. Bers. LabHEART: An interactive computer model of rabbit ventricular myocyte ion channels and Ca transport. *Am. J. Physiol.*, 281:C2049–C2060, 2001.

[216] A. J. Pullan, M. L. Buist, and L. K. Cheng. *Mathematically modelling the electrical activity of the heart.* World Scientific Publishing Co. Pte. Ltd., Hackensack, London, 2005.

[217] B. B. Punske. Cardiac resynchronization therapy: finding the true meaning of synchrony. *Heart Rhythm*, 3(3):311–312, 2006.

[218] N. Rajagopalan, M. S. Suffoletto, M. Tanabe, and et al. Right ventricular function following cardiac resynchronization therapy. *Am J Cardiol*, 100(9):1434–1436, 2007.

[219] R. J. Ramirez, S. Nattel, and M. Courtemanche. Mathematical analysis of canine atrial action potentials: Rate, regional factors, and electrical remodeling. *Am. J. Physiol.*, 279:H1767–H1785, 2000.

[220] S. Reisner, P. Lysyansky, Y. Agmon, D. Mutlak, J. Lessick, and Z. Friedman. Global longitudinal strain: a novel index of left ventricular systolic function. *J Am Soc Echocardiogr*, 17:630–633, 2004.

[221] M. Reumann, D. Farina, R. Miri, S. Lurz, B. Osswald, and O. Dössel. Computer model for the optimization of av and vv delay in cardiac resynchronization therapy. *Progress in Biophysics and Molecular Biology*, pages 845–854, 2007.

[222] Matthias Reumann. *Computer assisted optimisation on non-pharmacological treatment of congestive heart failure and supraventricular arrhythmia*. PhD thesis, Institut für Biomedizinische Technik, Universitätsverlag Karlsruhe ISBN 978-3-86644-122-4, 2007.

[223] S. Reuter, S. Garriage, S. S. Barold, and et al. Comparison of characteristics in responders versus non responders with biventricular pacing for drug resistant congestive heart failure. *Am J Cardiol*, 89:346–350, 2002.

[224] L. Riedlbauchova, J. Kautzner, and P. Fridl. Influence of different atrioventricular and interventricular delays on cardiac output during cardiac resynchronization therapy. *Pacing Clin Electrophysiol*, 28:19–23, 2005.

[225] P. Ritter, L. Padeletti, P. P. Dellenoy, S. Garrigue, and J. Silvester. Av delay optimization by peak endocardial acceleration in cardiac resynchronisation therapy: Comparison with standard echocardiographic procedure. *Europace*, 6:209, 2004.

[226] P. Ritter, L. Padeletti, and et al. Determination of the optimal atrioventricular delay in ddd pacing. comparison between echo and peak endocardial acceleration measurements. *Europace*, 1(2):126–130, 1999.

[227] B. Rodriguez and N. Trayanova et al. Modeling cardiac ischemia. *Ann NY Acad Sci*, 1080:395–414, 2006.

[228] R. Rom, J. Erel, M. Glikson, K. Rosenblum, R. Ginosar, and D. L. Hayes. Adaptive cardiac resynchronization therapy device: A simulation report. *PACE*, 28:1168–1173, 2005.

[229] M. Roos, S. Toggweiler, M. Zuber, and et al. Acoustic cardiographic parameters and their relationship to invasive haemodynamic measurements in patients with left ventricular systolic dysfunction. *Congest Heart Fail Suppl 1*, 12:19–24, 2006.

[230] S. Rosanio, E. R. Schwarz, M. Ahmad, P. Jammula, A. Vitarelli, B. F. Uretsky, Y. Birnbaum, D. L. Ware, S. Atar, and M. Saeed. Benefits, unresolved questions, and technical issues of cardiac resynchronization therapy for heart failure. *Am J Cardiol*, 96(5):710–717, Sep 2005.

[231] F. Rouleau, M. Merheb, S. Geffroy, and et al. Echocardiographic assessment of the interventricular delay of activation and correlation to the qrs width in dilated cardiomyopathy. *Clin Electrophysiol*, 24:1500–1506, 2001.

[232] F. B. Sachse. *Modelle des menschlichen Körpers zur Berechnung von physikalischen Feldern*. Shaker, Aachen, 1998.

[233] F. B. Sachse. *Computational Cardiology: Modeling of Anatomy, Electrophysiology, and Mechanics*. LNCS 2966. Springer Press, Heidelberg, 2004.

[234] L. E. Sade, H. Kanzaki, D. Severyn, K. Dohi, and J. Gorcsan. Quantification of radial mechanical dyssynchrony in patients with left bundle branch block and idiopathic dilated cardiomyopathy without conduction delay by tissue displacement imaging. *Am J Cardiol*, 94:514–518, 2004.

[235] L. E. Sade, D. A. Severyn, H. Kanzaki, and et al. Second-generation tissue doppler with angle-corrected color-coded wall displacement for quantitative assessment of regional left ventricular function. *Am J Cardiol*, 92:544–560, 2003.

[236] M. C. Sanguinetti and M. Tristani-Firouzi. Delayed and inward rectifier potassium channels. In D. P. Zipes and J. Jalife, editors, *Cardiac Electrophysiology. From Cell to Bedside*, chapter 9, pages 79–86. W. B. Saunders Company, Philadelphia, 3 edition, 1999.

[237] L. A. Saxon, T. De Marco, J. Schafer, and et al. Effects of long-term biventricular stimulation for resynchronization on echocardiographic measures of remodeling. *Circulation*, 105:1304–1310, 2002.

[238] C. Scharf. Atrial flutter and fibrillation. *Schweiz Rundsch Med Prax*, 94(45):1753–1759, Nov 2005. Article in German.

[239] G. Seemann. Elektrische Erregungsausbreitung im Herzen ausgehend von elektrophysiologischen Zellmodellen: Erregungsausbreitung im Zellverband, Parametrisierung Zellulärer Automaten. Master's thesis, Universität Karlsruhe (TH), Institut für Biomedizinische Technik, Aug. 2000. Diploma Thesis.

[240] G. Seemann, D. U. J. Keller, and et. al. Modeling human ventricular geometry and fiber orientation based on diffusion tensor mri. *Computers in Cardiology*, 33:80–804, 2006.

[241] Gunnar Seemann. *Modeling of electrophysiology and tension development in the human heart*. PhD thesis, Institut für Biomedizinische Technik, Universitätsverlag Karlsruhe ISBN 3-937300-66-X, 2005.

[242] M. Seger, G. fisher, and et al. Lead field computation for the electrocardiographic inverse problem-finite elements versus boundary elements. *Comp Meth Prog Biomed*, 77(3):51–88, 2005.

[243] M. Sermesant, K. Rhode, and et. al. Simulation of cardiac pathologies using an electromechanical biventricular model and xmr interventional imaging. *Medical Image Analysis*, 9:467–480, 2005.

[244] J. Shah, A. Michaels, and et al. Haemodynamic correlates of the third heart sound and systolic time intervals. *Congest Heart Fail Suppl 1*, 12:8–13, 2006.

[245] L. Sherwood. *Human Physiology: From Cells to Systems*. Brooks Cole, 6 edition, 2006.

[246] K. Shivkumar and J. N. Weiss. Adenosine triphospate-sensitive potassium channels. In D. P. Zipes and J. Jalife, editors, *Cardiac Electrophysiology. From Cell to Bedside*,

chapter 10, pages 86–93. W. B. Saunders Company, Philadelphia, 3 edition, 1999.

[247] G. Shou, L. Xia, and et al. Forward and inverse solutions of electrocardiography problem using an adaptive bem method. In F.B. Sachse and G. Seemann, editors, *LNCS*, volume 4466, pages 290–299. Springer-Verlag Berlin Heidelberg, 2007.

[248] Simplex. http://paula.univ.gda.pl/ dokgrk/simplex.html.

[249] O. Skipa. *Linear inverse problem of electrocardiography: epicardial potentials and transmembrane voltages.* PhD thesis, Universität Karlsruhe (TH), Institut für Biomedizinische Technik, 2004.

[250] G. Sleilaty, A. Sarkis, P. Achouh, V. Jebara, and J.N. Fabiani. Prevention and treatment of atrial fibrillation after cardiac surgery. *Arch Mal Coeur Vaiss*, 98(9):894–898, Sep 2005. Article in French.

[251] P. Sogaard, H. Egeblad, W. Y. Kim, H. K. Jensen, and et al. Tissue doppler imaging predicts improved systolic performance and left ventricular remodeling during long-term cardiac resynchronization therapy. *J Am Coll Cardiol*, 40:723–730, 2002.

[252] P. Sogaard, H. Egeblad, A. K. Pedersen, W. Y. Kim, B. O. Kristensen, P. S. Hansen, and P. T. Mortensen PT. Sequential versus simultaneous biventricular resynchronization for severe heart failure: evaluation by tissue doppler imaging. *Circulation*, 106:2078–2084, 2002.

[253] P. Sogaard, W. Y. Kim, and et al. Impact of acute biventricular pacing on left ventricular performance and volumes in patients with severe heart failure: a tissue doppler and three-dimensional echocardiographic study. *Cardiology*, 95:173–182, 2001.

[254] D. Steinhaus, D. W. Reynolds, F. Gadler, G. N. Kay, and et al. Implant experience with an implantable hemodynamic monitor for the management of symptomatic heart failure. *Pacing Clin Electrophysiol*, 28:747–753, 2005.

[255] C. Stellbrink, O. A. Breithardt, A. Franke, S. Sack, and et al. Impact of cardiac resynchronization therapy using hemodynamically optimized pacing on left ventricular remodelling in patients with congestive heart failure and ventricular conduction disturbances. *J Am Coll Cardiol*, 38:1957–1965, 2001.

[256] D.D. Streeter. Gross morphology and fiber geometry of the heart. *in Handbook of physiology: American Physiology Society*, 1:61–112, 1979.

[257] S. A. Strickberger, J. Conti, and et al. Patient selection for cardiac resynchronization therapy. *Circulation*, 111:2146–2150, 2005.

[258] M. S. Suffoletto, K. Dohi, M. Cannesson, S. Saba, and et al. Novel speckle tracking radial strain from routine black and white echocardiographic images to quantify dyssynchrony and predict response to cardiac resynchronization therapy. *Circulation*, 113:960–968, 2006.

[259] M. G. S. I. Sutton and N. Sharpe. Left ventricular remodeling after myocardial infarction: pathophysiology and therapy. *Circulation*, 101:2981–2988, 2000.

[260] M. G. St John Sutton, T. Plappert, W. T. Abraham, and et al. Effect of cardiac resynchronization therapy on left ventricular size and function in chronic heart failure. *Circulation*, 107:1985–1990, 2003.

[261] K. H. W. J. ten Tusscher, D. Noble, P. J. Noble, and A. V. Panfilov. A model for human ventricular tissue. *Am. J. Physiol.*, 286:H1573–H1589, 2004.

[262] K. H. W. J. ten Tusscher and A. V. Panfilov. Alternans and spiral breakup in a human ventricular tissue model. *Am J Physiol Heart Circ Physiol*, 291:H1088–H1100, 2006.

[263] K. H. W. J. ten Tusscher and A. V. Panfilov. Modelling of the ventricular conduction system. *Progress in Biophysics and Molecular Biology*, In Press, 2007.

[264] W. S. Teo, R. Kam, and L. F. Hsu. Treatment of heart failure - role of biventricular pacing for heart failure not responding well to drug therapy. *Singapore Med J*, 44(3):114–122, 2003.

[265] D. Terzopoulos, A. Witkin, and M. Kass. Constraints on deformable models: recovering 3d shape and nongrid motion. *Artificial Intelligence*, 36:91–123, 1988.

[266] Texas Heart Institute. http://www.texasheart.org/.

[267] M. S. Thaler. *The only EKG book you'll ever need.* Lippincott Williams and Wilkins, 5 edition, 2007.

[268] S. Toggweiler, M. Zuber, R. Kobza, and et al. Improved response to cardiac resynchronization therapy through optimization of atrioventricular and interventricular delay using acoustic cardiography: A pilot study. *J Cardiac Failure*, 13:637–642, 2007.

[269] H. F. Tse, C. Yu, E. Park, A. Hughes, and C. P. Lau. Impedance cardiography for atrioventricular interval optimization during permanent left ventricular pacing. *Pacing Clin Electrophysiol*, 26:189–191, 2003.

[270] M. S. Turner, R. A. Bleasdale, D. Vinereanu, and et al. Electrical and mechanical components of dyssynchrony in heart failure patients with normal qrs duration and left bundle-branch block. *Circulation*, 109:2544–2549, 2004.

[271] V. M. Unger, N. M. Kumar, N. B. Gilula, and M. Yeager. Three-dimensional structure of a recombinant gap junction membrane channel. *Science*, 283:1176–1180, 1999.

[272] USFDA. *New device approval- Guidant cardiac resynchronization therapy defibrillator system including the CONTACT CD pulse generator and the EASYTRAK left ventricular coronary venous lead. In*, 2002.

[273] L. C. M. van Campen, F. C: Visser, C. C. de Cock, D. h. S. Vos, O. Kamp, and C. A. Visser. Comparison of the haemodynamics of different pacing sites in patients undergoing ressynchronization therapy: need for individualization an optimal lead localization. *Heart*, 92:1795–1800, 2006.

[274] B. M. van Gelder, F. A. Bracke, A. Meijer, L. J. Lakerveld, and N. H. Pijls. Effect of optimizing the vv interval on left ventricular contractility in cardiac resynchroni-

sation therapy. *Am J Cardiol*, 93:1500–1503, 2004.

[275] R. S. Vasan and D. Levy. Defining diastolic heart failure: a call for standardized diagnostic criteria. *Circulation*, 101:2118–2121, 2000.

[276] M. Vassalle, H. Yu, and I. S. Cohen. Pacemaker channels and cardiac automaticity. In D. P. Zipes and J. Jalife, editors, *Cardiac Electrophysiology. From Cell to Bedside*, chapter 11, pages 94–103. W. B. Saunders Company, Philadelphia, 3 edition, 1999.

[277] X. A. A. M. Verbeek, Auricchio A, Y. Yu, J. Ding, T. Pochet, K. Vernooy, A. Kramer, J. Spinelli, and F. W. Prinzen. Tailoring cardiac resynchronization therapy using interventricular asynchrony. validation of a simple model. *Am J Physiol Heart Circ Physiol*, 290:H968–H977, 2006.

[278] X. A. A. M. Verbeek, K. Vernooy, M. Peschar, R. N. M. Cornelussen, and F. W. Prinzen. Intra-ventricular resynchronization for optimal left ventricular function during pacing in experimental left bundle branch block. *J Am Coll Cardiol*, 42:558–567, 2003.

[279] S. Verheule, M. J. A. van Kempen, P. H. J. A. te Welscher, B. R. Kwak, and H. J. Jongsma. Characterization of gap junction channels in adult rabbit atrial and ventricular myocardium. *Circ. Res.*, 80:673–681, 1997.

[280] G. A. Mensah W. A. Wattigney and et al. Increased atrial fibrillation mortality: United states. *Am. J. Epidemiol*, 155(9):819–826, 1980-1998.

[281] A. L. Waldo. The interrelationship between atrial fibrillation and atrial flutter. *Prog Cardiovasc Dis*, 48(1):41–56, Jul-Aug 2005.

[282] D. L. Weiß. Vergleich des Verhaltens eines Elektrophysiologischen Zellmodells mit einem Zellulären Automaten bei Simulierten Atrialen Fibrillationen. Master's thesis, Universität Karlsruhe (TH), Institut für Biomedizinische Technik, 2002. Student Research Project.

[283] D. L. Weiss and D. U. J. Keller andet al. The influence of fibre orientation, extracted from different segments of the human left ventricle, on the activation and repolarization sequence: a simulation study. *Europace*, 9:96–104, 2007.

[284] C. Werner. *Simulation der elektrischen Erregungsausbreitung in anatomischen Herzmodellen mit adaptiven Zellulären Automaten.* Tenea, Berlin, 2001. Dissertation.

[285] C. D. Werner. *Simulation der elektrischen Erregungsausbreitung in anatomischen Herzmodellen mit adaptiven zellulären Automaten.* PhD thesis, Universität Karlsruhe (TH), Institut für Biomedizinische Technik, 2001.

[286] C. D. Werner, F. B. Sachse, and O. Dössel. Electrical excitation propagation in the human heart. *Int. J. Bioelectromagnetism*, 2(2), 2000.

[287] Z. I. Whinnett, J. E. R. Davies, K. Willson, C. H. Manisty, A. W. Chow, R. A. Foale, D. W. Davies, A. D. Hughes, J. Mayet, and D. P. Francis. Haemodynamic effects of changes in av and vv delay in cardiac resynchronisation therapy show a consistent pattern: analysis of shape, magnitude and relative importance of av and vv delay. *Heart*, 92:1624–1634, 2006.

[288] R. L. Winslow, J. J. Rice, S. Jafri, E. Marbán, and B. O'Rourke. Mechanisms of altered excitation-contraction coupling in canine tachycardia-induced heart failure, II model studies. *Circ. Res.*, 84:571–586, 1999.

[289] K. Yanagihara, A. Noma, and H. Irisawa. Reconstruction of sinoatrial node pacemaker potential based on the voltage-clamp experiments. *Jpn. J. Physiol.*, 30:841–857, 1980.

[290] Mark Yeager. Molecular biology and structure of cardiac gap junction intercellular channels. In D. P. Zipes and J. Jalife, editors, *Cardiac Electrophysiology. From Cell to Bedside*, chapter 4, pages 31–40. W. B. Saunders Company, Philadelphia, 3 edition, 1999.

[291] K. Yoshida, Y. Seo, H. Yamasaki, and et al. Effect of triangle ventricular pacing on haemodynamics and dyssynchrony in patients with advanced heart failure: a comparison study with conventional bi-ventricular pacing therapy. *Eur Herat J*, 28:2610–2619, 2007.

[292] J. B. Young, W. T. Aabraham, A. L. Smith, A. R. Leon, R. Lieberman, B. Wilkoff, R. C. Canby, J. S. Schroeder, L. B. Liem, S. Hall, and et al. Multicenter insync icd randomized clinical evaluation (miracle icd) trial investigators. combined cardiac resynchronization and implantable cardioversion defibrillation in advanced chronic heart failure. *JAMA*, 289:2685–2694, 2003.

[293] C. M. Yu, Y. S. Chan, Q. Zhang, G. W. Yip, C. K. Chan, L. C. Kum, L. Wu, A. P. Lee, Y. Y. Lam, and J. W. Fung. Benefits of cardiac resynchronization therapy for heart failure patients with narrow qrs complexes and coexisting systolic asynchrony by echocardiography. *J Am Coll Cardiol*, 48:2251–2257, 2006.

[294] C. M. Yu, J. W. Fung, Q. Zhang, C. K. Chan, Y. S: Chan, H. Lin, L. C. Kum, S. L. Kong, Y. Zhang, and J. E: Sanderson. Tissue doppler imaging is superior to strain rate imaging and postsystolic shortening on the prediction of reverse remodeling in both ischemic and nonischemic heart failure after cardiac resynchronization therapy. *Circulation*, 110:66–73, 2004.

[295] C. M. Yu, W. H. Fung, H. Lin, and et al. Predictors of left ventricular reverse remodelling after cardiac resynchronisation therapy for heart failure secondary to idiopathic dilated or ishaemic cardiomyopathy. *Am J Cardiol*, 91:644–648, 2003.

[296] C. M. Yu, H. Lin, Q. Zhang, and J. E. Sanderson. High prevalence of left ventricular systolic and diastolic asynchrony in patients with congestive heart failure and normal qrs duration. *Heart*, 89:54–60, 2003.

[297] C. M. Yu, Q. Zhang, J. W. Fung, H. C. Chan, and et al. A novel tool to assess systolic asynchrony and identify responders of cardiac resynchronization therapy. *J Am Coll Cardiol*, 45:677–684, 2005.

[298] M. Zardini, M. Tritto, G. Bargiggia, and et al. analysis of clinical outcome and considerations on the selection of candidates to left ventricular resynchronization. *Eur Heart J*, 2:J16–J22, 2000.

[299] O. Zardkoohi, V. Nandigam, L. Murray, K. Heist, T. Mela, M. Orencole, J. N. Ruskin, and J. P. Singh. The impact of age and gender on cardiac resynchronization therapy outcome. *PACE*, 30:1344–1348, 2007.

[300] P. Zerfass, F. B. Sachse, C. D. Werner, and O. Dössel. Deformation of surface nets for interactive segmentation of tomographic data. In *Biomedizinische Technik*, volume 45-1, pages 483–484, Sep. 2000.

[301] H. Zhang, A. V. Holden, I. Kodama, H. Honjo, M. Lei, T. Varghese, and M. R. Boyett. Mathematical models of action potentials in the periphery and center of the rabbit sinoatrial node. *Am. J. Physiol.*, 279(1):397–421, 2000.

[302] M. R. Zile and D. L. Brutsaert. New concepts in diastolic dysfunction and diastolic heart failure ii. causal mechanisms and treatment. *Circulation*, 105:1503–1508, 2002.

[303] M. Zuber, P. Kipfer, and et al. Tissue synchronization imaging measures left ventricular dyssynchrony and predicts response to cardiac resynchronisation therapy. *Congest Heart Fail Suppl 1*, 12:14–18, 2006.

Acknowledgments

First and foremost, I should like to express my deep gratitude to my supervisor, Professor Dössel for his support and excellent advices throughout my PhD program. I am grateful to him for giving me the opportunity of working on interesting research and for correcting my dissertation precisely.

I should also like to thank Professor Wolpert for giving me the opportunity to do the clinical part of my research at University Hospital Mannheim. I am grateful for the introduction to Dr. Schimpf who has vigorously supported me with the data acquisition.

Special thanks go to Professor Meyer-Waarden for generously sharing his ideas. His patience, friendship, empathy, careful comments and great sense of humor are much appreciated.

I would especially like to thank our administrator, Mr. Schroll, for being a constant source of help and entertainment. I owe thanks to him who has continuously solved my problems with providing me the opportunity to implement the large amount of simulations.

I should like to thank Mrs. Talbott for reviewing my dissertation and listening to my presentation several times. I also appreciate Mrs. Meyer-Waarden for her incredible moral support and for being my good and trustful friend.

I am indebted to my intelligent friend Dr. Iulia Graf for correcting my english and motivating me to finish my project.

I wish to thank all my colleagues and students who helped me. Remarkable thanks go to my friends Farzaneh, Anne-Maria, Irandokht, Shida and Jose.

Special thanks are due to the Landesgraduiertenförderungsgesetz (LGFG) for funding my thesis with two and a half years scholarship.

Finally, I should like to express my profound appreciation towards my parents, Giti and Amir. I am indebted to them for all they have ever done for me and for all I have ever done. Most of all, this is in memory of my grandfather who spent his whole life instructing his students in philosophy and old literature. During his life he tutored me often and I learnt from him the value of education, the importance of combining research with humanity, loving people and helping one another. The reason why I did not give up while I had to deal with the day-to-day problems of programming and doing my thesis were due to his advice and guidance.

Curriculum Vitae

Place of birth	Tehran, Iran
Current address	Henriette-Obermüller-Str. 15
	76137 Karlsruhe, Germany
Phone number	+49 721 554302
	+49 163 691 1778 (mobile)
Email address	raz.miri@ibt.uni-karlsruhe.de

Research Interests

Modeling biological system, Biological signal and image processing, Biomedical instrumentation, Machine learning, Pattern recognition, Image compression.

Education

2005 - 2008
PhD in electrical engineering (Biomedical engineering), Universität Karlsruhe (TH) (The Elite University in Germany), Germany. Institute for Biomedical Engineering. PhD thesis: Computer-based optimization of Cardiac Resynchronization Therapy.

Oct. 2003 - Nov. 2004
Pre-PhD at Universität Karlsruhe (TH) (The Elite University in Germany), Germany. Institute for Biomedical Engineering. The three required courses for entrance were passed with excellent marks.

2000 - 2003
M. Sc. in electrical engineering (Bioelectronics), University of Tehran, Iran. Master thesis: Ultrasound image compression for data storage and transmission application.

1995 - 2000
B. Sc. in electrical engineering (Electronics), University of Tehran, Iran. Graduated with

distinction.

Professional Experience

2004 - 2008
Research Assistant at the Institute of Biomdical Engineering, Universität Karlsruhe (TH).

1998
Researcher at Telecommunication Research Center of Iran, Institute of RF

Selected Awards

1. Award at IEEE/EMBS student paper competition, 30th Annual International Conference of the IEEE Engineering in Medicine and Biology Society (EMBS), Vancouver, Canada, 2008 (3. place).
   R. Miri, et al. Comparison of the electrophysiologically based optimization methods with different pacing parameters in patient undergoing resynchronization treatment. In *Proceedings of The 30th Annual International Conference of the IEEE/EMBS, Aug 20-24, Vancouver, British Columbia, Canada*, pages 1741-1744, 2008.

2. Two and half years full scholarship from Landesgraduiertenförderungsgesetz (LGFG).

3. Prize at student competition, 3rd conference of electrical and computer engineering, Kermanshah, Iran, 2003 (1. place).
   R. Miri, et al. Applying 1-D EZW algorithm to the RF signal to compress the ultrasound images. In *Proceeding of the 3rd student conference in electrical and computer enginerring, Kermanshah, Iran*, 2003.

Publications

1. R. Miri, M. Reumann, D. Farina, and O. Dössel. Concurrent optimization of timing delays and electrode positioning in biventricular pacing based on a computer heart model assuming 17 left ventricular segments. *Biomed Tech,* vol. 54, pages 55-65, 2009.

2. R. Miri, I. M. Graf, and O. Dössel. Efficiency of Timing Delays and Electrode Positions in Optimization of Biventricular Pacing: a Simulation Study. *IEEE Transaction on Biomedical Engineering,* In Press, 2009.

3. R. Miri, I. M. Graf, J. V. Bayarri, and O. Dössel. Application of Body Surface Potential Map in Computerized Optimization of Biventricular Pacing Therapy. *Submitted 2009.*

4. R. Miri, C. Wolpert, and O. Dössel. Computer Model Optimization of Cardiac Resynchronization Therapy Using Body Surface Potential Map. *Submitted 2009.*

5. R. Miri, and O. Dössel. Computerized Optimization of Biventricular Pacing Using Body Surface Potential Map. *Submitted 2009.*

6. R. Miri, M. Reumann, D. Keller, D. Farina, and O. Dössel. Comparison of the electrophysiologically based optimization methods with different pacing parameters in patient undergoing resynchronization treatment. In *Proceedings of The 30th Annual International Conference of the IEEE/EMBS, Aug 20-24, Vancouver, British Columbia, Canada*, pages 1741-1744, 2008.

7. O. Dössel, G. Seemann, D. Farina, D. U. J. Keller, R. Miri, F. M. Weber, and D. L. Weiss. Visions in Modeling of Cardiac Arrhythmogenic Diseases and their Therapies. In *IFMBE Proceedings of 14th Nordic-Baltic Conference on Biomedical Engineering and Medical Physics, NBC 2008, June 16-20, 2008 Riga, Latvia*, vol. 20, pages 450-453, 2008.

8. R. Miri, M. Reumann, and et al. Computer based optimization of biventricular pacing according to the left ventricular 17 myocardial segments. In *Proceedings of The 29th Annual International Conference of the IEEE/EMBS, Aug 23-26. 2007, Lyon, France*, pages 1418-1421, 2007.

9. R. Miri, M. Reumann, D. Farina, B. Osswald, and O. Dössel. Optimizing a-v and v-v delay in cardiac resynchronization therapy in simulations including ventricular heterogeneity. In *Proceedings of the fifth IASTED International Conference on Biomedical Enginerring, Feb 14-16, Innsbruck, Austria*, pages 20-25, 2007.

10. R. Miri, M. Reumann, D. Farina, B. Osswald, and O. Dössel. Computer assisted optimization of biventricular pacing assuming ventricular heterogeneity. In *IFMBE Proceedings of 11th Mediterranean Conference on Medical and Biomedical Engineering and Computing, June 26-30, Ljubljana, Slovenia*, vol. 16, pages 541-544, 2007.

11. R. Miri, M. Reumann, D. Keller, D. Farina, and O. Dössel. A non-invasive computer based optimization strategy of biventricular pacing. In *Proc. CURAC, Oct 11-13,*

Karlsruhe, Germany, pages 133-136, 2007.

12. R. Miri, M. Reumann, D. Keller, D. Farina, C. Wolpert, and O. Dössel. Optimization of cardiac resynchronization therapy based on a computer heart model assuming 17 left ventricular segments. In *Proc. BMT, Sep 26-29, Aachen, Germany*, vol. 52, 2007.

13. M. Reumann, D. Farina, R. Miri, S. Lurz, B. Osswald, and O. Dössel. Computer model for the optimization of av and vv delay in cardiac resynchronization therapy. *Progress in Biophysics and Molecular Biology*, vol. 45(9), pages 845-854, 2007.

14. R. Miri, S. K. Setarehdan, and P. Jabbedar Maralani. Ultrasound data compression using 1-D EZW algorithm applied to the ultrasound RF signals. In *Proceedings of the fifth IASTED International Conference on Biomedical Enginerring, Jun 25-27, Salzburg, Austria*, pages 105-109, 2003.

15. R. Miri, S. K. Setarehdan, and P. Jabbedar Maralani. Ultrasound data compression in a tele-ultrasound system. In *Proceedings of the fifth IASTED International Conference on Biomedical Enginerring, Jun 25-27, Salzburg, Austria*, pages 110-113, 2003.

16. R. Miri, S. K. Setarehdan, and P. Jabbedar Maralani. Wavelet transform based ultrasound scanline compression in a tele-ultrasound system. In *Proceedings of the 7th world multi conference on systemics, cybernetics and informatics (SCI), July 27-30, Orlando, Florida, USA*, pages 164-169, 2003.

17. R. Miri, S. K. Setarehdan, and P. Jabbedar Maralani. Ultrasound data compression in a tele-ultrasound system. In *Proceedings of the World congress on medical physics and biomedical engineering, Aug 24-29, Sydney, Australia*, pages 110-113, 2003.

18. R. Miri, S. K. Setarehdan, and P. Jabbedar Maralani. Medical ultrasound image compression and coding. In *Proceeding of the International conference of ultrasonics, 30 Jun-3 July, Granda, Spain*, 2003.

19. R. Miri, S. K. Setarehdan, and P. Jabbedar Maralani. Design a data compression method in a tele-ultrasound system. In *Proceeding of the International Symposium on Telecommunications (IST), Isfahan, Iran*, pages 144-147, 2003.

20. R. Miri, S. K. Setarehdan, and P. Jabbedar Maralani. Applying 1-D EZW algorithm to the RF signal to compress the ultrasound images. In *Proceeding of the 3rd student conference in electrical and computer enginerring, Kermanshah, Iran*, 2003.

21. R. Miri, S. K. Setarehdan, and P. Jabbedar Maralani. Ultrasound scanline compression with a wavelet based method. In *Proceeding of the 3rd student conference in electrical and computer enginerring, Kermanshah, Iran*, 2003.

22. K. Tavakolian, A. M. Nasrabadi, S.K. Setarehdan, M.A. Khalilzadeh, R. Miri, and M. Falaknaz. Effects of different feature vectors and neural network topology on eeg mental task classification. In *Proceedings of the fifth IASTED International Conference on Biomedical Enginerring, Jun 25-27, Salzburg, Austria*, pages 39-43, 2003.

Supervised Master Theses

J. V. Bayarri Ribelles, Validation of optimized cardiac resynchronization therapy based on multichannels ECG of individual patients, Master thesis, Institute for Biomedical Engineering, Universität Karlsruhe (TH), 2008.

B. Carbonell Pascual, Optimization of cardiac resynchronization for patients with left bundle branch block and myocardial infarction, Master thesis, Institute for Biomedical Engineering, Universität Karlsruhe (TH), 2008.

Universität Karlsruhe (TH)
Institute of Biomedical Engineering

The efficacy of cardiac resynchronization therapy (CRT) through biventricular pacing (BVP) has been demonstrated by numerous studies in patients suffering from congestive heart failure. In order to achieve a guideline for optimal treatment with BVP devices, an automated non-invasive strategy based on an electrophysiological computer model of the heart is presented. The presented research investigates an off-line optimization algorithm based on different electrode positioning and timing delays. A computer model of the heart was used to simulate the left bundle branch block (LBBB), myocardial infarction (MI) and reduction of intraventricular conduction velocity. The optimization method evaluates the error between the healthy case and the pathology with/without pacing case in terms of activation times and QRS duration.The clinical measurements of body surface potential map (BSPM) are used to parameterize the computer model of the heart to represent the individual pathology by solving the inverse problem, which leads to a more realistic heart model for simulations. Afterwards, the simulated ECGs for optimal pacing are compared to the measured ECGs after implantation. The similarity in the QRS duration between measured and simulated ECG signals indicates the success of the method.

ISSN: 1864-5933
ISBN: 978-3-86644-360-0

www.uvka.de